Riesz-projection-based methods for the numerical simulation of resonance phenomena in nanophotonics

Dissertation
zur Erlangung des Grades eines
Doktors der Naturwissenschaften (Dr. rer. nat.)

am Fachbereich Mathematik und Informatik
der Freien Universität Berlin

vorgelegt von

Felix Binkowski

Berlin, 2023

Selbstständigkeitserklärung

Name: Binkowski
Vorname: Felix

Ich erkläre gegenüber der Freien Universität Berlin, dass ich die vorliegende Dissertation selbstständig und ohne Benutzung anderer als der angegebenen Quellen und Hilfsmittel angefertigt habe. Die vorliegende Arbeit ist frei von Plagiaten. Alle Ausführungen, die wörtlich oder inhaltlich aus anderen Schriften entnommen sind, habe ich als solche kenntlich gemacht. Diese Dissertation wurde in gleicher oder ähnlicher Form noch in keinem früheren Promotionsverfahren eingereicht. Mit einer Prüfung meiner Arbeit durch ein Plagiatsprüfungsprogramm erkläre ich mich einverstanden.

_____   _____

Datum   Unterschrift

Einzelarbeiten für die Dissertation

Diese Dissertation ist eine kumulative Arbeit basierend auf den folgenden fünf Einzelarbeiten:

- Lin Zschiedrich, Felix Binkowski, Niko Nikolay, Oliver Benson, Günter Kewes, and Sven Burger. Riesz-projection-based theory of light-matter interaction in dispersive nanoresonators. *Phys. Rev. A* 98, 043806 (2018).

- Felix Binkowski, Lin Zschiedrich, Martin Hammerschmidt, and Sven Burger. Modal analysis for nanoplasmonics with nonlocal material properties. *Phys. Rev. B* 100, 155406 (2019).

- Felix Binkowski, Fridtjof Betz, Rémi Colom, Martin Hammerschmidt, Lin Zschiedrich, and Sven Burger. Quasinormal mode expansion of optical far-field quantities. *Phys. Rev. B* 102, 035432 (2020).

- Felix Binkowski, Lin Zschiedrich, and Sven Burger. A Riesz-projection-based method for nonlinear eigenvalue problems. *J. Comput. Phys.* 419, 109678 (2020).

- Felix Binkowski, Fridtjof Betz, Martin Hammerschmidt, Philipp-Immanuel Schneider, Lin Zschiedrich, and Sven Burger. Computation of eigenfrequency sensitivities using Riesz projections for efficient optimization of nanophotonic resonators. *Commun. Phys.* 5, 202 (2022).

Weitere Publikationen

Während der Promotion sind die folgenden weiteren Publikationen entstanden:

- Fridtjof Betz, Felix Binkowski, Martin Hammerschmidt, Lin Zschiedrich, and Sven Burger. Resonance Expansion of Quadratic Quantities with Regularized Quasinormal Modes. *Phys. Status Solidi A*, 2200892 (2023).

- Eduardo López-Fraguas, Felix Binkowski, Sven Burger, Sylvia Hagedorn, Braulio García-Cámara, Ricardo Vergaz, Christiane Becker, and Phillip Manley. Tripling the light extraction efficiency of a deep ultraviolet LED using a nanostructured p-contact. *Sci. Rep.* 12, 11480 (2022).

- Rémi Colom, Felix Binkowski, Fridtjof Betz, Yuri Kivshar, and Sven Burger. Enhanced Purcell factor for nanoantennas supporting interfering resonances. *Phys. Rev. Res.* 4, 023189 (2022).

- Tong Wu, Denis Arrivault, Marc Duruflé, Alexandre Gras, Felix Binkowski, Sven Burger, Wei Yan, and Philippe Lalanne. Efficient hybrid method for the modal analysis of optical microcavities and nanoresonators. *J. Opt. Soc. Am. A* 38, 1224 (2021).

- Fridtjof Betz, Felix Binkowski, and Sven Burger. RPExpand: Software for Riesz projection expansion of resonance phenomena. *SoftwareX* 15, 100763 (2021).

- Kevin Martens, Felix Binkowski, Linh Nguyen, Li Hu, Alexander O. Govorov, Sven Burger, and Tim Liedl. Long- and short-ranged chiral interactions in DNA-assembled plasmonic chains. *Nat. Commun.* 12, 2025 (2021).

- Felix Binkowski, Tong Wu, Philippe Lalanne, Sven Burger, and Alexander O. Govorov. Hot Electron Generation through Near-Field Excitation of Plasmonic Nanoresonators. *ACS Photonics* 8, 1243 (2021).

- Philippe Lalanne, Wei Yan, Alexandre Gras, Christophe Sauvan, Jean-Paul Hugonin, Mondher Besbes, Guillaume Demésy, Minh Duy Truong, Boris Gralak, Frédéric Zolla, André Nicolet, Felix Binkowski, Lin Zschiedrich, Sven Burger, Jörn Zimmerling, Rob Remis, Paul Urbach, Haitao Liu, and Thomas Weiss. Quasinormal mode solvers for resonators with dispersive materials. *J. Opt. Soc. Am. A* 36, 686 (2019).

- Felix Binkowski, Lin Zschiedrich, and Sven Burger. An auxiliary field approach for computing optical resonances in dispersive media. *J. Eur. Opt. Soc.-Rapid Publ.* 15, 3 (2019).

- Günter Kewes, Felix Binkowski, Sven Burger, Lin Zschiedrich, and Oliver Benson. Heuristic Modeling of Strong Coupling in Plasmonic Resonators. *ACS Photonics* 5, 4089 (2018).

Zusammenfassung

Resonanzeffekte treten in allen physikalischen Systemen auf, die durch Wellen beschrieben werden, und sie sind für die Beschreibung von Wellenausbreitung und Interferenz unerlässlich. Auf dem Gebiet der Nanophotonik basieren viele Geräte auf den durch Lichtquellen angeregten Resonanzen mit ihren stark erhöhten elektromagnetischen Feldern. Die numerische Simulation von Resonanzen ist ein wichtiges Hilfsmittel für die Entwicklung und Optimierung der Geräte. Die Resonanzen sind die Lösungen der zeitharmonischen quellenfreien Maxwell-Gleichungen mit Verlustmechanismen. Die entsprechenden Eigenwertprobleme sind aufgrund der Verluste nicht-Hermitesch, was zu komplexwertigen Eigenwerten führt. Die Materialdispersion, die in der Nanophotonik typischerweise signifikant ist, führt zu nichtlinearen Eigenwertproblemen.

In dieser Dissertation entwickeln wir einen auf der Riesz-Projektion basierenden Ansatz für die Expansion von elektromagnetischen Feldern, die von Lichtquellen erzeugt werden, in Resonanzen. Wir berechnen die Riesz-Projektionen durch Konturintegration in der komplexen Frequenzebene. Die numerische Realisierung basiert im Wesentlichen auf der Lösung der Maxwell-Gleichungen mit einem Quellterm, das heißt der Lösung von linearen Gleichungssystemen. Dabei werden die Maxwell-Gleichungen direkt bei den gegebenen Frequenzen auf den Integrationskonturen ausgewertet, sodass eine Linearisierung der entsprechenden nichtlinearen Eigenwertprobleme nicht erforderlich ist. Das macht die auf der Riesz-Projektion basierenden Methoden zu einer natürlichen Wahl für die Behandlung von Eigenwertproblemen aus dem Bereich der Nanophotonik. Wir erweitern den Ansatz der Riesz-Projektions-Expansion auf optische Größen im Fernfeld, was aufgrund der räumlichen Divergenz der Resonanzen mit zunehmender Entfernung von den zugrunde liegenden Resonatoren problematisch ist. Basierend auf den Ideen der Riesz-Projektions-Expansion entwickeln wir außerdem Methoden zur Berechnung physikalisch relevanter Eigenwerte und zur Berechnung von Sensitivitäten von Eigenwerten. Physikalisch relevant bedeutet, dass die Eigenwerte in Bezug auf die Resonanzexpansion der interessierenden physikalischen Größe signifikant sind.

Durch die Verwendung physikalischer Lösungen der Maxwell-Gleichungen für die Konturintegration haben die entwickelten numerischen Methoden einen starken Bezug zur zugrunde liegenden Physik. Die Methoden können auf jedes Materialsystem und auf jede messbare physikalische Größe angewendet werden, die sich aus dem elektrischen Feld herleiten lässt. Wir wenden die numerischen Methoden auf mehrere aktuelle nanophotonische Strukturen an, wie zum Beispiel Einzelphotonenquellen aus dem Bereich der Quantentechnologie, plasmonische Nanostrukturen, die sich durch nichtlokale Materialeigenschaften auszeichnen, und Nanoantennen, die auf gebundenen Zuständen im Kontinuum basieren. Die in dieser Dissertation vorgestellten Ansätze werden für nanophotonische Systeme entwickelt, lassen sich aber auf jedes Resonanzproblem anwenden.

Danksagung

Ich möchte mich herzlichst bei Christof Schütte für die Unterstützung meines Promotionsvorhabens und für das Betreuen meiner Doktorarbeit bedanken und ich möchte Carsten Rockstuhl vielmals für die Erstellung des Zweitgutachtens danken.

Ich möchte Sven Burger ganz herzlich dafür danken, dass er mich in das Gebiet der Nanophotonik eingeführt hat und dass seine Tür immer für mich offen stand. Ich bedanke mich für die kontinuierliche Unterstützung in meinen Forschungsprojekten und für die vielen schönen Gespräche auf dem roten Sofa. Ich bin ihm sehr dankbar dafür, dass er mich immer wieder motiviert hat, meine Forschungsergebnisse zu veröffentlichen.

Ich danke Lin Zschiedrich herzlichst dafür, dass er seine mathematischen und physikalischen Forschungsideen mit mir geteilt und sich immer die Zeit genommen hat, meine vielen Fragen zu beantworten. Auch für die vielen privaten Gespräche möchte ich mich bedanken.

Ich möchte außerdem Martin Hammerschmidt meinen herzlichsten Dank aussprechen, für die vielen Diskussionen bezüglich numerischer Implementierungen, die sehr hilfreichen Bug-Fixes, die Hilfe bei Fragen zur Finiten-Elemente-Methode und die lustigen Unterhaltungen bei einer Tasse Kaffee.

Ich möchte mich bei Fridtjof Betz für die äußerst angenehme Zusammenarbeit in den letzten Jahren bedanken und bei Philipp-Immanuel Schneider für die sehr hilfreichen Erklärungen zur Quantenoptik.

Ich möchte auch Philippe Lalanne für die vielen anregenden Diskussionen über Resonanzen danken. Außerdem bedanke ich mich bei Günter Kewes, Tong Wu, Tim Liedl, Philip Kristensen, Guillaume Demésy, André Nicolet und Yuri Kivshar für die tolle Zusammenarbeit und für die wissenschaftlichen Gespräche während meiner Promotion.

Ein großer Dank geht an meine gesamte Arbeitsgruppe, die Computational Nanooptics Gruppe am Zuse Institute Berlin. Ich möchte hier, zusätzlich zu den bereits erwähnten Personen, Phillip Manley, Matthias Plock, Rémi Colom, Lilli Kuen, Peter Tillmann, Ivan Sekulic, Xavier Garcia Santiago, Theresa Höhne, Klaus Jäger und Frank Schmidt nennen. Vielen Dank für all die wissenschaftlichen Gespräche, die schönen Pausen und die tolle Arbeitsatmosphäre.

Ich möchte mich bei meiner Mutter Andrea und meinem Vater Volker für die immerwährende Unterstützung bedanken, die meinen Weg in der Wissenschaft erst möglich gemacht hat.

Ein ganz besonderer Dank geht an meine Frau Lisa. Ohne ihre liebevolle Unterstützung in allen Lebenslagen wäre diese Doktorarbeit nicht möglich gewesen. Und danke, Karl, dass du mich jeden Tag zum Lachen bringst.

Contents

1

Abstract

Resonance effects are ubiquitous in physics and essential for understanding wave propagation and interference. In the field of nanophotonics, devices are often based on the strong confinement of light by resonances. The numerical simulation of resonances plays a crucial role for the design and optimization of the devices. The resonances are electromagnetic field solutions to the time-harmonic source-free Maxwell's equations with loss mechanisms. The corresponding eigenproblems are non-Hermitian due to the losses leading to complex-valued eigenvalues. The material dispersion, which is typically significant in nanophotonics, results in nonlinear eigenproblems.

In this thesis, we develop an approach based on Riesz projections for the expansion of electromagnetic fields caused by light sources into resonances. The Riesz projection expansion is computed by contour integration in the complex frequency plane. The numerical realization essentially relies on solving Maxwell's equations with a source term, meaning solving linear systems of equations. For this, Maxwell's equations are directly evaluated at the given frequencies on the integration contours, which implies that linearization of the corresponding nonlinear eigenproblems is not required. This makes Riesz-projection-based approaches a natural choice for dealing with eigenproblems from the field of nanophotonics. We further extend the Riesz projection expansion approach to optical far-field quantities, which is not straightforward due to the spatial divergence of the resonances with increasing distance from the underlying resonators. Based on the ideas of the Riesz projection expansion, we introduce approaches for the calculation of physically relevant eigenvalues and for computing eigenvalue sensitivities. Physically relevant means that the eigenvalues are significant with respect to the resonance expansion of the physical observable of interest.

By using physical solutions to Maxwell's equations for the contour integration, the developed numerical methods have a strong relation to physics. The methods can be applied to any material system and to any measurable physical quantity that can be derived from the electric field. We apply the numerical methods to several recent nanophotonic applications, for example, single-photon sources from the field of quantum technology, plasmonic nanostructures characterized by nonlocal material properties, and nanoantennas based on bound states in the continuum. The approaches introduced in this thesis are developed for nanophotonic systems, but can be applied to any resonance problem.

1 Introduction

Optical technologies play a major role in the development of high-technology devices. Modern nanofabrication tools enable the scaling of material systems down to the wavelength scale of visible light, allowing the exploration of new regimes of light-matter interaction [1–4]. The resulting nanophotonic structures are used, for example, for ultrasensitive sensing to detect single molecules [5, 6], for tuning photochemistry in solar energy devices [7–9], and for designing devices in the emerging field of quantum technology [10–12].

All these cutting-edge applications are based on highly localized electromagnetic field energies of resonances excited by light sources [13–15]. Resonance phenomena occur not only in the form of electromagnetic waves in the field of nanophotonics, but in all physical systems characterized by waves. Examples include vibrations in mechanical systems [16, 17], acoustic resonances [18, 19], and scattering resonances in quantum mechanics [20–24]. The naturally occurring loss mechanisms, such as damping or open boundaries, cause the solutions of the associated wave equations to decay exponentially with time. These solutions are given by a superposition of eigenstates, the so-called quasinormal modes or resonances, where the rate of decay of each state is described by the imaginary part of the associated eigenvalue. The real parts of the eigenvalues describe the oscillation rates of the states. The numerical modeling and simulation of the corresponding eigenproblems is essential for the design and optimization of resonance-based devices. An important figure of merit for nanophotonic devices is the quality (Q) factor [25], which is directly linked to the eigenvalues. It can be calculated by the scaled ratio of the real and imaginary part of an eigenvalue. For low loss systems, the Q-factor of a resonance represents the relation between stored and dissipated electromagnetic field energy. Nanoresonators with high Q-factors are used to increase the brightness of quantum light sources or to enhance the sensitivity of sensors [26]. A further central figure of merit is the Purcell factor [27], which describes the emission enhancement of quantum light sources due to their coupling to the underlying resonances [28]. High Purcell factors are essential for increasing the photon extraction efficiencies of single-photon sources [29].

In nanophotonics, resonances are electromagnetic waves, which can be computed by solving the time-harmonic source-free Maxwell's equations with loss mechanisms [30–32]. The eigenproblems are non-Hermitian due to the underlying losses. After numerical discretization, they typically have the form $Au = \omega^2 B(\omega)u$, where $\omega \in \mathbb{C}$ is an eigenvalue and $u \in \mathbb{C}^n$ is an eigenvector corresponding to ω. The matrices $A \in \mathbb{C}^{n \times n}$ and $B(\omega) \in \mathbb{C}^{n \times n}$ are the system matrices. The eigenvalues are called eigenfrequencies and the eigenvectors, which are the resonances in a finite dimensional basis, are called eigenmodes. The angular frequency dependence of the mass matrix $B(\omega)$ describes the material dispersion and renders the eigenproblem nonlinear [33, 34]. In nanophotonics, the material dispersion is often significant and is usually described by rational func-

tions, for example, Drude-Lorentz models [35, 36] or rational fits to measured material data [36, 37]. To compute the eigenfrequencies and eigenmodes, the standard approach is linearization [30–32, 38] with a subsequent application of the Arnoldi method [39] to the linearized system. In many applications, the dimension of the system matrices is very large, while only a few eigenmodes are important for the physical characterization of the underlying problem. The connection between physical properties of a system and its eigenmodes is given by a resonance expansion, where physical observables are decomposed into a sum of weighted eigenmodes. Resonance expansion is a powerful tool for the investigation of light-matter interaction in nanoresonators and is an active area of research [15, 28, 38, 40–53].

In the last decade, contour-integral-based approaches for solving eigenproblems have attracted attention [54–63]. These methods compute contour integrals of the form $\oint_C \omega^k \left(A - \omega^2 B(\omega) \right)^{-1} f d\omega$, where $k \geq 0$, $f \in \mathbb{C}^n$ is some vector, and $C \in \mathbb{C}$ is a chosen integration contour. Quadrature formulas are used to numerically discretize the chosen contour, where a linear system of equations has to be solved at each integration point. The vector f is thereby projected onto the eigenspace associated with the eigenfrequencies within the contour. The resulting subspace can then be used to approximate the eigenfrequencies inside the contour and to approximate the corresponding eigenmodes. The eigenvector residual function $A - \omega^2 B(\omega)$ is directly evaluated at the complex-valued integration points lying on the contour. In this way, the eigenproblem need not be linearized, making contour integral methods a natural choice for the numerical treatment of nonlinear eigenproblems. However, in the field of nanophotonics, contour integral methods are rather rarely used.

Motivated by these findings, we developed contour-integral-based approaches for resonance expansion and for computing eigenfrequencies and eigenmodes in nanophotonics. This thesis is about these approaches and consists of the following five individual works:

- Ref. [64]: Lin Zschiedrich, Felix Binkowski, Niko Nikolay, Oliver Benson, Günter Kewes, and Sven Burger. Riesz-projection-based theory of light-matter interaction in dispersive nanoresonators. *Phys. Rev. A 98*, 043806 (2018).

  Author contributions: L.Z. and S.B. designed the research; L.Z. conceived the theoretical approach; F.Bi., L.Z., and S.B. developed the numerical method and wrote the initial manuscript; F.Bi. implemented the numerical method, performed the numerical simulations, and prepared the figures; All authors discussed the results and contributed to the final version of the manuscript.

- Ref. [65]: Felix Binkowski, Lin Zschiedrich, Martin Hammerschmidt, and Sven Burger. Modal analysis for nanoplasmonics with nonlocal material properties. *Phys. Rev. B 100*, 155406 (2019).

  Author contributions: F.Bi., M.H., and L.Z. designed the research and developed the numerical method; F.Bi. wrote the initial manuscript, implemented the numerical method, performed the numerical simulations, and prepared the figures; All authors discussed the results and contributed to the final version of the manuscript.

- Ref. [66]: Felix Binkowski, Fridtjof Betz, Rémi Colom, Martin Hammerschmidt, Lin Zschiedrich, and Sven Burger. Quasinormal mode expansion of optical far-field quantities. *Phys. Rev. B 102*, 035432 (2020).

Author contributions: F.Bi., L.Z., and S.B. designed the research; F.Bi., F.Be, and L.Z. developed the numerical method; F.Bi. wrote the initial manuscript; F.Bi. and F.Be. implemented the numerical method and performed the numerical simulations; F.Bi. prepared the figures; All authors discussed the results and contributed to the final version of the manuscript.

- Ref. [67]: Felix Binkowski, Lin Zschiedrich, and Sven Burger. A Riesz-projection-based method for nonlinear eigenvalue problems. *J. Comput. Phys.* 419, 109678 (2020).

  Author contributions: F.Bi., L.Z., and S.B. designed the research; F.Bi. developed the numerical method, wrote the initial manuscript, implemented the numerical method, performed the numerical simulations, and prepared the figures; All authors discussed the results and contributed to the final version of the manuscript.

- Ref. [68]: Felix Binkowski, Fridtjof Betz, Martin Hammerschmidt, Philipp-Immanuel Schneider, Lin Zschiedrich, and Sven Burger. Computation of eigenfrequency sensitivities using Riesz projections for efficient optimization of nanophotonic resonators. *Commun. Phys.* 5, 202 (2022).

  Author contributions: F.Bi., L.Z., and S.B. designed the research; F.Bi. developed the numerical method, wrote the initial manuscript, implemented the numerical method, and prepared the figures; F.Bi. and F.Be. performed the numerical simulations; All authors discussed the results and contributed to the final version of the manuscript.

We proposed a new resonance expansion approach based on contour integrals [64]. To obtain the expansion terms, projections onto eigenspaces, so-called Riesz projections, corresponding to eigenfrequencies of Maxwell's equations are used. Then, we investigated optical properties of nonlocal material systems [65], where linearization of the underlying nonlinear eigenproblems is not possible with standard eigensolvers. A contour integral method known from the literature was used to calculate eigenfrequencies and eigenmodes, and Riesz projections were applied for resonance expansion. Based on the knowledge gained through this research, we developed an approach for resonance expansion of optical quantities at large distances from the nanoresonators [66]. This is not straightforward because the eigenmodes diverge exponentially with increasing distance from the resonators due to the underlying loss mechanisms. Riesz projections were applied to overcome this problem. We further developed an algorithm based on Riesz projections to calculate physically relevant eigenfrequencies [67]. Specific eigenfrequencies are prioritized in the proposed algorithm by selecting physical source terms as vector f for the contour integration. The algorithm was applied to nanophotonic and quantum mechanical problems. We also introduced a Riesz-projection-based approach to compute eigenfrequency sensitivities [68]. The approach exploits direct differentiation, which enables an efficient numerical implementation. This was demonstrated by an optimization of a topical nanophotonic resonator with respect to several shape parameters.

This thesis contributes to the numerical modeling and simulation of resonance phenomena occurring in the field of nanophotonics. The approaches developed focus on

the physical quantities to be studied. Nanophotonic systems can be analyzed by resonance expansion of physical observables and by computation of physically relevant eigenfrequencies and their sensitivities. Contour integration allows the investigation of any physical observable that can be derived from the electric field in arbitrary material systems. Moreover, the numerical implementation is straightforward, since contour integration essentially relies on solving linear systems of equations. Corresponding solvers are implemented in state-of-the-art software libraries. The general applicability and ease of numerical implementation make the approaches presented in this thesis easily accessible to researchers from the computational nanophotonics community. Since the methods can be applied not only to resonance problems from the field of nanophotonics, but to any resonance problem, they can also be used in other areas of physics.

This thesis is divided into five chapters assigned to the five individual works [64–68]. Each chapter begins with a connecting text followed by one of the works. Within the connecting texts, important aspects, which are essential for the overall understanding of the thesis, are presented and important physical quantities are introduced and defined. The thesis concludes with a summary of all individual works. In the appendix, the three further individual works [69–71] of the doctoral candidate are presented, which are directly related to the thesis.

2 Riesz projection expansion for the investigation of light-matter interaction

In nanophotonics, in the steady-state regime, light scattering by an open material system can be described by the time-harmonic Maxwell's equation in second order form,

$$\nabla \times \mu(\mathbf{r}, \omega_0)^{-1} \nabla \times \mathbf{E}(\mathbf{r}, \omega_0) - \omega_0^2 \epsilon(\mathbf{r}, \omega_0) \mathbf{E}(\mathbf{r}, \omega_0) = i\omega_0 \mathbf{J}(\mathbf{r}), \qquad (2.1)$$

equipped with transparent boundary conditions, where $\mathbf{E}(\mathbf{r}, \omega_0) \in \mathbb{C}^3$ is the electric field, $\mathbf{J}(\mathbf{r}) \in \mathbb{C}^3$ is a source term corresponding to an optical source, $\omega_0 \in \mathbb{R}$ is the angular frequency, and $\mathbf{r} \in \mathbb{R}^3$ is the spatial position. For optical frequencies, the permeability typically equals the vacuum permeability μ_0. The permittivity $\epsilon(\mathbf{r}, \omega_0) = \epsilon_{\mathrm{r}}(\mathbf{r}, \omega_0)\epsilon_0$, where $\epsilon_{\mathrm{r}}(\mathbf{r}, \omega_0)$ is the relative permittivity and ϵ_0 is the vacuum permittivity, describes the material dispersion and the spatial distribution of material. Problems given by Equation (2.1) are called scattering problems. Note that, in the following, we consider losses due to open material systems. However, the proposed approaches are not limited to this loss channel. The inclusion of damping is also possible.

Resonance expansion approaches give a representation of the scattering solution $\mathbf{E}(\mathbf{r}, \omega_0)$ by a sum of terms related to the resonances of the underlying system, e.g.,

$$\mathbf{E}(\mathbf{r}, \omega_0) = \sum_{m=1}^{M} \alpha_m(\omega_0)\tilde{\mathbf{E}}_m(\mathbf{r}) + \mathbf{R}(\mathbf{r}, \omega_0), \qquad (2.2)$$

where $\alpha_m(\omega_0) \in \mathbb{C}$ are the expansion coefficients and $\mathbf{R}(\mathbf{r}, \omega_0) \in \mathbb{C}^3$ is the remainder of the expansion. The eigenmodes $\tilde{\mathbf{E}}_m(\mathbf{r}) \in \mathbb{C}^3$ are solutions to the eigenproblem

$$\nabla \times \mu_0^{-1}\nabla \times \tilde{\mathbf{E}}_m(\mathbf{r}) - \tilde{\omega}_m^2 \epsilon(\mathbf{r}, \tilde{\omega}_m)\tilde{\mathbf{E}}_m(\mathbf{r}) = 0 \qquad (2.3)$$

with transparent boundary conditions, where $\tilde{\omega}_m \in \mathbb{C}$ are the corresponding eigenfrequencies. Problems given by Equation (2.3) are called resonance problems. The typically applied framework [48] for the computation of the resonance expansion given by Eq. (2.2) is the computation of the eigenmodes $\tilde{\mathbf{E}}_m(\mathbf{r})$ by solving Eq. (2.3), an appropriate normalization of the eigenmodes, and the calculation of the expansion coefficients $\alpha_m(\omega_0)$ using, e.g., a scalar product. This framework relies on the chosen linearization of the nonlinear eigenproblem given by Eq. (2.3), which is often based on the underlying physics and called auxiliary field approach [38]. The reader is referred to Section 8.1 for the report on such an approach. Note that the resonance expansion given by Eq. (2.2) is not unique. Different formulas can be used for the calculation of the expansion coefficients [48].

In Ref. [64], we develop a resonance expansion approach based on Riesz projections,

$$\mathbf{E}(\mathbf{r}, \omega_0) = \sum_{m=1}^{M} \mathbf{E}_m(\mathbf{r}, \omega_0) + \mathbf{R}(\mathbf{r}, \omega_0),$$

$$\mathbf{E}_m(\mathbf{r}, \omega_0) = -\frac{1}{2\pi i} \oint_{C_m} \frac{\mathbf{E}(\mathbf{r}, \omega)}{\omega - \omega_0} d\omega \in \mathbb{C}^3, \quad \mathbf{R}(\mathbf{r}, \omega_0) = \frac{1}{2\pi i} \oint_{C_{\mathrm{nr}}} \frac{\mathbf{E}(\mathbf{r}, \omega)}{\omega - \omega_0} d\omega \in \mathbb{C}^3. \tag{2.4}$$

Each contour $C_m \in \mathbb{C}$ enclose one eigenfrequency $\tilde{\omega}_m$ and thus the expansion terms $\mathbf{E}_m(\mathbf{r}, \omega_0)$, which are Riesz projections [22], are directly related to the eigenfrequencies. Moreover, expansion coefficients $\alpha_m(\omega_0)$ from Eq. (2.2) can be derived such that there exists a relation between Riesz projections and normalized eigenmodes, given by $\mathbf{E}_m(\mathbf{r}, \omega_0) = \alpha_m(\omega_0)\tilde{\mathbf{E}}_m(\mathbf{r})$ [72]. The contour $C_{\mathrm{nr}} \in \mathbb{C}$ corresponds to the remainder of the expansion, which also comprises the nonresonant contributions. The terms $\mathbf{E}_m(\mathbf{r}, \omega_0)$ and the remainder $\mathbf{R}(\mathbf{r}, \omega_0)$ are computed by solving scattering problems given by Eq. (2.1) for complex-valued frequencies ω lying on the contours C_m and C_{nr}, respectively. In this way, the resonance problem given by Eq. (2.3) need not be solved, i.e., linearization of the nonlinear eigenproblem is not required. With regard to the notation, we note that, exclusively in Ref. [64], we perform the contour integration in the ω^2 plane. This has no effect on the derivation of the approach or on the calculation of the expansion terms. The reason for this choice is the appearance of ω^2 in Maxwell's equations.

We demonstrate the Riesz projection expansion for the electromagnetic field emitted by a quantum light source with material dispersion. The source is a nitrogen-vacancy (NV) center [73] in a diamond nanodisk. Such defects in diamond are topical candidates for single-photon sources [74]. We model the source with a dipole emitter $\mathbf{J}(\mathbf{r}) = \mathbf{j}\delta(\mathbf{r} - \mathbf{r}')$, where $\delta(\mathbf{r} - \mathbf{r}')$ is the Dirac delta distribution, $\mathbf{r}'$ is the location of the dipole emitter, and $\mathbf{j}$ is the dipole amplitude vector. We compute the resonance expansion of the Purcell factor,

$$\Gamma(\omega_0) = -\frac{1}{2}\mathrm{Re}\left(\mathbf{E}(\mathbf{r}', \omega_0) \cdot \mathbf{j}^*\right)/\Gamma_\mathrm{b}, \tag{2.5}$$

where Γ_b is the decay rate of the dipole emitter in homogeneous background material [28], and we identify the eigenmodes which are significant for the Purcell factor of the quantum light source.

To numerically realize the Riesz projection expansion given by Eq. (2.4) as well as the other contour integral approaches presented in the following chapters, we spatially discretize Eq. (2.1) with the finite element method (FEM) [75–77] using the software package JCMSUITE [78, 79]. The transparent boundary conditions are implemented using perfectly matched layers [80, 81]. The FEM discretization of Eq. (2.1) leads to the linear system of equations $\left(A - \omega_0^2 B(\omega_0)\right) u = f(\omega_0)$, where $A \in \mathbb{C}^{n \times n}$ and $B(\omega_0) \in \mathbb{C}^{n \times n}$ are the sparse FEM system matrices and $f(\omega_0) \in \mathbb{C}^n$ is a vector containing the source term. With $u \in \mathbb{C}^n$ as the electric field in a finite dimensional FEM basis, we obtain the discretized form of the Riesz projection expansion. For example, the discretized expansion terms are given by

$$u_m = -\frac{1}{2\pi i} \oint_{C_m} \frac{u}{\omega - \omega_0} d\omega = -\frac{1}{2\pi i} \oint_{C_m} \frac{\left(A - \omega^2 B(\omega)\right)^{-1} f(\omega)}{\omega - \omega_0} d\omega \in \mathbb{C}^n,$$

where the linear systems of equations $\left(A - \omega^2 B(\omega)\right) u = f(\omega)$ are solved using the scattering solver within JCMsuite for complex-valued frequencies ω lying on the integration contours C_m. The scattering solver is based on direct solvers for sparse linear systems of equations [82, 83]. For the contours, a circular or elliptical shape is chosen and the integrals are numerically realized using the trapezoidal rule, which leads to exponential convergence with respect to the number of integration points [84].

In the following, Ref. [64] is reprinted with permission from [Lin Zschiedrich, Felix Binkowski, Niko Nikolay, Oliver Benson, Günter Kewes, and Sven Burger. Riesz-projection-based theory of light-matter interaction in dispersive nanoresonators. *Phys. Rev. A* 98, 043806 (2018). DOI: 10.1103/PhysRevA.98.043806.] Copyright 2018 by the American Physical Society.

Riesz-projection-based theory of light-matter interaction in dispersive nanoresonators

Lin Zschiedrich,[1] Felix Binkowski,[2] Niko Nikolay,[3] Oliver Benson,[3] Günter Kewes,[3] and Sven Burger[1,2]

[1]*JCMwave GmbH, Bolivarallee 22, 14050 Berlin, Germany*
[2]*Zuse Institute Berlin, Takustraße 7, 14195 Berlin, Germany*
[3]*Institut für Physik & IRIS Adlershof, Humboldt-Universität zu Berlin, Newtonstraße 15, 12489 Berlin, Germany*

We introduce a theory to analyze the behavior of light emitters in nanostructured environments rigorously. Based on spectral theory, the approach opens the possibility to quantify precisely how an emitter decays to resonant states of the structure and how it couples to a background, also in the presence of general dispersive media. Quantification on this level is essential for designing and analyzing topical nanophotonic setups, e.g., in quantum technology applications. We use a numerical implementation of the theory for computing modal and background decay rates of a single-photon emitter in a diamond nanoresonator.

DOI: 10.1103/PhysRevA.98.043806

Introduction. Resonance phenomena are omnipresent in physics. Storage and transfer of energy between different resonant states allows one to explore wave effects in atomic, molecular, and optical physics as well as in nuclear and condensed-matter physics and in other fields of science. Optical resonators are scaled down to the wavelength scale and below by using modern nanotechnology, as demonstrated in various material systems [1,2], including plasmonic [3] and dielectric structures [4]. Placing pointlike sources in the vicinity of such nanoresonators or antennas enables exploration of new regimes of light-matter interaction. Examples are single-photon emission with high directivity [5–7], nanoscopic plasmon lasers [8,9], and modification of chemical reaction rates by exploiting strong coupling in microcavities [10].

Theoretical models of light-matter interaction are needed to understand and optimize the performance of related photonic devices. Maxwell's equations can be solved directly to obtain solutions for the electromagnetic field. For a deeper insight into physical properties, it is a common approach to use a modal description. The resonant response of metallic nanostructures is governed by surface plasmon polaritons. High-index dielectrics hosts electric and magnetic Mie-like modes which can be exploited in antenna design [4]. For understanding the interaction of emitters with nanoresonators, it is essential to precisely describe the coupling of the emitter to specific modes [11,12]. This coupling is quantified by individual modal Purcell factors [13,14]. Thus, in most approaches, the study of the (eigen-)modes and associated eigenfrequencies of the resonating structure is essential.

The simplest model for modal analysis, a closed nondissipative system, yields a Hermitian linear operator with a complete set of orthogonal eigenmodes. By duality and based on a scalar product, these eigenmodes also serve as projectors which allow for an expansion of the electromagnetic field into a sum of eigenmodes to characterize the light-matter interaction. In the past decades, the more challenging study of open systems, which are usually described by non-Hermitian operators, is an often addressed research topic in various applications including quantum mechanics [15–18] and

nano-optics [14,19–22]. In a nutshell, the concept of eigenmodes has been generalized to the theory of resonant states, also called quasinormal modes (QNMs). QNMs are orthogonal with respect to an unconjugated scalar product [23] which allows identification of QNMs with projectors again. Also, in the case of dispersive materials which are ubiquitously present in nano-optical resonators [3,24], there exist approaches for QNM expansion [14,21]. However, the orthogonality and normalization of the QNMs, especially in the case of dispersive media, are still under active research and discussed controversially in the literature [14,21,25–28]. The discrete set of QNMs is supplemented by the continuous spectrum of the operator capturing the nonresonant background scattering [29]. State-of-the-art approaches using QNM expansion do not incorporate the continuous spectrum. These can well be applied when coupling to the background is negligible [14]. However, important application classes rely on designs with significant background coupling which is present when low-quality (Q) factor resonances are involved [13]. For realizing integrated single-photon sources, the involved resonant states are preferably at low Q factor, enabling fast, pulsed operation [30]. Also, for modifying photochemical reactions, coupling of molecules to resonant states with a low Q factor is used due to better accessibility compared to high Q factor resonances [10]. Theoretical description and numerical optimization of related setups therefore essentially require precise treatment and precise distinction of coupling to the background and to the resonant states.

Riesz projections (RPs) can be used to compute these quantities in an elegant way. RPs are a well-known concept in spectral theory [15] and they do not rely on orthogonality relations and the explicit knowledge of eigenfunctions. RPs are based on contour integration and provide a powerful means to analyze the spectrum of partial differential operators. Note that parallel to this work, a scalar product involving auxiliary fields has been proposed to ensure the orthogonality of QNMs for typical dispersive media [31].

In this work, we present a theory for modeling dispersive light-matter interaction based on RPs. We show that RPs can
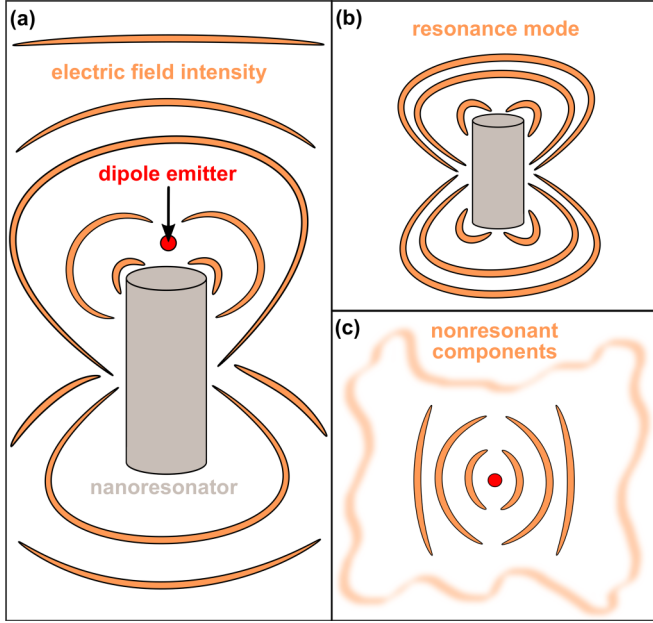
FIG. 1. Schematic decomposition of the electromagnetic field caused by a dipole emitter in the vicinity of a nanoresonator. (a) Total electromagnetic field. (b) A resonance mode of the nanoresonator. (c) Nonresonant components of the electromagnetic field. This part includes also the singularity resulting from the dipole source.

also be used to model the nonresonant background interaction in a closed form. The theory allows for a straightforward numerical implementation which essentially requires solving time-harmonic scattering problems for complex frequencies. We apply the method to compute modal decay rates of a dipole emitter embedded in a diamond nanodisk antenna showing a weak coupling to the QNMs and a significant background coupling.

Riesz projection expansion. In the following, we consider electromagnetic fields in the vicinity of optical nanostructures, as illustrated in Fig. 1. The total field, sketched in Fig. 1(a), is decomposed into resonant and nonresonant components [see Figs. 1(b) and 1(c)]. In the steady-state regime, the corresponding electric fields $\mathbf{E}(\mathbf{r}, \omega)$ are solutions to the time-harmonic Maxwell's equations in the second-order form

$$\nabla \times \mu^{-1} \nabla \times \mathbf{E}(\mathbf{r}, \omega) - \omega^2 \epsilon(\omega) \mathbf{E}(\mathbf{r}, \omega) = i\omega \mathbf{J}(\mathbf{r}), \quad (1)$$

where $\omega \in \mathbb{C}$ is a complex angular frequency. The material dispersion is described by the permittivity tensor $\epsilon(\omega)$, and the permeability tensor μ typically equals the vacuum permeability μ_0. The source term $\mathbf{J}(\mathbf{r})$ relates to impressed currents. For open problems, Eq. (1) is equipped with outgoing radiation conditions which can be realized by complex scaling in space of the corresponding partial differential operator. Incident exterior light sources can be incorporated in $\mathbf{J}(\mathbf{r})$. Physically relevant scattering solutions have real frequencies $\omega_0 \in \mathbb{R}$. The fields $\mathbf{E}(\mathbf{r}, \omega)$ can be regarded as an analytical continuation of $\mathbf{E}(\mathbf{r}, \omega_0)$ into the complex plane. In this context, the QNMs correspond to complex frequencies $\omega_m \in \mathbb{C}$, $m = 1, \ldots, M$, where $\mathbf{E}(\mathbf{r}, \omega)$ has a resonance pole, i.e., a singularity.

To decompose $\mathbf{E}(\mathbf{r}, \omega_0)$ into its resonant and nonresonant parts, we consider the $z = \omega^2$ plane and write $\mathbf{E}(\mathbf{r}, z) =$
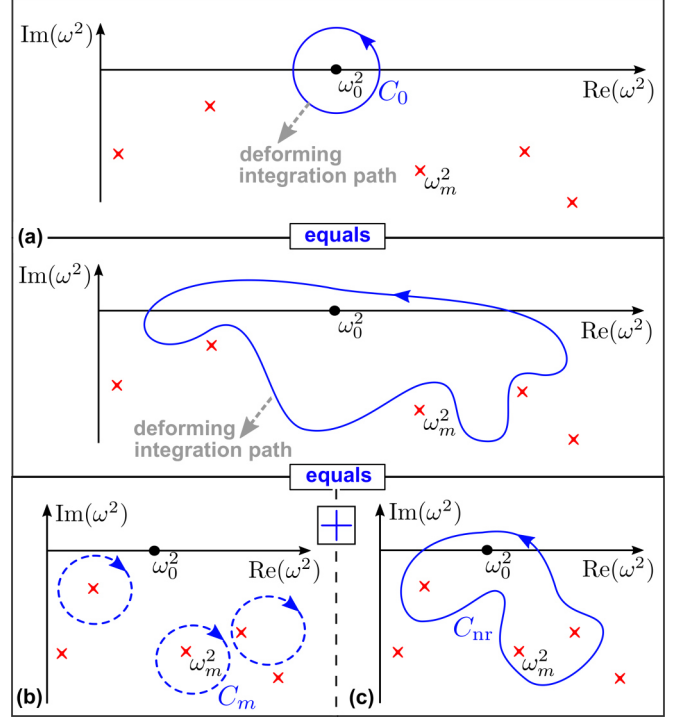

FIG. 2. Contour integration in the complex ω^2 plane for computing the Riesz projection expansion, Eq. (3). The red crosses represent resonance poles ω_m^2, the blue curves are the integration curves for Eqs. (2)–(5). (a) Top: Integration path C_0 around ω_0^2, see Eq. (2). Bottom: Deforming the integration path without enclosing resonance poles does not modify the integral. (b) Integration curves C_m in negative direction for computing Riesz projections, see Eq. (4). (c) Outer integration path C_{nr} for quantifying the interaction with nonresonant components, see Eq. (5).

$\mathbf{E}(\mathbf{r}, \omega = \sqrt{z})$. Cauchy's residue theorem gives

$$\mathbf{E}(\mathbf{r}, \omega_0) = \frac{1}{2\pi i} \oint_{C_0} \frac{\mathbf{E}(\mathbf{r}, z)}{z - \omega_0^2} dz, \quad (2)$$

where C_0 is a closed curve around ω_0^2 so that $\mathbf{E}(\mathbf{r}, z)$ is holomorphic inside of C_0, as shown in Fig. 2(a). Then, deforming the path of integration so that an outer curve C_{nr} includes ω_0^2, the resonance poles $\omega_1^2, \ldots, \omega_M^2$ and no further poles yields

$$\oint_{C_0} \frac{\mathbf{E}(\mathbf{r}, z)}{z - \omega_0^2} dz = -\oint_{C_1} \frac{\mathbf{E}(\mathbf{r}, z)}{z - \omega_0^2} dz - \cdots - \oint_{C_M} \frac{\mathbf{E}(\mathbf{r}, z)}{z - \omega_0^2} dz$$
$$+ \oint_{C_{\mathrm{nr}}} \frac{\mathbf{E}(\mathbf{r}, z)}{z - \omega_0^2} dz,$$

see Figs. 2(b) and 2(c). Thereby, we obtain the expansion

$$\mathbf{E}(\mathbf{r}, \omega_0) = \sum_{m=1}^{M} \mathbf{E}_m(\mathbf{r}, \omega_0) + \mathbf{E}_{\mathrm{nr}}(\mathbf{r}, \omega_0), \quad (3)$$

where the fields

$$\mathbf{E}_m(\mathbf{r}, \omega_0) = -\frac{1}{2\pi i} \oint_{C_m} \frac{\mathbf{E}(\mathbf{r}, z)}{z - \omega_0^2} dz \quad (4)$$

are related to the resonance poles $\omega_1^2, \ldots, \omega_M^2$. The field

$$\mathbf{E}_{\mathrm{nr}}(\mathbf{r}, \omega_0) = \frac{1}{2\pi i} \oint_{C_{\mathrm{nr}}} \frac{\mathbf{E}(\mathbf{r}, z)}{z - \omega_0^2} dz \qquad (5)$$

quantifies the nonresonant components and contributions from possible resonance poles outside of the integration curve C_{nr}. It has to be ensured that C_{nr} does not cross the branch cut in the $z = \omega^2$ plane starting from $z = 0$. The fields in Eq. (4) are essentially RPs applied to Eq. (1); see results from spectral theory [15]. The RP expansion offers a general physical understanding of resonance phenomena without the need to normalize exponentially diverging fields. Clearly, the integrals in Eqs. (4) and (5) are independent of the particular choice of the contours C_m and C_{nr}. Therefore, precise locations of the resonance poles are not required. Also, when a contour includes multiple resonance poles the contour integral gives the projector onto the space of corresponding QNMs. In this way, it is possible to construct projectors for frequency ranges without detailed *a priori* knowledge. This case implies that a specific choice of the number M in Eq. (3) is not necessary.

RP expansion can be applied to any light source; however, of special interest are pointlike sources. These can be modeled as dipole emitters $\mathbf{J}(\mathbf{r}_0) = \mathbf{j}\delta(\mathbf{r} - \mathbf{r}_0)$, where $\mathbf{j} = -i\omega\mathbf{p}$ with dipole moment $\mathbf{p}$ at position $\mathbf{r}_0$. Its enhanced emission rate in the vicinity of a nanoresonator is characterized by the Purcell factor [13], also termed normalized decay rate,

$$\Gamma(\omega_0) = -\tfrac{1}{2}\mathrm{Re}[\mathbf{E}(\mathbf{r}_0, \omega_0) \cdot \mathbf{j}^*]/\Gamma_{\mathrm{b}}, \qquad (6)$$

where Γ_{b} is the decay rate of the emitter in homogeneous background material [14,32]. To quantify the coupling of the emitter to each of the single RPs $\mathbf{E}_m(\mathbf{r}, \omega_0)$, we introduce the modal normalized decay rate

$$\Gamma_m(\omega_0) = -\tfrac{1}{2}\mathrm{Re}[\mathbf{E}_m(\mathbf{r}_0, \omega_0) \cdot \mathbf{j}^*]/\Gamma_{\mathrm{b}}. \qquad (7)$$

The nonresonant normalized decay rate is analogously given by

$$\Gamma_{\mathrm{nr}}(\omega_0) = -\tfrac{1}{2}\mathrm{Re}[\mathbf{E}_{\mathrm{nr}}(\mathbf{r}_0, \omega_0) \cdot \mathbf{j}^*]/\Gamma_{\mathrm{b}}. \qquad (8)$$

Numerics. For the numerical realization of the RP expansion, we calculate the contour integrals in Eqs. (4) and (5) using a simple trapezoidal rule. At each integration point, it is required to solve Eq. (1) for a complex frequency which is done with a finite-element method (FEM solver, JCMSUITE). Perfectly matched layers (PMLs) [33] are used to enforce outgoing radiation conditions. To ensure an accurate FEM discretization for singular dipole sources, we use a subtraction field approach $\mathbf{E}(\mathbf{r}, \omega) = \mathbf{E}_{\mathrm{b}}(\mathbf{r}, \omega) + \mathbf{E}_{\mathrm{c}}(\mathbf{r}, \omega)$. The field $\mathbf{E}_{\mathrm{b}}(\mathbf{r}, \omega)$ is the analytically given solution to a dipole source in homogeneous bulk material. The correction field $\mathbf{E}_{\mathrm{c}}(\mathbf{r}, \omega)$ is suitable for an accurate FEM discretization [32]. Furthermore, for problem setups with geometries of cylindrical symmetry, we reduce the three-dimensional computation to a series of two-dimensional simulations with angular modes $e^{in_\varphi\varphi}$. The resonance poles are computed with a linear eigenvalue solver using an augmented field formulation. However, as mentioned above, the precise locations of the eigenvalues could be replaced by rough guesses. Self-adaptive approaches can be used for constructing suitable integration paths and to avoid crossing resonance poles. To run scans of the frequency ω_0
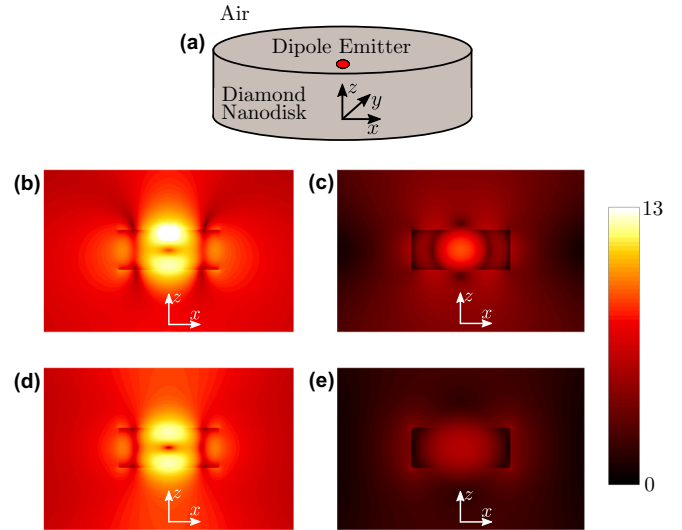

FIG. 3. (a) Sketch of a diamond nanodisk antenna (diameter 400 nm, height 160 nm) in air with an embedded dipole emitter placed 15 nm below the upper surface and on the cylindrical symmetry axis (z axis). The dipole with normalized strength is oriented in x direction and oscillates at frequency $\omega_0 = 2\pi c/455$ nm. (b) Log plot (a.u.) of the total electric field intensity. (c)–(e) Log plots (a.u.) of the electric field intensity of the three RPs for the complex eigenfrequencies $\omega_1 = 2\pi c/(406 + 16i$ nm), $\omega_2 = 2\pi c/(454 + 13i$ nm), and $\omega_3 = 2\pi c/(655 + 55i$ nm), respectively.

in the range $[\omega_{\min}, \ldots, \omega_{\max}]$, note that the integrand in the RPs, Eq. (4), only depends on ω_0 by the factor $1/(z - \omega_0^2)$. Therefore, for the whole scan, the fields $\mathbf{E}(\mathbf{r}, \omega)$ need to be evaluated only once at each integration point. Furthermore, all calculations can be performed in parallel. Due to these properties, the numerical realization is remarkably fast. We mention that RPs have also been used for algebraic eigenvalue solvers [34–36].

Application. Next, we apply the presented method to a highly topical example: a stable solid-state emitter in a nanoantenna. There is an urgent need for such systems to be used as single-photon sources for optical quantum technologies [37]. Room-temperature operation and directional emission at high rate are mandatory. As diamond is known to host various interesting defects; we consider a setup where a nitrogen-vacancy (N-V) center [38] is hosted in a (dielectric) diamond nanoantenna. An all-diamond realization would be ultracompact and ideal for large-scale integration. The specific geometry is depicted in Fig. 3(a). The dipole emitter is placed on the symmetry axis and polarized in the xy plane; therefore only angular modes with $n_\varphi = \pm 1$ are populated. The diamond permittivity $\epsilon(\omega)$ is described by a two-pole Lorentz model $\epsilon(\omega) = \epsilon_0(1 + \epsilon_{p_1} + \epsilon_{p_2})$, where $\epsilon_{p_{1,2}} = \Delta_{\epsilon_{1,2}}\omega_{p_{1,2}}^2/(\omega_{p_{1,2}}^2 - 2i\omega\gamma - \omega^2)$, with $\Delta_{\epsilon_1} = 0.3306$, $\Delta_{\epsilon_2} = 4.3356$, $\omega_{p_1} = 2\pi c/175$ nm, $\omega_{p_2} = 2\pi c/106$ nm, and damping $\gamma = 0$ [39].

We investigate the device within the wavelength range of $\lambda_0 \in [400$ nm$, \ldots, 800$ nm$]$. For computing the RPs, we use four integration points in Eq. (4). Figure 4(a) shows the modal normalized decay rates Γ_m of the three RPs corresponding to the resonance poles with smallest imaginary parts. Each spectrum shows a maximum at the wavelength corresponding
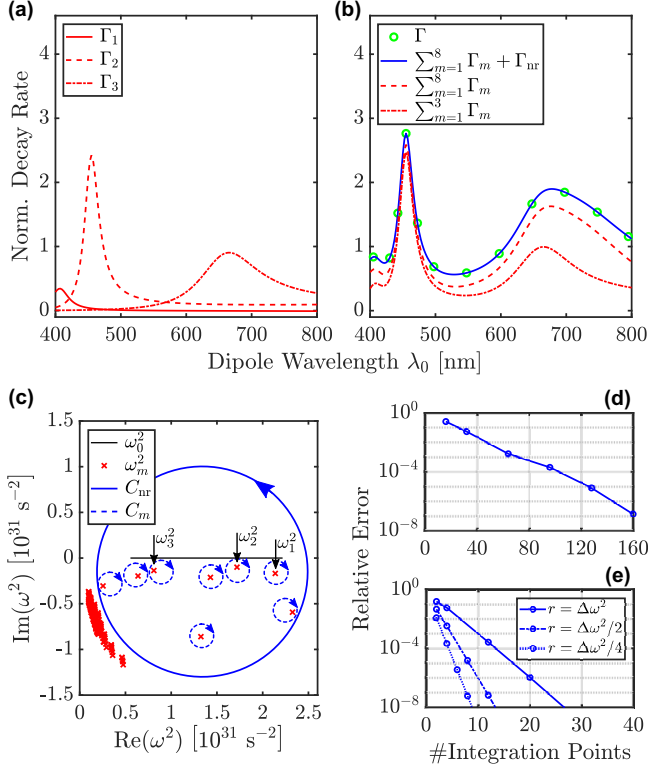
FIG. 4. Numerical results for the nanoantenna shown in Fig. 3(a). (a) Γ_m spectra of the three dominant RPs from Figs. 3(c)–3(e). (b) Normalized decay rates: Γ (quasiexact solution), $\sum_m \Gamma_m + \Gamma_{nr}$ (complete RP expansion), $\sum_{m=1}^{M} \Gamma_m$ (RPs for first M resonance poles). (c) Resonance poles of the nanoresonator and integration curves for computing Γ_m (C_m not to scale) and Γ_{nr}. (d) Convergence of Γ_{nr} with respect to C_{nr}: Maximum relative error $(\sum_{m=1}^{8} \Gamma_m + \Gamma_{nr} - \Gamma)/\Gamma$ as a function of the number of integration points [integration path as in (c)]. (e) Convergence of $\Gamma_2(\omega_0 = 2\pi c/455\text{ nm})$ with respect to the numerical parameters of the contour integration: Relative error of Γ_2 as a function of the number of integration points, for different integration paths (circle C_2 with radii r where $\Delta\omega^2 = 5 \times 10^{29}\text{ s}^{-2}$), reference solution computed with $r = \Delta\omega^2/4$, and 64 integration points.

to the real part of the respective pole. The highest decay rate is observed at around $\lambda_0 = 455$ nm. The RPs at $\omega_0 = 2\pi c/\lambda_0$ for three significant eigenfrequencies ω_m are shown in Figs. 3(c)–3(e). For comparison, the total field solution computed from Eq. (1) is shown in Fig. 3(b). We note that for the investigated case where a single pole is enclosed in each contour integral, the RP is a multiple of the corresponding QNM. However, as mentioned above, from the QNMs only it is not possible to compute modal expansion coefficients without an orthogonality relation, i.e., without scalar products, yielding a separation of the Maxwell's equations in a modal sense. The presented approach is not restricted to specific geometrical setups. Therefore, also handling complex environments of the nanodisk antenna, including, e.g., layered structures, waveguides, and arbitrarily shaped objects, is straightforward.

Figure 4(b) validates the completeness of the expansion in Eq. (3). The quasiexact solution Γ is gained from solving the scattering problem in Eq. (1) and applying Eq. (6). Using Eq. (4) and Eq. (7) for the first three resonance poles

yields an incomplete RP expansion $\sum_{m=1}^{3} \Gamma_m$ which already reproduces the characteristics of Γ. Using the first eight poles, the agreement of the incomplete RP expansion $\sum_{m=1}^{8} \Gamma_m$ with the quasiexact solution improves. Adding the nonresonant part Γ_{nr}, calculated with Eq. (8), gives the theoretically expected match to the quasiexact solution. Here, for the computation of $\mathbf{E}_{nr}(\mathbf{r}, \omega_0)$ in Eq. (5), we use 128 integration points. We attribute the fact that the nonresonant components are of significant quantitative impact to the nature of the diamond nanodisk antenna. Due to its relatively low refractive index, the structure hosts many weakly localized modes of low Q factor. Thus, the coupling to the background continuum of modes plays an important role for the Purcell factor.

Figure 4(c) details the position of the resonance poles in the complex plane and the used contour integral curves for this example. We distinguish between physical resonance poles and so-called PML poles [29,31]. Physical poles are stable with respect to a change of the numerical parameters and are therefore related to the discrete part of the operator spectrum. The PML poles stem from the continuous part of the spectrum of the operator and yield algebraic eigenvalues due to the discretization and truncation of the open resonator system. In this sense, the integral over the outer contour C_{nr} comprises the continuous part of the operator (PML modes) as well as further QNMs which might be present outside of C_{nr}. Note that the bulk emission term $\mathbf{E}_b(\mathbf{r}, \omega)$ in the subtraction field approach $\mathbf{E}(\mathbf{r}, \omega) = \mathbf{E}_b(\mathbf{r}, \omega) + \mathbf{E}_c(\mathbf{r}, \omega)$ is an analytic function in the entire complex plane. Hence, $\mathbf{E}_b(\mathbf{r}, \omega)$ does not contribute to the RPs $\mathbf{E}_m(\mathbf{r}, \omega_0)$, which are therefore smooth fields, cf., Figs. 3(c)–3(e), whereas $\mathbf{E}_{nr}(\mathbf{r}, \omega_0)$ produces the singularity.

The numerical efficiency of the RP expansion depends on the numerical convergence of the contour integral with respect to the number of integration points. For the outer contour C_{nr}, as plotted in Fig. 4(c), we observe convergence with respect to the number of integration points, see Fig. 4(d). For the contours of the single RPs, we verified that four integration points are sufficient to reach a relative accuracy of the derived modal decay rate better than 10^{-6}, see Fig. 4(e).

Conclusions. In conclusion, we presented a theoretical approach to explain the coupling of light sources to dispersive nanoresonators by means of an electromagnetic field expansion with Riesz projections. The method allows for the precise definition and computation of the field expansion into modal and background parts and for the evaluation of linear functionals, e.g., modal and background decay rates. We applied the approach to model the coupling of an emitting defect center in diamond to a nanodisk antenna supporting several weakly localized resonant states. The method is applicable to systems with any material dispersion obeying Kramers-Kronig relation. We therefore expect that the approach will prove especially useful for understanding and designing novel photonic devices with material properties that can only be accurately modeled using high-order rational fits to measured data. Riesz projection expansion further establishes a route for quantitative modal analysis of omnipresent nano-optical systems with relevant nonresonant background. The presented concepts may also be applied to explore open resonators in other fields of physics, e.g., in phononic structures [40] and acoustic metamaterials [41].

[1] K. J. Vahala, Nature (London) **424**, 839 (2003).

[2] P. Bharadwaj, B. Deutsch, and L. Novotny, Adv. Opt. Photonics **1**, 438 (2009).

[3] V. Giannini, A. I. Fernández-Domínguez, S. C. Heck, and S. A. Maier, Chem. Rev. **111**, 3888 (2011).

[4] A. I. Kuznetsov, A. E. Miroshnichenko, M. L. Brongersma, Y. S. Kivshar, and B. Luk'yanchuk, Science **354**, aag2472 (2016).

[5] A. G. Curto, G. Volpe, T. H. Taminiau, M. P. Kreuzer, R. Quidant, and N. F. van Hulst, Science **329**, 930 (2010).

[6] X. Ding, Y. He, Z.-C. Duan, N. Gregersen, M.-C. Chen, S. Unsleber, S. Maier, C. Schneider, M. Kamp, S. Höfling, C.-Y. Lu, and J.-W. Pan, Phys. Rev. Lett. **116**, 020401 (2016).

[7] A. F. Koenderink, ACS Photonics **4**, 710 (2017).

[8] R. F. Oulton, V. J. Sorger, T. Zentgraf, R.-M. Ma, C. Gladden, L. Dai, G. Bartal, and X. Zhang, Nature (London) **461**, 629 (2009).

[9] M. A. Noginov and J. B. Khurgin, Nat. Mater. **17**, 116 (2018).

[10] J. A. Hutchison, T. Schwartz, C. Genet, E. Devaux, and T. W. Ebbesen, Angew. Chem. Int. Ed. **51**, 1592 (2012).

[11] M. Kamandar Dezfouli, R. Gordon, and S. Hughes, Phys. Rev. A **95**, 013846 (2017).

[12] T. Feichtner, S. Christiansen, and B. Hecht, Phys. Rev. Lett. **119**, 217401 (2017).

[13] E. M. Purcell, Phys. Rev. **69**, 681 (1946).

[14] C. Sauvan, J.-P. Hugonin, I. S. Maksymov, and P. Lalanne, Phys. Rev. Lett. **110**, 237401 (2013).

[15] P. Hislop and I. Sigal, *Introduction to Spectral Theory, With Applications to Schrödinger Operators* (Springer, New York, 1996).

[16] M. Zworski, Notices Amer. Math. Soc. **46**, 319 (1999).

[17] D. Bindel and M. Zworski, Theory and Computation of Resonances in 1D Scattering, http://www.cs.cornell.edu/~bindel/cims/resonant1d/.

[18] G. García-Calderón, in *Unstable States in the Continuous Spectra, Part I: Analysis, Concepts, Methods, and Results*, Advances in Quantum Chemistry Vol. 60 (Academic Press, New York, 2010).

[19] E. A. Muljarov, W. Langbein, and R. Zimmermann, Europhys. Lett. **92**, 50010 (2010).

[20] P. T. Kristensen and S. Hughes, ACS Photonics **1**, 2 (2014).

[21] E. A. Muljarov and W. Langbein, Phys. Rev. B **93**, 075417 (2016).

[22] P. Lalanne, W. Yan, K. Vynck, C. Sauvan, and J.-P. Hugonin, Laser Photonics Rev. **12**, 1700113 (2018).

[23] P. T. Leung, S. Y. Liu, and K. Young, Phys. Rev. A **49**, 3057 (1994).

[24] M. K. Dezfouli, C. Tserkezis, N. A. Mortensen, and S. Hughes, Optica **4**, 1503 (2017).

[25] P. T. Kristensen, R.-C. Ge, and S. Hughes, Phys. Rev. A **92**, 053810 (2015).

[26] C. Sauvan, J.-P. Hugonin, and P. Lalanne, Proc. SPIE **9546**, 95461C (2015).

[27] E. A. Muljarov and W. Langbein, Phys. Rev. B **94**, 235438 (2016).

[28] E. A. Muljarov and W. Langbein, Phys. Rev. A **96**, 017801 (2017).

[29] B. Vial, F. Zolla, A. Nicolet, and M. Commandré, Phys. Rev. A **89**, 023829 (2014).

[30] M. Gschrey, A. Thoma, P. Schnauber, M. Seifried, R. Schmidt, B. Wohlfeil, L. Krüger, J.-H. Schulze, T. Heindel, S. Burger, F. Schmidt, A. Strittmatter, S. Rodt, and S. Reitzenstein, Nat. Commun. **6**, 7662 (2015).

[31] W. Yan, R. Faggiani, and P. Lalanne, Phys. Rev. B **97**, 205422 (2018).

[32] L. Zschiedrich, H. J. Greiner, S. Burger, and F. Schmidt, Proc. SPIE **8641**, 86410B (2013).

[33] J.-P. Berenger, J. Comput. Phys. **114**, 185 (1994).

[34] J. Asakura, T. Sakurai, H. Tadano, T. Ikegami, and K. Kimura, JSIAM Lett. **1**, 52 (2009).

[35] W.-J. Beyn, Linear Algebra Appl. **436**, 3839 (2012).

[36] B. Gavin, A. Miedlar, and E. Polizzi, J. Comput. Phys. **27**, 107 (2018).

[37] S. K. H. Andersen, S. Bogdanov, O. Makarova, Y. Xuan, M. Y. Shalaginov, A. Boltasseva, S. I. Bozhevolnyi, and V. M. Shalaev, ACS Photonics **5**, 692 (2018).

[38] F. Jelezko, C. Tietz, A. Gruber, I. Popa, A. Nizovtsev, S. Kilin, and J. Wrachtrup, Single Mol. **2**, 255 (2001).

[39] F. Peter, Z. Phys. **15**, 358 (1923).

[40] M. I. Hussein, M. J. Leamy, and M. Ruzzene, Appl. Mech. Rev. **66**, 040802 (2014).

[41] S. A. Cummer, J. Christensen, and A. Alù, Nat. Rev. Mater. **1**, 16001 (2016).

3 Nanoresonators with nonlocal material properties

In metal nanoresonators, the material dispersion can usually be described by Drude-Lorentz models [35, 36, 85]. The interaction of light with the free electron gas of the metal takes place locally. Numerical implementations of linearizations of the resulting nonlinear eigenproblems are available in state-of-the-art eigensolvers for Maxwell's equations [30–32]. However, when the nanostructures are only a few nanometers in size, nonlocal material models are required [86]. A typically applied nonlocal model is the hydrodynamic Drude model [86–91], which considers the motions in the electron gas as a hydrodynamic flow. Numerical implementations for such material models are usually not available in standard eigensolvers.

In Ref. [65], we apply contour integral methods for the investigation of optical resonances in nonlocal material systems. We implement the coupled system of equations

$$\nabla \times \mu_0^{-1} \nabla \times \mathbf{E}(\mathbf{r}, \omega_0) - \omega_0^2 \epsilon_0 \epsilon_\infty \mathbf{E}(\mathbf{r}, \omega_0) = i\omega_0 \mathbf{J}_{\mathrm{hd}}(\mathbf{r}, \omega_0) + i\omega_0 \mathbf{J}(\mathbf{r}), \qquad (3.1)$$

$$\beta^2 \nabla \left(\nabla \cdot \mathbf{J}_{\mathrm{hd}}(\mathbf{r}, \omega_0) \right) + \omega_0 \left(\omega_0 + i\gamma \right) \mathbf{J}_{\mathrm{hd}}(\mathbf{r}, \omega_0) = i\omega_0 \omega_{\mathrm{p}}^2 \epsilon_0 \mathbf{E}(\mathbf{r}, \omega_0) \qquad (3.2)$$

with appropriate boundary conditions, where $\mathbf{E}(\mathbf{r}, \omega_0) \in \mathbb{C}^3$ is the electric field and $\mathbf{J}_{\mathrm{hd}}(\mathbf{r}, \omega_0) \in \mathbb{C}^3$ is the nonlocal hydrodynamic current density [89, 90]. The damping constant γ and the plasma frequency ω_{p} correspond to the local Drude model $\epsilon_{\mathrm{d}}(\omega_0) = \epsilon_0 \left(\epsilon_\infty - \omega_{\mathrm{p}}^2 / \left(\omega_0^2 + i\gamma\omega_0 \right) \right)$, where ϵ_∞ is the relative permittivity at infinity. The factor β is a system constant. Note that, when $\beta \to 0$, the coupled system simplifies to Maxwell's equation given by Eq. (2.1).

We apply the contour integral method proposed in Ref. [56] to compute the eigenmodes and eigenfrequencies of a nanowire [88]. For this, we implement the coupled system given by Eq. (3.1) and Eq. (3.2) and solve the resulting linear system of equations for random vectors, where the system matrix depends on the frequency lying on the chosen integration contour and the random vectors are frequency independent. Furthermore, we extend the Riesz projection expansion approach given by Eq. (2.4) so that a resonance expansion of the extinction cross section [89] can be performed. Due to the dependence of the extinction cross section on the complex conjugated electric field, the complex conjugated eigenfrequencies must also be considered for the expansion. With the Riesz projection expansion of the extinction cross section, we identify the eigenmodes which are important for understanding the physics of the nanowire.

In the following, Ref. [65] is reprinted with permission from [Felix Binkowski, Lin Zschiedrich, Martin Hammerschmidt, and Sven Burger. Modal analysis for nanoplasmonics with nonlocal material properties. *Phys. Rev. B* 100, 155406 (2019). DOI: 10.1103/PhysRevB.100.155406.] Copyright 2019 by the American Physical Society.

Modal analysis for nanoplasmonics with nonlocal material properties

Felix Binkowski,[1] Lin Zschiedrich,[2] Martin Hammerschmidt,[2] and Sven Burger [1,2]

[1]*Zuse Institute Berlin, Takustraße 7, D-14195 Berlin, Germany*
[2]*JCMwave GmbH, Bolivarallee 22, D-14050 Berlin, Germany*

Plasmonic devices with feature sizes of a few nanometers exhibit effects which can be described by the nonlocal hydrodynamic Drude model. We demonstrate how to exploit contour integral methods for computing eigenfrequencies and resonant states of such systems. We propose an approach for deriving the modal expansion of relevant physical observables. We use the methods to perform a modal analysis for a metal nanowire. All complex eigenfrequencies in a large frequency range and the corresponding resonant states are computed. We identify those resonant states which are relevant for the extinction cross section of the nanowire.

I. INTRODUCTION

Nanofabrication technologies allow for a rapid progress in engineering nano-optical devices [1]. Plasmonic resonances are the center of attention for many topical applications exploring new regimes of physics. Examples comprise the demonstration of plasmonic lasers [2], tailoring light emission of nanoantennas [3,4], probing single molecules and nanoparticles by Raman scattering [5], plasmonic photochemistry [6], and quantum emitters interacting with metal nanoresonators [7].

An adequate description of material dispersion plays an important role for the investigation of light-matter interaction in plasmonic structures [8]. In many cases, the material dispersion can be described by the Drude-Lorentz model or by a rational function fit to measured material data [9,10]. Such models are based on spatially local interactions between the light and the free electron gas of the plasmonic scatterers [11]. When the scatterers are at the size of a few nanometers, nonlocal material models are required [12]. These models lead to additional resonances of the electromagnetic field with sub-nm wavelengths. Recently, surface plasmon resonance blueshifts have been observed in metal nanoparticles [13,14] which could be explained [15] using the nonlocal hydrodynamic Drude model (HDM) [16]. This model assumes that the motion of the electron gas behaves as a hydrodynamic flow and allows for the investigation of nonlocal physical effects [17–23].

For the study of physical phenomena in nanoplasmonic systems, a deeper understanding of the effects based on the HDM is required. A modal description is the most instructive approach [24,25]. In the case of local material models, numerically computed resonant states of plasmonic systems have been successfully used to derive modal expansions [26–29]. However, in the case of the HDM, a coupled system of equations has to be solved [30–33]. To the best of our knowledge, for this system, the computations of eigenfrequencies in a large frequency range with corresponding resonant states and modal expansions have not yet been reported.

In this work, we investigate plasmonic resonances based on the HDM. We present a contour-integral-based framework for a modal analysis. Typical physical observables are sesquilinear forms which involve a complex conjugation of the solution fields. We propose a general approach for the computation of modal sesquilinear quantities. The framework is applied to calculate the eigenfrequencies and corresponding resonant states of a metal nanowire. Furthermore, the modal extinction cross section of the nanowire illuminated by plane waves is computed. This allows one to classify the resonant states of the nanowire into states which couple to the light sources and into states which have no contribution to the extinction cross section.

This work is structured as follows. Section II introduces a coupled system of equations describing the HDM and summarizes numerical methods for modal analysis. In the subsection *Modal expansion of sesquilinear quantities*, we extend the framework of the Riesz projection expansion (RPE) [28] in order to obtain modal expansions of physical observables, such as the extinction cross section. Section III applies these methods for an investigation of the resonances of a metal nanowire. Section IV concludes the study.

II. PLASMONIC RESONANCES BASED ON THE HYDRODYNAMIC DRUDE MODEL

The HDM is based on the interaction of a nonlocal polarization current and its resulting electric field. In the frequency domain and for nonmagnetic materials, this is described by the coupled system of equations,

$$\nabla \times \mu_0^{-1} \nabla \times \mathbf{E}(\mathbf{r}, \omega) - \omega^2 \epsilon_{\text{loc}}(\mathbf{r}, \omega)\mathbf{E}(\mathbf{r}, \omega)$$
$$= i\omega \mathbf{J}_{\text{hd}}(\mathbf{r}, \omega) + i\omega \mathbf{J}(\mathbf{r}, \omega), \tag{1}$$

$$\beta^2 \nabla(\nabla \cdot \mathbf{J}_{\text{hd}}(\mathbf{r}, \omega)) + \omega(\omega + i\gamma)\mathbf{J}_{\text{hd}}(\mathbf{r}, \omega)$$
$$= i\omega \omega_{\text{p}}^2 \epsilon_0 \mathbf{E}(\mathbf{r}, \omega), \tag{2}$$

for the electric field $\mathbf{E}(\mathbf{r}, \omega)$ and the nonlocal hydrodynamic current density $\mathbf{J}_{\text{hd}}(\mathbf{r}, \omega)$, where $\mathbf{J}(\mathbf{r}, \omega)$ is a given
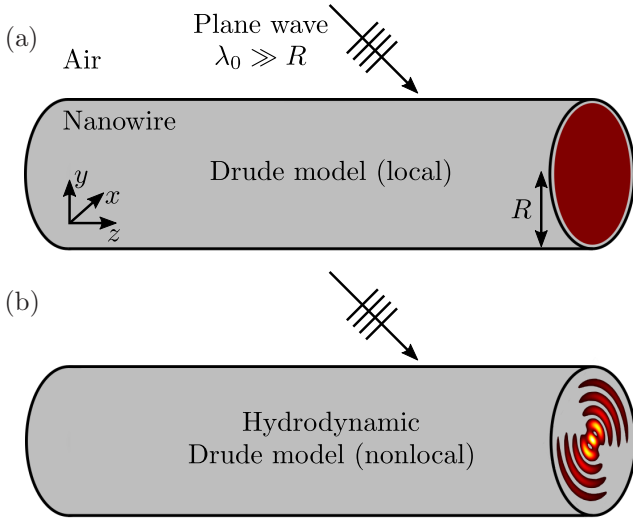
FIG. 1. Schematics of a metal nanowire illuminated by a plane wave of wavelength λ_0. Electric field intensity sketched on a cut through the nanowire. (a) Nearly constant electric field intensity in case of the local Drude model. (b) Radially oscillating field pattern in case of the nonlocal hydrodynamic Drude model.

impressed current density, ω is the frequency, $\epsilon_{loc}(\mathbf{r}, \omega)$ is the permittivity resulting from the local material response, ϵ_0 is the vacuum permittivity, and μ_0 is the vacuum permeability. The damping constant γ and the plasma frequency ω_p correspond to the local Drude model $\epsilon_d(\omega) = \epsilon_0(\epsilon_\infty - \omega_p^2/(\omega^2 + i\gamma\omega))$, where ϵ_∞ is the relative permittivity at infinity. The factor $\beta = \sqrt{3/5}\, v_F$ relates to the Fermi velocity v_F [16].

The nonlocal material response is caused by $\mathbf{J}_{hd}(\mathbf{r}, \omega)$, which affects the permittivity function for the free electron gas. If $\beta \to 0$, then the coupled system simplifies to Maxwell's equations for the local Drude model. For an illustration of the effect of the HDM, a nanowire excited by a plane wave is sketched in Fig. 1. While, for the local Drude model, the electric field intensity inside of the nanowire is nearly constant, the electric field pattern is radially oscillating considering the HDM [see Figs. 1(a) and 1(b), respectively]. The reader is referred to [31,32] for a detailed derivation of Eqs. (1) and (2) including the applied assumptions and approximations.

Physical scattering solutions $\mathbf{E}(\mathbf{r}, \omega_0)$ and $\mathbf{J}_{hd}(\mathbf{r}, \omega_0)$ of the coupled system can be obtained for real frequencies $\omega_0 \in \mathbb{R}$. The eigenfrequencies are defined as the complex resonance poles $\tilde{\omega}_k \in \mathbb{C}$ of the analytical continuation of $\mathbf{E}(\mathbf{r}, \omega_0)$ and $\mathbf{J}_{hd}(\mathbf{r}, \omega_0)$ into the complex plane yielding $\mathbf{E}(\mathbf{r}, \omega)$ and $\mathbf{J}_{hd}(\mathbf{r}, \omega)$, where $\omega \in \mathbb{C}$ [28]. The resonant states, also called eigenmodes, of the coupled system correspond to these eigenfrequencies.

A. Numerical methods for modal analysis

The contour integral method BEYN'S ALGORITHM [34] is applied to numerically solve the nonlinear eigenproblem [35] corresponding to the coupled system given by Eqs. (1) and (2). Contour integral methods for such problems require the

definition of an integration path in the complex frequency plane which encloses the eigenfrequencies corresponding to the eigenmodes of interest. The numerical integration along this contour projects vector fields onto the space spanned by these eigenmodes. In this way, an approximate eigenspace is constructed. Then, e.g., the methods proposed in [34,36] apply a singular-value decomposition (SVD) to this approximate eigenspace and solve a linear eigenproblem of small dimension. The approach presented in [37] applies the Rayleigh-Ritz method to the approximate eigenspace and solves a nonlinear eigenproblem of small dimension. The common property of these methods is that they essentially require the solution of scattering problems for the integration points on the chosen contour. This is in contrast to standard approaches for solving nonlinear eigenproblems, such as the Arnoldi method, which are based on linearization of the nonprojected problems using auxiliary fields [38,39].

For the modal expansion of scattering problems, an unconjugated scalar product can be used [29]. In this context, it is an open problem how to deal with the expansion of nonholomorphic quantities, e.g., the extinction cross section. The contour-integral-based RPE [28] allows one to perform a modal expansion without a scalar product. A solution $\mathbf{E}(\mathbf{r}, \omega_0)$ to the coupled system given by Eqs. (1) and (2) can be expanded into a weighted sum of eigenmodes yielding the coupling of the modes to specific sources $\mathbf{J}(\mathbf{r}, \omega_0)$ with $\omega_0 \in \mathbb{R}$. Cauchy's integral formula,

$$\mathbf{E}(\mathbf{r}, \omega_0) = \frac{1}{2\pi i} \oint_{C_0} \frac{\mathbf{E}(\mathbf{r}, \omega)}{\omega - \omega_0} d\omega,$$

is exploited, where $\mathbf{E}(\mathbf{r}, \omega)$, $\omega \in \mathbb{C}$, is the analytical continuation of $\mathbf{E}(\mathbf{r}, \omega_0)$ into the complex plane and C_0 is a closed integration path around ω_0 so that $\mathbf{E}(\mathbf{r}, \omega)$ is holomorphic inside of C_0. Deforming the integration path and applying Cauchy's residue theorem yield

$$\mathbf{E}(\mathbf{r}, \omega_0) = -\frac{1}{2\pi i} \oint_{\tilde{C}_1} \frac{\mathbf{E}(\mathbf{r}, \omega)}{\omega - \omega_0} d\omega - \ldots - \frac{1}{2\pi i} \oint_{\tilde{C}_K} \frac{\mathbf{E}(\mathbf{r}, \omega)}{\omega - \omega_0} d\omega + \frac{1}{2\pi i} \oint_{C_{nr}} \frac{\mathbf{E}(\mathbf{r}, \omega)}{\omega - \omega_0} d\omega,$$

where $\tilde{C}_1, \ldots, \tilde{C}_K$ are contours around the eigenfrequencies $\tilde{\omega}_1, \ldots, \tilde{\omega}_K$ and C_{nr} is a contour including ω_0, the eigenfrequencies $\tilde{\omega}_1, \ldots, \tilde{\omega}_K$, and no additional eigenfrequencies. The Riesz projections,

$$\tilde{\mathbf{E}}_k(\mathbf{r}, \omega_0) = -\frac{1}{2\pi i} \oint_{\tilde{C}_k} \frac{\mathbf{E}(\mathbf{r}, \omega)}{\omega - \omega_0} d\omega,$$

corresponding to $\tilde{\omega}_k$ describe the coupling of the eigenmodes to the considered source field. The field,

$$\mathbf{E}_{nr}(\mathbf{r}, \omega_0) = \frac{1}{2\pi i} \oint_{C_{nr}} \frac{\mathbf{E}(\mathbf{r}, \omega)}{\omega - \omega_0} d\omega,$$

contains nonresonant components as well as components corresponding to eigenfrequencies outside of the contour C_{nr}. For this modal expansion approach, instead of projecting random

vectors as for BEYN'S ALGORITHM, the numerical integration is performed by solving the coupled system using physical source fields at the integration points.

Equations (1) and (2) are spatially discretized with the finite element method (FEM) [40,41]. The FEM solver JCM-SUITE is used to solve scattering problems. Perfectly matched layers (PMLs) are applied to realize outgoing radiation conditions [42]. High order polynomial ansatz functions and mesh refinements are used to reach a sufficient numerical accuracy [43]. We write

$$T(\omega)v = f(\omega),$$

for the coupled system given by Eqs. (1) and (2), where $T(\omega) \in \mathbb{C}^{n \times n}$ is the system matrix resulting from the FEM discretization and $v \in \mathbb{C}^n$ is the vector corresponding to $\mathbf{E}(\mathbf{r}, \omega)$ and $\mathbf{J}_{\mathrm{hd}}(\mathbf{r}, \omega)$. The dimension n results from the spatial mesh and from the degrees of the polynomial ansatz functions of the FEM discretization. The right-hand side $f(\omega)$ corresponds to the impressed current density $\mathbf{J}(\mathbf{r}, \omega)$ and incoming source fields. In this notation, $T(\tilde{\omega}_k)\tilde{v}_k = 0$ holds for an eigenfrequency $\tilde{\omega}_k$ and an eigenmode $\tilde{v}_k$. Solving $T(\omega)v = f(\omega)$ with $f(\omega) \neq 0$ corresponds to solving a scattering problem.

B. Modal expansion of sesquilinear quantities

Typical physical quantities are quadratic forms associated with a sesquilinear map $q(v, v^*)$ for solution fields v and their complex conjugates v^*. Examples include the electromagnetic absorption and the electromagnetic energy flux. For two reasons, the construction of a meaningful modal expansion of sesquilinear forms $q(v, v^*)$ is not straightforward. First, the missing orthogonality $q(\tilde{v}_k, \tilde{v}_l^*) \neq 0$ yields cross terms in the expansion. Secondly, the conjugation $v^*(\omega_0)$ renders $q(v(\omega_0), v^*(\omega_0))$ nonholomorphic and the evaluation of this expression for complex eigenfrequencies $\tilde{\omega}_k$ is problematic.

To derive a modal expansion of sesquilinear quantities with well-defined expansion coefficients, we extend the framework of the RPE. The method is based on an analytical continuation of the sesquilinear form $q(v(\omega_0), v^*(\omega_0))$ from the real axis $\omega_0 \in \mathbb{R}$ into the complex plane $\omega \in \mathbb{C}$. We remark that $v^*(\omega_0)$ is the solution to $T^*(\omega_0)v^*(\omega_0) = f^*(\omega_0)$. The system matrix $T^*(\omega_0)$ and the right-hand side $f^*(\omega_0)$ have analytical continuations, which we denote by $T^{\circ}(\omega)$ and $f^{\circ}(\omega)$. Consequently, the analytical continuation of $v^*(\omega_0)$ reads as

$$v^{\circ}(\omega) = T^{\circ}(\omega)^{-1} f^{\circ}(\omega). \tag{3}$$

Finally, this gives the analytical continuation $q(v(\omega), v^{\circ}(\omega))$ into the complex plane and the modal expansion can be computed.

Note that if a solution of the coupled system given by Eqs. (1) and (2) has a pole in $\omega = \tilde{\omega}_k$, then its complex conjugate has a pole in $\omega = \tilde{\omega}_k^*$. Thus, $q(v(\omega), v^{\circ}(\omega))$ has poles in $\tilde{\omega}_k$ and also in $\tilde{\omega}_k^*$. This has to be taken into account for the RPE. The calculation of a modal quantity corresponding to a specific $\tilde{\omega}_k$ involves the summation of the Riesz projections for $\tilde{\omega}_k$ and $\tilde{\omega}_k^*$.

As the derivation of $v^{\circ}(\omega)$ is given formally, we remark, for a better physical understanding, that the complex conjugation of the system matrix and the right-hand side corresponds to

solving the coupled system for $\omega = -\omega_0$ with sign-inverted radiation conditions.

III. RESONANCES OF A NANOWIRE

We consider a specific setup, a cylindrical metal nanowire which has also been investigated in the literature, to study HDM-based effects theoretically [17]. For typical nanoplasmonic applications, a quantity of interest is the extinction cross section. In the following, we first compute eigenfrequencies and eigenmodes of the nanowire. Based on this, we then investigate the extinction cross section in a modal sense, i.e., it is shown which of the eigenmodes scatter and absorb an incoming source field and which of the modes do not interact with the light source. When the nonlocal HDM is replaced by a local Drude model, only a single resonance is observed in the extinction cross section [17,22,31].

The investigated sodium nanowire of radius $R = 2$ nm, infinitely extended in the z direction [see Fig. 1(a)], is described by $\epsilon_{\infty} = 1$, $\omega_{\mathrm{p}} = 8.65 \times 10^{15} \, \mathrm{s}^{-1}$, $\gamma = 0.01 \, \omega_{\mathrm{p}}$, and $\epsilon_{\mathrm{loc}} = \epsilon_0 \epsilon_{\infty}$. The Fermi velocity is given by $v_{\mathrm{F}} = 1.07 \times 10^6 \, \mathrm{ms}^{-1}$. The nanowire is surrounded by free space with refractive index equal to one. The source field is a y polarized plane wave with unit amplitude propagating in the x direction. For the FEM discretization, a mesh containing about 2000 triangles with edge lengths from about 0.05 to 1 nm is applied. The polynomial degree of the finite elements is set to $p = 3$.

The frequency range $0.4 \, \omega_0 < \omega_0 < 1.4 \, \omega_{\mathrm{p}}$ is selected for the modal analysis. To compute eigenmodes $\tilde{v}_k$ using BEYN'S ALGORITHM, an integration contour around this range is defined. The parameters for the algorithm are $N = 160$ integration points, $l = 200$ random vectors, and, for the rank drop detection within the SVD, a tolerance of $\mathrm{tol}_{\mathrm{rank}} = 10^{-8}$ is chosen. The SVD and the solution of the resulting small linear eigenproblem are performed within MATLAB. We obtain 118 eigenfrequencies inside the integration contour. The imaginary parts of these eigenfrequencies are $\mathrm{Im}(\tilde{\omega}_k) = -0.0050 \, \omega_{\mathrm{p}}$, except for $\tilde{\omega}_1 = (0.7313 - 0.0054i)\omega_{\mathrm{p}}$. We note that the eigenmodes corresponding to eigenfrequencies with $\mathrm{Im}(\tilde{\omega}_k) = -0.0050 \, \omega_{\mathrm{p}}$ are localized in the nanowire material, which is modeled with a constant damping γ. Other loss channels are not significant for these modes. This results in the very similar imaginary parts of the eigenfrequencies. To numerically assess the quality of the approximations of the eigenfrequencies and eigenmodes, we compute the residuals $\mathrm{res}(\tilde{\omega}_k) = ||T(\tilde{\omega}_k)\tilde{v}_k||_2 / ||T(\tilde{\omega}_k)||_F$, where $||\tilde{v}_k||_2 = 1$. The residuals for eigenfrequencies within the integration contour are smaller than 6×10^{-15}. The residuals for computed eigenfrequencies outside the integration contour increase with the distance to the contour. The integration points, all computed eigenfrequencies, and the residuals are shown in Fig. 2(a). Plots of the electric field intensity of an exemplary selection of eigenmodes corresponding to eigenfrequencies in frequency ranges below and beyond the plasma frequency are shown in Figs. 2(b) and 2(c), respectively. Note that these eigenfrequencies are semisimple with an algebraic and geometric multiplicity of two. The chosen indicies of the eigenfrequencies and eigenmodes are increasing with increasing real parts of the eigenfrequencies and are intended to guide the reader through the figures.
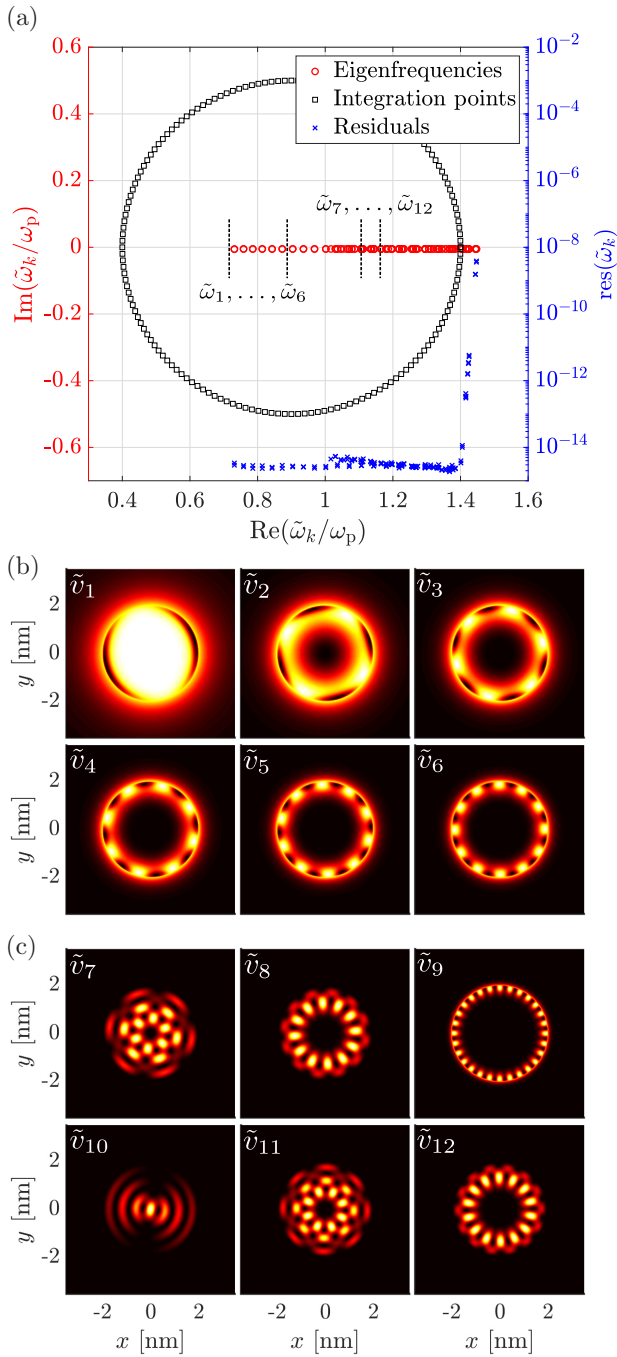
FIG. 2. Eigenfrequencies $\tilde{\omega}_k$ and eigenmodes $\tilde{v}_k$ of the nanowire. (a) Eigenfrequencies, integration points, and residuals $\mathrm{res}(\tilde{\omega}_k) = ||T(\tilde{\omega}_k)\tilde{v}_k||_2 / ||T(\tilde{\omega}_k)||_F$, where $||\tilde{v}_k||_2 = 1$. Inside of the integration contour, 118 eigenfrequencies are located (including multiplicities). (b) Plots (a.u.) of the electric field intensity of an exemplary selection of eigenmodes corresponding to eigenfrequencies below the plasma frequency, $\tilde{\omega}_1 = (0.7313 - 0.0054i)\omega_p$, $\tilde{\omega}_2 = (0.7585 - 0.0050i)\omega_p$, $\tilde{\omega}_3 = (0.7857 - 0.0050i)\omega_p$, $\tilde{\omega}_4 = (0.8138 - 0.0050i)\omega_p$, $\tilde{\omega}_5 = (0.8429 - 0.0050i)\omega_p$, and $\tilde{\omega}_6 = (0.8729 - 0.0050i)\omega_p$. (c) As above, for eigenfrequencies beyond the plasma frequency, $\tilde{\omega}_7 = (1.1341 - 0.0050i)\omega_p$, $\tilde{\omega}_8 = (1.1373 - 0.0050i)\omega_p$, $\tilde{\omega}_9 = (1.1434 - 0.0050i)\omega_p$, $\tilde{\omega}_{10} = (1.1453 - 0.0050i)\omega_p$, $\tilde{\omega}_{11} = (1.1651 - 0.0050i)\omega_p$, and $\tilde{\omega}_{12} = (1.1654 - 0.0050i)\omega_p$. Color scale from zero (black) to one (white).
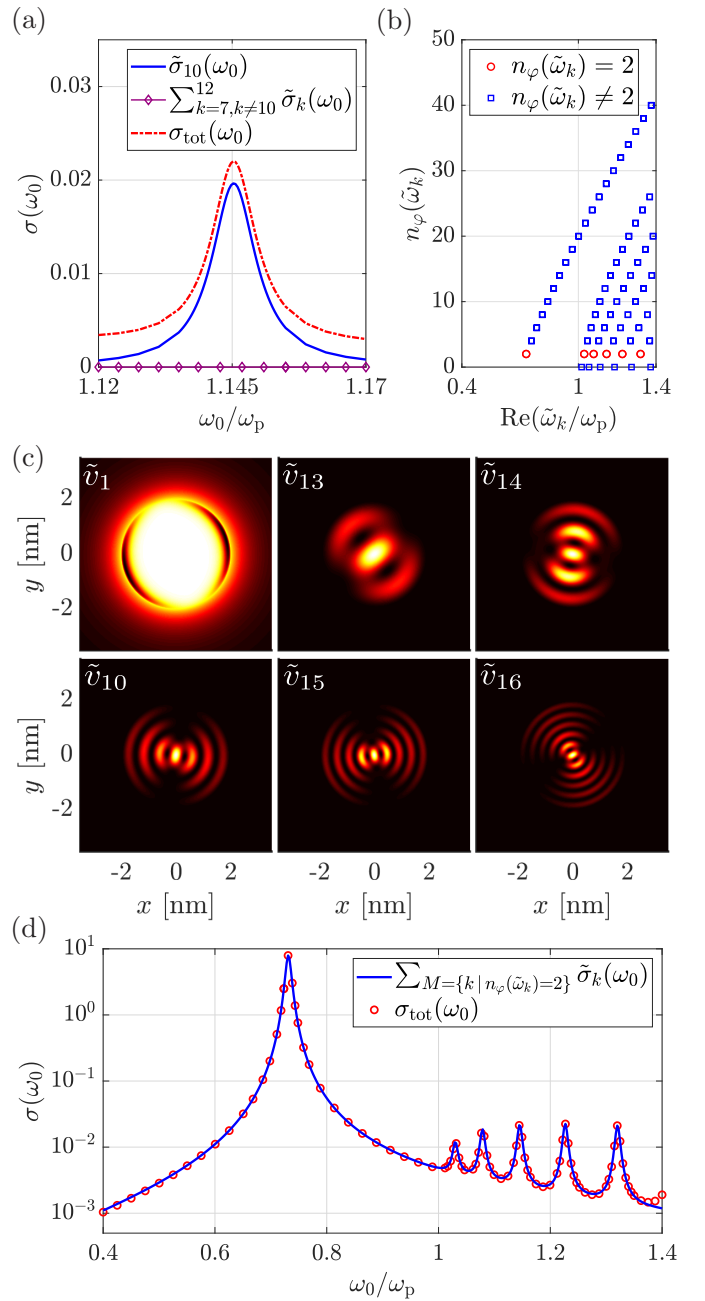
FIG. 3. Modal analysis of the extinction cross section $\sigma(\omega_0)$ of the nanowire. (a) $\sigma(\omega_0)$ for the frequency range $1.12\,\omega_p < \omega_0 < 1.17\,\omega_p$. Modal extinction cross section $\tilde{\sigma}_{10}(\omega_0)$ corresponding to the eigenfrequency $\tilde{\omega}_{10} = (1.1453 - 0.0050i)\omega_p$ and the sum $\sum_{k=7, k\neq 10}^{12} \tilde{\sigma}_k(\omega_0)$ corresponding to the remaining eigenfrequencies in the frequency range. Total extinction cross section $\sigma_{\mathrm{tot}}(\omega_0)$ for comparison. (b) Classification parameter $n_\varphi(\tilde{\omega}_k)$ for the eigenfrequencies $\tilde{\omega}_k$ in the frequency range $0.4\,\omega_p < \mathrm{Re}(\tilde{\omega}_k) < 1.4\,\omega_p$. (c) Plots (a.u.) of the electric field intensities of the eigenmodes with $n_\varphi(\tilde{\omega}_k) = 2$. Color scale from zero (black) to one (white). (d) Modal expansion of the extinction cross section $\sum_M \tilde{\sigma}_k(\omega_0)$, $M = \{k \,|\, n_\varphi(\tilde{\omega}_k) = 2\}$, corresponding to the six eigenfrequencies $\tilde{\omega}_1 = (0.7313 - 0.0054i)\omega_p$, $\tilde{\omega}_{13} = (1.0301 - 0.0050i)\omega_p$, $\tilde{\omega}_{14} = (1.0788 - 0.0050i)\omega_p$, $\tilde{\omega}_{10} = (1.1453 - 0.0050i)\omega_p$, $\tilde{\omega}_{15} = (1.2267 - 0.0050i)\omega_p$, and $\tilde{\omega}_{16} = (1.3202 - 0.0050i)\omega_p$. The total extinction cross section $\sigma_{\mathrm{tot}}(\omega_0)$ is plotted as a reference solution.

Based on the computed spectrum, we investigate the extinction cross section,

$$\sigma(\omega_0) = \frac{1}{P_{\text{pw}}} \left[\int_{\delta\Omega} \frac{1}{2} \text{Re}(\mathbf{E}^*(\mathbf{r}, \omega_0) \times \mathbf{H}(\mathbf{r}, \omega_0)) dS \right.$$
$$\left. + \int_{\Omega_{\text{nw}}} \frac{1}{2} \text{Re}(\mathbf{E}^*(\mathbf{r}, \omega_0) \cdot \mathbf{J}_{\text{hd}}(\mathbf{r}, \omega_0)) dV \right],$$

where the first term is the power flux across the boundary of the entire computational domain, denoted by $\delta\Omega$, and the second term is the energy loss in the domain where the nanowire exists, denoted by Ω_{nw} [31]. The incoming plane wave with real frequencies ω_0 is normalized so that the power flux through the geometrical cross section of the nanowire is $P_{\text{pw}} = 4 \times 10^{-9}$ W. To quantify the coupling of the light source to specific eigenmodes, the RPE is applied. This requires the holomorphic evaluation of sesquilinear quantities from Eq. (3) and yields the modal extinction cross section $\tilde{\sigma}_k(\omega_0)$ corresponding to an eigenfrequency $\tilde{\omega}_k$. The direct solution of the coupled system given by Eqs. (1) and (2) yields the total extinction cross section $\sigma_{\text{tot}}(\omega_0)$.

First, we investigate the modal extinction cross section in a small frequency range including $\tilde{\omega}_7, \ldots, \tilde{\omega}_{12}$. Figure 3(a) shows $\tilde{\sigma}_7(\omega_0), \ldots, \tilde{\sigma}_{12}(\omega_0)$, and $\sigma_{\text{tot}}(\omega_0)$. The eigenmode $\tilde{v}_{10}$ has a significant contribution to $\sigma_{\text{tot}}(\omega_0)$. The contributions of the eigenmodes $\tilde{v}_7, \tilde{v}_8, \tilde{v}_9, \tilde{v}_{11}$, and $\tilde{v}_{12}$ are negligible.

Secondly, in order to understand why a specific eigenmode couples to the incoming plane wave, a fast Fourier transform of the electric field intensities of the eigenmodes on a circle inside the nanowire is performed. This yields the number of intensity maxima of the eigenmodes along the boundary of the nanowire, which we denote by $n_\varphi(\tilde{\omega}_k)$. In this way, it is possible to classify the eigenmodes. Figure 3(b) shows $n_\varphi(\tilde{\omega}_k)$ for the frequency range $0.4\,\omega_{\text{p}} < \text{Re}(\tilde{\omega}_k) < 1.4\,\omega_{\text{p}}$. The field intensities of the six eigenmodes with $n_\varphi(\tilde{\omega}_k) = 2$ are plotted in Fig. 3(c). It can be seen that these modes are dipolelike. Due to the relation of the radius of the nanowire and the wavelength of the plane wave, $R \ll \lambda_0$, the overlap integral of source field and eigenmode field has a significant contribution only for these modes.

Finally, the modal extinction cross sections $\tilde{\sigma}_k(\omega_0)$ for the eigenfrequencies with $n_\varphi(\tilde{\omega}_k) = 2$ are computed. Figure 3(d) shows the sum of the modal extinction cross sections $\sum_M \tilde{\sigma}_k(\omega_0)$, $M = \{k \mid n_\varphi(\tilde{\omega}_k) = 2\}$. For the investigated scattering of a plane wave, the agreement of the expansion with the total extinction cross section $\sigma_{\text{tot}}(\omega_0)$ demonstrates that the complex scattering behavior of the HDM-based nanowire is governed by a few eigenmodes only. Note that the total extinction cross section is in agreement with results from the literature [17,31].

For illumination with different types of source fields, e.g., dipole sources, also the remaining eigenmodes of the rich spectrum can be excited.

IV. CONCLUSIONS

We investigated the light-matter interaction in nanoplasmonic systems described by the HDM. We presented a contour-integral-based framework for modal analysis, which enables the direct computation of the spectrum of nonlocal material systems. We introduced an approach for the modal expansion of sesquilinear quantities. This opens the possibility to investigate typical physical observables, e.g., the energy flux, the energy absorption, and overlap integrals for extraction efficiencies. Due to the generality of this approach, we expect that it will prove useful also in other fields of physics. Resonant states and the modal extinction cross section of a metal nanowire were calculated. While the spectrum of this system consists of many eigenfrequencies, only a few resonant states have a significant contribution to the extinction cross section. These resonant states were identified and used to expand the quantity of interest.

As demonstrated, nanoplasmonic systems on small length scales exhibit a large number of additional resonant states described by the HDM. A typical feature of these states is their high local field energy concentration. With precisely defined source fields, specific states can be excited. We expect that this will allow for additional degrees of freedom in tailoring light-matter interactions. A modal picture is a prerequisite for the understanding and for the design of corresponding nanoplasmonic devices.

[1] N. C. Lindquist, P. Nagpal, K. M. McPeak, D. J. Norris, and S.-H. Oh, Rep. Prog. Phys. **75**, 036501 (2012).

[2] R. F. Oulton, V. J. Sorger, T. Zentgraf, R.-M. Ma, C. Gladden, L. Dai, G. Bartal, and X. Zhang, Nature (London) **461**, 629 (2009).

[3] A. G. Curto, G. Volpe, T. H. Taminiau, M. P. Kreuzer, R. Quidant, and N. F. van Hulst, Science **329**, 930 (2010).

[4] V. Giannini, A. I. Fernández-Domínguez, S. C. Heck, and S. A. Maier, Chem. Rev. **111**, 3888 (2011).

[5] S. Nie and S. R. Emory, Science **275**, 1102 (1997).

[6] Y. Zhang, S. He, W. Guo, Y. Hu, J. Huang, J. R. Mulcahy, and W. D. Wei, Chem. Rev. **118**, 2927 (2018).

[7] R. Chikkaraddy, B. de Nijs, F. Benz, S. J. Barrow, O. A. Scherman, E. Rosta, A. Demetriadou, P. Fox, O. Hess, and J. J. Baumberg, Nature (London) **535**, 127 (2016).

[8] W. A. Murray and W. L. Barnes, Adv. Mater. **19**, 3771 (2007).

[9] H. S. Sehmi, W. Langbein, and E. A. Muljarov, Phys. Rev. B **95**, 115444 (2017).

[10] M. Garcia-Vergara, G. Demésy, and F. Zolla, Opt. Lett. **42**, 1145 (2017).

[11] P. B. Johnson and R. W. Christy, Phys. Rev. B **6**, 4370 (1972).

[12] S. Raza, S. I. Bozhevolnyi, M. Wubs, and N. A. Mortensen, J. Phys. Condens. Matter **27**, 183204 (2015).

[13] J. A. Scholl, A. L. Koh, and J. A. Dionne, Nature (London) **483**, 421 (2012).

[14] S. Raza, N. Stenger, S. Kadkhodazadeh, S. V. Fischer, N. Kostesha, A.-P. Jauho, A. Burrows, M. Wubs, and N. A. Mortensen, Nanophotonics **2**, 131 (2013).

[15] T. Christensen, W. Yan, S. Raza, A.-P. Jauho, N. A. Mortensen, and M. Wubs, ACS Nano **8**, 1745 (2014).

[16] A. D. Boardman, *Electromagnetic Surface Modes. Hydrodynamic Theory of Plasmon-Polaritons on Plane Surfaces* (Wiley, New York, 1982).

[17] R. Ruppin, Opt. Commun. **190**, 205 (2001).

[18] S. Palomba, L. Novotny, and R. Palmer, Opt. Commun. **281**, 480 (2008).

[19] F. J. García de Abajo, J. Phys. Chem. C **112**, 17983 (2008).

[20] F. Intravaia and K. Busch, Phys. Rev. A **91**, 053836 (2015).

[21] G. Toscano, J. Straubel, A. Kwiatkowski, C. Rockstuhl, F. Evers, N. A. Mortensen, and M. Wubs, Nat. Commun. **6**, 7132 (2015).

[22] O. Schnitzer, V. Giannini, S. A. Maier, and R. V. Craster, Proc. Royal Soc. A **472**, 20160258 (2016).

[23] M. Moeferdt, T. Kiel, T. Sproll, F. Intravaia, and K. Busch, Phys. Rev. B **97**, 075431 (2018).

[24] P. T. Kristensen and S. Hughes, ACS Photonics **1**, 2 (2014).

[25] P. Lalanne, W. Yan, K. Vynck, C. Sauvan, and J.-P. Hugonin, Laser Photonics Rev. **12**, 1700113 (2018).

[26] C. Sauvan, J.-P. Hugonin, I. S. Maksymov, and P. Lalanne, Phys. Rev. Lett. **110**, 237401 (2013).

[27] M. Kamandar Dezfouli, R. Gordon, and S. Hughes, Phys. Rev. A **95**, 013846 (2017).

[28] L. Zschiedrich, F. Binkowski, N. Nikolay, O. Benson, G. Kewes, and S. Burger, Phys. Rev. A **98**, 043806 (2018).

[29] W. Yan, R. Faggiani, and P. Lalanne, Phys. Rev. B **97**, 205422 (2018).

[30] J. M. McMahon, S. K. Gray, and G. C. Schatz, Phys. Rev. Lett. **103**, 097403 (2009).

[31] K. R. Hiremath, L. Zschiedrich, and F. Schmidt, J. Comput. Phys. **231**, 5890 (2012).

[32] G. Toscano, S. Raza, A.-P. Jauho, N. A. Mortensen, and M. Wubs, Opt. Express **20**, 4176 (2012).

[33] M. Kamandar Dezfouli, C. Tserkezis, N. A. Mortensen, and S. Hughes, Optica **4**, 1503 (2017).

[34] W.-J. Beyn, Linear Algebra Its Appl. **436**, 3839 (2012).

[35] S. Güttel and F. Tisseur, Acta Numer. **26**, 1 (2017).

[36] J. Asakura, T. Sakurai, H. Tadano, T. Ikegami, and K. Kimura, JSIAM Lett. **1**, 52 (2009).

[37] B. Gavin, A. Miedlar, and E. Polizzi, J. Comput. Sci **27**, 107 (2018).

[38] Y. Saad, *Numerical Methods for Large Eigenvalue Problems,* 2nd ed. (SIAM, Philadelphia, 2011).

[39] Y. Brûlé, B. Gralak, and G. Demésy, J. Opt. Soc. Am. B **33**, 691 (2016).

[40] P. Monk, *Finite Element Methods for Maxwell's Equations* (Clarendon Press, Oxford, 2003).

[41] M. Weiser, *Inside Finite Elements* (De Gruyter, Berlin, 2016).

[42] J.-P. Berenger, J. Comput. Phys. **114**, 185 (1994).

[43] P. Lalanne, W. Yan, A. Gras, C. Sauvan, J.-P. Hugonin, M. Besbes, G. Demésy, M. D. Truong, B. Gralak, F. Zolla, A. Nicolet, F. Binkowski, L. Zschiedrich, S. Burger, J. Zimmerling, R. Remis, P. Urbach, H. T. Liu, and T. Weiss, J. Opt. Soc. Am. A **36**, 686 (2019).

4 Resonances and optical far-field quantities

Nanophotonic observables are usually measured in the far field of the corresponding devices. The resonance expansion of optical far-field quantities is not straightforward because, due to the open material systems, the eigenmodes diverge with increasing distance from the underlying nanoresonators [15, 47].

In Ref. [66], we introduce an approach for the resonance expansion of far-field quantities. The approach is based on Riesz projections and builds on the results presented in the previous chapters. We investigate the energy flux density [92] in the far field of a nanophotonic device,

$$s(\mathbf{E}(\mathbf{r}, \omega_0), \mathbf{E}^*(\mathbf{r}, \omega_0)) = \frac{1}{2} \mathrm{Re} \left(\mathbf{E}^*(\mathbf{r}, \omega_0) \times \frac{1}{i\omega_0 \mu_0} \nabla \times \mathbf{E}(\mathbf{r}, \omega_0) \right) \cdot \mathbf{n},$$

where $\mathbf{n}$ is the normal on the corresponding far-field sphere. The energy flux density, which is a quadratic quantity with a sesquilinear map, is nonholomorphic due to the complex conjugation of the electric field. This implies that the analytical continuation of $s(\mathbf{E}(\mathbf{r}, \omega_0), \mathbf{E}^*(\mathbf{r}, \omega_0))$ into the complex frequency plane, which is required for the contour integration within the Riesz projection expansion given by Eq. (2.4), is problematic. To overcome this issue, we use the relation $\mathbf{E}^*(\mathbf{r}, \omega_0) = \mathbf{E}(\mathbf{r}, -\omega_0)$ and introduce the field $\mathbf{E}^\circ(\mathbf{r}, \omega)$, where $\omega \in \mathbb{C}$, as the analytical continuation of $\mathbf{E}(\mathbf{r}, -\omega_0)$ into the complex frequency plane. This yields the Riesz projection expansion of the energy flux density,

$$\begin{aligned}
s(\mathbf{E}(\mathbf{r}, \omega_0), \mathbf{E}^*(\mathbf{r}, \omega_0)) = & -\sum_{m=1}^{M} \frac{1}{2\pi i} \oint_{C_m} \frac{s(\mathbf{E}(\mathbf{r}, \omega), \mathbf{E}^\circ(\mathbf{r}, \omega))}{\omega - \omega_0} \, \mathrm{d}\omega \\
& -\sum_{m=1}^{M} \frac{1}{2\pi i} \oint_{C_m^*} \frac{s(\mathbf{E}(\mathbf{r}, \omega), \mathbf{E}^\circ(\mathbf{r}, \omega))}{\omega - \omega_0} \, \mathrm{d}\omega \\
& + \frac{1}{2\pi i} \oint_{C_{\mathrm{nr}}} \frac{s(\mathbf{E}(\mathbf{r}, \omega), \mathbf{E}^\circ(\mathbf{r}, \omega))}{\omega - \omega_0} \, \mathrm{d}\omega,
\end{aligned} \tag{4.1}$$

where the contours C_m enclose the eigenfrequencies $\tilde{\omega}_m$, the complex conjugated contours C_m^* enclose the complex conjugated eigenfrequencies $\tilde{\omega}_m^*$, and C_{nr} corresponds to the remainder of the expansion. The contour integrals for C_m^* take into account the eigenfrequencies corresponding to the field $\mathbf{E}^*(\mathbf{r}, \omega_0)$. The electric fields $\mathbf{E}(\mathbf{r}, \omega)$ and $\mathbf{E}^\circ(\mathbf{r}, \omega)$ are computed by solving scattering problems given by Eq. (2.1). Equation (4.1) can be used to perform a resonance expansion of the energy flux density in the far field, since the calculation of the product involving $\mathbf{E}(\mathbf{r}, \omega)$ and $\mathbf{E}^\circ(\mathbf{r}, \omega)$ leads to nondiverging expansion terms.

We apply the Riesz projection expansion given by Eq. (4.1) to an example from the literature, the electromagnetic field emitted by a quantum dot acting as single-photon source [93]. The expansion of the energy flux density $s(\mathbf{E}(\mathbf{r}, \omega_0), \mathbf{E}^*(\mathbf{r}, \omega_0))$ in the far field of the nanophotonic device is computed. This provides information about how the eigenmodes radiate in different directions. We also compute the expansion of the photon collection efficiency [93], which is directly related to the energy flux density. Furthermore, we compute the Riesz projection expansion of the Purcell factor given by Eq. (2.5). This provides information on how the individual eigenmodes can enhance the emission of the single-photon source.

In the following, Ref. [66] is reprinted with permission from [Felix Binkowski, Fridtjof Betz, Rémi Colom, Martin Hammerschmidt, Lin Zschiedrich, and Sven Burger. Quasi-normal mode expansion of optical far-field quantities. *Phys. Rev. B* 102, 035432 (2020). DOI: 10.1103/PhysRevB.102.035432.] Copyright 2020 by the American Physical Society.

Quasinormal mode expansion of optical far-field quantities

Felix Binkowski ⬤,[1] Fridtjof Betz,[1] Rémi Colom,[1] Martin Hammerschmidt ⬤,[2] Lin Zschiedrich ⬤,[2] and Sven Burger ⬤[1,2]

[1]*Zuse Institute Berlin, Takustraße 7, 14195 Berlin, Germany*
[2]*JCMwave GmbH, Bolivarallee 22, 14050 Berlin, Germany*

Quasinormal mode (QNM) expansion is a popular tool to analyze light-matter interaction in nanoresonators. However, expanding far-field quantities such as the energy flux is an open problem because QNMs diverge with an increasing distance to the resonant systems. We introduce a theory to compute modal expansions of far-field quantities rigorously. The presented approach is based on the complex eigenfrequencies of QNMs. The divergence problem is circumvented by using contour integration with an analytical continuation of the far-field quantity into the complex frequency plane. We demonstrate the approach by computing the angular resolved modal energy flux in the far field of a nanophotonic device.

I. INTRODUCTION

Modern nanotechnology allows for exploring new regimes in tailoring light-matter interaction [1]. Applications comprise the design of nanoantennas for quantum information technology [2], tuning photochemistry applications with nanoresonators [3], using plasmonic nanoparticles for biosensing [4], and miniaturization of optical components using dielectric metasurfaces [5]. Most approaches are based on resonance phenomena. Optical resonances are characterized by their wavelength-dependent localized and radiated field energies. They may appear as, e.g., plasmonic resonances in metals [6] or resonances in dielectric materials, such as Mie resonances [7] or bound states in the continuum [8]. The theoretical description of the resonances is essential for understanding the physical properties of the systems and for designing and optimizing related devices. A popular approach is the modeling with QNMs, which are the eigensolutions of resonant systems [9,10]. In typical nanophotonic setups, outgoing radiation conditions have to be fulfilled yielding complex eigenfrequencies and an exponential decay of the QNMs in time. This means that the QNMs diverge exponentially with an increasing distance to the resonators [9–12]. Due to the conceptual difficulties of exponential growth, this behavior has been termed "exponential catastrophe" [12]. Nevertheless, QNM-based expansion approaches, where electromagnetic fields are expanded into weighted sums of QNMs, have been derived to describe light-matter interaction in various applications [13–18]. These approaches are based on the expansion of electromagnetic fields inside and in the close vicinity of the resonators. In this way, modal near-field quantities, such as the modal Purcell enhancement [19–21], can be computed. For time-dependent problems, methods have been proposed to overcome the divergence problem [22–24].

In many applications, time-averaged far-field quantities are of special interest [1,2,5]. However, the divergence of QNMs is a key issue for modal expansion of such quantities [9,10]. From a physics perspective, for time-harmonic sources, the excited electromagnetic near- and far-field dis-

tributions are clearly nondiverging. This has motivated a discussion about the general applicability of QNMs [25]. Alternative approaches based on model approximations which yield eigenmodes with real-valued frequencies in the far-field regions have been proposed [25–27]. Further methods use the Dyson equation approach [28,29] or near-field to far-field transformations [30] of the QNMs resulting in approximations of the computed far-field quantities [18,31]. Also, the intensively discussed question of how to normalize QNMs is related to their exponential divergence [9,10,32–35].

In this work, we present a general approach for modal analysis which allows for expansions of physical observables in the far-field region. The approach is based on the complex eigenfrequencies of the resonant systems; however, the diverging behavior of the corresponding QNMs is circumvented by using contour integration of the relevant far-field quantities. Therefore, the presented approach paves the way for avoiding an exponential catastrophe while retaining the rigorous model. No approximation regarding the modeling of the naturally complex-valued frequencies of a resonant system is required. The method is validated by comparing the modal expansion to a direct solution of the corresponding scattering problem. The approach is applied to compute the modal expansion of the angular resolved energy flux density radiated to the far field by a localized source in a resonant nanostructure.

II. MODAL EXPANSION OF FAR-FIELD QUANTITIES

The QNMs of a resonant system are diverging outgoing waves. Figure 1(a) illustrates the electric field corresponding to a QNM in a one-dimensional resonator defined by layers with different refractive indices. In nano-optics, in the steady-state regime, electric fields $\mathbf{E}(\omega_0) \in \mathbb{C}^3$ are solutions to the time-harmonic Maxwell's equations in second-order form,

$$\nabla \times \mu(\omega_0)^{-1} \nabla \times \mathbf{E}(\omega_0) - \omega_0^2 \epsilon(\omega_0)\mathbf{E}(\omega_0) = i\omega_0\mathbf{J}, \quad (1)$$

where $\omega_0 \in \mathbb{R}$ is the angular frequency and $\mathbf{J} \in \mathbb{C}^3$ is the source field. For a simpler notation, we omit the spatial
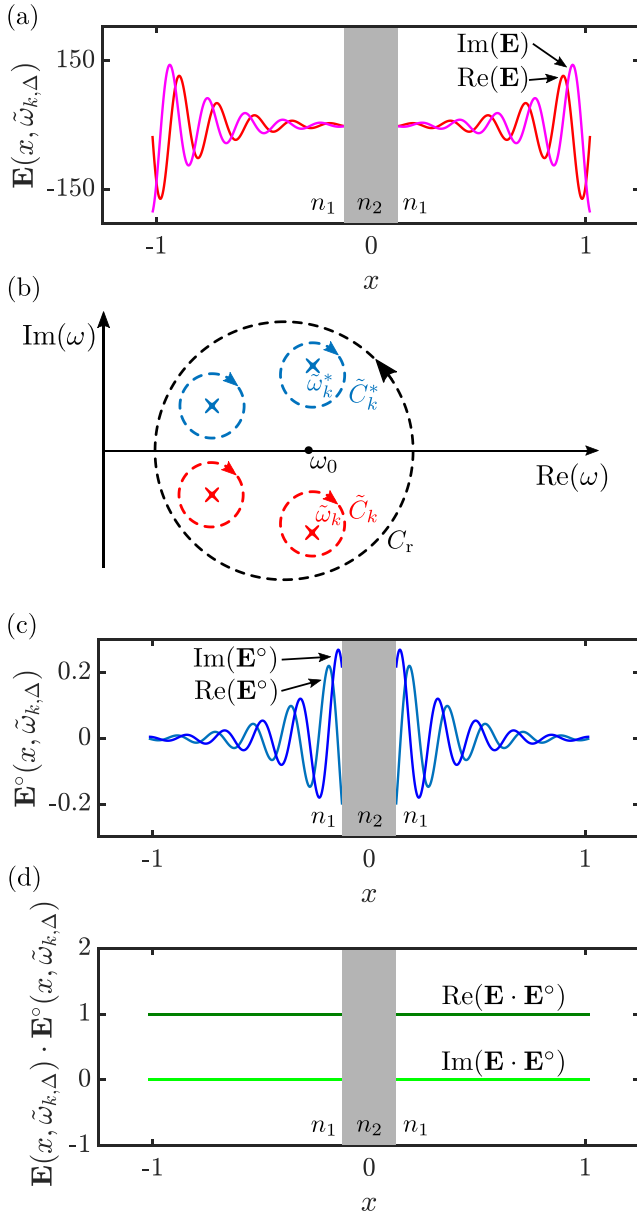
FIG. 1. One-dimensional resonator defined by layers with different refractive indices, where $n_2 > n_1$. Electric field solutions, $\mathbf{E}(x, \omega)$ and $\mathbf{E}^{\circ}(x, \omega)$, are obtained by solving the Helmholtz equation with a source term corresponding to incoming plane waves with unit amplitude. Only scattered fields (a.u.) outside the resonator are shown. (a) Diverging field $\mathbf{E}(x, \tilde{\omega}_{k,\Delta}) = A\, e^{i(n_1 \tilde{\omega}_{k,\Delta}/c)|x|}$, where $\tilde{\omega}_k$ is a resonance pole of $\mathbf{E}(x, \omega)$ and $\tilde{\omega}_{k,\Delta} = \tilde{\omega}_k + \Delta \tilde{\omega}_k$ is a frequency close to $\tilde{\omega}_k$. (b) Illustration of resonance poles and integration contours corresponding to the RPE for the energy flux density given by Eq. (2). The analytical continuation of the energy flux density has resonance poles with negative and with positive imaginary parts. (c) Nondiverging field $\mathbf{E}^{\circ}(x, \tilde{\omega}_{k,\Delta}) = B\, e^{-i(n_1 \tilde{\omega}_{k,\Delta}/c)|x|}$. (d) Constant product $\mathbf{E}(x, \tilde{\omega}_{k,\Delta}) \cdot \mathbf{E}^{\circ}(x, \tilde{\omega}_{k,\Delta})$, which relates to the energy flux density.

dependence of the quantities and write, e.g., $\mathbf{E}(\omega_0)$ instead of $\mathbf{E}(\mathbf{r}, \omega_0)$, where $\mathbf{r} \in \mathbb{R}^3$ is the position. The permittivity tensor and the permeability tensor are defined by $\epsilon(\omega_0)$ and $\mu(\omega_0)$, respectively. For optical frequencies, $\mu(\omega_0)$ is typically equal

to the vacuum permeability μ_0. QNMs are solutions to Eq. (1) equipped with outgoing radiation conditions and without a source, i.e., $\mathbf{J} = 0$. The eigenfrequencies $\tilde{\omega}_k \in \mathbb{C}$ have negative imaginary parts and are given by the complex resonance poles of the analytical continuation $\mathbf{E}(\omega)$ of the electric field $\mathbf{E}(\omega_0)$ into the complex plane $\omega \in \mathbb{C}$.

We use the Riesz projection expansion (RPE) [17,36] for modal expansion of the energy flux density in the far field, which can be expressed as a quadratic form with a sesquilinear map. The energy flux density [37] is defined by

$$s(\mathbf{E}(\omega_0), \mathbf{E}^*(\omega_0)) = \frac{1}{2}\mathrm{Re}\left(\mathbf{E}^*(\omega_0) \times \frac{1}{i\omega_0\mu_0}\nabla \times \mathbf{E}(\omega_0)\right) \cdot \mathbf{n},$$

where $\mathbf{E}^*(\omega_0)$ is the complex conjugate of the electric field and $\mathbf{n}$ is the normal on the corresponding far-field sphere. The RPE is based on contour integration in the complex frequency plane. Since the complex conjugation of the electric field makes $s(\mathbf{E}(\omega_0), \mathbf{E}^*(\omega_0))$ nonholomorphic, the evaluation of this function for complex frequencies is problematic. This challenge can be addressed by exploiting the relation $\mathbf{E}^*(\omega_0) = \mathbf{E}(-\omega_0)$ for $\omega_0 \in \mathbb{R}$. The field $\mathbf{E}(-\omega_0)$ is a solution to Eq. (1) as well. For the harmonic time dependency $e^{-i\omega_0 t}$ with a negative frequency, the radiation conditions are sign inverted. The field $\mathbf{E}(-\omega_0)$ has an analytical continuation into the complex plane $\omega \in \mathbb{C}$, which we denote by $\mathbf{E}^{\circ}(\omega)$. This yields the required analytical continuation of $s(\mathbf{E}(\omega_0), \mathbf{E}^*(\omega_0))$, which is given by $s(\mathbf{E}(\omega), \mathbf{E}^{\circ}(\omega))$. Note that $\mathbf{E}^{\circ}(\omega)$ introduces resonance poles in the upper complex half-plane, which are usually not considered in the literature. These poles are an essential part of the presented approach. To expand $s(\mathbf{E}(\omega_0), \mathbf{E}^*(\omega_0)) = s(\mathbf{E}(\omega_0), \mathbf{E}^{\circ}(\omega_0))$ into modal contributions, Cauchy's integral formula,

$$s(\mathbf{E}(\omega_0), \mathbf{E}^{\circ}(\omega_0)) = \frac{1}{2\pi i}\oint_{C_0} \frac{s(\mathbf{E}(\omega), \mathbf{E}^{\circ}(\omega))}{\omega - \omega_0}d\omega,$$

is then exploited. The contour C_0 is a closed integration path around ω_0 so that $s(\mathbf{E}(\omega), \mathbf{E}^{\circ}(\omega))$ is holomorphic inside of C_0. Deforming the integration path and applying Cauchy's residue theorem yield

$$
\begin{aligned}
s(\mathbf{E}(\omega_0), \mathbf{E}^{\circ}(\omega_0)) = &-\sum_{k=1}^{K}\frac{1}{2\pi i}\oint_{\tilde{C}_k} \frac{s(\mathbf{E}(\omega), \mathbf{E}^{\circ}(\omega))}{\omega - \omega_0}d\omega \\
&-\sum_{k=1}^{K}\frac{1}{2\pi i}\oint_{\tilde{C}_k^*} \frac{s(\mathbf{E}(\omega), \mathbf{E}^{\circ}(\omega))}{\omega - \omega_0}d\omega \\
&+\frac{1}{2\pi i}\oint_{C_r} \frac{s(\mathbf{E}(\omega), \mathbf{E}^{\circ}(\omega))}{\omega - \omega_0}d\omega,
\end{aligned}
\tag{2}
$$

where $\tilde{C}_1, \ldots, \tilde{C}_K$ are contours around the resonance poles of $\mathbf{E}(\omega)$, given by $\tilde{\omega}_1, \ldots, \tilde{\omega}_K$, and $\tilde{C}_1^*, \ldots, \tilde{C}_K^*$ are contours around the resonance poles of $\mathbf{E}^{\circ}(\omega)$, given by $\tilde{\omega}_1^*, \ldots, \tilde{\omega}_K^*$. The outer contour C_r includes ω_0, the resonance poles $\tilde{\omega}_1, \ldots, \tilde{\omega}_K$ and $\tilde{\omega}_1^*, \ldots, \tilde{\omega}_K^*$, and no further poles, as sketched in Fig. 1(b). The Riesz projections

$$
\begin{aligned}
\tilde{s}_k(\mathbf{E}(\omega_0), \mathbf{E}^{\circ}(\omega_0)) = &-\frac{1}{2\pi i}\oint_{\tilde{C}_k} \frac{s(\mathbf{E}(\omega), \mathbf{E}^{\circ}(\omega))}{\omega - \omega_0}d\omega \\
&-\frac{1}{2\pi i}\oint_{\tilde{C}_k^*} \frac{s(\mathbf{E}(\omega), \mathbf{E}^{\circ}(\omega))}{\omega - \omega_0}d\omega
\end{aligned}
$$

TABLE I. Eigenfrequencies of the resonator shown in Fig. 2(a). The eigenfrequencies $\tilde{\omega}_k$ are contained in the circular contour C_r, which is centered at 1.41×10^{15} s^{-1} and has a radius of 6.8×10^{13} s^{-1}.

k	Re($\tilde{\omega}_k$) (10^{15} s^{-1})	Im($\tilde{\omega}_k$) (10^{13} s^{-1})
1	1.441	-0.109
2	1.428	-0.182
3	1.399	-0.232
4	1.372	-0.568
5	1.370	-1.025
6	1.398	-2.475
7	1.406	-0.470
8	1.422	-0.875
9	1.435	-1.942

are modal contributions for the energy flux density. The Riesz projections $\tilde{s}_k(\mathbf{E}(\omega_0), \mathbf{E}^\circ(\omega_0))$ are associated with the eigenfrequencies $\tilde{\omega}_k$ as the integration is performed along the contours $\tilde{C}_k$ and $\tilde{C}_k^*$. The contribution

$$s_r(\mathbf{E}(\omega_0), \mathbf{E}^\circ(\omega_0)) = \frac{1}{2\pi i} \oint_{C_r} \frac{s(\mathbf{E}(\omega), \mathbf{E}^\circ(\omega))}{\omega - \omega_0} d\omega$$

is the remainder of the expansion containing nonresonant components as well as components corresponding to eigenfrequencies outside of the contour C_r.

The RPE is based on evaluating $s(\mathbf{E}(\omega), \mathbf{E}^\circ(\omega))$ by solving Eq. (1) for the frequencies ω and $-\omega$. Consequently, the quadratic form $s(\mathbf{E}(\omega), \mathbf{E}^\circ(\omega))$, where a product of $\mathbf{E}(\omega)$ and $\mathbf{E}^\circ(\omega)$ is involved, does not diverge. This is due to the cancellation of the factors $e^{i(n\omega/c)r}$ and $e^{-i(n\omega/c)r}$ of the fields in the far-field region, where $r = \|\mathbf{r}\|$. In this way, it becomes possible to compute modal expansions of far-field quantities with nondiverging expansion terms. To illustrate this, we consider a one-dimensional resonator and compute electric fields, $\mathbf{E}(x, \omega)$ and $\mathbf{E}^\circ(x, \omega)$, fulfilling the corresponding Helmholtz equation. Figures 1(a) and 1(c) sketch the diverging field $\mathbf{E}(x, \tilde{\omega}_{k,\Delta})$ and the nondiverging field $\mathbf{E}^\circ(x, \tilde{\omega}_{k,\Delta})$ outside of the resonator, respectively. The frequency $\tilde{\omega}_{k,\Delta} = \tilde{\omega}_k + \Delta\tilde{\omega}_k$ represents an evaluation point on an integration contour $\tilde{C}_k$. Figure 1(d) shows the nondiverging product $\mathbf{E}(x, \tilde{\omega}_{k,\Delta}) \cdot \mathbf{E}^\circ(x, \tilde{\omega}_{k,\Delta})$, which relates to the energy flux density. The approach also applies to arbitrary three-dimensional problems, where, in the far-field region, $\mathbf{E}(\mathbf{r}, \omega) \sim e^{i(n\omega/c)r}(1/r)$ and $\mathbf{E}^\circ(\mathbf{r}, \omega) \sim e^{-i(n\omega/c)r}(1/r)$.

III. APPLICATION

The presented approach is used for modal analysis of a quantum technology device. We revisit an example from the literature [38], where a quantum dot acts as a single-photon source. For a specific far-field region, the photon collection efficiency (PCE) has been enhanced by using a numerically optimized circular Bragg grating nanoresonator. Such devices can be realized experimentally by using deterministic fabrication technologies [39]. For more details on the specific device and material properties, the reader is referred to [38]. The geometry is sketched in Fig. 2(a). To numerically analyze the
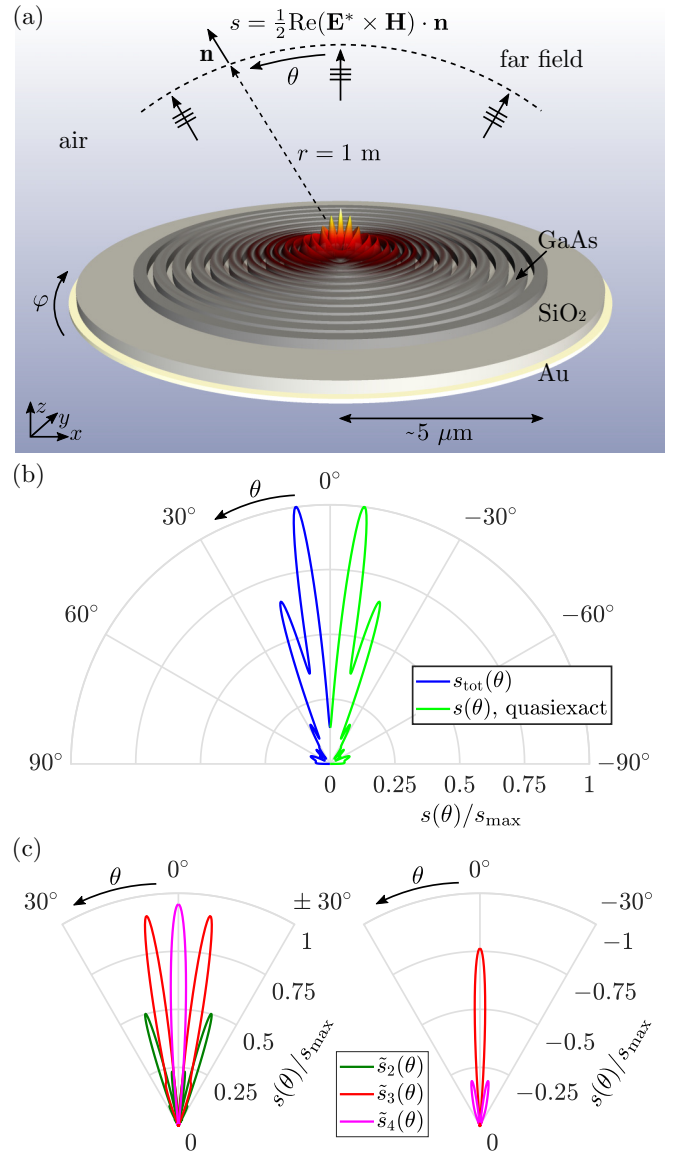

FIG. 2. Circular Bragg grating resonator with localized light source. (a) Geometry with an illustration of the electric field intensity (a.u.) of the QNM corresponding to the eigenfrequency $\tilde{\omega}_2$; see Table I. The gallium arsenide (GaAs) grating has a thickness of 240 nm and consists of an inner disk with a radius of 550 nm and 10 rings with a width of 340 nm and a periodicity of 500 nm. The grating is placed on a silicon dioxide (SiO$_2$) layer with a thickness of 240 nm, which is coated from below with a gold (Au) layer of 300 nm thickness. The light source is modeled by a dipole emitter placed at the center of the inner disk. The dipole radiates at the frequency ω_0 and is oriented in x direction. (b) Radiation diagram at $\omega_0 = 2\pi c/(1360 \text{ nm})$ for the total modal expansion $s_{tot}(\theta)$ computed by Eq. (2) and for the quasiexact solution of the energy flux density $s(\theta)$. The quantities are evaluated at $r = 1$ m and $\varphi = 90°$, which corresponds to the yz plane. (c) Modal decomposition of the radiation diagram for the contributions $\tilde{s}_2(\theta)$, $\tilde{s}_3(\theta)$, and $\tilde{s}_4(\theta)$.

light source, we spatially discretize the system with the finite element method (FEM) using the solver JCMSUITE [40].

The quantity of interest is the energy flux density in the far field $s(\omega_0, \theta) = s(\mathbf{E}(\omega_0, \theta), \mathbf{E}^\circ(\omega_0, \theta))$, see Eq. (2), where

θ is the inclination angle as shown in Fig. 2(a). For the modal expansion of $s(\omega_0, \theta)$, the outer contour C_r is chosen to enclose the wavelength range of interest, 1280 nm $\leqslant$ $\lambda_0 \leqslant 1400$ nm, where $\lambda_0 = 2\pi c/\omega_0$. We compute all eigenfrequencies inside of the contour, which are listed in Table I. Note that only those rotationally symmetric QNMs which can couple to the dipole source are computed. Figure 2(a) sketches the electric field intensity of the QNM corresponding to $\tilde{\omega}_2$ in the near field of the structure. The QNM exhibits a maximum of the field intensity at the center of the resonator and it diverges in the far-field region.

For a fixed dipole frequency, the radiation diagrams for the total modal expansion $s_{\text{tot}}(\omega_0, \theta) = \sum_{k=1}^{9} \tilde{s}_k(\omega_0, \theta) + s_r(\omega_0, \theta)$ and for the quasiexact solution $s(\omega_0, \theta)$ are depicted in Fig. 2(b). The quasiexact solution is computed by solving scattering problems given by Eq. (1) directly. The total modal expansion coincides with the quasiexact solution with an absolute error of $s(\theta)/s_{\text{max}} < 5 \times 10^{-3}$ and, for the angle region $-60° < \theta < 60°$, with a relative error smaller than 3×10^{-5}. The differences in these solutions are related to numerical discretization errors and would decrease further by refining the numerical parameters. The agreement demonstrates that, although the associated QNMs diverge in the far field, the RPE of the energy flux density gives correct results with nondiverging expansion terms. Figure 2(c) shows the modal energy flux densities $\tilde{s}_2(\omega_0, \theta)$, $\tilde{s}_3(\omega_0, \theta)$, and $\tilde{s}_4(\omega_0, \theta)$. These are the significant contributions for the total energy flux density and they have different directivities corresponding to the different diffraction intensities of the Bragg grating. The contributions $\tilde{s}_3(\omega_0, \theta)$ and $\tilde{s}_4(\omega_0, \theta)$ also have negative values. A negative modal energy flux density can be understood as suppression of light emission into specific directions arising from the interference of various modes excited by the source at the frequency ω_0. Negative modal contributions have been reported also for QNM expansions of near-field quantities [19]. Note that, as physically expected, the total modal expansion of the energy flux density, $s_{\text{tot}}(\omega_0, \theta)$, is positive for all angles θ.

Next, the RPE is used to obtain insight into the properties of the device for the wavelength range 1280 nm $\leqslant \lambda_0 \leqslant$ 1400 nm. Figure 3(a) shows the normalized decay rate, also termed Purcell enhancement,

$$\Gamma(\omega_0) = -\frac{1}{2}\text{Re}(\mathbf{E}(\omega_0) \cdot \mathbf{j}^*)/\Gamma_b,$$

where $\mathbf{j} = -i\omega\mathbf{p}$ with the dipole moment $\mathbf{p}$ and Γ_b is the dipole emission in homogeneous background material [17]. It can be observed that, in the wavelength range of interest, the three resonances corresponding to the eigenfrequencies $\tilde{\omega}_2$, $\tilde{\omega}_3$, and $\tilde{\omega}_4$ are significant for the Purcell enhancement. The resonance with the eigenfrequency $\tilde{\omega}_1$ has a very small influence. The nonresonant contributions and the contributions associated with other eigenfrequencies are negligible. Figure 3(b) shows the PCE,

$$\eta(\omega_0) = \frac{1}{P_{\text{DE}}} \int_{\delta\Omega} \frac{1}{2}\text{Re}\left(\mathbf{E}^*(\omega_0) \times \frac{1}{i\omega_0\mu_0}\nabla \times \mathbf{E}(\omega_0)\right) \cdot d\mathbf{S},$$

where $\delta\Omega$ is the far-field region corresponding to NA = 0.8 and P_{DE} is the emitted power of the dipole emitter into the upper hemisphere. In the case of the PCE, the resonances corresponding to $\tilde{\omega}_1$, $\tilde{\omega}_2$, $\tilde{\omega}_3$, and $\tilde{\omega}_4$ play an important role. In
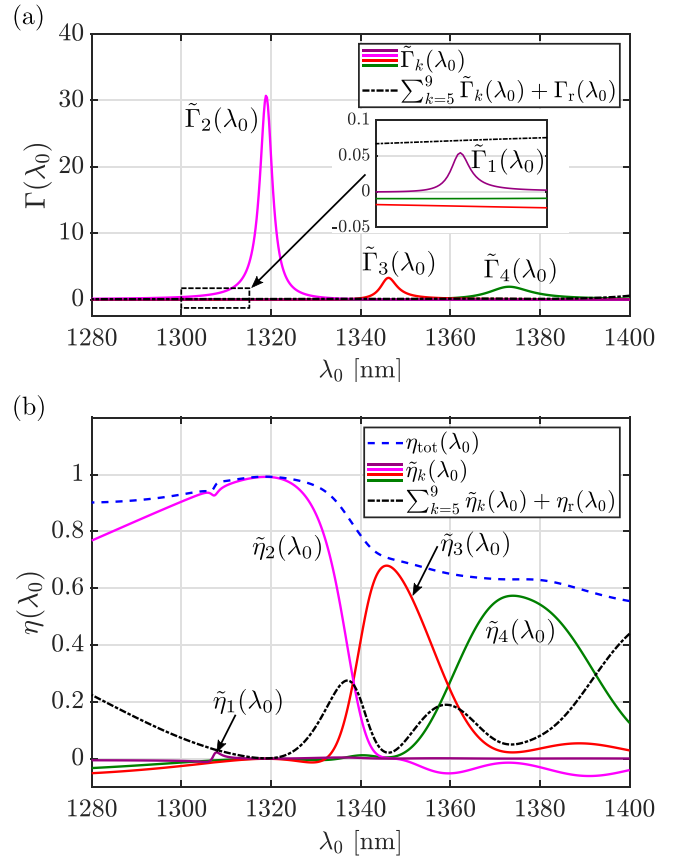

FIG. 3. Modal expansions of Purcell enhancement and PCE for the resonator with a localized light source shown in Fig. 2(a). Eigenfrequencies $\tilde{\omega}_1, \ldots, \tilde{\omega}_9$ are considered; see Table I. (a) Modal expansion of the Purcell enhancement. The contributions $\tilde{\Gamma}_1(\lambda_0), \ldots, \tilde{\Gamma}_4(\lambda_0)$ correspond to the eigenfrequencies $\tilde{\omega}_1, \ldots, \tilde{\omega}_4$, respectively. The remaining modal contributions are added to the remainder of the expansion $\sum_{k=5}^{9} \tilde{\Gamma}_k(\lambda_0) + \Gamma_r(\lambda_0)$. The term $\Gamma_r(\lambda_0)$ includes also modal contributions corresponding to eigenfrequencies outside the integration contour C_r. (b) Modal expansion of the PCE. Total modal expansion, $\eta_{\text{tot}}(\lambda_0) = \sum_{k=1}^{9} \tilde{\eta}_k(\lambda_0) + \eta_r(\lambda_0)$, single modal contributions, $\tilde{\eta}_1(\lambda_0), \ldots, \tilde{\eta}_4(\lambda_0)$, and the sum of other contributions, $\sum_{k=5}^{9} \tilde{\eta}_k(\lambda_0) + \eta_r(\lambda_0)$.

contrast to the Purcell enhancement, the modal contribution $\tilde{\eta}_1(\omega_0)$ is significant for the PCE. It contributes to $\eta_{\text{tot}}(\omega_0)$ for the wavelength region near to its maximum. Note that the behavior of the remaining contributions, $\sum_{k=5}^{9} \tilde{\eta}_k(\lambda_0) + \eta_r(\lambda_0)$, is partially based on resonances with eigenfrequencies outside the integration contour C_r.

IV. CONCLUSIONS

A theoretical approach to investigate modal quantities in the far field of resonant systems was presented. Although the QNMs decay exponentially in time and thus represent diverging outgoing waves, modal expansions can be computed rigorously. The approach was applied to expand the energy flux density in the far field of a nanoresonator with an embedded point source. It was demonstrated that, by computing modal far-field patterns, those resonances which contribute significantly to the scattering response of the nanophotonic

device can be identified. Thus deeper physical insights into the system are gained.

The method cannot only be used to efficiently compute the scattering response and to compare to experimental results, but also for an optimization of devices for a tailored functionality. It can be applied to far-field as well as to near-field quantities. Examples are quantities involving the electromagnetic energy flux density or the electromagnetic absorption. However, the investigations in this work are limited to quadratic forms with a sesquilinear map. We expect that, with resolving the key issue of the far-field treatment in QNM modeling, the presented approach will enable usage of QNMs in various fields. Applications include systems in nano-optics with any material dispersion and any resonant system in general, e.g., in acoustics or quantum mechanics.

[1] L. Novotny and N. van Hulst, Nat. Photon. **5**, 83 (2011).

[2] X. Ding, Y. He, Z.-C. Duan, N. Gregersen, M.-C. Chen, S. Unsleber, S. A. Maier, C. Schneider, M. Kamp, S. Höfling, C.-Y. Lu, and J.-W. Pan, Phys. Rev. Lett. **116**, 020401 (2016).

[3] Y. Zhang, S. He, W. Guo, Y. Hu, J. Huang, J. R. Mulcahy, and W. D. Wei, Chem. Rev. **118**, 2927 (2018).

[4] J. N. Anker, W. P. Hall, O. Lyandres, N. C. Shah, J. Zhao, and R. P. Van Duyne, Nat. Mater. **7**, 442 (2008).

[5] N. Yu and F. Capasso, Nat. Mater. **13**, 139 (2014).

[6] M. S. Tame, K. R. McEnery, S. K. Özdemir, J. Lee, S. A. Maier, and M. S. Kim, Nat. Phys. **9**, 329 (2013).

[7] A. I. Kuznetsov, A. E. Miroshnichenko, M. L. Brongersma, Y. S. Kivshar, and B. Luk'yanchuk, Science **354**, aag2472 (2016).

[8] C. W. Hsu, B. Zhen, A. D. Stone, J. D. Joannopoulos, and M. Soljačić, Nat. Rev. Mater. **1**, 16048 (2016).

[9] P. Lalanne, W. Yan, K. Vynck, C. Sauvan, and J.-P. Hugonin, Laser Photon. Rev. **12**, 1700113 (2018).

[10] P. T. Kristensen, K. Hermann, F. Intravaia, and K. Busch, Adv. Opt. Photon. (2020), doi:10.1364/AOP.377940.

[11] H. Lamb, Proc. London Math. Soc. **s1-32**, 208 (1900).

[12] G. Beck and H. M. Nussenzveig, Nuovo Cimento (1955-1965) **16**, 416 (1960).

[13] E. S. C. Ching, P. T. Leung, A. Maassen van den Brink, W. M. Suen, S. S. Tong, and K. Young, Rev. Mod. Phys. **70**, 1545 (1998).

[14] E. A. Muljarov, W. Langbein, and R. Zimmermann, EPL **92**, 50010 (2010).

[15] B. Vial, F. Zolla, A. Nicolet, and M. Commandré, Phys. Rev. A **89**, 023829 (2014).

[16] F. Zolla, A. Nicolet, and G. Demésy, Opt. Lett. **43**, 5813 (2018).

[17] L. Zschiedrich, F. Binkowski, N. Nikolay, O. Benson, G. Kewes, and S. Burger, Phys. Rev. A **98**, 043806 (2018).

[18] W. Yan, R. Faggiani, and P. Lalanne, Phys. Rev. B **97**, 205422 (2018).

[19] C. Sauvan, J.-P. Hugonin, I. S. Maksymov, and P. Lalanne, Phys. Rev. Lett. **110**, 237401 (2013).

[20] X. Zambrana-Puyalto and N. Bonod, Phys. Rev. B **91**, 195422 (2015).

[21] E. A. Muljarov and W. Langbein, Phys. Rev. B **94**, 235438 (2016).

[22] R. Colom, R. McPhedran, B. Stout, and N. Bonod, Phys. Rev. B **98**, 085418 (2018).

[23] M. I. Abdelrahman and B. Gralak, OSA Continuum **1**, 340 (2018).

[24] M. K. Dezfouli and S. Hughes, Phys. Rev. B **97**, 115302 (2018).

[25] P. Y. Chen, D. J. Bergman, and Y. Sivan, Phys. Rev. Appl. **11**, 044018 (2019).

[26] D. J. Bergman, Phys. Rev. B **19**, 2359 (1979).

[27] H. E. Türeci, A. D. Stone, and B. Collier, Phys. Rev. A **74**, 043822 (2006).

[28] R.-C. Ge, P. T. Kristensen, J. F. Young, and S. Hughes, New J. Phys. **16**, 113048 (2014).

[29] S. Franke, S. Hughes, M. K. Dezfouli, P. T. Kristensen, K. Busch, A. Knorr, and M. Richter, Phys. Rev. Lett. **122**, 213901 (2019).

[30] J. Yang, J.-P. Hugonin, and P. Lalanne, ACS Photon. **3**, 395 (2016).

[31] J. Ren, S. Franke, A. Knorr, M. Richter, and S. Hughes, Phys. Rev. B **101**, 205402 (2020).

[32] P. T. Kristensen, R.-C. Ge, and S. Hughes, Phys. Rev. A **92**, 053810 (2015).

[33] E. A. Muljarov and W. Langbein, Phys. Rev. A **96**, 017801 (2017).

[34] P. T. Kristensen, R.-C. Ge, and S. Hughes, Phys. Rev. A **96**, 017802 (2017).

[35] B. Stout, R. Colom, N. Bonod, and R. McPhedran, arXiv:1903.07183.

[36] F. Binkowski, L. Zschiedrich, M. Hammerschmidt, and S. Burger, Phys. Rev. B **100**, 155406 (2019).

[37] J. D. Jackson, *Classical Electrodynamics*, 3rd ed. (Wiley, New York, 1998).

[38] L. Rickert, T. Kupko, S. Rodt, S. Reitzenstein, and T. Heindel, Opt. Express **27**, 36824 (2019).

[39] P. Senellart, G. Solomon, and A. White, Nat. Nanotechnol. **12**, 1026 (2017).

[40] J. Pomplun, S. Burger, L. Zschiedrich, and F. Schmidt, Phys. Status Solidi B **244**, 3419 (2007).

5 Computing physically relevant eigenmodes and eigenfrequencies

With the expansion of the electric field $\mathbf{E}(\mathbf{r}, \omega_0)$ into a sum of Riesz projections $\mathbf{E}_m(\mathbf{r}, \omega_0)$, given by Eq. (2.4), the Riesz projections have a physical meaning in terms of the electric field caused by a light source. Furthermore, a simple connection between Riesz projections and eigenmodes is given by $\mathbf{E}_m(\mathbf{r}, \omega_0) = \alpha_m(\omega_0)\tilde{\mathbf{E}}_m(\mathbf{r})$, where $\mathbf{E}_m(\mathbf{r}, \omega_0)$ are the Riesz projections from Eq. (2.4), $\tilde{\mathbf{E}}_m(\mathbf{r})$ are normalized eigenmodes from Eq. (2.3), and $\alpha_m(\omega_0)$ are expansion coefficients calculated with a certain formula [72] from the resonance expansion given in Eq. (2.2).

In Ref. [67], based on these ideas from the previous chapters, we develop an approach to compute physically relevant eigenfrequencies. Physically relevant refers to the resonance expansion of the physical observable of interest, i.e., eigenfrequencies are relevant if the corresponding expansion terms are significant for the resonance expansion of the observable. We consider a physical observable $\mathcal{L}(\mathbf{E}(\mathbf{r}, \omega_0))$, where $\mathcal{L} : \mathbb{C}^3 \to \mathbb{C}$ is linear and $\omega_0 \in \mathbb{R}$, and its analytical continuation $\mathcal{L}(\mathbf{E}(\mathbf{r}, \omega))$, where $\omega \in \mathbb{C}$, into the complex frequency plane. Furthermore, a contour C_m enclosing the single eigenfrequency $\tilde{\omega}_m$, which is a pole of order one, is considered. Then, the Laurent expansion of $\mathcal{L}(\mathbf{E}(\mathbf{r}, \omega))$ about $\tilde{\omega}_m$ is given by

$$\mathcal{L}(\mathbf{E}(\mathbf{r}, \omega)) = \sum_{k=-1}^{\infty} a_k(\omega - \tilde{\omega}_m)^k, \quad a_k = \frac{1}{2\pi i} \oint_{C_m} \frac{\mathcal{L}(\mathbf{E}(\mathbf{r}, \omega))}{(\omega - \tilde{\omega}_m)^{k+1}} \, d\omega \in \mathbb{C}.$$

Application of Cauchy's integral formula yields

$$\oint_{C_m} \omega \mathcal{L}(\mathbf{E}(\mathbf{r}, \omega)) \, d\omega = \oint_{C_m} \frac{\omega}{\omega - \tilde{\omega}_m} a_{-1} \, d\omega = \tilde{\omega}_m \oint_{C_m} \mathcal{L}(\mathbf{E}(\mathbf{r}, \omega)) \, d\omega,$$

where the regular terms in the expansion vanish due to the closed contour integral. Rearranging gives the formula for the eigenfrequency,

$$\tilde{\omega}_m = \frac{\oint_{C_m} \omega \mathcal{L}(\mathbf{E}(\mathbf{r}, \omega)) \, d\omega}{\oint_{C_m} \mathcal{L}(\mathbf{E}(\mathbf{r}, \omega)) \, d\omega}, \tag{5.1}$$

where the contour integrals are Riesz projections corresponding to $\mathcal{L}(\mathbf{E}(\mathbf{r}, \omega))$ and C_m. This approach is generalized to multiple eigenfrequencies that lie within a contour, resulting in a nonlinear system of equations that must be solved. Since the method is based on Riesz projections corresponding to $\mathcal{L}(\mathbf{E}(\mathbf{r}, \omega))$ and C_m, the eigenfrequencies relevant to the physical observable $\mathcal{L}(\mathbf{E}(\mathbf{r}, \omega_0))$ are prioritized in the computation.

We apply the Riesz-projection-based approach to a quantum mechanical problem from the literature, which is a quadratic nonlinear eigenproblem resulting from the Schrödinger equation [60, 94]. We further apply the approach to the two nanophotonic systems already investigated in the Chapters 2 and 3, which are rational nonlinear eigenproblems. It is possible to access mainly physical eigenfrequencies, although the integration contours also contain many non-physical eigenfrequencies resulting from, e.g., the truncation of the open systems [38].

In the following, Ref. [67] is reprinted with permission from [Felix Binkowski, Lin Zschiedrich, and Sven Burger. A Riesz-projection-based method for nonlinear eigenvalue problems. *J. Comput. Phys.* 419, 109678 (2020). DOI: 10.1016/j.jcp.2020.109678.] Copyright 2020 Elsevier Inc.
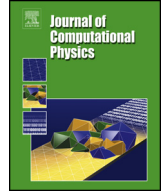
A Riesz-projection-based method for nonlinear eigenvalue problems

Felix Binkowski [a], Lin Zschiedrich [b], Sven Burger [a,b,*]

[a] *Zuse Institute Berlin, Takustraße 7, 14195 Berlin, Germany*
[b] *JCMwave GmbH, Bolivarallee 22, 14050 Berlin, Germany*

A B S T R A C T

We propose an algorithm for general nonlinear eigenvalue problems to compute physically relevant eigenvalues within a chosen contour. Eigenvalue information is explored by contour integration incorporating different weight functions. The gathered information is processed by solving a nonlinear system of equations of small dimension prioritizing eigenvalues with high physical impact. No auxiliary functions have to be introduced since linearization is not used. The numerical implementation is straightforward as the evaluation of the integrand can be regarded as a blackbox. We apply the method to a quantum mechanical problem and to two nanophotonic systems.

© 2020 Elsevier Inc. All rights reserved.

1. Introduction

Nonlinear eigenvalue problems (NLEVPs) occur in many fields in physics, from the dynamic analysis of macroscopic structures [1] to the investigation of photonic resonators on the nanoscale [2], or scattering resonances in quantum mechanics [3]. The NLEVPs are solved numerically [4,5] in order to physically characterize the systems [6,7].

We address the most general problem class of NLEVPs

$$T(\lambda)v = 0, \tag{1}$$

where $T(\lambda) \in \mathbb{C}^{n \times n}$ is the eigenvector residual function, $\lambda \in \mathbb{C}$ is an eigenvalue, and $v \in \mathbb{C}^n$ is an eigenvector corresponding to λ. In physics, NLEVPs often have the form $A(\lambda)v = \lambda B(\lambda)v$, which can be brought into the above form with $T(\lambda) = A(\lambda) - \lambda B(\lambda)$. In many applications, $T(\lambda)$ is a very large matrix, while just a few eigenpairs (λ, v) are responsible for the physical behavior of the described problem.

For rational residual functions $T(\lambda)$, the NLEVPs can be cast into a linear form, so that standard approaches, such as the Arnoldi or the Jacobi-Davidson method, are applicable. Such a linearization introduces auxiliary functions and increases the dimension of the problem [5,8]. Material dispersion is often significant in physical systems and modeled by measured material data. To apply the approach of linearization, material data have to be fitted by rational functions [9] and numerical costs grow with the order and number of poles of the fit. Note that the Arnoldi and the Jacobi-Davidson method have been adapted to solve NLEVPs directly [10,11].

---

* Corresponding author at: Zuse Institute Berlin, Takustraße 7, 14195 Berlin, Germany.
  E-mail address: burger@zib.de (S. Burger).

In recent years, eigensolvers based on contour integration attracted attention as they inherently support solving NLEVPs [12–15]. Contour integral methods essentially involve solving linear systems of equations $T(\lambda)^{-1}y$ with random vectors y along a chosen integration contour. The contour integration gives a projection onto the eigenspace corresponding to the eigenvalues inside the contour. In [14,15], the Rayleigh-Ritz method is then used to achieve approximations of eigenpairs. The nonlinear structure is still inherited to the lower dimensional projected system and needs to be given explicitly in a rational form. The methods of [12,13] extract eigenvalue and eigenvector information by applying a singular-value decomposition to the subspace generated by the contour integration and then solving a linear eigenproblem. An alternative way of extracting this information is based on canonical polyadic tensor decomposition [16].

The methods proposed in [12–15] yield eigenpairs whose eigenvalues are located inside a specific region in the complex plane. This region is typically chosen according to the underlying physical problem. However, due to the numerical discretization, insignificant eigenvalues may occur close to the physically relevant eigenvalues. A prominent example are eigenvalues resulting from the truncation of open resonant systems [8]. Due to the application of random vectors for the contour integral methods, in such cases, many eigenpairs have to be computed and they are not classified according to their physical relevance.

In this work, we present a contour integral method which only projects onto the physically relevant eigenspaces. This is done by the choice of the vector y corresponding to a physical source field which does not significantly couple to the undesired eigenvectors. These may arise due to the numerical discretization. The insignificant eigenvalues are then filtered out by a fit to a nonlinear model based on Cauchy's residue theorem. Instead of computing individual eigenvectors, spectral projections are calculated. As linearization is circumvented in any stage of the procedure, any material dispersion relation can be included.

2. Riesz projection method for NLEVPs

This section derives an approach to compute eigenvalues λ fulfilling Eq. (1) which are located inside a chosen contour and to compute associated spectral projections, so-called Riesz projections. To start with, notation and theoretical background on elements of complex analysis are introduced [17, Section 4.4]. We consider Eq. (1) with a regular matrix function $T : \Omega \to \mathbb{C}^{n \times n}$, where $\Omega \subset \mathbb{C}$. Let $\mathcal{G} : \mathbb{C}^n \to \mathbb{C}$ be a meromorphic function and $y \in \mathbb{C}^n$ be a random vector. Let $\Gamma_k \subset \Omega$ be a contour which encloses a single eigenvalue λ_k of the residual function $T(\lambda)$ and on which the function $\mathcal{G}\left(T(\lambda)^{-1}y\right)$ is holomorphic. The eigenvalue λ_k is a pole of $\mathcal{G}\left(T(\lambda)^{-1}y\right)$ and the pole is assumed to be of order p. Then, the Laurent series for $\mathcal{G}\left(T(\lambda)^{-1}y\right)$ about λ_k is given by

$$\mathcal{G}\left(T(\lambda)^{-1}y\right) = \sum_{n=-p}^{\infty} a_n (\lambda - \lambda_k)^n, \qquad a_n(\lambda_k) := \frac{1}{2\pi i} \oint_{\Gamma_k} \frac{\mathcal{G}\left(T(\xi)^{-1}y\right)}{(\xi - \lambda_k)^{n+1}} \, d\xi \in \mathbb{C}. \tag{2}$$

The coefficient $a_{-1}(\lambda_k)$ is the so-called residue

$$\text{Res}_{\lambda_k}\left(\mathcal{G}\left(T(\lambda)^{-1}y\right)\right) = \frac{1}{2\pi i} \oint_{\Gamma_k} \mathcal{G}\left(T(\lambda)^{-1}y\right) \, d\lambda \tag{3}$$

of $\mathcal{G}\left(T(\lambda)^{-1}y\right)$ at λ_k.

2.1. Sketch of the approach

To show the idea of this work, a simple eigenvalue λ_k of $T(\lambda)$ is assumed, i.e., λ_k is a pole of $\mathcal{G}\left(T(\lambda)^{-1}y\right)$ and has the order $p = 1$. With the aim of extracting eigenvalue information from Eq. (3), the scalar function $f(\lambda) = \lambda$ is introduced. Then, Cauchy's integral formula leads to

$$\text{Res}_{\lambda_k}\left(\lambda \mathcal{G}\left(T(\lambda)^{-1}y\right)\right) = \frac{1}{2\pi i} \oint_{\Gamma_k} \lambda \mathcal{G}\left(T(\lambda)^{-1}y\right) \, d\lambda = \frac{1}{2\pi i} \oint_{\Gamma_k} \frac{\lambda}{\lambda - \lambda_k} a_{-1}(\lambda_k) \, d\lambda = \lambda_k \text{Res}_{\lambda_k}\left(\mathcal{G}\left(T(\lambda)^{-1}y\right)\right),$$

where the regular part of the Laurent series vanishes and only the principal part remains. Rearranging yields the eigenvalue

$$\lambda_k = \frac{\text{Res}_{\lambda_k}\left(\lambda \mathcal{G}\left(T(\lambda)^{-1}y\right)\right)}{\text{Res}_{\lambda_k}\left(\mathcal{G}\left(T(\lambda)^{-1}y\right)\right)}$$

inside of the contour Γ_k.

2.2. Generalized approach

The idea of the previous subsection can be generalized. Firstly, we assume that the pole λ_k has an order $p \geq 1$ and consider a function $f : \Omega \to \mathbb{C}$ which is holomorphic on Γ_k and inside of Γ_k yielding

$$\frac{1}{2\pi i} \oint_{\Gamma_k} f(\lambda) \mathcal{G}\left(T(\lambda)^{-1}y\right) d\lambda = \sum_{n=-p}^{-1} a_n(\lambda_k) \frac{1}{2\pi i} \oint_{\Gamma_k} f(\lambda)(\lambda - \lambda_k)^n d\lambda = \sum_{n=-p}^{-1} a_n(\lambda_k) \frac{f(\lambda_k)^{(-n-1)}}{(-n-1)!}. \tag{4}$$

The coefficients $a_{-p}(\lambda_k), \ldots, a_{-1}(\lambda_k)$ correspond to the Laurent series for $\mathcal{G}\left(T(\lambda)^{-1}y\right)$ in Eq. (2). Secondly, we choose a contour $\Gamma \subset \Omega$ on which $\mathcal{G}\left(T(\lambda)^{-1}y\right)$ is holomorphic and which encloses finitely many poles $\lambda_1, \ldots, \lambda_m$ of $\mathcal{G}\left(T(\lambda)^{-1}y\right)$. Cauchy's residue theorem is used [17] so that Eq. (4) can be extended to

$$\frac{1}{2\pi i} \oint_{\Gamma} f(\lambda) \mathcal{G}\left(T(\lambda)^{-1}y\right) d\lambda = \sum_{j=1}^{m} \sum_{n=-p}^{-1} a_n(\lambda_j) \frac{f(\lambda_j)^{(-n-1)}}{(-n-1)!}, \tag{5}$$

where $f(\lambda)$ has to be holomorphic on Γ and inside of Γ. Equation (5) contains the eigenvalues $\lambda_1, \ldots, \lambda_m$ of the residual function $T(\lambda)$. To explore the information for these m unknowns, we introduce several *weight functions* $f_1(\lambda), \ldots, f_M(\lambda)$ and construct the nonlinear system of equations (NLSE)

$$\mu_k = F_k(\lambda_1, \ldots, \lambda_m), \qquad k = 1, \ldots, M, \tag{6}$$

where

$$\mu_k := \frac{1}{2\pi i} \oint_{\Gamma} f_k(\lambda) \mathcal{G}\left(T(\lambda)^{-1}y\right) d\lambda, \qquad F_k(\lambda_1, \ldots, \lambda_m+) = \sum_{j=1}^{m} \sum_{n=-p}^{-1} a_n(\lambda_j) \frac{f_k(\lambda_j)^{(-n-1)}}{(-n-1)!}.$$

Solving this NLSE yields the eigenvalues inside of the contour Γ. The NLSE can be solved with standard solvers, e.g., nonlinear system solvers based on least-square algorithms. In this work, we use *fsolve* from MATLAB. Note that the residues $a_{-1}(\lambda_k)$ are functions depending on λ_k. Instead of evaluating these functions, we regard them as unknowns themselves. We further note that the function $\mathcal{G}\left(T(\lambda)^{-1}y\right)$ can be chosen according to the underlying physical problem, e.g., it can be a physical observable. In this way, the numerical solution of $T(\lambda)^{-1}y$ is considered as a blackbox.

2.3. Riesz projections with physical source fields

The Riesz projector

$$P(T(\lambda), \Gamma) := \frac{1}{2\pi i} \oint_{\Gamma} T(\lambda)^{-1} d\lambda \tag{7}$$

for a matrix function $T(\lambda)$ and a contour Γ projects vectors y onto the eigenspace associated with the eigenvalues inside of Γ [18]. In particular, for a contour Γ_k enclosing one simple eigenvalue λ_k and a random vector y as in Sec. 2.1, the corresponding eigenvector is given by $v_k = P(T(\lambda), \Gamma_k)y$.

By choosing y corresponding to a physical source field, it is possible to distinguish between physically relevant and nonrelevant eigenvalues. To illustrate this, a discretized partial differential equation $T(\lambda)u = y$, where $y \in \mathbb{C}^n$ is a source field and $u \in \mathbb{C}^n$ is the solution of the problem, is regarded. We consider an eigenvalue λ_k to be insignificant if the Riesz projection $P(T(\lambda), \Gamma_k)y$, where Γ_k encloses only λ_k, is of the order of a given target accuracy. If the physical source field y is orthogonal to an eigenvector v_k, then $P(T(\lambda), \Gamma_k)y$ is of the order of the discretization error. However, for many problems with insignificant eigenvalues, $P(T(\lambda), \Gamma_k)y$ is larger than the discretization error as the physical source field y has a small coupling to the corresponding eigenvector. The target accuracy has to be chosen according to this. Note that insignificant eigenvalues have a small influence on the NLSE given by Eq. (6) and are therefore filtered out by solving the NLSE.

In this work, we aim at computing spectral projections instead of individual eigenvectors. When an eigenvalue λ_k is approximated by the NLSE, we define a further contour $\tilde{\Gamma}_k$ around this eigenvalue and compute the Riesz projection $P(T(\lambda), \tilde{\Gamma}_k)y$. This contour may include also insignificant eigenvalues which are fully incorporated in the Riesz projection. Note that $\tilde{\Gamma}_k$ could be chosen, so that clustered physically relevant eigenvalues lie inside the contour. In this way, the corresponding eigenvectors are treated as a single spectral projection [19].

Algorithm 1: For NLEVPs $T(\lambda)v = 0$, $T(\lambda) \in \mathbb{C}^{n \times n}, v \in \mathbb{C}^n, \lambda \in \mathbb{C}$.

1:	Choose:	contour Γ, quadrature rule, integration points $\hat{\lambda}_1, \ldots, \hat{\lambda}_N$,
		size M of NLSE, weight functions $f_1(\lambda), \ldots, f_M(\lambda)$,
		model $F_k(\lambda_1, \ldots, \lambda_m)$ with number of unknowns m,
		initial guess for NLSE
2:	Define:	physical source field $y \in \mathbb{C}^n$, function $\mathcal{G} : \mathbb{C}^n \to \mathbb{C}$, e.g., physical observable
3:	Solve:	linear systems $T(\hat{\lambda}_k)\hat{v}_k = y$, $k = 1, \ldots, N$
4:	Compute:	$\mu_k := \frac{1}{2\pi i} \oint_\Gamma f_k(\lambda) \mathcal{G}\left(T(\lambda)^{-1} y\right) d\lambda$, $k = 1, \ldots, M$,
		using quadrature rule with $\hat{v}_1, \ldots, \hat{v}_N$
5:	Solve:	NLSE $\mu_k = F_k(\lambda_1, \ldots, \lambda_m)$, $k = 1, \ldots, M$
6:	Define:	contours $\tilde{\Gamma}_1, \ldots, \tilde{\Gamma}_m$ enclosing eigenvalues $\lambda_1, \ldots, \lambda_m$
7:	Compute:	Riesz projections $P(T(\lambda), \tilde{\Gamma}_k)y := \frac{1}{2\pi i} \oint_{\tilde{\Gamma}_k} T(\lambda)^{-1} y \, d\lambda$, $k = 1, \ldots, m$
8:	**return**	approximate eigenvalues $\lambda_1, \ldots, \lambda_m$, Riesz projections $P(T(\lambda), \tilde{\Gamma}_1)y, \ldots, P(T(\lambda), \tilde{\Gamma}_m)y$

2.4. Algorithm

To study physical systems where NLEVPs given by Eq. (1) occur, we propose Algorithm 1. The algorithm can be sketched as follows. A contour Γ which encloses the eigenvalues of interest has to be chosen (Step 1). Depending on the physical problem, a source field y and a function $\mathcal{G}$ are defined (Step 2). The contour integrals in Eq. (6) are computed with a suitable quadrature rule (Step 3-4). The evaluation of the integrand at the integration points essentially requires to solve linear systems of equations $T(\lambda)^{-1} y$.

The calculated integrals serve as the input data for solving the NLSE given by Eq. (6) (Step 5). The nonlinear model $F_k(\lambda_1, \ldots, \lambda_m)$ is chosen based on the expected order of the physically relevant poles within Γ and based on the expected number m of poles. The number m can be estimated with physical a priori knowledge or, e.g., with Cauchy's argument principle counting the zeros and poles of a meromorphic function. If m is greater than the number of physically relevant poles within Γ, then the algorithm returns relevant eigenvalues and also results which are insignificant. Here, the used nonlinear solver exploits more degrees of freedom, where some insignificant unknowns λ_k and $a_{-1}(\lambda_k)$ have a very small influence on the physically relevant solutions. For example, an insignificant eigenvalue λ_k could be close to the integration contour and the corresponding residue $a_{-1}(\lambda_k)$ could be so small that the product of these two unknowns is of the order of the given target accuracy. On the other hand, if m is smaller than the number of physically relevant eigenvalues, then the nonlinear model $F_k(\lambda_1, \ldots, \lambda_m)$ does not fit to the physical problem and Algorithm 1 returns unsuitable results. The error can be estimated by computing Riesz projections and the algorithm has to be restarted with an increasing m. To solve the NLSE, an initial guess is required. If no a priori information about the eigenvalues is available, then randomly chosen numbers inside of the contour Γ are a possible choice.

The results of solving the NLSE are approximations to eigenvalues where eigenvalues with high physical impact regarding the source field y are prioritized. By defining contours $\tilde{\Gamma}_k$ around these eigenvalues (Step 6), Riesz projections $P(T(\lambda), \tilde{\Gamma}_k)y$ can be computed (Step 7). Note that more than one eigenvalue can be inside of $\tilde{\Gamma}_k$. The algorithm returns approximations $\lambda_1, \ldots, \lambda_m$ and Riesz projections $P(T(\lambda), \tilde{\Gamma}_1)y, \ldots, P(T(\lambda), \tilde{\Gamma}_m)y$ (Step 8).

Algorithm 1 is parallelizable on two levels. Firstly, the complete algorithm can be performed for different contours Γ simultaneously. This can be useful if eigenvalues in different regions are of interest. Secondly, solving the linear systems for the numerical integration can be done in parallel.

2.5. Numerical realization

We realize the numerical integration in Algorithm 1 with an N-point trapezoidal rule. The integration path Γ is a circular contour, which leads to exponential convergence [20]. The equidistant integration points are given by $\hat{\lambda}_k = \lambda_0 + r e^{2\pi i k/N}$, $k = 1, \ldots, N$, where λ_0 and r are the center and the radius of Γ, respectively. Note that recently, rational filter functions for contour integral discretizations have been designed using optimization techniques [21]. However, for the sake of simplicity, we use a trapezoidal rule. To solve the linear systems of equations $T(\hat{\lambda}_k)^{-1} y$, an LU decomposition can be used. The LU decomposition needs not to be updated at each integration point. Instead, for sufficiently small changes in $\hat{\lambda}_k$, the LU decomposition of a previous evaluation can be used as a preconditioner for iterative solving. This leads to a more efficient numerical implementation.

In the following section, we consider physical examples with simple eigenvalues, i.e., the nonlinear model in Eq. (6) simplifies to

$$F_k(\lambda_1, \ldots, \lambda_m) = \sum_{j=1}^{m} a_{-1}(\lambda_j) f_k(\lambda_j).$$

Equation (6) is solved with the nonlinear solver *fsolve* from MATLAB. We regard the residues $a_{-1}(\lambda_1), \ldots, a_{-1}(\lambda_m)$ as unknown variables themselves and set $M = 2m$ to construct non-underdetermined NLSEs. This handling of the residues allows for a simpler numerical realization. For the weight functions, we choose the scaled polynomials

$$f_k(\lambda) = \left(\frac{\lambda - \lambda_0}{r}\right)^{k-1}, \qquad k = 1, \ldots, M.$$

Due to the fact that the weight functions are known and that we treat the residues as unknowns, also the Jacobians can be provided for the nonlinear solver.

3. Application of the method

We apply Algorithm 1 to a quadratic NLEVP resulting from the Schrödinger equation and to two rational NLEVPs resulting from Maxwell's equations. These quantum mechanical and nanophotonic examples are open systems, which are described by non-Hermitian operators. In physics, the eigensolutions of such problems are usually called resonant states or quasinormal modes (QNMs) [22–24]. Material dispersion is omnipresent in such systems and the physical understanding of the resonance phenomena through numerical simulations is an active research topic. A common approach is a resonance expansion [8,25], where the solutions of the open systems are expanded into weighted sums of QNMs. In this context, the coupling of a QNM to a source field is quantified by the corresponding single expansion term. Physically relevant QNMs lead to significant contributions in the resonance expansion.

The physical systems are numerically discretized with the finite element method (FEM) [26,27]. We use the software package JCMsuite to discretize and to solve the nanophotonic problems in Secs. 3.2 and 3.3. Note that also other numerical methods and implementations could be used for applying Algorithm 1.

3.1. Resonant states in an open quantum system

Propagation of a quantum particle of effective mass m^* through a one-dimensional potential $V(x)$ can be described by the time-independent Schrödinger equation

$$-\frac{\hbar}{2}\frac{\partial}{\partial x}\left(\frac{1}{m^*}\frac{\partial \Psi(x)}{\partial x}\right) + V(x)\Psi(x) = E\Psi(x), \tag{8}$$

where $\hbar$ is the Planck constant, E is the energy and $\Psi(x)$ is the unknown wave function. For a detailed description and motivation of this example, see [28]. To compute the eigenvalues of this problem in the domain $[-L, L]$, we use the approach of [15] to scale and discretize Eq. (8) yielding the quadratic NLEVP

$$T(\lambda)v = \left(\lambda^2 A_2 + i\lambda A_1 - A_0\right)v = 0,$$

where

$$A_2 = \frac{h}{6}\begin{bmatrix} 2 & 1 & 0 & 0 & \ldots & 0 \\ 1 & 4 & 1 & 0 & \ldots & 0 \\ 0 & 1 & 4 & 1 & \ldots & 0 \\ \vdots & & & \ddots & & \vdots \\ 0 & \ldots & 0 & 1 & 4 & 1 \\ 0 & \ldots & 0 & 0 & 1 & 2 \end{bmatrix}, \quad A_1 = \begin{bmatrix} 1 & 0 & \ldots & 0 & 0 \\ 0 & 0 & \ldots & 0 & 0 \\ \vdots & \vdots & \vdots & \vdots & \vdots \\ 0 & 0 & \ldots & 0 & 0 \\ 0 & 0 & \ldots & 0 & 1 \end{bmatrix},$$

$$A_0 = \frac{1}{h}\begin{bmatrix} 1 & -1 & 0 & 0 & \ldots & 0 \\ -1 & 2 & -1 & 0 & \ldots & 0 \\ 0 & -1 & 2 & -1 & \ldots & 0 \\ \vdots & & & \ddots & & \vdots \\ 0 & \ldots & 0 & -1 & 2 & -1 \\ 0 & \ldots & 0 & 0 & -1 & 1 \end{bmatrix} - V_0 A_2 \in \mathbb{R}^{n+2 \times n+2}.$$

The same parameters as in [15] are chosen, where $L = \pi/\sqrt{2}$, $V(x) = V_0 = 10$, and the spatial step size is $h = 2L/(n+1)$ with $n = 302$.

In order to demonstrate a numerical realization of Algorithm 1 which yields all eigenvalues inside a chosen contour, we choose a unit random vector $y \in \mathbb{C}^{304}$ and the function $\mathcal{G}(T(\lambda)^{-1}y) = x^H T(\lambda)^{-1}y$, where $x \in \mathbb{C}^{304}$ is also a unit random vector. A circular contour Γ with the center $\lambda_0 = 5$ and the radius $r = 2.5$ is considered. Solutions for an increasing number N of integration points and for different numbers of unknown eigenvalues, $m = 6, \ldots, 8$, are computed. The maximum relative errors $\max_k \text{Re}(\lambda_k - \lambda_{k,\text{ref}})/\text{Re}(\lambda_{k,\text{ref}})$ and $\max_k \text{Im}(\lambda_k - \lambda_{k,\text{ref}})/\text{Im}(\lambda_{k,\text{ref}})$ are shown in Fig. 1(a). Exponential convergence
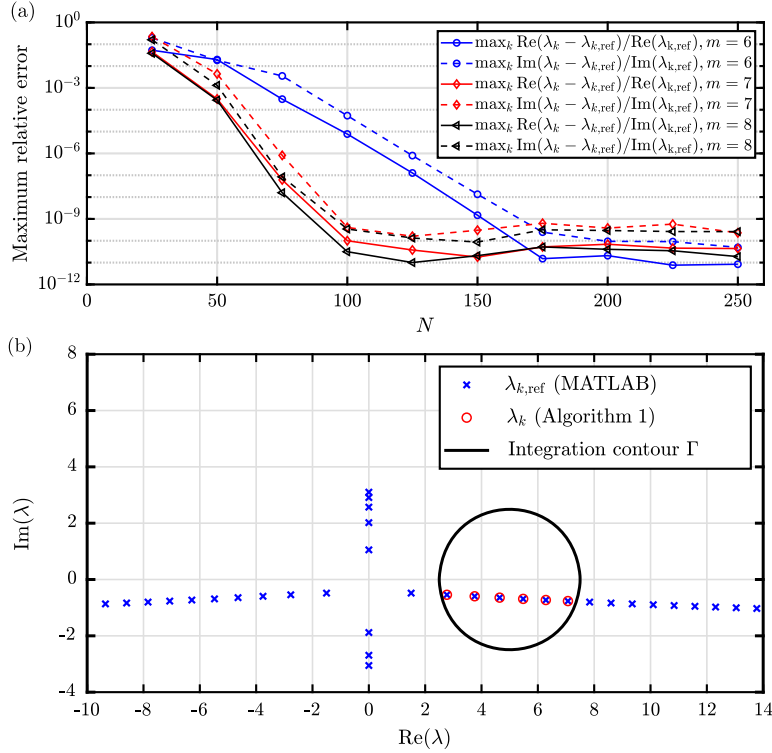
Fig. 1. Results for computing eigenvalues of an open quantum system [28]. (a) Maximum relative errors, $\max_k \mathrm{Re}(\lambda_k - \lambda_{k,\mathrm{ref}})/\mathrm{Re}(\lambda_{k,\mathrm{ref}})$ and $\max_k \mathrm{Im}(\lambda_k - \lambda_{k,\mathrm{ref}})/\mathrm{Im}(\lambda_{k,\mathrm{ref}})$, $k = 1, \ldots, m$, as a function of the number N of integration points. The eigenvalues λ_k are computed with Algorithm 1. The reference solutions $\lambda_{k,\mathrm{ref}}$ are computed by applying MATLAB's function *eigs* to the linearized problem. (b) Eigenvalues and integration contour. The numerical integration is performed with $N = 150$ integration points and the NLSE is solved for $m = 6$ unknowns.

up to a certain accuracy is obtained. It can be further observed that for small N and an increasing m, the residuals become smaller. Here, the nonlinear solver can exploit more degrees of freedom, i.e., also eigenvalues outside the contour can be approximated. These solutions are discarded. The results of Algorithm 1 can be compared with solutions of the linearized problem [15] computed with MATLAB's function *eigs*. These reference solutions and the eigenvalues computed by Algorithm 1 with $N = 150$ and $m = 6$ are shown in Fig. 1(b). Six eigenvalues inside of Γ are obtained by solving the linearized system. The eigenvalues resulting from Algorithm 1 coincide with these reference solutions.

3.2. Photonic nanoantenna

In the second numerical experiment, we consider a nanophotonic structure. Nanoantennas allow, e.g., for realizing single-photon emitters for quantum technology devices [29]. We apply Algorithm 1 to an example from [19], where a defect in a diamond nanodisk is considered as solid-state single-photon emitter. In the steady-state regime, the light-matter interaction of such a structure can be described by the time-harmonic Maxwell's equations in the second-order form

$$\nabla \times \mu(\mathbf{r}, \omega)^{-1} \nabla \times \mathbf{E}(\mathbf{r}, \omega) - \omega^2 \epsilon(\mathbf{r}, \omega)\mathbf{E}(\mathbf{r}, \omega) = i\omega \mathbf{J}(\mathbf{r}), \tag{9}$$

with the electric field $\mathbf{E}(\mathbf{r}, \omega) \in \mathbb{C}^3$ and the source term $\mathbf{J}(\mathbf{r}) \in \mathbb{C}^3$ as impressed current, where $\mathbf{r} \in \mathbb{R}^3$ is the position. The permittivity tensor $\epsilon(\mathbf{r}, \omega)$ characterizes the spatial distribution of materials and, through its dependence on the complex angular frequency $\omega \in \mathbb{C}$, the material dispersion. In the regime of optical frequencies, the permeability tensor $\mu(\mathbf{r}, \omega)$ can typically be set to the vacuum permeability μ_0. Equation (9) is discretized and solved with the software package JCMsuite. The scattering solutions, i.e., solutions of Eq. (9) in presence of a source term, are computed in the ω^2 plane. The outgoing radiation conditions for the diamond nanoresonator are realized with perfectly matched layers (PMLs) [30]. We refer to [19] for details on the FEM implementation and for details on the physical system.

The aim is to compute eigenfrequencies ω_k of the discretized NLEVP associated with Eq. (9). As the permittivity tensor $\epsilon(\mathbf{r}, \omega)$ is a rational function, this is a rational NLEVP. The interest is in eigenfrequencies corresponding to physically relevant eigenvectors, the QNMs of the system, and, in particular, in eigenfrequencies which QNMs couple to specific source fields. We use the source fields described in [19], which are dipole emitters located inside the nanoresonator. Accordingly, physical source fields y for Algorithm 1 are chosen as Eq. (9) is solved with dipole emitters for complex frequencies ω at the
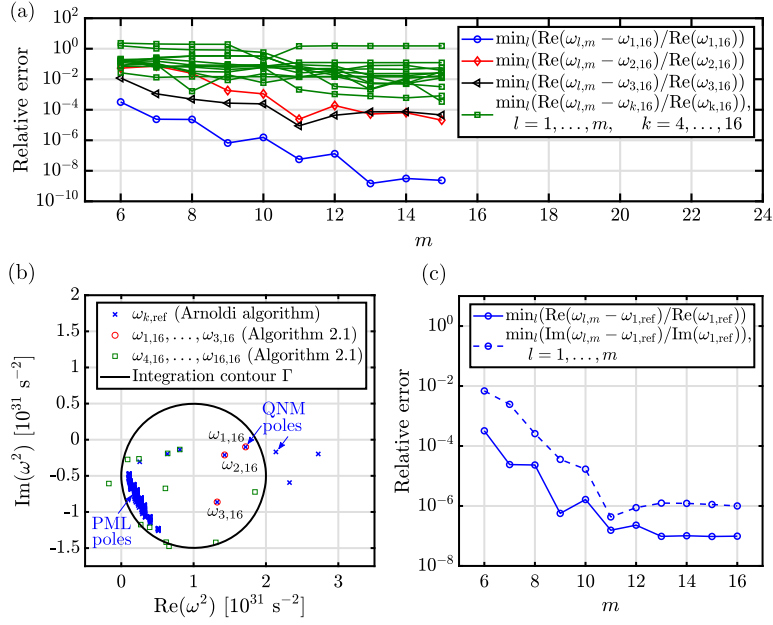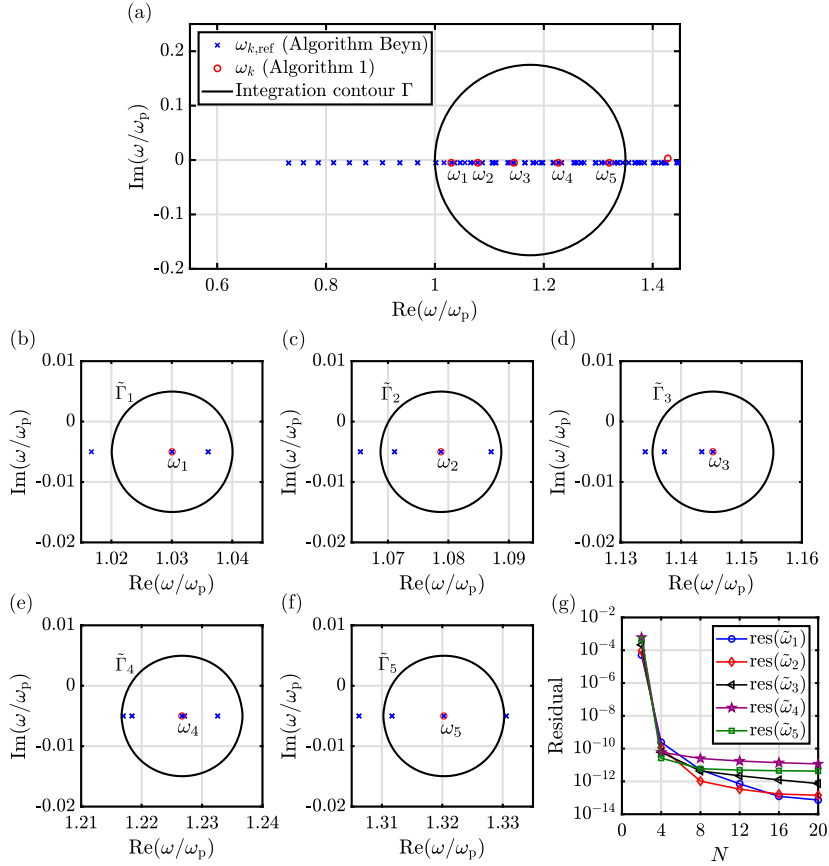
Fig. 2. Results for computing eigenfrequencies of a dielectric nanoantenna [19]. Algorithm 1 leads to numerical convergence for the eigenfrequency $\omega_{1,16} = (1.7190 - 0.0992i) \times 10^{31}$ s^{-2}. The numerical integration is performed using $N = 200$ integration points. (a) Relative errors for the real parts are shown as a function of the number of unknowns m for the NLSE. The reference solutions $\omega_{k,16}$ are computed with $m = 16$. (b) Eigenfrequencies $\omega_{k,16}$ computed with Algorithm 1 using $m = 16$ unknowns. The reference solutions $\omega_{k,\text{ref}}$ are computed with an Arnoldi algorithm. Physically relevant QNM poles are isolated eigenfrequencies and the physically nonrelevant PML poles lie in a cluster. (e) Relative errors for the real and imaginary parts of the most accurate solution $\omega_{1,16}$, where the reference solution $\omega_{1,\text{ref}}$ results from the Arnoldi algorithm.

integration contour. The function $\mathcal{G}(T(\omega)^{-1}y)$ is a point evaluation of the electric field at one chosen spatial point with a suitable scaling.

A circular contour Γ is selected where the center is $\omega_0^2 = (1 - 0.5i) \times 10^{31}$ s^{-2} and the radius is $r = 1 \times 10^{31}$ s^{-2}. We apply Algorithm 1 while setting $N = 200$ integration points and solving the NLSE for $m = 6, \ldots, 16$ unknowns. The l-th solution of the algorithm is denoted by $\omega_{l,m}$, where $l = 1, \ldots, m$. To study the numerical convergence of the real parts of the solutions, we use the computed eigenfrequencies $\omega_{k,16}$, $k = 1, \ldots, 16$, as reference solutions. Fig. 2(a) shows, for each $m = 6, \ldots, 16$ and $k = 1, \ldots, 16$, the minimum relative errors $\min_l(\text{Re}(\omega_{l,m} - \omega_{k,16})/\text{Re}(\omega_{k,16}))$, where $l = 1, \ldots, m$. This means that at each step, the eigenfrequencies which are closest to the reference solutions $\omega_{k,16}$ are identified. Note that we investigate this error quantity because the aim is to show which of the solutions $\omega_{k,16}$, $k = 1, \ldots, 16$, are physically relevant. It is expected that physically relevant eigenfrequencies converge with respect to m and, for insignificant eigenfrequencies, Algorithm 1 shows no convergence. For the eigenfrequency $\omega_{1,16} = (1.7190 - 0.0992i) \times 10^{31}$ s^{-2}, relative errors smaller than 10^{-8} are observed. For the eigenfrequencies $\omega_{2,16} = (1.429 - 0.211i) \times 10^{31}$ s^{-2} and $\omega_{3,16} = (1.326 - 0.863i) \times 10^{31}$ s^{-2}, relative errors smaller than 10^{-4} are obtained. The results $\omega_{4,16}, \ldots, \omega_{16,16}$ have relative errors larger than 10^{-4}.

Fig. 2(b) shows the solutions $\omega_{k,16}$ using $m = 16$ and solutions $\omega_{k,\text{ref}}$ computed with the eigensolver from JCMsuite, which applies an Arnoldi algorithm using auxiliary fields. Fig. 2(c) shows the relative errors for the real and imaginary parts of the solutions of Algorithm 1 which are closest to the reference solution $\omega_{1,\text{ref}}$ computed with the Arnoldi algorithm. For $m = 16$, we observe relative errors of about 10^{-7} and 10^{-6} for the real and imaginary part, respectively. The accuracy limitation can be attributed to the accuracy of the scattering problem solver from JCMsuite.

The eigenvectors of the investigated NLEVP associated with Eq. (9) can be classified into QNMs and PML modes [31, 8]. The QNMs have a physical meaning and the corresponding eigenfrequencies, the QNM poles, are associated with the discrete spectrum of the underlying operator. The PML modes correspond to eigenfrequencies which are associated with the continuous spectrum of the operator. These PML poles are algebraic eigenfrequencies depending on the FEM discretization of the open resonator system. As shown in Fig. 2(b), the PML poles are clustered in the complex plane [31]. With this numerical experiment, we show that with Algorithm 1 it is possible to compute a physically relevant eigenfrequency which is close to insignificant eigenfrequencies. The eigenfrequency $\omega_{1,16}$ corresponds to the QNM which is responsible for the largest peak of the normalized dipole emission, the Purcell factor, in the frequency range 0.5×10^{31} s$^{-2} \leq \text{Re}(\omega^2) \leq 2.5 \times 10^{31}$ s^{-2}, see [19]. This means that this QNM has a significant coupling to the used dipole sources in this frequency range [19]. The eigenfrequencies $\omega_{2,16}$ and $\omega_{3,16}$ also correspond to QNMs, however, the coupling is less significant. Algorithm 1 does not converge to PML poles due to the small coupling of the PML modes to the applied dipole sources.

Fig. 3. Results for computing eigenfrequencies and Riesz projections for a nanowire based on the hydrodynamic Drude model [32]. (a) Algorithm 1 yields five eigenfrequencies, $\omega_1, \ldots, \omega_5$, inside a chosen contour. The numerical integration is performed using $N = 32$ integration points and the NLSE is solved for $m = 6$ unknowns. The reference solutions $\omega_{k,\text{ref}}$ are taken from [32], where an algorithm proposed by Beyn [13] is applied. (b-f) Integration contours $\tilde{\Gamma}_1, \ldots, \tilde{\Gamma}_5$ around the eigenfrequencies $\omega_1, \ldots, \omega_5$. (g) Residuals $\text{res}(\tilde{\omega}_k) = ||T(\tilde{\omega}_k)(P(T(\omega), \tilde{\Gamma}_k)y)||_2 / ||T(\tilde{\omega}_k)||_F$, where $||P(T(\omega), \tilde{\Gamma}_k)||_2 = 1$, for each of the Riesz projections $P(T(\omega), \tilde{\Gamma}_1)y, \ldots, P(T(\omega), \tilde{\Gamma}_5)y$ computed with a different number of integration points N. The eigenfrequencies $\tilde{\omega}_k$ are computed by Algorithm 1 for the contours $\tilde{\Gamma}_k$ with $m = 1$ and the corresponding N.

3.3. Resonances based on the hydrodynamic Drude model

In the third numerical experiment, Algorithm 1 is applied to a nanostructure described by the hydrodynamic Drude model. This material model takes spatially nonlocal interactions of the electron gas and the light into account and is used for describing light-matter interaction in nanostructures on the scale of a few nanometers [33,34]. For nonmagnetic materials, the inclusion of nonlocal material properties leads to the coupled system of equations

$$\nabla \times \mu_0^{-1} \nabla \times \mathbf{E}(\mathbf{r}, \omega) - \omega^2 \epsilon_{\text{loc}}(\mathbf{r}, \omega) \mathbf{E}(\mathbf{r}, \omega) = i\omega \mathbf{J}_{\text{hd}}(\mathbf{r}, \omega) + i\omega \mathbf{J}(\mathbf{r}, \omega), \tag{10}$$

$$\beta^2 \nabla \left(\nabla \cdot \mathbf{J}_{\text{hd}}(\mathbf{r}, \omega) \right) + \omega \left(\omega + i\gamma \right) \mathbf{J}_{\text{hd}}(\mathbf{r}, \omega) = i\omega \omega_{\text{p}}^2 \epsilon_0 \mathbf{E}(\mathbf{r}, \omega) \tag{11}$$

for the electric field $\mathbf{E}(\mathbf{r}, \omega)$ and the hydrodynamic current density $\mathbf{J}_{\text{hd}}(\mathbf{r}, \omega)$. The current density $\mathbf{J}(\mathbf{r}, \omega)$ is the impressed source field. The permittivity tensor $\epsilon_{\text{loc}}(\mathbf{r}, \omega)$ corresponds to the local material response, ϵ_0 is the vacuum permittivity, and μ_0 is the vacuum permeability. The plasma frequency ω_{p} and the damping constant γ are associated with the local Drude model $\epsilon_{\text{d}}(\omega) = \epsilon_0(\epsilon_\infty - \omega_{\text{p}}^2/(\omega^2 + i\gamma\omega))$, where ϵ_∞ is the relative permittivity at infinity. The system constant $\beta = \sqrt{3/5}\, v_{\text{F}}$ includes the Fermi velocity v_{F} [35]. The coupled system given by Eqs. (10) and (11) is discretized and solved with the software package JCMsuite.

We consider a metal nanowire from [32], where the eigenpairs have been computed using the contour integral method proposed by Beyn [13]. Furthermore, a modal analysis of the extinction cross section has been performed. The nanowire has been illuminated by plane waves. We refer to [32] for details on the physical parameters describing the nanowire and for details on the FEM realization. Here, the aim is to compute only those eigenfrequencies which QNMs have a significant coupling to these plane waves. Physical source fields y for Algorithm 1 are chosen by solving the coupled system given by Eqs. (10) and (11) for plane waves with frequencies at the centers of the integration contours. For all computations, we choose $\mathcal{G}(T(\omega)^{-1}y) = \beta y^T T(\omega)^{-1} y$, where $\beta \in \mathbb{R}$ is a scaling factor.

First, for the integration contour Γ with a center at $\omega_0 = 1.175\omega_p$ and a radius of $r = 0.175\omega_p$, where $\omega_p = 8.65 \times 10^{15}$ s^{-1}, Algorithm 1 is applied with $N = 32$ integration points and $m = 6$ unknowns. Fig. 3(a) shows the results of Algorithm 1 and reference solutions from [32]. Algorithm 1 yields five eigenfrequencies, $\omega_1 = (1.030 - 0.005i)\omega_p$, $\omega_2 = (1.079 - 0.005i)\omega_p$, $\omega_3 = (1.145 - 0.005i)\omega_p$, $\omega_4 = (1.227 - 0.005i)\omega_p$, $\omega_5 = (1.320 - 0.005i)\omega_p$, inside of Γ. With respect to the reference solutions, the relative errors of their real and imaginary parts are smaller than 1.7×10^{-5} and 1.5×10^{-3}, respectively.

Secondly, the Riesz projections $P(T(\omega), \tilde{\Gamma}_k)y$ are computed for contours $\tilde{\Gamma}_k$ around each of the eigenfrequencies $\omega_1, \ldots, \omega_5$. The contours $\tilde{\Gamma}_1, \ldots, \tilde{\Gamma}_5$ are shown in Fig. 3(b), 3(c), 3(d), 3(e), and 3(f), respectively. Fig. 3(g) shows the residuals res$(\tilde{\omega}_k) = ||T(\tilde{\omega}_k)(P(T(\omega), \tilde{\Gamma}_k)y)||_2/||T(\tilde{\omega}_k)||_F$, where $||P(T(\omega), \tilde{\Gamma}_k))||_2 = 1$, for each of the Riesz projections computed with different numbers of integration points. The eigenfrequencies $\tilde{\omega}_k$ are obtained by applying Algorithm 1 for $\tilde{\Gamma}_k$ with different N and a fixed $m = 1$. The residuals become smaller with an increasing N. For $N = 20$, all residuals are smaller than 1.2×10^{-11}.

Algorithm 1 allows for computing only those eigenfrequencies which QNMs couple to the plane wave defined by the source field y. The remaining eigenvectors which eigenfrequencies are located inside the contour Γ are also QNMs and they may are relevant for another physical problem, however, they are insignificant regarding the here applied source field [32]. This means that small residuals can be observed in Fig. 3(g) although the contours $\tilde{\Gamma}_k$ contain several eigenfrequencies. The Riesz projections $P(T(\omega), \tilde{\Gamma}_k)y$ are physically meaningful as they mainly consist of contributions from the physically relevant QNMs. In [32], the same eigenfrequencies have been identified as the physically relevant eigenfrequencies for the plane wave excitation. However, the approach from [32] requires calculation and investigation of the full electric fields corresponding to the QNMs and is not as much straightforward.

4. Conclusions

We presented a method based on contour integration for computing eigenvalues and associated spectral projections of general NLEVPs. Due to choosing specific physical source fields y for the projection by contour integrals, only physically meaningful eigenvalues are accessed. Instead of computing individual eigenvectors corresponding to these eigenvalues, Riesz projections for frequency ranges of interest are computed. In this way, an expensive computation of a multitude of eigenpairs where most of them are not physically relevant can be circumvented. Numerical realizations were applied to non-Hermitian problems from the fields of quantum mechanics and nanophotonics.

We considered the numerical solution of $T(\lambda)^{-1}y$ as a blackbox and extracted eigenvalue information by introducing the meromorphic function $\mathcal{G}(T(\omega)^{-1}y)$, which can be a physical observable, e.g., a point evaluation as in Sec. 3.2. Instead of global eigenfunctions, modal contributions in form of Riesz projections, e.g., modal Purcell factors [19] or modal extinction cross sections [32], can be computed. In this way, eigenvalues can still be extracted without the need of a global approximation of the solution field $T(\lambda)^{-1}y$. Therefore, we expect that the algorithm will prove especially useful for approaches without a vector representation of the solution field, such as semi-analytical methods. Recently, the presented approach has been compared with standard eigensolvers for NLEVPs resulting from applications in nanophotonics [7].

Declaration of competing interest

The authors declare that they have no known competing financial interests or personal relationships that could have appeared to influence the work reported in this paper.

Acknowledgements

References

[1] F. Tisseur, K. Meerbergen, The quadratic eigenvalue problem, SIAM Rev. 43 (2001) 235–286.
[2] L. Novotny, B. Hecht, Principles of Nano-Optics, 2nd ed., Cambridge University Press, Cambridge, 2012.
[3] S. Dyatlov, M. Zworski, Mathematical Theory of Scattering Resonances, American Mathematical Society, Providence, Rhode Island, 2019.
[4] V. Mehrmann, H. Voss, Nonlinear eigenvalue problems: a challenge for modern eigenvalue methods, GAMM-Mitt. 27 (2005) 121–152.
[5] S. Güttel, F. Tisseur, The nonlinear eigenvalue problem, Acta Numer. 26 (2017) 1–94.
[6] A. Taflove, A. Oskooi, S.G. Johnson (Eds.), Advances in FDTD Computational Electrodynamics: Photonics and Nanotechnology, Artech House, Boston, 2013.
[7] P. Lalanne, W. Yan, A. Gras, C. Sauvan, J.-P. Hugonin, M. Besbes, G. Demésy, M.D. Truong, B. Gralak, F. Zolla, A. Nicolet, F. Binkowski, L. Zschiedrich, S. Burger, J. Zimmerling, R. Remis, P. Urbach, H.T. Liu, T. Weiss, Quasinormal mode solvers for resonators with dispersive materials, J. Opt. Soc. Am. A 36 (2019) 686–704.
[8] W. Yan, R. Faggiani, P. Lalanne, Rigorous modal analysis of plasmonic nanoresonators, Phys. Rev. B 97 (2018) 205422.

[9] M. Garcia-Vergara, G. Demésy, F. Zolla, Extracting an accurate model for permittivity from experimental data: hunting complex poles from the real line, Opt. Lett. 42 (2017) 1145–1148.
[10] H. Voss, An Arnoldi method for nonlinear eigenvalue problems, BIT Numer. Math. 44 (2004) 387–401.
[11] H. Voss, A Jacobi-Davidson method for nonlinear and nonsymmetric eigenproblems, Comput. Struct. 85 (2007) 1284–1292.
[12] J. Asakura, T. Sakurai, H. Tadano, T. Ikegami, K. Kimura, A numerical method for nonlinear eigenvalue problems using contour integrals, JSIAM Lett. 1 (2009) 52–55.
[13] W.-J. Beyn, An integral method for solving nonlinear eigenvalue problems, Linear Algebra Appl. 436 (2012) 3839–3863.
[14] S. Yokota, T. Sakurai, A projection method for nonlinear eigenvalue problems using contour integrals, JSIAM Lett. 5 (2013) 41–44.
[15] B. Gavin, A. Miedlar, E. Polizzi, FEAST eigensolver for nonlinear eigenvalue problems, J. Comput. Sci. 27 (2018) 107–117.
[16] M.V. Barel, P. Kravanja, Nonlinear eigenvalue problems and contour integrals, J. Comput. Appl. Math. 292 (2016) 526–540.
[17] W. Nolting, Theoretical Physics 3. Electrodynamics, Springer, Cham, 2016.
[18] P. Hislop, I. Sigal, Introduction to Spectral Theory. With Applications to Schrödinger Operators, Springer, New York, 1996.
[19] L. Zschiedrich, F. Binkowski, N. Nikolay, O. Benson, G. Kewes, S. Burger, Riesz-projection-based theory of light-matter interaction in dispersive nanoresonators, Phys. Rev. A 98 (2018) 043806.
[20] L. Trefethen, J. Weideman, The exponentially convergent trapezoidal rule, SIAM Rev. 56 (2014) 385–458.
[21] M.V. Barel, Designing rational filter functions for solving eigenvalue problems by contour integration, Linear Algebra Appl. 502 (2016) 346–365.
[22] M. Zworski, Resonances in physics and geometry, Not. Am. Math. Soc. 46 (1999) 319–328.
[23] P. Lalanne, W. Yan, K. Vynck, C. Sauvan, J.-P. Hugonin, Light interaction with photonic and plasmonic resonances, Laser Photonics Rev. 12 (2018) 1700113.
[24] P.T. Kristensen, K. Hermann, F. Intravaia, K. Busch, Modeling electromagnetic resonators using quasinormal modes, arXiv:1910.05412, 2019.
[25] E.S.C. Ching, P.T. Leung, A. Maassen van den Brink, W.M. Suen, S.S. Tong, K. Young, Quasinormal-mode expansion for waves in open systems, Rev. Mod. Phys. 70 (1998) 1545–1554.
[26] P. Monk, Finite Element Methods for Maxwell's Equations, Clarendon Press, Oxford, 2003.
[27] M. Weiser, Inside Finite Elements, De Gruyter, Berlin, 2016.
[28] Z. Shao, W. Porod, C.S. Lent, D.J. Kirkner, An eigenvalue method for open-boundary quantum transmission problems, J. Appl. Phys. 78 (1995) 2177–2186.
[29] A.F. Koenderink, Single-photon nanoantennas, ACS Photonics 4 (2017) 710–722.
[30] J.-P. Berenger, A perfectly matched layer for the absorption of electromagnetic waves, J. Comput. Phys. 114 (1994) 185–200.
[31] B. Vial, F. Zolla, A. Nicolet, M. Commandré, Quasimodal expansion of electromagnetic fields in open two-dimensional structures, Phys. Rev. A 89 (2014) 023829.
[32] F. Binkowski, L. Zschiedrich, M. Hammerschmidt, S. Burger, Modal analysis for nanoplasmonics with nonlocal material properties, Phys. Rev. B 100 (2019) 155406.
[33] S. Raza, S.I. Bozhevolnyi, M. Wubs, N.A. Mortensen, Nonlocal optical response in metallic nanostructures, J. Phys. Condens. Matter 27 (2015) 183204.
[34] N. Schmitt, C. Scheid, J. Viquerat, S. Lanteri, Simulation of three-dimensional nanoscale light interaction with spatially dispersive metals using a high order curvilinear DGTD method, J. Comput. Phys. 373 (2018) 210–229.
[35] A.D. Boardman, Electromagnetic Surface Modes. Hydrodynamic Theory of Plasmon-Polaritons on Plane Surfaces, Wiley, New York, 1982.

6 Computing eigenfrequency sensitivities using Riesz projections

Nanoresonators with high Q-factors are used in various applications [95, 96]. The Q-factor of a resonance characterizes its spectral confinement, which is directly related to the corresponding eigenfrequency $\tilde{\omega}_m$,

$$Q = \frac{\mathrm{Re}(\tilde{\omega}_m)}{-2\mathrm{Im}(\tilde{\omega}_m)}.$$

In the case of a high-Q resonance, the Q-factor describes the relation between stored and radiated electromagnetic field energy [25]. For the fabrication of high-Q nanoresonators [26] and for the computation and optimization of the corresponding Q-factors, the knowledge of the eigenfrequency sensitivities is essential. The eigenfrequency sensitivities are usually computed with the finite difference method, which is a costly approach in terms of computational effort.

In Ref. [68], we develop a Riesz-projection-based approach for the computation of eigenfrequency sensitivities. The approach is based on the considerations from Chapter 5, where Riesz projections are used to compute the eigenfrequency $\tilde{\omega}_m$. Partial differentiation of Eq. (5.1) with respect to a parameter p directly gives the corresponding eigenfrequency sensitivity,

$$
\begin{aligned}
\frac{\partial \tilde{\omega}_m}{\partial p} &= \left(\frac{\partial g}{\partial p}\, h - g\, \frac{\partial h}{\partial p} \right) \frac{1}{h^2}, \\
g &= \oint_{C_m} \omega \mathcal{L}\left(\mathbf{E}(\mathbf{r}, \omega) \right) d\omega, \quad h = \oint_{C_m} \mathcal{L}(\mathbf{E}(\mathbf{r}, \omega))\, d\omega, \\
\frac{\partial g}{\partial p} &= \oint_{C_m} \omega \mathcal{L}\left(\frac{\partial \mathbf{E}(\mathbf{r}, \omega)}{\partial p} \right) d\omega, \quad \frac{\partial h}{\partial p} = \oint_{C_m} \mathcal{L}\left(\frac{\partial \mathbf{E}(\mathbf{r}, \omega)}{\partial p} \right) d\omega.
\end{aligned}
\tag{6.1}
$$

The computation of the contour integrals requires the solution of scattering problems given by Eq. (2.1). In order to solve the corresponding linear system of equations $\left(A - \omega^2 B(\omega) \right) u = f(\omega)$, where u is the scattered electric field $\mathbf{E}(\mathbf{r}, \omega)$ in a finite dimensional FEM basis, an LU-decomposition of the matrix $A - \omega^2 B(\omega)$ is calculated. This LU-decomposition, which is a computationally expensive step in the FEM context, can also be used to solve the linear system of equations for $\partial u / \partial p$,

$$\left(A - \omega^2 B(\omega) \right) \frac{\partial u}{\partial p} = \frac{\partial f(\omega)}{\partial p} - \frac{\partial \left(A - \omega^2 B(\omega) \right)}{\partial p} u.$$

This approach is referred to as direct differentiation [97, 98] and allows for an efficient numerical implementation of Eq. (6.1).

We apply the Riesz-projection-based approach combined with direct differentiation to a resonance which is based on exploiting a quasi bound state in the continuum (BIC) [99]. We compute the eigenfrequency sensitivities of the resonance with respect to several shape parameters of the underlying nanoresonator. A significant reduction in computational effort compared to the use of finite differences can be observed. The computation of the sensitivities is then exploited to optimize the Q-factor of the resonance.

In the following, Ref. [68] is reprinted, which is an open access article distributed under the terms of the Creative Commons CC BY license; [Felix Binkowski, Fridtjof Betz, Martin Hammerschmidt, Philipp-Immanuel Schneider, Lin Zschiedrich, and Sven Burger. Computation of eigenfrequency sensitivities using Riesz projections for efficient optimization of nanophotonic resonators. *Commun. Phys.* 5, 202 (2022). DOI: 10.1038/s42005-022-00977-1.]

ARTICLE

Check for updates

Computation of eigenfrequency sensitivities using Riesz projections for efficient optimization of nanophotonic resonators

Felix Binkowski [1], Fridtjof Betz [1], Martin Hammerschmidt [2], Philipp-Immanuel Schneider[2], Lin Zschiedrich[2] & Sven Burger [1,2 ✉]

Resonances are omnipresent in physics and essential for the description of wave phenomena. We present an approach for computing eigenfrequency sensitivities of resonances. The theory is based on Riesz projections and the approach can be applied to compute partial derivatives of the complex eigenfrequencies of any resonance problem. Here, the method is derived for Maxwell's equations. Its numerical realization essentially relies on direct differentiation of scattering problems. We use a numerical implementation to demonstrate the performance of the approach compared to differentiation using finite differences. The method is applied for the efficient optimization of the quality factor of a nanophotonic resonator.

[1] Zuse Institute Berlin, 14195 Berlin, Germany. [2] JCMwave GmbH, 14050 Berlin, Germany. ✉email: burger@zib.de

Resonance phenomena are ubiquitous in nanophotonics and play an important role for tailoring light–matter interactions[1,2]. They are exploited in, e.g., single-photon sources for quantum technology[3], biosensors[4], nanolasers[5], or solar energy devices[6,7]. All these applications rely on the highly localized electromagnetic field energies in the vicinity of the underlying nanoresonators[8]. A central figure of merit for the description of resonance effects is the quality (Q) factor, which quantifies, in the case of low-loss systems, the relation between stored and radiated field energies of the resonances[9]. Nanoresonators with low energy dissipation, i.e., with high Q-factors, have been proposed to improve the efficiencies of nanophotonic devices[2,10]. For example, high-Q resonators can boost the brightness of quantum emitters, the sensitivity of sensors, or the emission processes in plasmonic lasers[11]. Designing devices with numerical optimization is a time and cost-effective approach. The resonances are numerically computed by solving the source-free Maxwell's equations equipped with open boundary conditions[12]. This yields non-Hermitian eigenproblems and the solutions are eigenmodes with complex-valued eigenfrequencies. In this context, the Q-factor is defined as the scaled ratio of the real and imaginary parts of the eigenfrequency.

Nanoresonators with high Q-factors have been theoretically presented, but fabrication of these resonators is a limiting task[11]. The sensitivity analysis of eigenfrequencies can show a way to reduce the sensitivities of the Q-factors. This can support the nanofabrication processes. Furthermore, the sensitivity analysis of eigenfrequencies is essential for numerical simulation. For example, the numerical accuracies of the calculated eigenfrequencies are strongly influenced by the sensitivities of the eigenfrequencies when the systems are subject to small perturbations[13,14]. In particular, for high-Q resonators, the accuracy requirements are demanding since the real and imaginary parts of the eigenfrequencies differ by several orders of magnitude. Sensitivities are also directly exploited in numerical optimization algorithms using gradients[15], for gradient-enhanced surrogate modeling[16], and for local sensitivity analyses[17]. The computation of eigenfrequency sensitivities is usually based on perturbation theory[18,19], where the sensitivity of the underlying operator, the left and the right eigenmodes, and a proper normalization of the eigenmodes are required. The solution of the perturbed systems, on the other hand, is not necessary. For resonance problems, left and right eigenmodes are in general not identical, which increases the computational effort, and normalization requires additional attention. There are specialized approaches that, e.g., exploit magnetic fields for extracting the left eigenmodes[20], introduce an adjoint system for computing sensitivities[21], or that rely on internal and external electric fields at the boundaries of the nanoresonators[22]. It is also possible to completely omit the use of eigenmodes for sensitivity analysis[23]. A further approach is the straightforward application of finite differences. However, this also includes the solution of the perturbed resonance problems, which increases the computational effort.

In this work, we present an approach for computing eigenfrequency sensitivities that completely avoids solving resonance problems. The approach is based on Riesz projections given by contour integrals in the complex frequency plane. The contour integrals are numerically accessed by solving Maxwell's equations with a source term enabling an efficient numerical realization using direct differentiation. The numerical experiments show a significant reduction in computational effort compared to applying finite differences. A Bayesian optimization algorithm with the incorporation of eigenfrequency sensitivities is used to optimize a resonator hosting a resonance with a high Q-factor.

Results

Theoretical background and numerical realization. We start with an introduction of the theoretical background on resonance phenomena occurring in nanophotonics. Based on this, Riesz projections for computing eigenfrequency sensitivities and an efficient approach for its numerical realization are presented.

Resonances in nanophotonics. In nanophotonics, in the steady-state regime, light–matter interactions can be described by the time-harmonic Maxwell's equations in second-order form,

$$\nabla \times \mu_0^{-1} \nabla \times \mathbf{E}(\mathbf{r}, \omega_0) - \omega_0^2 \epsilon(\mathbf{r}, \omega_0) \mathbf{E}(\mathbf{r}, \omega_0) = i\omega_0 \mathbf{J}(\mathbf{r}), \qquad (1)$$

where $\mathbf{E}(\mathbf{r}, \omega_0) \in \mathbb{C}^3$ is the electric field, $\mathbf{r} \in \mathbb{R}^3$ is the position, $\omega_0 \in \mathbb{R}$ is the angular frequency, and $\mathbf{J}(\mathbf{r}) \in \mathbb{C}^3$ is the electric current density corresponding to a light source. In the optical regime, the permeability tensor $\mu(\mathbf{r}, \omega_0)$ typically equals the vacuum permeability μ_0. The permittivity tensor $\epsilon(\mathbf{r}, \omega_0) = \epsilon_r(\mathbf{r}, \omega_0)\epsilon_0$, where $\epsilon_r(\mathbf{r}, \omega_0)$ is the relative permittivity and ϵ_0 the vacuum permittivity, describes the spatial distribution of material and the material dispersion. Solutions to Eq. (1) are called scattering solutions as light from a source is scattered by a material system.

Resonances are solutions to Eq. (1) without a source term, i.e., $\mathbf{J}(\mathbf{r}) = 0$, and with transparent boundary conditions. The boundary conditions lead to non-Hermitian eigenproblems, and, if material dispersion is also present, the eigenproblems become nonlinear. The electric field distribution of an eigenmode is denoted by $\tilde{\mathbf{E}}(\mathbf{r}) \in \mathbb{C}^3$ and the corresponding complex-valued eigenfrequency by $\tilde{\omega} \in \mathbb{C}$. The Q-factor of a resonance is defined by

$$Q = \frac{\mathrm{Re}(\tilde{\omega})}{-2\mathrm{Im}(\tilde{\omega})}$$

and describes its spectral confinement. In the limiting case of vanishing losses, this definition agrees with the energy definition, according to which the Q-factor quantifies the relation between stored and dissipated electromagnetic field energy of a resonance[9].

In the following, a nanophotonic resonator supporting a resonance with a high Q-factor is investigated. We compute the eigenfrequency sensitivities with respect to various parameters to optimize the Q-factor of the nanoresonator. Figure 1 sketches the applied framework for an exemplary problem, a one-dimensional resonator defined by layers with different permittivities. Changes δp of the parameter p lead to changes in the eigenmode $\tilde{\mathbf{E}}$ and in the corresponding eigenfrequency $\tilde{\omega}$, which describes the sensitivity of $\tilde{\mathbf{E}}$ and $\tilde{\omega}$ with respect to the parameter p. To compute the eigenfrequency sensitivity, we introduce a contour-integral-based approach using Riesz projections, where physical observables are extracted from scattering problems. Solving the scattering problems, which are linear systems, can be regarded as a blackbox[24,25].

Riesz projections for eigenfrequency sensitivities. To derive a Riesz-projection-based approach for computing eigenfrequency sensitivities, which are the partial derivatives of the eigenfrequency, we consider the electric field $\mathbf{E}(\mathbf{r}, \omega_0 \in \mathbb{R})$ as a solution of Eq. (1) and $\mathbf{E}(\mathbf{r}, \omega \in \mathbb{C})$ as an analytical continuation of $\mathbf{E}(\mathbf{r}, \omega_0)$ into the complex frequency plane. The field $\mathbf{E}(\mathbf{r}, \omega)$ is a meromorphic function with resonance poles at the eigenfrequencies. To simplify the notation, we omit the spatial and frequency dependency of the electric field and write $\mathbf{E}$ when we mean $\mathbf{E}(\mathbf{r}, \omega)$.

Let $\mathcal{L}(\mathbf{E})$ be a physical observable, where $\mathcal{L} : \mathbb{C}^3 \to \mathbb{C}$ is a linear functional, and $\tilde{C}$ be a contour enclosing the pole $\tilde{\omega}$ of the order m and no other poles. Then, the Laurent expansion of $\mathcal{L}(\mathbf{E})$
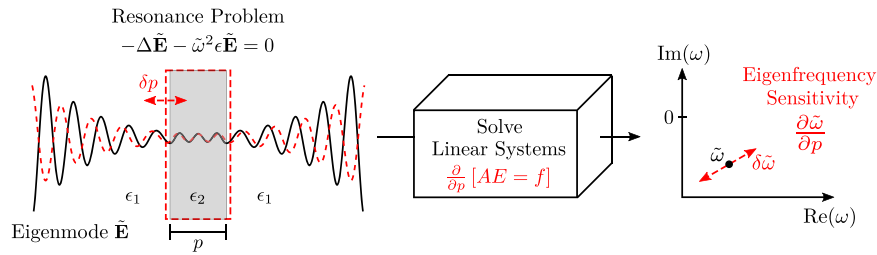
Fig. 1 Schematic representation of computing eigenfrequency sensitivities of a resonator using contour integration. The system is defined by layers with different permittivities ϵ_1 and ϵ_2 and is described by the one-dimensional Helmholtz equation $-\Delta\tilde{\mathbf{E}} - \tilde{\omega}^2\epsilon\tilde{\mathbf{E}} = 0$. A solution to the resonance problem is given by the eigenmode $\tilde{\mathbf{E}}$ and the corresponding complex-valued eigenfrequency $\tilde{\omega} \in \mathbb{C}$. The real part of the electric field of the eigenmode is sketched with the solid black curve. A perturbation δp of the middle layer width p leads to a perturbed electric field, represented by the dashed red curve, and to a perturbation $\delta\tilde{\omega}$ of the eigenfrequency. Computing contour integrals by solving linear systems $AE = f$ and $\partial/\partial p[AE = f]$ in the complex frequency plane yields the eigenfrequency sensitivity $\partial\tilde{\omega}/\partial p$. Solving the linear systems is considered as a blackbox.

about $\tilde{\omega}$ is given by

$$\mathcal{L}(\mathbf{E}) = \sum_{k=-m}^{\infty} a_k(\omega - \tilde{\omega})^k, \text{ where}$$
$$a_k(\tilde{\omega}) = \frac{1}{2\pi\mathrm{i}} \oint_{\tilde{C}} \frac{\mathcal{L}(\mathbf{E}(\omega))}{(\omega - \tilde{\omega})^{k+1}} \, \mathrm{d}\omega \in \mathbb{C}. \tag{2}$$

The coefficient $a_{-1}(\tilde{\omega})$ is the so-called residue of $\mathcal{L}(\mathbf{E})$ at $\tilde{\omega}$. Using Eq. (2) with the assumption that $\tilde{\omega}$ has the order $m = 1$ and applying Cauchy's integral formula yield

$$\oint_{\tilde{C}} \omega\mathcal{L}(\mathbf{E}) \, \mathrm{d}\omega = \oint_{\tilde{C}} \frac{\omega}{\omega - \tilde{\omega}} a_{-1}(\tilde{\omega}) \, \mathrm{d}\omega = \tilde{\omega} \oint_{\tilde{C}} \mathcal{L}(\mathbf{E}) \, \mathrm{d}\omega,$$

where, due to the closed integral in the complex plane, the regular terms in the expansion vanish. With this, the eigenfrequency $\tilde{\omega}$ is given by

$$\tilde{\omega} = \frac{\oint_{\tilde{C}} \omega\mathcal{L}(\mathbf{E}) \, \mathrm{d}\omega}{\oint_{\tilde{C}} \mathcal{L}(\mathbf{E}) \, \mathrm{d}\omega}. \tag{3}$$

The contour integrals in this equation are essentially Riesz projections for $\mathcal{L}(\mathbf{E})$ and $\tilde{C}$[24]. Partial differentiation with respect to a parameter p directly gives the desired expression for the eigenfrequency sensitivity,

$$\frac{\partial\tilde{\omega}}{\partial p} = \left(\frac{\partial u}{\partial p}v - u\frac{\partial v}{\partial p}\right)\frac{1}{v^2}, \text{ where}$$
$$u = \oint_{\tilde{C}} \omega\mathcal{L}(\mathbf{E}) \, \mathrm{d}\omega, v = \oint_{\tilde{C}} \mathcal{L}(\mathbf{E}) \, \mathrm{d}\omega,$$
$$\frac{\partial u}{\partial p} = \oint_{\tilde{C}} \omega\mathcal{L}\left(\frac{\partial\mathbf{E}}{\partial p}\right) \, \mathrm{d}\omega, \frac{\partial v}{\partial p} = \oint_{\tilde{C}} \mathcal{L}\left(\frac{\partial\mathbf{E}}{\partial p}\right) \, \mathrm{d}\omega. \tag{4}$$

For the interchangeability of integral and derivative, $\mathbf{E}$ and $\partial\mathbf{E}/\partial p$ are assumed to be continuously differentiable with respect to the frequency ω and the parameter p. The eigenmode $\tilde{\mathbf{E}}$ and its sensitivity $\partial\tilde{\mathbf{E}}/\partial p$ can be represented by the contour integrals

$$\tilde{\mathbf{E}} = \oint_{\tilde{C}} \mathbf{E} \, \mathrm{d}\omega \text{ and } \frac{\partial\tilde{\mathbf{E}}}{\partial p} = \oint_{\tilde{C}} \frac{\partial\mathbf{E}}{\partial p} \, \mathrm{d}\omega,$$

respectively, which are Riesz projections applied to Maxwell's equations given by Eq. (1). This approach can be generalized for multiple eigenfrequencies inside a contour as well as for higher order poles; cf. Binkowski et al.[24]. Note that Riesz projections can also be used to compute modal expansions of physical

observables, where scattering solutions are expanded into weighted sums of eigenmodes[26].

Numerical realization and direct differentiation. For the numerical realization of the presented approach, the finite element method (FEM) is applied. Scattering problems are solved by applying the solver JCMSUITE[27]. The FEM discretization of Eq. (1) leads to the linear system of equations $AE = f$, where $A \in \mathbb{C}^{n \times n}$ is the system matrix, $E \in \mathbb{C}^n$ is the scattered electric field in a finite-dimensional FEM basis, and $f \in \mathbb{C}^n$ contains the source term. The solver employs adaptive meshing and higher order polynomial ansatz functions. In all subsequent simulations, it is ensured that sufficient accuracies are achieved with respect to the FEM discretization parameters. Note that also other methods can be used for numerical discretization. In the field of nanophotonics, common approaches are, e.g., the finite-difference time-domain method, the Fourier modal method, or the boundary element method[12,28].

In order to calculate eigenfrequencies $\tilde{\omega}$ and their sensitivities $\partial\tilde{\omega}/\partial p_i$ with respect to parameters p_i, the electric fields $\mathbf{E}$ and their sensitivities $\partial\mathbf{E}/\partial p_i$ are computed for complex frequencies $\omega \in \mathbb{C}$ on the contours given in Eqs. (3) and (4). For the calculation of $\partial\mathbf{E}/\partial p_i$, we apply an approach based on directly using the FEM system matrix[29,30]. With this direct differentiation method, the sensitivities of scattering solutions can be computed by

$$\frac{\partial E}{\partial p_i} = A^{-1}\left(\frac{\partial f}{\partial p_i} - \frac{\partial A}{\partial p_i}E\right). \tag{5}$$

In a first step, instead of directly computing A^{-1}, an LU-decomposition of A, which can be seen as the matrix variant of Gaussian elimination, is computed to efficiently solve the linear system $AE = f$. In the FEM context, this step is usually a computationally expensive step in solving scattering problems, so reusing an LU-decomposition can significantly reduce computational costs. In a second step, the partial derivatives of the system matrix, $\partial A/\partial p_i$, and of the source term, $\partial f/\partial p_i$, are obtained quasi analytically, i.e., with negligible computational effort. Then, $A = LU$, E, $\partial A/\partial p_i$, and $\partial f/\partial p_i$ are used to compute $\partial E/\partial p_i$ in Eq. (5). The LU-decomposition can be used to obtain both E and $\partial E/\partial p_i$.

For the calculation of the contour integrals, a numerical integration with a circular integration contour and a trapezoidal rule is used, which leads to an exponential convergence behavior with respect to the integration points[31]. At each integration point, we calculate $\mathbf{E}$ and $\partial\mathbf{E}/\partial p_i$ by solving Eq. (1) with oblique incident plane waves as source terms. The linear functional $\mathcal{L}(\mathbf{E})$ corresponds to a spatial point evaluation of one component of the electric field, which can be understood as physical observable. Note that, with Eqs. (3) and (4), an eigenfrequency $\tilde{\omega}$ and its
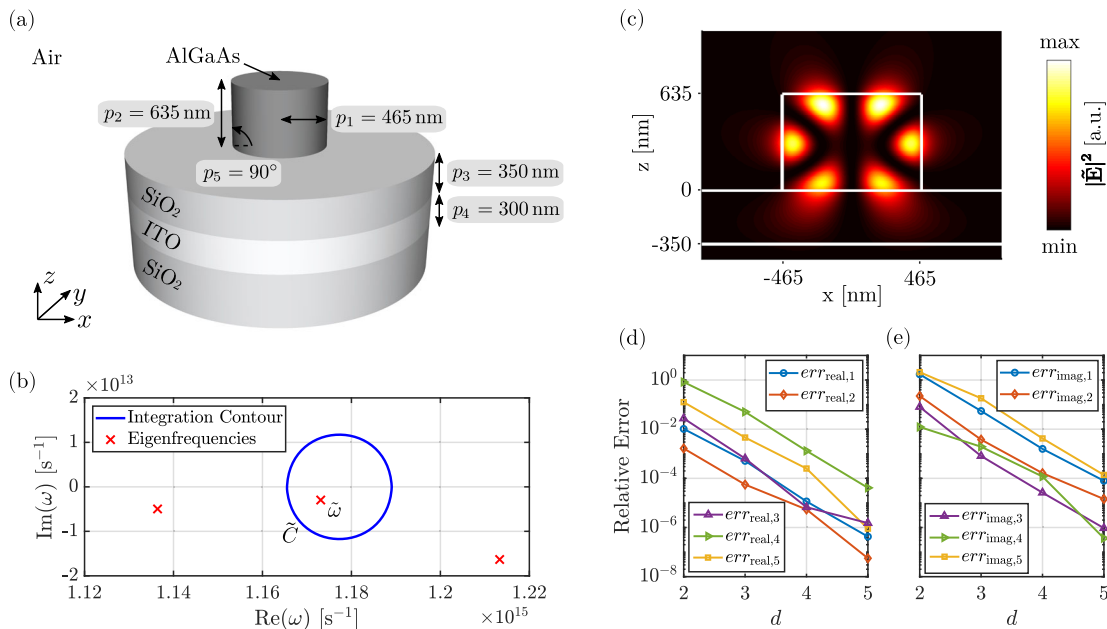
Fig. 2 Numerical investigation of the high-Q resonance of a nanophotonic resonator. a Nanoresonator on a three-layer substrate. The substrate is infinitely extended in x and y direction. The geometrical parameters $p_1, p_2, ..., p_5$ are the reference values from Koshelev et al.[32]. **b** Calculated eigenfrequency $\tilde{\omega} = (1.17309 - 0.00296i) \times 10^{15}$ s^{-1} corresponding to the high-Q resonance. The other red crosses shown are the two eigenfrequencies which are closest to $\tilde{\omega}$. The circular integration contour $\tilde{C}$ with the center $\omega_0 = 2\pi c/(1600$ nm$)$ and the radius $r_0 = \omega_0 \times 10^{-2}$ is used for computing Riesz projections. **c** Electric field intensity $|\tilde{\mathbf{E}}|^2$ corresponding to the high-Q resonance. **d** Convergence of the eigenfrequency sensitivities $\partial\tilde{\omega}/\partial p_i$ with respect to the polynomial degree d of the FEM ansatz functions. The sensitivities are computed at the parameter reference values given in (**a**). Relative errors err$_{\text{real},i} = |\text{Re}(\frac{\partial\tilde{\omega}}{\partial p_i}(d) - \frac{\partial\tilde{\omega}}{\partial p_i}(d_{\text{ref}}))/\text{Re}(\frac{\partial\tilde{\omega}}{\partial p_i}(d_{\text{ref}}))|$, where $d_{\text{ref}} = 6$. **e** Relative errors err$_{\text{imag},i}$ for the imaginary parts of the sensitivities; cf. (**d**).

sensitivity $\partial\tilde{\omega}/\partial p_i$ can be calculated without solving resonance problems $\nabla \times \mu^{-1}\nabla \times \tilde{\mathbf{E}} - \tilde{\omega}^2\epsilon\tilde{\mathbf{E}} = 0$ directly. Instead, scattering problems, where Eq. (5) can be exploited, are solved. We call the described approach, which combines Riesz projections and direct differentiation (DD), the *Riesz projection DD method*. Equation (4) and its numerical implementation exploiting Eq. (5) are the main results of this work and represent the difference from previous works on Riesz projections; cf. Zschiedrich et al.[26].

Note that the Riesz projection DD method is not limited to the field of nanophotonics, but can be applied to other eigenproblems as well. Maxwell's equations can be replaced by another partial differential equation, and then instead of the analytical continuation of the electric field **E**, the analytical continuation of another quantity is evaluated for the contour integration.

Application

Eigenfrequency sensitivities of a nanophotonic resonator. We investigate an example from the literature, a dielectric nanoresonator of cylindrical shape placed on a three-layer substrate, where constructive and destructive eigenmode interference has been used to engineer a bound state in the continuum (BIC)[32]. The nanoresonator has been designed taking into account various parameters to suppress radiation losses: The radius, the layer thicknesses, and the layer materials have been chosen to obtain a high-Q resonance. The nanoresonator is made of the high-index material aluminum gallium arsenide (AlGaAs) with 20% aluminum. A silicon dioxide (SiO$_2$) spacer is placed between the nanoresonator and a film of indium tin oxide (ITO) on a SiO$_2$ substrate. A sketch of the designed system is shown in Fig. 2a. For this specific configuration, a high-Q resonance with a Q-factor of $Q = 188 \pm 5$ has been experimentally observed, and numerical simulations have resulted in $Q = 197$, where the real part of the resonance wavelength is in the telecommunication wavelength

regime, close to 1600 nm. The nanophotonic resonator has been exploited as a nanoantenna for nonlinear nanophotonics[32].

In the following simulations, we consider the constant relative permittivities $\epsilon_{\text{r}} = 10.81$ and $\epsilon_{\text{r}} = 2.084$ for AlGaAs and for SiO$_2$, respectively, which are extracted from experimental data[32,33]. For the ITO layer, the Drude model $\epsilon_{\text{r}}(\omega_0) = \epsilon_{\text{inf}} - \omega_{\text{p}}^2/(\omega_0^2 + i\omega_0\gamma)$ is chosen, where $\epsilon_{\text{inf}} = 3.8813$, $\omega_{\text{p}} = 3.0305 \times 10^{15}$ s^{-1}, and $\gamma = 1.2781 \times 10^{14}$ s^{-1}. This Drude model is obtained by a rational fit[34] to experimental data[32] and describes the material dispersion of the system. We further exploit the rotational symmetry of the geometry. On the one hand, this reduces the computational effort and, on the other hand, the eigenmodes can be easily distinguished by their azimuthal quantum numbers m, which correspond to the number of oscillations in the radial and axial directions. When the light sources used for computing Riesz projections are not rotationally symmetric, such as oblique incident plane waves, the source fields can be expanded into Fourier modes in the angular direction. Considering Fourier modes with certain quantum numbers, only the eigenmodes, eigenfrequencies, and corresponding sensitivities associated with these quantum numbers are accessed.

We start with computing a Riesz projection to obtain the eigenfrequency $\tilde{\omega}$ of the high-Q resonance. Figure 2b shows the complex frequency plane with the calculated eigenfrequency, $\tilde{\omega} = (1.17309 - 0.00296i) \times 10^{15}$ s^{-1}, and the corresponding circular integration contour $\tilde{C}$ for the computation of the Riesz projection. The center and the radius of the contour are selected based on a-priori knowledge from Koshelev et al.[32]. Alternatively, without a-priori knowledge, a larger integration contour can be used[25]. The simulations are performed using eight integration points on the contour $\tilde{C}$, where a sufficient accuracy with respect to the integration points is ensured. The computations are based on a FEM mesh consisting of 306 triangles. To compare the size of the contour with the distances between the eigenfrequencies

Table 1 Computed eigenfrequency sensitivities.

i	$\mathrm{Re}(\partial\tilde{\omega}/\partial p_i)\times 10^{-10}$	$\mathrm{Im}(\partial\tilde{\omega}/\partial p_i)\times 10^{-10}$
1	-128.750 (s nm)$^{-1}$	-0.324 (s nm)$^{-1}$
2	-84.568 (s nm)$^{-1}$	2.660 (s nm)$^{-1}$
3	-7.192 (s nm)$^{-1}$	-1.955 (s nm)$^{-1}$
4	-0.065 (s nm)$^{-1}$	0.208 (s nm)$^{-1}$
5	15.047 (s deg)$^{-1}$	0.039 (s deg)$^{-1}$

The sensitivities $\partial\tilde{\omega}/\partial p_i$ correspond to the high-Q resonance of the nanoresonator shown in Fig. 2a and are computed at the shown parameter reference values.

within the spectrum of the nanoresonator, the two eigenfrequencies which are closest to $\tilde{\omega}$ are also shown. We obtain a Q-factor of $Q = 198$ for the high-Q resonance, which is in good agreement with the experimental and numerical results from Koshelev et al.[32]. The corresponding electric field intensity $|\tilde{\mathbf{E}}|^2$ is shown in Fig. 2c. The eigenmode $\tilde{\mathbf{E}}$ has the quantum number $m = 0$ and is strongly localized in the vicinity of the nanoresonator.

Next, the eigenfrequency sensitivities $\partial\tilde{\omega}/\partial p_i$ with respect to the parameters $p_1, p_2, \ldots, p_5$ sketched in Fig. 2a are computed. In order to validate the approach, a convergence study for the polynomial degree d of the FEM ansatz functions is performed. Figure 2d, e shows the relative errors for the real and imaginary parts, respectively. Exponential convergence can be observed for all sensitivities with increasing d. The computed sensitivities for $d = 5$ are shown in Table 1. Exemplary source code for the Riesz projection DD method and simulation results are presented in Binkowski et al.[35].

Performance benchmark. The computational effort of the numerical realization of the Riesz projection DD method is compared with the computational effort of the finite difference method. We choose the central difference scheme $\partial\tilde{\omega}/\partial p_i \approx \left(\tilde{\omega}(p_i + \delta p_i) - \tilde{\omega}(p_i - \delta p_i)\right)/\left(2\delta p_i\right)$ for the comparison. Computing central differences is more computationally expensive than computing forward or backward differences. However, more accurate results can be achieved as the error decreases with $(\delta p_i)^2$. To achieve an adequate accuracy, sufficiently small step sizes δp_i are selected. For example, for the radius of the nanoresonator, we choose $\delta p_1 = 0.1$ nm. Note that, also for the finite difference method, we compute the eigenfrequencies by using the contour-integral-based formula in Eq. (3).

We increase the degrees of freedom of the system shown in Fig. 2a by deforming the cylindrical nanoresonator to an ellipsoidal nanoresonator. This breaks the rotational symmetry yielding a full three-dimensional system with new parameters, the radius of the nanoresonator in x direction and the radius in y direction. Figure 3 shows, for the three-dimensional implementation and for the rotational symmetric implementation, the normalized computational effort for different numbers of computed sensitivities. We compute the eigenfrequency $\tilde{\omega}$ and then we add the sensitivities, starting with $\partial\tilde{\omega}/\partial p_1$, one after the other. It can be observed that the Riesz projection DD method requires less computational effort than the finite difference method, for any number of computed sensitivities, i.e., for all $N \geq 1$. In the case of using finite differences, the computational effort has a slope of about 200% because for each sensitivity two additional problems with typically the same dimension as the unperturbed problem have to be solved. In the three-dimensional case, a linear regression for the computational effort gives a slope of about 4% for the Riesz projection DD method. The computational effort needed for the LU-decomposition is significant compared to the matrix assembly and to the other solution steps, so the possibility of exploiting Eq. (5) gives a great benefit for the Riesz projection DD method. For $N = 5$, the CPU
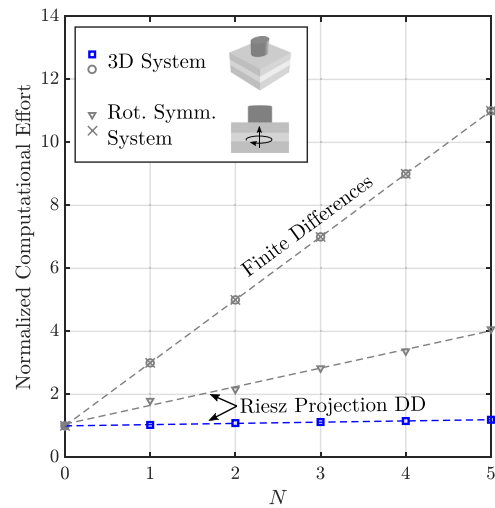

Fig. 3 Performance of the Riesz projection DD method. The normalized computational effort over the number N of computed sensitivities $\partial\tilde{\omega}/\partial p_i$ with respect to parameters $p_1, p_2, ..., p_N$ is shown. The sensitivities are computed at the reference values shown in Fig. 2a. The computational effort is the total CPU time normalized to the CPU time spent for computing the eigenfrequency $\tilde{\omega}$, which corresponds to $N = 0$. The time is measured with JCMSUITE using four threads on a machine with a 24-core Intel Xeon Processor running at 3.3 GHz. For all calculations, to ensure high accuracies, eight integration points at the integration contour $\tilde{C}$ depicted in Fig. 2b are used. The degree of the FEM ansatz functions is fixed with $d = 5$. The mesh of the three-dimensional system consists of 4160 prisms and the mesh of the rotational symmetric system consists of 306 triangles.

time required to solve the linear system of equations, which includes the LU-decomposition, takes 81% of the accumulated CPU time. In the rotational symmetric case, the time for solving the linear system is negligible. However, the trend is the same for the three-dimensional and for the computationally cheaper rotational symmetric case: The advantage of using Riesz projections significantly increases with an increasing number of computed sensitivities.

Note that contour integral methods are well suited for parallelization because the scattering problems can be solved in parallel on the integration contour. However, as total CPU times are considered for Fig. 3, this is not reflected by the time measurements.

Q-factor optimization. The Riesz projection DD method is applied to further optimize the Q-factor of the high-Q resonance of the nanophotonic resonator from Koshelev et al.[32] shown in Fig. 2a. A rotational symmetric nanoresonator is considered because simulations show that an ellipsoidal shape does not lead to a significant increase of the Q-factor. We use a Bayesian optimization algorithm[36] with the incorporation of sensitivity information. This global optimization algorithm is well suited for problems with computationally expensive objective functions and benchmarks show that providing sensitivities can significantly reduce computational effort[37]. However, other optimization approaches could be used as well.

For the optimization, we choose the parameter ranges 435 nm $\leq p_1 \leq$ 495 nm, 575 nm $\leq p_2 \leq$ 695 nm, 150 nm $\leq p_3 \leq$ 550 nm, 100 nm $\leq p_4 \leq$ 500 nm, and 60° $\leq p_5 \leq$ 90°. To ensure that the optimized nanoresonator can also be used as nanoantenna in the telecommunication wavelength regime, like the original system, we add the constraint that the optimized eigenfrequency must lie in the circular contour with the center $\omega_0 = 2\pi c/(1600$ nm$)$ and the radius $r_0 = 4 \times 10^{13}$ s^{-1}. In each optimization step, the Riesz
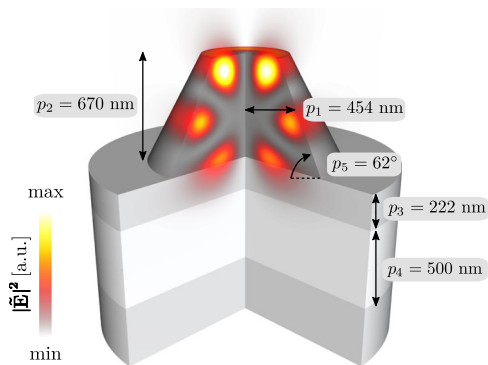
Fig. 4 Optimization of a nanophotonic resonator. The optimized nanophotonic resonator with a sketch of the electric field intensity $|\tilde{\mathbf{E}}|^2$ corresponding to the high-Q resonance is shown. The high-Q resonance has a Q-factor of $Q = 292$. The materials of the nanoresonator are the same as for the reference structure in Fig. 2a.

projection DD method is used to compute the eigenfrequency with a quantum number of $m = 0$ lying inside the contour and to calculate the corresponding sensitivities.

A nanoresonator with a Q-factor of $Q = 292$ is obtained after 61 iterations of the optimizer yielding an increase of about 47.5% over the original resonator. More iterations yield only a negligible increase of the Q-factor. The optimized nanoresonator with a sketch of the electric field intensity of its high-Q resonance and the values for all underlying parameters are shown in Fig. 4. The corresponding eigenfrequency is given by $\tilde{\omega}_{\mathrm{opt}} = (1.176897 - 0.002015i) \times 10^{15}\,\mathrm{s}^{-1}$. Note that, in the optimization domain, the average sensitivity of the Q-factor with respect to the ITO layer thickness p_4 is negligible.

Conclusions

An approach for computing eigenfrequency sensitivities of resonance problems was presented. The numerical realization of the Riesz projection DD method relies on computing scattering solutions and their sensitivities by solving Maxwell's equations with a source term, i.e., solving linear systems of equations. This enables direct differentiation for the efficient calculation of eigenfrequency sensitivities. Although sensitivities of resonances are computed, no eigenproblems have to be solved directly. The performance of the approach was demonstrated by a comparison with the finite difference method. The Riesz projection DD method was incorporated into a gradient-based optimization algorithm to maximize the Q-factor of a nanophotonic resonator.

The savings in computational effort are particularly significant for optimization with respect to several parameters, which is a common task in nanophotonics. Therefore, we expect the approach to prove especially useful when many sensitivities are to be calculated. The Riesz projection DD method can not only be applied to problems in nanophotonics, but to any resonance problem.

Data availability

All relevant data generated or analyzed during this study are included in this published article. Tabulated data files are included in a corresponding data publication[35].

Code availability

Source code for performing the numerical experiments can be found in Binkowski et al.[35].

References

1. Novotny, L. & van Hulst, N. Antennas for light. *Nat. Photonics* **5**, 83–90 (2011).
2. Kuznetsov, A. I., Miroshnichenko, A. E., Brongersma, M. L., Kivshar, Y. S. & Luk'yanchuk, B. Optically resonant dielectric nanostructures. *Science* **354**, aag2472 (2016).
3. Senellart, P., Solomon, G. & White, A. High-performance semiconductor quantum-dot single-photon sources. *Nat. Nanotechnol.* **12**, 1026–1039 (2017).
4. Anker, J. N. et al. Biosensing with plasmonic nanosensors. *Nat. Mater.* **7**, 442–453 (2008).
5. Ma, R.-M. & Oulton, R. F. Applications of nanolasers. *Nat. Nanotechnol.* **14**, 12–22 (2019).
6. Ma, X.-C., Dai, Y., Yu, L. & Huang, B.-B. Energy transfer in plasmonic photocatalytic composites. *Light Sci. Appl.* **5**, e16017 (2016).
7. Zhang, Y. et al. Surface-plasmon-driven hot electron photochemistry. *Chem. Rev.* **118**, 2927–2954 (2018).
8. Lalanne, P. et al. Light interaction with photonic and plasmonic resonances. *Laser Photonics Rev.* **12**, 1700113 (2018).
9. Wu, T., Gurioli, M. & Lalanne, P. Nanoscale light confinement: The Q's and V's. *ACS Photonics* **8**, 1522–1538 (2021).
10. West, P. R. et al. Searching for better plasmonic materials. *Laser Photonics Rev.* **4**, 795–808 (2010).
11. Wang, B. et al. High-Q plasmonic resonances: Fundamentals and applications. *Adv. Opt. Mater.* **9**, 2001520 (2021).
12. Lalanne, P. et al. Quasinormal mode solvers for resonators with dispersive materials. *J. Opt. Soc. Am. A* **36**, 686–704 (2019).
13. Bindel, D. & Hood, A. Localization theorems for nonlinear eigenvalue problems. *SIAM J. Matrix Anal. Appl.* **34**, 1728–1749 (2013).
14. Güttel, S. & Tisseur, F. The nonlinear eigenvalue problem. *Acta Numer.* **26**, 1–94 (2017).
15. Jensen, J. S. & Sigmund, O. Topology optimization for nano-photonics. *Laser Photonics Rev.* **5**, 308–321 (2011).
16. Bouhlel, M. A. et al. A python surrogate modeling framework with derivatives. *Adv. Eng. Softw.* **135**, 102662 (2019).
17. Cacuci, D. G., Ionescu-Bujor, M. & Navon, I. M. *Sensitivity and Uncertainty Analysis, Volume II: Applications to Large-Scale Systems* 1st edn (CRC Press, 2005).
18. Kato, T. *Perturbation Theory for Linear Operators* 2nd edn (Springer-Verlag, 1995).
19. Sakurai, J. J. & Napolitano, J. *Modern Quantum Mechanics* 3rd edn (Cambridge University Press, 2020).
20. Burschäpers, N., Fiege, S., Schuhmann, R. & Walther, A. Sensitivity analysis of waveguide eigenvalue problems. *Adv. Radio Sci.* **9**, 85–89 (2011).
21. Swillam, M. A., Bakr, M. H., Li, X. & Deen, M. J. Efficient sensitivity analysis of the time independent Schrödinger equation with application to quantum lasers. *Opt. Commun.* **281**, 4459–4463 (2008).
22. Yan, W., Lalanne, P. & Qiu, M. Shape deformation of nanoresonator: A quasinormal-mode perturbation theory. *Phys. Rev. Lett.* **125**, 013901 (2020).
23. Alam, R. & Safique Ahmad, S. K. Sensitivity analysis of nonlinear eigenproblems. *SIAM J. Matrix Anal. Appl.* **40**, 672–695 (2019).
24. Binkowski, F., Zschiedrich, L. & Burger, S. A Riesz-projection-based method for nonlinear eigenvalue problems. *J. Comput. Phys.* **419**, 109678 (2020).
25. Betz, F., Binkowski, F. & Burger, S. RPExpand: Software for Riesz projection expansion of resonance phenomena. *SoftwareX* **15**, 100763 (2021).
26. Zschiedrich, L. et al. Riesz-projection-based theory of light–matter interaction in dispersive nanoresonators. *Phys. Rev. A* **98**, 043806 (2018).
27. Pomplun, J., Burger, S., Zschiedrich, L. & Schmidt, F. Adaptive finite element method for simulation of optical nano structures. *Phys. Status Solidi B* **244**, 3419–3434 (2007).
28. Hohenester, U. & Trügler, A. MNPBEM—A Matlab toolbox for the simulation of plasmonic nanoparticles. *Comput. Phys. Commun.* **183**, 370–381 (2012).
29. Nikolova, N. K., Bandler, J. W. & Bakr, M. H. Adjoint techniques for sensitivity analysis in high-frequency structure CAD. *IEEE Trans. Microw. Theory Technol.* **52**, 403–419 (2004).
30. Burger, S., Zschiedrich, L., Pomplun, J., Schmidt, F. & Bodermann, B. Fast simulation method for parameter reconstruction in optical metrology. *Proc. SPIE* **8681**, 380–386 (2013).
31. Trefethen, L. N. & Weideman, J. A. C. The exponentially convergent trapezoidal rule. *SIAM Rev.* **56**, 385–458 (2014).
32. Koshelev, K. et al. Subwavelength dielectric resonators for nonlinear nanophotonics. *Science* **367**, 288–292 (2020).
33. Malitson, I. H. Interspecimen comparison of the refractive index of fused silica. *J. Opt. Soc. Am.* **55**, 1205–1209 (1965).
34. Sehmi, H. S., Langbein, W. & Muljarov, E. A. Optimizing the Drude–Lorentz model for material permittivity: Method, program, and examples for gold, silver, and copper. *Phys. Rev. B* **95**, 115444 (2017).
35. Binkowski, F. et al. Source code and simulation results for Computation of eigenfrequency sensitivities using Riesz projections for efficient optimization of nanophotonic resonators. Zenodo https://doi.org/10.5281/zenodo.6614951 (2022).

36. Pelikan, M., Goldberg, D. E. & Cantú-Paz, E. BOA: The Bayesian optimization algorithm. *GECCO'99: Proc. Gen. Ev. Comp. Conf.* **1**, 525 (1999).
37. Schneider, P.-I. et al. Benchmarking five global optimization approaches for nano-optical shape optimization and parameter reconstruction. *ACS Photonics* **6**, 2726–2733 (2019).

Author contributions

F.Bi., L.Z., and S.B. conceived and designed the research; F.Bi. and F.Be. performed the numerical simulations with input from M.H. and P.-I.S.; All authors discussed the results; F.Bi. wrote the manuscript with input from all authors.

Competing interests

The authors declare no competing interests.

Additional information

Supplementary information The online version contains supplementary material available at https://doi.org/10.1038/s42005-022-00977-1.

Correspondence and requests for materials should be addressed to Sven Burger.

Peer review information *Communications Physics* thanks Zhiyuan Fan and the other anonymous reviewer(s) for their contribution to the peer review of this work. Peer reviewer reports are available.

Reprints and permission information is available at http://www.nature.com/reprints

Publisher's note Springer Nature remains neutral with regard to jurisdictional claims in published maps and institutional affiliations.

7 Conclusion

Resonance phenomena are omnipresent in physics and their numerical modeling and simulation is essential for understanding wave propagation and interference effects. In nanophotonics, resonances are solutions to the time-harmonic source-free Maxwell's equations with loss mechanisms. The corresponding eigenproblems are non-Hermitian due to losses and they are typically nonlinear due to material dispersion. Computing the eigenmodes and eigenfrequencies and expanding the physical observable of interest into a weighted sum of eigenmodes is an instructive approach to obtain a deeper understanding of the physical properties of the underlying nanostructure. This understanding is essential for the design and optimization of nanophotonic devices.

In this thesis, we considered resonances arising in open material systems. In Chapter 2, we introduced a resonance expansion approach based on Riesz projections. The approach relies on spectral projection by contour integration where Maxwell's equations with a source term are solved for complex-valued frequencies lying on the integration contours. This allows for the resonance-based-investigation of arbitrary material systems since the material models can be directly evaluated for the given frequencies, which means that no linearization of the nonlinear eigenproblems is required. In Chapter 3, we demonstrated this property of the Riesz projection expansion, where a nonlocal material model is considered for the study of a nanowire with a diameter of only a few nanometers. In Chapter 4, we extended the Riesz projection expansion approach to optical far-field quantities, such as the energy flux density in the far field of a nanophotonic device. In Chapter 5, motivated by Riesz projection expansions, we developed a Riesz-projection-based method to compute physically relevant eigenfrequencies. Physically relevant means that the eigenfrequencies are relevant with respect to the resonance expansion of the physical observable of interest. The proposed method prioritizes such eigenfrequencies when multiple eigenfrequencies lie within the integration contour. In Chapter 6, based on this approach, we introduced a method to compute eigenfrequency sensitivities using Riesz projections. This method combines contour integration and direct differentiation for numerical implementations of Maxwell's equations enabling an efficient numerical realization. We used the proposed method to optimize an important figure of merit of a nanophotonic resonator, the Q-factor of a specific resonance, with respect to several shape parameters of the resonator.

We applied the Riesz projection expansion approaches developed in this thesis also in other works, for example, for the study of strong coupling in plasmonic resonators [100] and for the study of the Purcell factor of coupled eigenmodes [71]. In the eigensolver benchmark in Ref. [30], we compared the Riesz-projection-based method proposed in Chapter 5 with other methods for calculating eigenfrequencies and eigenmodes. The benchmark was performed in collaboration with several research groups from the field of computational nanophotonics. The results obtained using Riesz projections are in agreement with the results of the other methods. Recently, in Ref. [72], we exploited

Riesz projections to extend the resonance expansion approach given by Eq. (2.2) to quadratic and far-field quantities. This extension shares important properties with the previously proposed Riesz projection expansion given by Eq. (4.1), but is based on the direct computation of eigenmodes.

Riesz projections can be used to compute resonance expansions in a very elegant way. Any physical observable that can be derived from the electric field can be expanded in any material system, and the remainder of the expansion can be calculated by a single additional contour integral. The strength of the Riesz-projection-based approaches proposed in this thesis lies, in particular, in the possibility of combining resonance expansion and calculation of physically relevant eigenfrequencies and their sensitivities. This combination possibility is already demonstrated in our published software package RPExpand [101]. In both cases, the contour integrals are based on scattering problems in the form of Maxwell's equations with a physical source term, which can be exploited for an efficient numerical realization. This relation to physics is also the main difference to other contour integral methods for solving eigenproblems.

Further research on Riesz projection methods for nanophotonic problems is already being carried out. For example, in order to show the advantages and disadvantages of different resonance expansion approaches, a benchmark for resonance expansion is being developed. We also expect that approaches based on Riesz projections can be very useful in other areas of physics. It is planned to apply Riesz projections to investigate eigenmodes of quantum mechanical systems.

8 Appendix

In the appendix of this thesis, the three further individual works [69–71] of the doctoral candidate are presented, which are closely related to the thesis.

In Ref. [69], we review a linearization approach for nonlinear eigenproblems in the field of nanophotonics. In Ref. [70], we apply this approach to compute eigenmodes and eigenfrequencies of a system described by a quantum model combined with classical electromagnetic wave simulations. In Ref. [71], we use the linearization approach together with the Riesz projection expansion approaches for the investigation of the influence of interfering resonances on the Purcell enhancement of a dipole emitter placed in a nanodisk.

8.1 Linearization of resonance problems in dispersive material systems

For the investigation of resonance phenomena in nanophotonics, the linearization of the nonlinear eigenproblems given by Eq. (2.3) with an application of an eigensolver to the resulting linear eigenproblems is a common approach [30–32, 38]. The Arnoldi method [39] is often used for solving the linear eigenproblems. The nonlinearity of the eigenproblems is caused by the material dispersion and the corresponding models are often based on rational functions, as in the case of Drude-Lorentz models or rational fits to measured material data [36].

In Ref. [69], we report on a linearization approach based on modeling the permittivity by rational functions. The linearization introduces auxiliary fields increasing the dimension of the underlying problem. The computational effort for solving the linear eigenproblem increases with the number of introduced auxiliary fields, which depends on the order and number of the poles of the rational function.

In the following, Ref. [69] is reprinted, which is an open access article distributed under the terms of the Creative Commons CC BY license; [Felix Binkowski, Lin Zschiedrich, and Sven Burger. An auxiliary field approach for computing optical resonances in dispersive media. *J. Eur. Opt. Soc.-Rapid Publ.* 15, 3 (2019). DOI: 10.1186/s41476-019-0098-z.]

SHORT REPORT

Open Access

An auxiliary field approach for computing optical resonances in dispersive media

Felix Binkowski[1] ![ORCID], Lin Zschiedrich[2] ![ORCID] and Sven Burger[1,2*] ![ORCID]

Abstract

We report on an auxiliary field approach for solving nonlinear eigenvalue problems occurring in nano-optical systems with material dispersion. The material dispersion can be described by a rational function for the frequency-dependent permittivity, e.g., by a Drude-Lorentz model or a rational function fit to measured material data. The approach is applied to compute plasmonic resonances of a metallic grating.

Keywords: Maxwell's equations, Material dispersion, Nonlinear eigenvalue problems, Auxiliary field approach

Introduction

Detailed knowledge on the resonant states of nano-optical systems is essential for understanding the physical properties of the systems and for designing related photonic devices [1–3]. With numerical approaches it is possible to compute the resonant states, which are typically solutions to nonlinear eigenvalue problems (NLEVPs) arising from Maxwell's equations. The material dispersion described by the permittivity causes the nonlinearity of the eigenproblems. A multitude of numerical solution techniques are used for solving the NLEVPs, such as linearization, iterative projection methods and contour integral methods [4–6].

In nano-optics, linearization with physically derived auxiliary fields is a common approach [7–12]. In this work, we report on an auxiliary field approach based on modeling the permittivity with rational functions. We implement the approach using an iterative projection method. Motivated by scatterometry applications, the numerical realization is applied to compute resonant states of a metallic line grating.

Auxiliary field approach for dispersive nano-optical systems

In the steady-state regime, the resonant states of nano-optical systems satisfy the time-harmonic Maxwell's equations in a source-free medium, given in the second-order form by

*Correspondence: burger@zib.de
[1] Zuse Institute Berlin, Takustraße 7, 14195 Berlin, Germany
[2] JCMwave GmbH, Bolivarallee 22, 14050 Berlin, Germany

$$\nabla \times \mu(\mathbf{r}, \omega)^{-1} \nabla \times \mathbf{E}(\mathbf{r}, \omega) - \omega^2 \epsilon(\mathbf{r}, \omega)\mathbf{E}(\mathbf{r}, \omega) = 0, \quad (1)$$

where $\mathbf{E}(\mathbf{r}, \omega)$ is the electric field. The permittivity tensor $\epsilon(\mathbf{r}, \omega)$, depending on the complex angular frequency ω and the position $\mathbf{r}$, describes the material dispersion and the spatial distribution of materials. For optical frequencies, the permeability tensor $\mu(\mathbf{r}, \omega)$ typically equals the vacuum permeability μ_0. Equation 1 becomes a non-Hermitian problem in the presence of open boundary conditions or lossy materials.

To obtain a numerical solution to Eq. (1), we apply the finite element method (FEM) [13, 14]. This discretization technique leads to an algebraic NLEVP of the form

$$Au = \omega^2 B(\omega)u, \quad (2)$$

where $A, B(\omega) \in \mathbb{C}^{n \times n}$ are the system matrices, $\omega \in \mathbb{C}$ is an eigenvalue and $u \in \mathbb{C}^n$ is the corresponding eigenvector. The problem is nonlinear through the eigenvalue-dependence of the mass matrix $B(\omega)$, which is based on $\epsilon(\mathbf{r}, \omega)$. If the permittivity model $\epsilon(\mathbf{r}, \omega)$ is a rational function of the frequency with poles of order one, e.g., a Drude model [15] or a rational fit of measured material data, the matrix $B(\omega)$ has the form

$$B(\omega) = B_0 + \frac{1}{\omega - \omega_1}B_1 + \cdots + \frac{1}{\omega - \omega_N}B_N, \quad (3)$$

where $B_0, \ldots, B_N \in \mathbb{C}^{n \times n}$ are matrices resulting from the partial fraction decomposition and $\omega_1, \ldots, \omega_N \in \mathbb{C}$ are the poles of the rational function. Note that physical

dispersion models have to satisfy Kramers-Kronig relations to ensure causality.

To compute eigenvalues ω and corresponding eigenvectors u, an implementation of the shift-and-invert Arnoldi method is applied [16]. For this, the shifted eigenvalue $\tilde{\omega} = \omega - \sigma$, the shifted poles $\tilde{\omega}_i = \omega_i - \sigma, i = 1, \ldots, N$, and the auxiliary fields

$$u_0 = \frac{\omega}{\sigma} u, \qquad u_i = \frac{\omega}{\omega - \omega_i} u, \qquad i = 1, \ldots, N,$$

are defined, where σ is the chosen shift. As the matrices $B_1, \ldots, B_N$ have only non-zero entries for degrees of freedom of the discretization corresponding to the dispersive object, the auxiliary fields $u_1, \ldots, u_N$ can be restricted to this subset. However, for the sake of a simpler notation, we define them on the entire domain. Using the auxiliary fields with Eq. (3) to reformulate Eq. (2) yields

$$
\begin{bmatrix}
A & -\sigma^2 B_0 & -\sigma B_1 & -\sigma B_2 & \ldots & -\sigma B_N \\
-\sigma I & \sigma I & 0 & 0 & \ldots & 0 \\
\sigma I & 0 & \tilde{\omega}_1 I & 0 & \ldots & 0 \\
\sigma I & 0 & 0 & \ddots & \ddots & \vdots \\
\vdots & \vdots & \vdots & \ddots & \tilde{\omega}_{N-1} I & 0 \\
\sigma I & 0 & 0 & \ldots & 0 & \tilde{\omega}_N I
\end{bmatrix}
\begin{bmatrix}
u \\ u_0 \\ u_1 \\ u_2 \\ \vdots \\ u_N
\end{bmatrix}
$$

$$
= \tilde{\omega}
\begin{bmatrix}
0 & \sigma B_0 & B_1 & B_2 & \ldots & B_N \\
I & 0 & 0 & 0 & \ldots & 0 \\
-I & 0 & I & 0 & \ldots & 0 \\
-I & 0 & 0 & \ddots & \ddots & \vdots \\
\vdots & \vdots & \vdots & \ddots & I & 0 \\
-I & 0 & 0 & \ldots & 0 & I
\end{bmatrix}
\begin{bmatrix}
u \\ u_0 \\ u_1 \\ u_2 \\ \vdots \\ u_N
\end{bmatrix}, \qquad (4)
$$

where $I \in \mathbb{R}^{n \times n}$ is the identity matrix. This is a linear eigenvalue problem of the form

$$\tilde{A} \tilde{u} = \tilde{\omega} \tilde{B} \tilde{u}, \qquad (5)$$

where $\tilde{A}, \tilde{B}$ are augmented system matrices and $\tilde{u}$ is an augmented field containing the original eigenvector u and the auxiliary fields $u_0, \ldots, u_N$. The linear eigenvalue problem in Eq. (5) is solved by applying the Arnoldi method to

$$\tilde{A}^{-1} \tilde{B} \tilde{u} = \frac{1}{\tilde{\omega}} \tilde{u} \qquad (6)$$

assuming that $\tilde{u}$ is suitably scaled. The Arnoldi iteration typically converges to the largest eigenvalue, i.e., to the smallest shifted eigenvalue $\tilde{\omega} = \omega - \sigma$. Thus, the eigenvalue ω of the NLEVP in Eq. (2) which is closest to the shift σ is obtained. Note that the auxiliary field approach increases the dimension of the eigenvalue problem with the number of poles of the rational function.

Remark For the computation of the Krylov subspace

$$\mathcal{K}_m = \mathrm{span} \left\{ \tilde{v}, \tilde{A}^{-1} \tilde{B} \tilde{v}, \ldots, (\tilde{A}^{-1} \tilde{B})^{m-1} \tilde{v} \right\}$$

within the Arnoldi iteration for Eq. (6), the linear system $\tilde{A} \tilde{u} = \tilde{B} \tilde{v}$ is considered for the given input vector

$$\tilde{B} \tilde{v} = \left[f^T, f_0^T, f_1^T, \ldots, f_N^T \right]^T,$$

where $\tilde{v} \in \mathbb{C}^{(N+2)n}$ is an initial vector and $f, f_0, \ldots, f_N \in \mathbb{C}^n$. The first n rows in Eq. (4) with the initial vector $\tilde{v}$ for the right-hand side lead to

$$Au - \sigma^2 B_0 u_0 - \sigma B_1 u_1 - \cdots - \sigma B_N u_N = \tilde{\omega} f$$

and substitution of the auxiliary fields

$$
\begin{aligned}
u_0 &= \frac{\tilde{\omega}}{\sigma} f_0 + u, \\
u_i &= \frac{\tilde{\omega}}{\tilde{\omega}_i} f_i - \frac{\sigma}{\tilde{\omega}_i} u, \qquad i = 1 \ldots, N, \qquad (7)
\end{aligned}
$$

yields

$$
\begin{aligned}
\hat{A} u &= \left[A - \sigma^2 B_0 + \frac{\sigma^2}{\tilde{\omega}_1} B_1 + \cdots + \frac{\sigma^2}{\tilde{\omega}_N} B_N \right] u \\
&= \tilde{\omega} f + \tilde{\omega} \sigma \left[B_0 f_0 + \frac{1}{\tilde{\omega}_1} B_1 f_1 + \cdots + \frac{1}{\tilde{\omega}_N} B_N f_N \right] \\
&= \tilde{\omega} \hat{f}.
\end{aligned}
$$

Instead of solving the linear system $\tilde{A} \tilde{u} = \tilde{B} \tilde{v}$ to generate the Krylov subspace $\mathcal{K}_m$, the system $\hat{A} u = \tilde{\omega} \hat{f}$ is solved yielding u and Eq. (7) is used to achieve $u_0, \ldots, u_N$.

This approach has the advantage that the matrix $\hat{A}$ is equal to the matrix which is considered for solving Maxwell's equations in presence of a source. Such a scattering problem has the form

$$\left[A - \omega^2 B(\omega) \right] u_{\mathrm{sc}} = s(\omega),$$

where $s(\omega)$ is a source term. Setting $\omega = \sigma$ yields $\hat{A} = \left[A - \sigma^2 B(\sigma) \right]$. Thus, the implementation of a scattering solver can also be used in the framework of solving eigenproblems.

Application to metallic grating

The presented approach is applied to a line grating consisting of gold struts surrounded by air. We revisit an experimentally realized setup supporting plasmonic resonances [17]. This system has been recently numerically investigated [18]. The geometry is sketched in Fig. 1. Grating structures are of interest in, e.g., scatterometry. It has been proposed to employ the resonant states of gratings for increasing the sensitivity in measurements of their spatial dimensions [19].

We apply the auxiliary field approach using the FEM solver JCMsuite to compute the resonant state which corresponds to an absorption peak near the wavelength $\lambda = 650$ nm [18]. For the relative permittivity of the gold grating, a one-pole Drude model
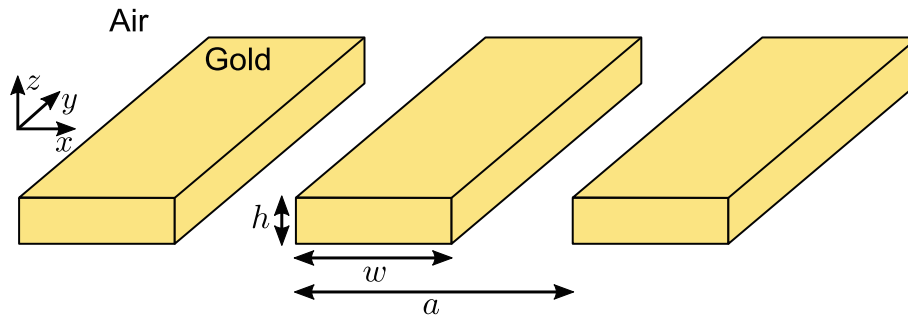
Fig. 1 Sketch of a line grating consisting of gold surrounded by air. The structure is periodic in *x* direction and infinitely extended in *y* direction. The period is $a = 482.5$ nm, the rod width is $w = 347.5$ nm and the rod height is $h = 130$ nm

$$\epsilon_r(\omega) = 1 - \frac{\omega_p^2}{\omega^2 + i\gamma\omega}$$

is considered, where $\omega_p = 1.26\text{e}{+}16\,\text{s}^{-1}$ is the plasma frequency and $\gamma = 1.41\text{e}{+}14\,\text{s}^{-1}$ is the damping coefficient. The permittivity is then given by $\epsilon(\omega) = \epsilon_0\epsilon_r(\omega)$, where ϵ_0 is the vacuum permittivity. The chosen shift is $\sigma = 2\pi c/(650\,\text{nm})$, where c is the speed of light. Different finite element degrees $p = 1,\ldots,6$ and a fixed mesh containing about $1\text{e}{+}03$ triangles are applied. Corners are a known issue considering systems containing metals. To deal with the occurring field singularities at the corners, refinements with a minimum edge length of about 0.016 nm are used. Bloch boundary conditions with a Bloch vector of $[2\pi/(5a), 0, 0]$ enforce the periodicity in x direction. To realize the open boundary conditions in z direction, perfectly matched layers (PMLs) are used. Convergence of the PML method is ensured by applying an adaptive numerical realization of the PML method [13]. The relative error of the eigenvalue ω is shown in Fig. 2,

where the reference solution ω_{ref} is the eigenvalue computed with $p = 6$. Convergence to the reference solution is observed. For the finite element degree $p = 5$, the eigenvalue $\omega = 2\pi c/(649.1397576 + 11.0601049i\,\text{nm} \pm (6.2\text{e}{-}06 + 1.5\text{e}{-}06i\,\text{nm}))$ is obtained.

In order to validate the results of the auxiliary field approach, eigenvalues are calculated using a fixed-point iteration. The same shift $\sigma = 2\pi c/(650\,\text{nm})$ as before is used to initialize the mass matrix $B(\sigma)$. Equation 2 becomes linear and is solved with the shift-and-invert Arnoldi method. The resulting eigenvalue ω_{iter} is then used to update $B(\omega_{\text{iter}})$ and to repeat the procedure until ω_{iter} does not change up to a chosen tolerance. In Table 1, the relative difference between the results from the auxiliary field approach, denoted by ω, and the results from the fixed-point iteration, denoted by ω_{iter}, are shown. An abort condition for the fixed-point iteration with a tolerance of $1\text{e}{-}08$ is chosen for the real and imaginary parts of ω_{iter}. This leads to about 10 iterations. For all finite element degrees $p = 1,\ldots,5$, matching results for the two
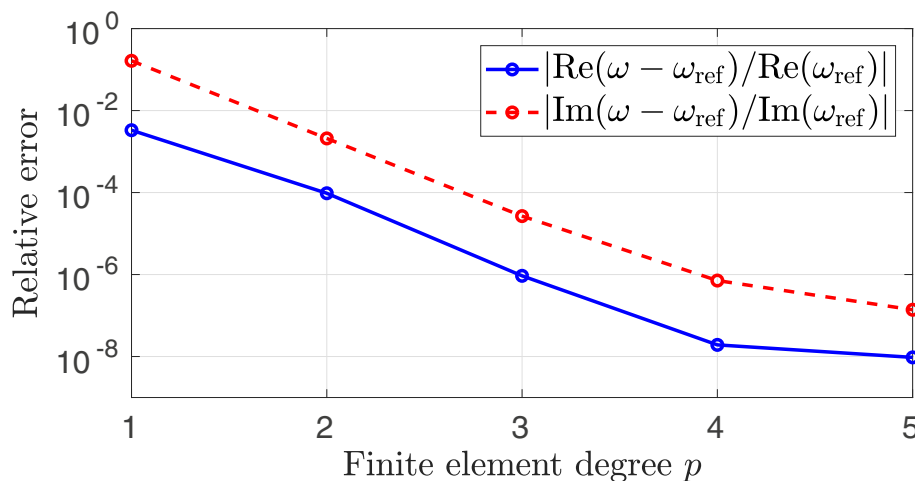
Fig. 2 Convergence of the eigenvalue. Relative error of the eigenvalue computed with the auxiliary field approach with respect to the numerical resolution. The reference solution ω_{ref} is computed with the finite element degree $p = 6$

Table 1 Comparison of eigenvalues computed with the auxiliary field approach and with the fixed-point iteration, denoted by ω and ω_{iter}, respectively

p	$\frac{\text{Re}(\omega-\omega_{iter})}{\text{Re}(\omega_{iter})}$	$\frac{\text{Im}(\omega-\omega_{iter})}{\text{Im}(\omega_{iter})}$
1	6.6e−13	1.2e−10
2	1.0e−12	4.1e−10
3	9.9e−13	4.0e−10
4	9.4e−13	4.1e−10
5	9.3e−13	4.0e−10

approaches with a relative difference smaller than 4.1e−10 are obtained.

Conclusions

We have reported on an approach for computing eigensolutions to Maxwell's equations in dispersive media. Auxiliary fields are used to linearize the corresponding NLEVP. The resulting linear eigenvalue problem is then solved with the shift-and-invert Arnoldi method. The approach has been applied to a metallic line grating and the results for the eigenvalues have been validated by an implementation of a fixed-point iteration.

Authors' contributions
LZ implemented the numerical method. FB and SB performed the numerical experiments. FB wrote the manuscript with input from all authors. All authors read and approved the final manuscript.

Competing interests
The authors declare that they have no competing interests.

Publisher's Note
Springer Nature remains neutral with regard to jurisdictional claims in published maps and institutional affiliations.

References
1. Zworski, M.: Resonances in physics and geometry. Not. Amer. Math. Soc. **46**, 319–328 (1999)
2. Novotny, L., Hecht, B.: Principles of Nano-Optics. 2nd Ed. Cambridge University Press, Cambridge (2012)
3. Lalanne, P., Yan, W., Vynck, K., Sauvan, C., Hugonin, J.-P.: Light Interaction with Photonic and Plasmonic Resonances. Laser Photonics Rev. **12**, 1700113 (2018)
4. Tisseur, F., Meerbergen, K.: The Quadratic Eigenvalue Problem. SIAM Rev. **43**, 235–286 (2001)
5. Mehrmann, V., Voss, H.: Nonlinear eigenvalue problems: a challenge for modern eigenvalue methods. GAMM Mitt. **27**, 121–152 (2005)
6. Güttel, S., Tisseur, F.: The Nonlinear Eigenvalue Problem. Acta Numer. **26**, 1–94 (2017)
7. Joseph, R. M., Hagness, S. C., Taflove, A.: Direct time integration of Maxwell's equations in linear dispersive media with absorption for scattering and propagation of femtosecond electromagnetic pulses. Opt. Lett. **16**, 1412–1414 (1991)
8. Tip, A.: Linear absorptive dielectrics. Phys. Rev. A. **57**, 4818–4841 (1998)
9. Raman, A., Fan, S.: Photonic Band Structure of Dispersive Metamaterials Formulated as a Hermitian Eigenvalue Problem. Phys. Rev. Lett. **104**, 087401 (2010)
10. Brûlé, Y., Gralak, B., Demésy, G.: Calculation and analysis of the complex band structure of dispersive and dissipative two-dimensional photonic crystals. J. Opt. Soc. Am. B. **33**, 691–702 (2016)
11. Yan, W., Faggiani, R., Lalanne, P.: Rigorous modal analysis of plasmonic nanoresonators. Phys. Rev. B. **97**, 205422 (2018)
12. Demésy, G., Nicolet, A., Gralak, B., Geuzaine, C., Campos, C., Roman, J. E.: Eigenmode computations of frequency-dispersive photonic open structures: A non-linear eigenvalue problem. arXiv:1802.02363v2 (2018)
13. Zschiedrich, L., Burger, S., Kettner, B., Schmidt, F.: Advanced finite element method for nano-resonators. Proc. SPIE. **6115**, 611515 (2006)
14. Weiser, M.: Inside Finite Elements. De Gruyter, Berlin (2016)
15. Jackson, J. D.: Classical Electrodynamics. 3rd Ed. Wiley, New York (1998)
16. Saad, Y.: Numerical Methods for Large Eigenvalue Problems. 2nd Ed. SIAM, Philadelphia (2011)
17. Collin, S., Vincent, G., Haïdar, R., Bardou, N., Rommeluère, S., Pelouard, J.-L.: Nearly Perfect Fano Transmission Resonances through Nanoslits Drilled in a Metallic Membrane. Phys. Rev. Lett. **104**, 027401 (2010)
18. Lalanne, P., Yan, W., Gras, A., Sauvan, C., Hugonin, J.-P., Besbes, M., Demésy, G., Truong, M. D., Gralak, B., Zolla, F., Nicolet, A., Binkowski, F., Zschiedrich, L., Burger, S., Zimmerling, J., Remis, R., Urbach, P., Liu, H. T., Weiss, T.: Quasinormal mode solvers for resonators with dispersive materials. arXiv:1811.11751v1 (2018)
19. Wurm, M., Endres, J., Probst, J., Schoengen, M., Diener, A., Bodermann, B.: Metrology of nanoscale grating structures by UV scatterometry. Opt. Express. **25**, 2460–2468 (2017)

8.2 Combining quantum and classical models for emitter-resonator systems

When light is absorbed at metal surfaces, individual electrons can be released from the surfaces. Resonance effects can significantly enhance this quantum effect due to the resulting highly localized electromagnetic field energies at the surfaces. The so-called hot electrons can be transferred from the surfaces to adjacent semiconductors and then be used in, e.g., photocatalytic processes [7, 102–104].

In Ref. [70], we investigate a nanoresonator on a metal surface and study the generation of hot electrons due to a resonance effect resulting from an excitation of a resonance by a dipole emitter. We show how to combine a quantum model with classical electromagnetic wave simulations to compute the hot electron generation rate. For the classical wave simulations, the scattered electric field at the metal surface is computed by solving Maxwell's equation given by Eq. (2.1). It can be observed that the generation rate is overestimated when the dipole emitter is very close to the metal surface. To account for this, we correct the underlying material model, given by a Drude-Lorentz model, with respect to the surface response caused by the generation of hot electrons. The results are explained by analyzing the resonances of the nanoresonator, where the eigenmodes and eigenfrequencies are computed by the linearization approach presented in Section 8.1.

In the following, Ref. [70] is reprinted with permission from [Felix Binkowski, Tong Wu, Philippe Lalanne, Sven Burger, and Alexander O. Govorov. Hot electron generation through near-field excitation of plasmonic nanoresonators. *ACS Photonics* 8, 1243 (2021). DOI: 10.1021/acsphotonics.1c00231.] Copyright 2021 American Chemical Society. ACS Articles on Request link.

Article

Hot Electron Generation through Near-Field Excitation of Plasmonic Nanoresonators

Felix Binkowski, Tong Wu, Philippe Lalanne, Sven Burger,* and Alexander O. Govorov

Cite This: *ACS Photonics* 2021, 8, 1243−1250

Read Online

ACCESS | Metrics & More | Article Recommendations

ABSTRACT: We theoretically study hot electron generation through the emission of a dipole source coupled to a nano-resonator on a metal surface. In our hybrid approach, we solve the time-harmonic Maxwell's equations numerically and apply a quantum model to predict the efficiency of hot electron generation. Strongly confined electromagnetic fields and the strong enhancement of hot electron generation at the metal surface are predicted and are further interpreted with the theory of quasinormal modes. In the investigated nanoresonator setup, both the emitting source and the acceptor resonator are localized in the same volume, and this configuration looks promising to achieve high efficiencies of hot electron generation. By comparing with the efficiency calculated in the absence of the plasmonic nanoresonator, that is, the dipole source is located near a flat, unstructured metal surface, we show that the effective excitation of the modes of the nanoresonator boosts the generation efficiency of energetic charge carriers. The proposed scheme can be used in tip-based spectroscopies and other optoelectronic applications.

KEYWORDS: hot electron generation, localized light source, near-field excitation, plasmonic nanoresonators
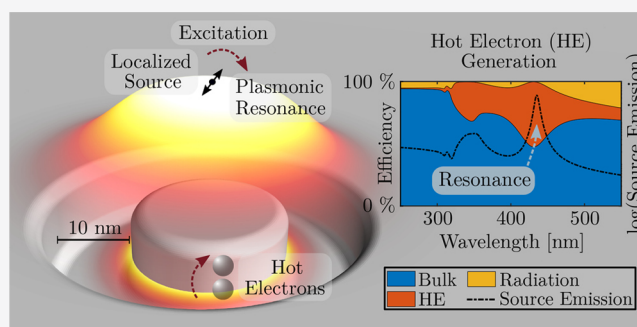
Light−matter interactions in metal nanostructures can be strongly enhanced by plasmonic resonance effects.[1,2] Hot electron generation, which attracted significant attention in recent years,[3−10] is one important effect resulting from the absorption of plasmons by metal surfaces. With this effect, visible light can be harvested and its energy can be transferred to an adjacent semiconductor, where the energy can then be used for photocatalytic processes.[11] The impact of morphology and materials on local field enhancement and hot electron generation is typically investigated in setups with illumination from the far field, for example, solar illumination and other macroscopic illumination settings.[12−14] However, there are also various types of localized light sources accessible, such as plasmonic tips, single molecules, quantum wells, or quantum dots,[15−17] which have so far not been considered for the generation of excited charge carriers.

The efficiency of hot electron generation in metal nanostructures depends on the magnitude of the electric fields in the vicinity of the nanostructures.[5] Nanofabrication technologies allow fabrication of plasmonic nanoresonators of various shape and characteristic size well below 100 nm,[18] which enables light confinements at the nanometre scale: The plasmonic resonances of the deep-subwavelength resonators can be efficiently excited by localized emitters resulting in highly localized electromagnetic fields at the metal surfaces.[19,20] For the design and optimization of nanophotonic devices based on emitter-resonator excitations, modal

approaches are a common theoretical tool.[21] The localized surface plasmon resonances of the systems, which are quasinormal modes (QNMs),[21,22] are electromagnetic field solutions to the time-harmonic source-free Maxwell's equations. The corresponding resonance problems are solved numerically,[23] and the solutions allow to obtain insights into the physical properties of the nanophotonic devices.

In this work, we investigate hot electron generation with a localized emitter placed in the near field of a metal nanostructure. In particular, we numerically study a circular nanogroove resonator on a silver surface with a characteristic size of ∼40 nm and compare the efficiency of hot electron generation in the presence and absence of the nanoresonator. We compute and analyze the hot electron generation with a quantum model assisted by full-wave simulations and further investigate the impact of geometrical parameters. We numeri-cally demonstrate that the excited localized resonance of the nanoresonator leads to an enhancement of the hot electron
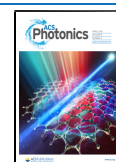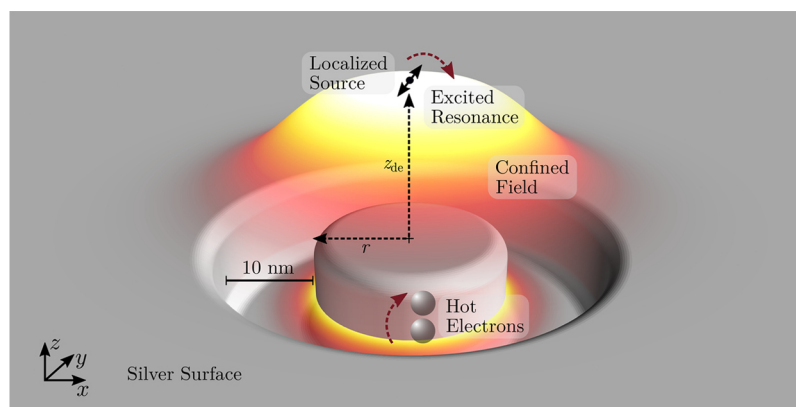
Figure 1. Circular nanogroove resonator with radius r on a silver surface interacting with a localized emitter placed at the dipole-to-surface distance z_{de}. The sketched electric field intensity $|\tilde{\mathbf{E}}|^2$ corresponds to an excited localized surface plasmon resonance. Placing a dipole emitter close to the metal surface leads to hot electron generation. The coupling of the emitter with the resonance yields high electric field values localized at the nanogroove, which enhances the efficiency of hot electron generation.

generation efficiency of more than 1 order of magnitude compared to the flat surface.

◼ EXCITATION OF PLASMONIC RESONANCES WITH LOCALIZED EMITTERS

Theoretical Background and Numerical Methods. In nano-optics, in the steady-state regime, the electric fields $\mathbf{E}(\mathbf{r}, \omega_0) \in \mathbb{C}^3$ resulting from a source field are solutions to the time-harmonic Maxwell's equations in second-order form,

$$\nabla \times \mu^{-1} \nabla \times \mathbf{E}(\mathbf{r}, \omega_0) - \omega_0^2 \epsilon(\mathbf{r}, \omega_0) \mathbf{E}(\mathbf{r}, \omega_0) = i\omega_0 \mathbf{J}(\mathbf{r}) \tag{1}$$

where $\omega_0 \in \mathbb{R}$ is the angular frequency, $\mathbf{r}$ is the spatial position, and $\mathbf{J}(\mathbf{r}) \in \mathbb{C}^3$ is the electric current density corresponding to the source. The source field for a localized source can be modeled by a dipole source $\mathbf{J}(\mathbf{r}) = \mathbf{j}\delta(\mathbf{r} - \mathbf{r}')$, where $\delta(\mathbf{r} - \mathbf{r}')$ is the delta distribution, $\mathbf{r}'$ is the position of the emitter, and $\mathbf{j}$ is the dipole amplitude vector. In the optical regime, the permeability tensor μ typically equals the vacuum permeability μ_0. The permittivity tensor $\epsilon(\mathbf{r}, \omega_0)$ describes the spatial distribution of material and the material dispersion.

We investigate a dipole emitter placed close to a nanoresonator. The nanoresonator is a circular slit on a silver surface with a depth and width of 10 nm. The structure has corner roundings with a radius of 2 nm. Figure 1 shows a sketch of the geometry of the resonant system. The dipole emitter is polarized parallel to the z direction and located on axis above the central nanocylinder at a separation distance z_{de} of the metal surface. For clearly separating the effect of localized resonances supported by the circular nanogroove resonator, we also investigate a second setup: A localized source is placed at z_{de} above a flat, unstructured silver surface. In both cases, the permittivity of the silver material is described by a generalized Drude−Lorentz model resulting from a rational fit[24,25] to experimental data,[26] see Table 1. For the investigations, we choose a spectral region in the optical regime, 200 nm $\leq \lambda_0 \leq$ 700 nm, with the wavelength $\lambda_0 = 2\pi c/\omega_0$.

To numerically analyze the dipole emitter interacting with the nanoresonator and with the flat surface, we use the finite element method. Scattering and resonance problems are solved by applying the solver JCMsuite.[27] The solver employs a subtraction field approach for localized sources, adaptive

Table 1. Permittivity Model for Silver[a]

k	Ω_k (eV)	σ_k (eV)
1	$3.9173 - 0.06084i$	$0.09267 + 0.01042i$
2	$3.988 - 0.04605i$	$-0.0015342 - 0.062233i$
3	$4.0746 - 0.63141i$	$1.4911 + 0.40655i$
4	$4.6198 - 2.8279i$	$4.2843 + 4.2181i$

[a]Poles Ω_k and amplitudes σ_k for the generalized Drude−Lorentz model[24] $\epsilon_{metal,bulk}(\omega_0) = \epsilon_0(\epsilon_\infty - \omega_p^2/(\omega_0^2 + i\gamma_D\omega_0)) + \epsilon_0\sum_{k=1}^4[i\sigma_k/(\omega_0 - \Omega_k) + i\sigma_k^*/(\omega_0 + \Omega_k^*)]$, where ϵ_0 is the vacuum permittivity, $\epsilon_\infty = 0.77259$, $\gamma_D = 0.02228$ eV, and $\omega_p = 9.1423$ eV.

meshing, higher order polynomial ansatz functions, and allows to exploit the rotational symmetry of the geometry.[28]

Quasinormal Mode Analysis. When a localized emitter is placed close to a nanostructure, then the optical properties of the system are determined by its underlying resonances. Localized surface plasmon resonances, which are QNMs of the system, are one important resonance phenomena. Figure 1 contains a sketch of a QNM of the nanoresonator which is investigated in this study. QNMs are solutions to eq 1 with outgoing wave conditions and without a source field, that is, $\mathbf{J}(\mathbf{r}) = 0$. We denote the electric and magnetic field distributions of a QNM by $\tilde{\mathbf{E}}(\mathbf{r})$ and $\tilde{\mathbf{H}}(\mathbf{r})$, respectively. The QNMs are characterized by complex eigenfrequencies $\tilde{\omega} \in \mathbb{C}$ with negative imaginary parts. The quality factor Q of a resonance,

$$Q = \frac{\text{Re}(\tilde{\omega})}{-2\text{Im}(\tilde{\omega})}$$

describes its spectral confinement and quantifies the relation between the stored and the dissipated electromagnetic field energy. In the following section, we investigate how hot electron generation can be increased by the excitation of localized resonances. The physical intuition behind this effect is the following: When a localized source radiating at the frequency ω_0 efficiently couples to a localized resonance, that is, it is spectrally ($\omega_0 \approx \text{Re}(\tilde{\omega})$) and spatially matched with the resonance, then a large electric field $\mathbf{E}(\omega_0, \mathbf{r})$ around the nanoresonator can be induced by the source. At the resonance frequency $\omega_0 = \text{Re}(\tilde{\omega})$, the induced field intensity $|\mathbf{E}(\omega_0, \mathbf{r})|^2$ is proportional to Q^2, which can significantly enhance the hot electron generation. Note that $|\mathbf{E}(\omega_0, \mathbf{r})|^2$ is also proportional

to $(\mathrm{Re}(1/\tilde{V}))^2$, where $\tilde{V}$ is the mode volume[29] describing the spatial confinement of the electromagnetic field of a resonance.

In the optical regime, the circular nanogroove resonator sketched in Figure 1 supports one dominant localized resonance. The resonance wavelength $\tilde{\lambda} = \mathrm{Re}(2\pi c/\tilde{\omega})$ decreases with an increasing circular slit radius r, see Figure 2a. Figure 2b shows Q, depending on r, where $Q = 120$ can be
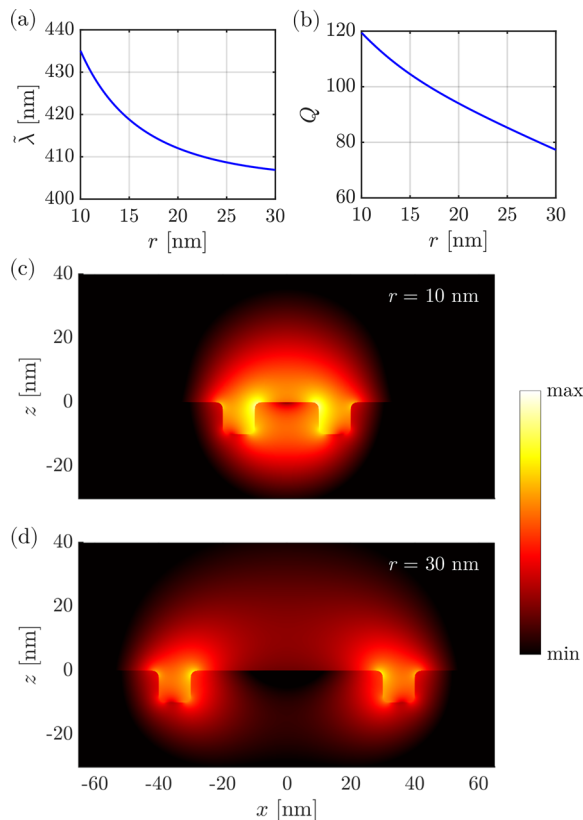
Figure 2. Simulations of the circular nanogroove resonator supporting one dominant localized resonance in the spectral region of visible light. The associated QNM and its eigenfrequency $\tilde{\omega}$ depend on the radius r of the nanoresonator. The permittivity model $\epsilon_{\mathrm{metal,bulk}}$ given in Table 1 is used. (a, b) Resonance wavelength $\tilde{\lambda} = \mathrm{Re}(2\pi c/\tilde{\omega})$ and quality factor Q of the dominant QNM, respectively. (c) Log-plot (a.u.) of the electric field intensity $|\tilde{\mathbf{E}}|^2$ corresponding to the dominant QNM of the nanoresonator with $r = 10$ nm. The QNM is normalized[29] such that $\int_\Omega \left[\tilde{\mathbf{E}} \cdot \frac{\partial \omega \epsilon}{\partial \omega} \tilde{\mathbf{E}} - \mu_0 \tilde{\mathbf{H}} \cdot \tilde{\mathbf{H}} \right] \mathrm{d}V = 1$, that is, the map allows a direct estimation and visual comparison of the interaction strength of the mode with point-like unpolarized dipoles. The corresponding eigenfrequency is $\tilde{\omega} = (4.330 - 0.018i) \times 10^{15}$ s^{-1} and the resonance wavelength is $\tilde{\lambda} = 435$ nm. (d) Log-plot of the electric field intensity of the normalized QNM corresponding to the circular nanogroove resonator with $r = 30$ nm.

observed for $r = 10$ nm. Note that, for smaller radii, due to the decreasing radiation loss, the quality factor would increase further. However, we restrict the investigations to $r \geq 10$ nm. Figure 2c shows the electric field intensity of the dominant resonance for $r = 10$ nm. The resonance is strongly localized at the circular slit and is characterized by high electric field values inside and close to the metal. Figure 2d shows the electric field intensity of the dominant resonance for $r = 30$ nm. It can be observed that, in comparison to the resonance for $r = 10$ nm, the electric field intensity becomes smaller at the metal surface. The ratio between stored and dissipated electromagnetic field

energy decreases with an increasing radius. For the following investigations, we consider the circular nanogroove resonator shown in Figure 2c, which has a radius of $r = 10$ nm and a quality factor of $Q = 120$.

Dipole Emission and Absorption. To quantify the interaction of the circular nanogroove resonator with a dipole emitter close to the resonator, we investigate the total power emitted by the dipole, which is also called dipole emission. The dipole emission can be computed by

$$p_{\mathrm{de}}(\omega_0) = -\frac{1}{2}\mathrm{Re}(\mathbf{E}^*(\mathbf{r}', \omega_0) \cdot \mathbf{j})$$

where $\mathbf{E}^*(\mathbf{r}, \omega_0)$ is the complex conjugate of the electric field, $\mathbf{r}'$ is the position of the emitter, and $\mathbf{j}$ is the dipole amplitude vector. The electric field $\mathbf{E}(\mathbf{r}, \omega_0)$ is computed by solving eq 1 with a dipole source.

Based on the modal results from the previous subsection, we place the dipole emitter at $z_{\mathrm{de}} = 20$ nm, which is in a spatial region of high electric field intensity of the dominant resonance shown in Figure 2c. In this way, the localized resonance of the circular nanogroove resonator has a significant influence on the emission properties of the dipole emitter. Figure 3a shows the dipole emission $p_{\mathrm{de}}(\lambda_0)$. In the
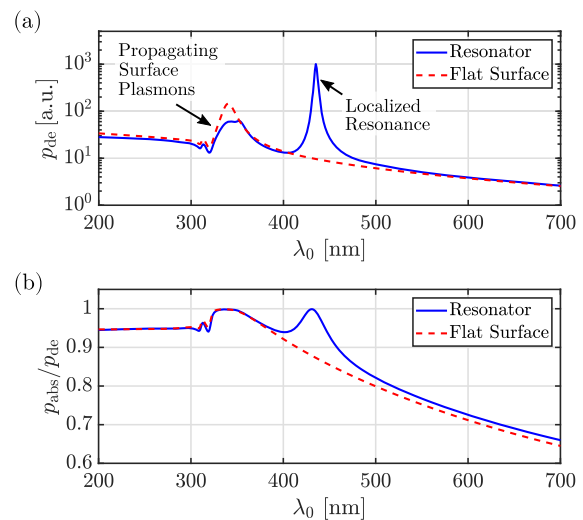
Figure 3. Simulations of dipole emission and normalized absorption for a localized source placed at the dipole-to-surface distance $z_{\mathrm{de}} = 20$ nm. Investigation for the circular nanogroove resonator with $r = 10$ nm and comparison to a flat surface. The permittivity model $\epsilon_{\mathrm{metal,bulk}}$ given in Table 1 is used. (a) Dipole emission p_{de}. (b) Normalized absorption in metal $p_{\mathrm{abs}}/p_{\mathrm{de}}$.

case of the nanoresonator, the spectrum is characterized by two significant maxima, which are based on different resonance effects: The dipole emitter couples to the dominant localized resonance with the resonance wavelength $\tilde{\lambda} = 435$ nm and it couples also to a continuum of surface plasmons, which are propagating on the metal surface. As expected, the propagating surface plasmons occur not only in the presence of the nanoresonator, but also in the case of the flat surface. Their high density of states give rise to a peak in the spectrum between $\lambda_0 = 300$ nm and $\lambda_0 = 400$ nm, as indicated in Figure 3a, where the coupling of the dipole emitter to the propagating surface plasmons is stronger in absence of the nanoresonator.

It can be expected that, for the investigated systems, all energy that is not radiated into the upper hemisphere is

absorbed by the metal. Therefore, the total absorbed energy can be computed using the expression

$$p_{\text{abs}}(\omega_0) = p_{\text{de}}(\omega_0) - p_{\text{rad}}(\omega_0)$$

The dipole emission radiated into the upper hemisphere, $p_{\text{rad}}(\omega_0)$, is computed by a near-field to far-field transformation and an integration of the Poynting vector over the upper hemisphere. Figure 3b shows the absorption $p_{\text{abs}}(\lambda_0)$ normalized by the dipole emission $p_{\text{de}}(\lambda_0)$ for $z_{\text{de}} = 20$ nm. It can be observed that, close to the wavelength of the localized resonance, most of the energy is absorbed. As the presence of the nanoresonator increases the electromagnetic field energy in the metal, the system with the nanoresonator leads to a higher absorption efficiency than the system with the flat surface.

To summarize, the simulations in this subsection show that a localized source can efficiently excite localized resonances supported by a nanoresonator, as well as propagating surface plasmons on flat metal surfaces. In the following section, it is shown that especially excited localized resonances can have a significant impact on the rate at which hot electrons can be generated in our model system.

■ HOT ELECTRON GENERATION

Theoretical Background. Considering quantum surface effects in plasmonics, one should start from an elegant theory by Feibelman developed to describe a surface plasmon dispersion in metals.[30,31] The so-called Feibelman's *d*-parameters characterize the dispersion and damping of the surface plasmon mode beyond the classical electromagnetic theory. Furthermore, it was discovered that the plasmon excitations in small nanoparticles experience an additional damping mechanism, the so-called surface-scattering decay.[32] In this quantum mechanism, collective plasmon excitations turn into hot electrons due to scattering at the surfaces.[33–38] A full kinetic picture of the plasmon excitation in a nanostructure involves both low-energy "Drude" electrons forming the coherent plasmon oscillation and the energetic (hot) electrons generated through the surface-assisted Kreibig's mechanism.[39] The low-energy excitations, regarded above as Drude electrons, can also be derived directly from the quasi-classical theory based on the Boltzmann equation.[40,41] Another related work, which should be mentioned here, is the theory of hot electron photocurrents generated at metal—semiconductor interfaces.[42–45] In our approach, we combine some of the quantum formalisms mentioned above[33,38,39,45] with the classical formalism of computing the electromagnetic fields at the surfaces by solving Maxwell's equations. The theoretical treatment below, which incorporates the surface-assisted generation of hot electrons, is very convenient since it allows to investigate nanostructures with arbitrarily complex shapes, in which hot-spot and shape effects determine the formation of plasmonic modes. We note that our formalism does not include a bulk mechanism of hot electron generation due to the electron—phonon scattering.[46] However, such a phonon-assisted channel should not play a dominant role in relatively small nanostructures where plasmonic mode sizes are less than 40 nm.[46] In our case, the groove size of the nanostructure is just 10 nm, and we expect that the leading mechanism is the surface-assisted hot electron generation. Another argument for the importance of the surface-generated hot electrons is that those carriers are created at the surface and, therefore, can be

transferred to surface acceptor states for photochemistry or for other detection methods.

Quantum Efficiency of Hot Electron Generation. The rate of energy dissipation based on the generation of hot electrons at a surface is given by[47]

$$p_{\text{he}}(\omega_0) = \frac{1}{2\pi^2} \frac{e^2 E_F^2}{\hbar} \frac{1}{(\hbar\omega_0)^2} \int_S \left| \mathbf{E}_n(\mathbf{r}, \omega_0) \right|^2 \, dS \tag{2}$$

where e is the elementary charge, E_F is the Fermi energy, and $\hbar$ is the reduced Planck constant. The normal component of the electric field $\mathbf{E}_n(\mathbf{r}, \omega_0)$ is integrated over the surface S. For a detailed derivation of eq 2, the reader is referred to ref 47.

The quantum dissipation $p_{\text{he}}(\omega_0)$ is based on optically induced quantum transitions of electrons near to the surface: The energy of photons can be transferred to the electrons because of breaking of linear momentum conservation. This surface scattering effect can be accounted for by a phenomenological approach for metal nanostructures.[34,37,38] An additional damping mechanism with the quantum decay parameter γ_s is incorporated in the material model,

$$\epsilon(\omega_0) = \epsilon_{\text{metal,bulk}}(\omega_0) + \epsilon_0 \frac{\omega_p^2}{\omega_0(\omega_0 + i\gamma_D)} - \epsilon_0 \frac{\omega_p^2}{\omega_0(\omega_0 + i(\gamma_D + \gamma_s))} \tag{3}$$

where $\epsilon_{\text{metal,bulk}}(\omega_0)$ is the permittivity model for the metal bulk material, and ω_p and γ_D are the plasma frequency and the damping constant from the Drude model, respectively, see Table 1. The quantum decay parameter γ_s describes the broadening due to the scattering of electrons at the surface. For the calculation of γ_s, we consider the total absorption power in a metal nanostructure, given by $p_{\text{abs}} = \text{Im}(\epsilon(\omega_0))\frac{\omega_0}{2}\int_V \mathbf{E}\cdot\mathbf{E}^* \, dV$, where $\epsilon(\omega_0)$ is the permittivity model from eq 3. It is assumed that $\omega_0^2 \gg (\gamma_D + \gamma_s)^2$, which holds for typical cases in nanophotonics. Applying the resulting simplification $\text{Im}(\epsilon(\omega_0)) \approx \text{Im}(\epsilon_{\text{metal,bulk}}(\omega_0)) + \epsilon_0 \frac{\omega_p^2 \gamma_s}{\omega_0^3}$ and splitting the absorption power p_{abs} into contributions corresponding to bulk and surface effects yield, in particular, the surface-scattering term $p_s = \epsilon_0 \frac{\omega_p^2 \gamma_s}{\omega_0^3} \frac{\omega_0}{2} \int_V \mathbf{E}\cdot\mathbf{E}^* \, dV$.[37,38] This term can be also computed using eq 2. The equation $p_{\text{he}} = p_s$ can be transformed and allows to compute the quantum decay parameter γ_s. A corresponding numerical iterative approach is given by[38]

$$\gamma_{s,n} = \frac{3}{4}\nu_F \frac{\int_S \left| \mathbf{E}_n(\mathbf{r}, \omega_0, \gamma_{s,n-1}) \right|^2 \, dS}{\int_V \mathbf{E}(\mathbf{r}, \omega_0, \gamma_{s,n-1})\cdot\mathbf{E}^*(\mathbf{r}, \omega_0, \gamma_{s,n-1}) \, dV}, \quad n = 0, 1, \dots \tag{4}$$

where $\gamma_{s,0} = 0$, ν_F is the Fermi velocity, and the electric fields are computed by solving eq 1 numerically, and subsequently, they are integrated over the surface S and the volume V of the considered nanostructure. For the computation of the electric fields within the iteration, the material model given by eq 3 is used. Note that, for $\gamma_{s,0} = 0$, we obtain $\epsilon(\omega_0) = \epsilon_{\text{metal,bulk}}(\omega_0)$ as used for the calculations for the optical problem in the previous section. We further note that a formalism for $\gamma_{s,n}$ can also be derived without the assumption $\omega_0^2 \gg (\gamma_D + \gamma_s)^2$.[38]

The consideration of the quantum decay parameter $\gamma_{s,n}$ is equivalent of solving a self-consistent quantum-classical formalism which fully accounts for the change of the surface response caused by the generation of hot electrons. With this

approach, the total power emitted by a dipole can be expressed as

$$p_{de}(\omega_0) = p_{abs,bulk}(\omega_0) + p_{he}(\omega_0) + p_{rad}(\omega_0)$$

where $p_{abs,bulk}(\omega_0)$ is the absorption in the metal bulk. We define the quantum efficiency of hot electron generation as the ratio $\eta_{he}(\omega_0) = p_{he}(\omega_0)/p_{de}(\omega_0)$. This parameter describes the fraction of the dipole energy converted into hot electrons. The efficiency of the absorption in the metal bulk and the radiation efficiency are defined as $\eta_{abs,bulk}(\omega_0) = p_{abs,bulk}(\omega_0)/p_{de}(\omega_0)$ and $\eta_{rad}(\omega_0) = p_{rad}(\omega_0)/p_{de}(\omega_0)$, respectively.

To investigate the effect of hot electron generation for the circular nanogroove resonator, we choose, as in the previous section, the dipole-to-surface distance $z_{de} = 20$ nm and solve eq 1 with the introduced permittivity model in eq 3. The Fermi energy and the Fermi velocity of silver are given by $E_F = 5.48$ eV and $v_F = 1.39 \times 10^6$ m/s,[48] respectively. The quantum decay parameter $\gamma_{s,n}$ is obtained by the iteration in eq 4, where the abort condition for the iteration is $|\gamma_{s,n} - \gamma_{s,n-1}|/\gamma_{s,n} < 10^{-2}$. For all simulations, with an initial value of $\gamma_{s,0} = 0$, this convergence condition can be achieved within a maximum of four iterations. The electric fields $\mathbf{E}(\mathbf{r}, \omega_0)$ resulting from this procedure are used to compute $p_{de}(\omega_0)$, $p_{he}(\omega_0)$, and $p_{rad}(\omega_0)$. To obtain the absorption in the metal bulk, we use the expression $p_{abs,bulk}(\omega_0) = p_{de}(\omega_0) - p_{he}(\omega_0) - p_{rad}(\omega_0)$. Note that the quantum decay parameter $\gamma_{s,n}$ and, therefore, the quantum dissipation $p_{de}(\omega_0)$ depend on the size of the surface S and on the size of the volume V in eq 4. For example, for a system radiating at the wavelength of the localized resonance shown in Figure 2c, $p_{he}(\lambda_0 = 435$ nm$)$ changes less than 1% when the radius of the integration domains is doubled from 1 to 2 μm. We choose a fixed integration radius of 2 μm for all simulations.

Figure 4a shows the computed efficiencies $\eta_{abs,bulk}(\lambda_0)$, $\eta_{he}(\lambda_0)$, and $\eta_{rad}(\lambda_0)$ and the corresponding absolute values for the dipole emission $p_{de}(\lambda_0)$. In the full spectral range, due to the small dipole-to-surface distance, a large part of the power emitted by the dipole is absorbed in the metal bulk, and only a smaller part is radiated to the upper hemisphere. The quantum efficiency of hot electron generation $\eta_{he}(\lambda_0)$ is significant in the spectral regions corresponding to the localized resonance shown in Figure 2c and corresponding to the propagating surface plasmons. A comparison of the results for $p_{de}(\lambda_0)$ in Figures 4a and 3a shows a slight reduction of $p_{de}(\lambda_0)$ when the quantum decay parameter $\gamma_{s,n}$ is incorporated in the material model. However, the peaks of $p_{de}(\lambda_0)$ are still present, which demonstrates that the optical resonance effects are the main drivers for hot electron generation in our model system. In both cases, with and without including the surface-scattering effect in the material model, the maximum of the dipole emission $p_{de}(\lambda_0)$ is located at the resonance wavelength of the localized resonance, at $\lambda_0 = 435$ nm.

Next, we compare the quantum efficiency in the presence of the nanoresonator with the quantum efficiency for a flat, unstructured surface. Figure 4b shows the corresponding spectra $\eta_{he}(\lambda_0)$. In the case of the nanoresonator, the maximum of the quantum efficiency is located close to the resonance wavelength of the localized resonance, and is given by $\eta_{he}(\lambda_0 = 431$ nm$) = 0.52$, which is about 1 order of magnitude larger than in case of the flat surface. The propagating surface plasmons are responsible for another maximum $\eta_{he}(\lambda_0 = 346$ nm$) = 0.32$. In the case of the flat surface, the quantum
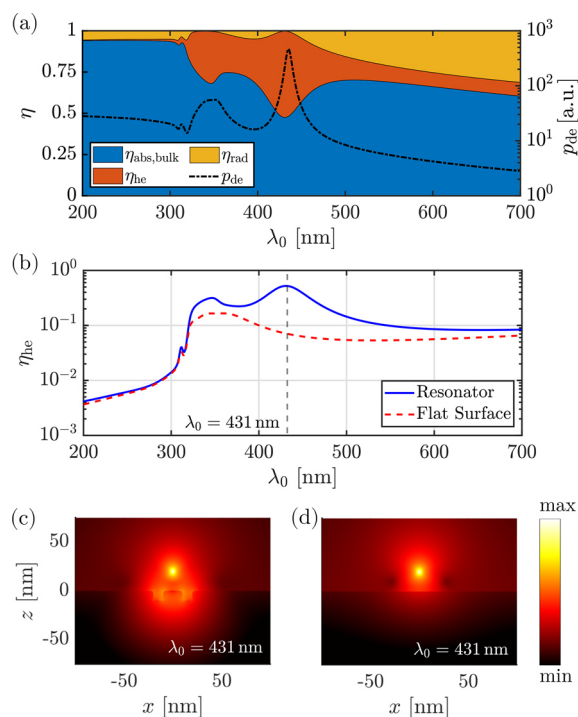
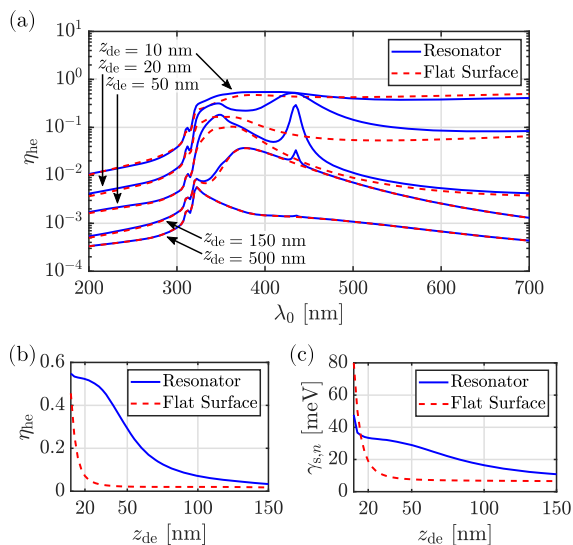**Figure 4.** Simulations of hot electron generation for a localized emitter placed at the dipole-to-surface distance $z_{de} = 20$ nm for the circular nanogroove resonator with $r = 10$ nm and a flat surface. The modified permittivity function given by eq 3 is used. (a) Left y axis: Area plot for the absorption efficiency $\eta_{abs} = p_{abs,bulk}/p_{de}$, hot electron efficiency $\eta_{he} = p_{he}/p_{de}$, and radiation efficiency $\eta_{rad} = p_{rad}/p_{de}$ for the nanoresonator. Right y axis: Dipole emission p_{de} for the nanoresonator. (b) Quantum efficiency of hot electron generation η_{he} for the nanoresonator and a flat surface. (c, d) Log-plot (a.u.) of the electric field intensity $|\mathbf{E}|^2$ resulting from a dipole emitter radiating at the wavelength $\lambda_0 = 431$ nm for the nanoresonator and a flat surface, respectively.

efficiency shows one maximum at the wavelength $\lambda_0 = 360$ nm, given by $\eta_{he}(\lambda_0 = 360$ nm$) = 0.17$. The spectra $\eta_{he}(\lambda_0)$ demonstrate that the presence of the nanoresonator has a significant influence on the generation of energetic charge carriers. Figure 4c,d emphasizes this by showing, for the circular nanogroove resonator and the flat surface, respectively, the electric field intensities in the vicinity of the dipole emitter radiating at the wavelength $\lambda_0 = 431$ nm, where the quantum efficiency is maximal. The localized source strongly excites the localized resonance of the nanoresonator, which leads to high electric field values at the metal surface enabling enhanced hot electron generation. Note that, close to the wavelength of the localized resonance, the absolute values for the dipole emission $p_{de}(\lambda_0)$ are more than 1 order of magnitude larger for the system with the nanoresonator than for the system without the nanoresonator, see also Figure 3a.

Dependence of Hot Electron Generation on Emitter Placement. Localized light sources can excite resonances that cannot be excited by illumination from the far field, such as dark surface plasmon modes[19] or modes where the overlap integral with the field caused by the far-field illumination is negligible. This allows for additional degrees of freedom in tailoring the light−matter interaction. It can be expected that the position of the dipole emitter in our model system is a degree of freedom that has a significant influence on the generation of excited charge carriers. For investigating this

impact, we perform simulations of the hot electron generation with various dipole-to-surface distances. The corresponding results are shown in Figure 5a. In the full spectral range, with a

Figure 5. Simulations of hot electron generation for a localized emitter placed at different dipole-to-surface distances z_{de}, for the circular nanogroove resonator with $r = 10$ nm and a flat surface. The modified permittivity function given by eq 3 is used. (a) Quantum efficiency η_{he} as a function of emitter wavelength for various distances z_{de}. (b, c) Quantum efficiency η_{he} and quantum decay parameter $\gamma_{s,n}$, respectively, depending on z_{de}. The number n is the last step of the iteration in eq 4. Note that the emitter wavelength changes as z_{de} is varied to match the spectral position of the peak in the spectrum due to the localized resonance. The same wavelength is used for the flat surface.

decreasing dipole-to-surface distance from $z_{de} = 500$ nm to $z_{de} = 10$ nm, the quantum efficiency $\eta_{he}(\lambda_0)$ strongly increases. The most significant effect can be observed at the peak in the spectrum corresponding to the localized resonance. This can be explained through the z_{de}-dependent overlap between localized resonance and source near-fields: The resonance excitation and the resulting electromagnetic near-fields increase when the dipole-to-surface distance becomes smaller. Note that, below 20 nm, the efficiency at the peak does not further increase significantly with a decrease in the distance. This can be understood by considering that, below 20 nm, almost all emitted energy has already been funneled into the localized resonance, and a further decrease of the distance does not change the electric field distribution near the metal surface. Such a saturation of the hot electron generation efficiency can only be predicted with self-consistent formulas, as given by eqs 1, 3, and 4.

Next, we investigate the behavior of the resonance-induced hot electron generation peak by performing a fine sampling of the dipole-to-surface distance z_{de}. Figure 5b shows the corresponding dependence of the quantum efficiency η_{he}. In the case of the nanoresonator, the quantum efficiency varies over 1 order of magnitude, from 3% to 52%, when the distance decreases from 150 to 20 nm. In the case of the flat surface, the quantum efficiency only increases from 2% to 7% when the distance decreases from 150 to 20 nm.

By changing the dipole-to-surface distance further, from $z_{de} = 20$ nm to $z_{de} = 10$ nm, an additional significant effect can be observed in the case of the flat surface: The quantum efficiency

increases by more than 1 order of magnitude, up to $\eta_{he} = 0.46$. For such small distances, high-k surface plasmon polaritons can be excited.[49] These high-k surface plasmons have a very small skin depth, which leads to strongly confined electric fields close to the metal surface. This strong effect is not observed when the nanoresonator is present because, in this case, the response is fully dominated by the localized resonance and the energy does not funnel into high-k surface plasmons. As a result, when $z_{de} = 10$ nm, the same order of magnitude of quantum efficiency is obtained in the presence and in the absence of the nanoresonator. Figure 5c shows the dependence of the quantum decay parameter $\gamma_{s,n}$ on the distance z_{de}. The quantum dissipation at the surface and the absorption power in the metal bulk are related to the nominator and the denominator in eq 4, respectively. For decreasing dipole-to-surface distances, the quantum dissipation increases faster than the absorption in the metal bulk leading to an increase of $\gamma_{s,n}$.

Along with the additional broadening of the plasmon resonance described by $\gamma_{s,n}$, the surface-assisted hot electron generation processes create a peculiar, nonthermal energy distribution of excited electrons inside a driven plasmonic nanocrystal.[38,47] The computed shapes of nonthermal energy distributions in a nanocrystal can be found in the refs 38 and 47. The intraband hot electrons, which we study here, are generated near the surface, and their spectral generation rate has a nearly flat distribution in the energy interval $E_F < E < E_F + \hbar\omega_0$. Because of the frequent electron–electron collisions, the high-energy hot electrons experience fast energy relaxation. Therefore, the resulting numbers of hot electrons in the steady states of plasmonic nanostructures are always limited. However, those hot electrons, when generated, have a good chance to be injected into electronic acceptor states at the surface.[3,6,7,10,50,51] These electronic acceptors can be in the form of semiconductor clusters (TiO_2)[50,51] or adsorbed molecular species.[7,10] Consequently, the injected long-lived hot electrons can cause chemical reactions in a solution[6,7,10] or surface growth.[52] Such chemical and shape transformations can be observed in experiments.

Based on the above results, we expect that in potential experimental setups that use hot electron generation by localized sources and nanostructured samples, the significant spectral dependence and position dependence of the generation rate can provide strong experimental signatures and thus can provide guidelines for settings with high-efficiency hot electron generation.

■ CONCLUSIONS

We analyzed the hot electron generation due to the emission of light by a localized emitter placed in the near-field of a metal nanoresonator with electromagnetic field calculations and an approximate quantum model. For a resonant nanostructure on the metal surface, enhanced hot electron generation was observed. This enhancement is based on a plasmonic resonance excited by the emitter. We showed that, for a specific nanoresonator on a silver surface, the quantum efficiency is about 1 order of magnitude larger than the quantum efficiency of hot electron generation in the case of a flat silver surface. We further demonstrated a strong spectral and position dependence of the hot electron generation on the placement of the emitter. In particular, the resonance significantly favors these effects.

The physical reason behind the efficient energy conversion in our system is that both the exciting source and the

nanoresonator have the same dimensionality: They are zero-dimensional and, therefore, highly localized. Experimentally, a zero-dimensional source of radiation is the key element in the field of tip-enhanced spectroscopies, which includes scanning near-field optical microscopy (SNOM),[53,54] hot electron nanoscopy,[55] and hot electron tunneling settings.[56] In tip-driven spectroscopy, electromagnetic fields and the related hot electron excitation processes become strongly confined in small volumes, leading to a strong enhancement of light–matter interaction. Our approach can also be used to investigate coatings with quantum dots or other emitters on resonance-supporting surfaces. The presented study provides a theoretical background for hot electron generation with localized light sources.

◼ AUTHOR INFORMATION

Corresponding Author

Sven Burger − *Zuse Institute Berlin, 14195 Berlin, Germany; JCMwave GmbH, 14050 Berlin, Germany;* orcid.org/0000-0002-3140-5380; Email: burger@zib.de

Authors

Felix Binkowski − *Zuse Institute Berlin, 14195 Berlin, Germany;* orcid.org/0000-0002-4728-8887

Tong Wu − *LP2N, Institut d'Optique Graduate School, CNRS, Univ. Bordeaux, 33400 Talence, France*

Philippe Lalanne − *LP2N, Institut d'Optique Graduate School, CNRS, Univ. Bordeaux, 33400 Talence, France;* orcid.org/0000-0003-1979-2290

Alexander O. Govorov − *Department of Physics and Astronomy, Ohio University, Athens, Ohio 45701, United States;* orcid.org/0000-0003-1316-6758

Complete contact information is available at:
https://pubs.acs.org/10.1021/acsphotonics.1c00231

Notes

The authors declare no competing financial interest.

◼ ACKNOWLEDGMENTS

◼ REFERENCES

(1) Barnes, W. L.; Dereux, A.; Ebbesen, T. W. Surface plasmon subwavelength optics. *Nature* **2003**, *424*, 824.

(2) Novotny, L.; van Hulst, N. Antennas for light. *Nat. Photonics* **2011**, *5*, 83.

(3) Linic, S.; Christopher, P.; Ingram, D. B. Plasmonic-metal nanostructures for efficient conversion of solar to chemical energy. *Nat. Mater.* **2011**, *10*, 911.

(4) Brongersma, M. L.; Halas, N. J.; Nordlander, P. Plasmon-induced hot carrier science and technology. *Nat. Nanotechnol.* **2015**, *10*, 25.

(5) Hartland, G. V.; Besteiro, L. V.; Johns, P.; Govorov, A. O. What's so Hot about Electrons in Metal Nanoparticles? *ACS Energy Lett.* **2017**, *2*, 1641.

(6) Kim, Y.; Smith, J. G.; Jain, P. K. Harvesting multiple electron-hole pairs generated through plasmonic excitation of Au nanoparticles. *Nat. Chem.* **2018**, *10*, 763.

(7) Wu, N. Plasmonic metal-semiconductor photocatalysts and photoelectrochemical cells: a review. *Nanoscale* **2018**, *10*, 2679.

(8) DuChene, J. S.; Tagliabue, G.; Welch, A. J.; Cheng, W.-H.; Atwater, H. A. Hot Hole Collection and Photoelectrochemical CO2 Reduction with Plasmonic Au/p-GaN Photocathodes. *Nano Lett.* **2018**, *18*, 2545.

(9) Pensa, E.; Gargiulo, J.; Lauri, A.; Schlücker, S.; Cortés, E.; Maier, S. A. Spectral Screening of the Energy of Hot Holes over a Particle Plasmon Resonance. *Nano Lett.* **2019**, *19*, 1867.

(10) Mascaretti, L.; Naldoni, A. Hot electron and thermal effects in plasmonic photocatalysis. *J. Appl. Phys.* **2020**, *128*, 041101.

(11) Zhang, Y.; He, S.; Guo, W.; Hu, Y.; Huang, J.; Mulcahy, J. R.; Wei, W. D. Surface-Plasmon-Driven Hot Electron Photochemistry. *Chem. Rev.* **2018**, *118*, 2927.

(12) Harutyunyan, H.; Martinson, A. B. F.; Rosenmann, D.; Khorashad, L. K.; Besteiro, L. V.; Govorov, A. O.; Wiederrecht, G. P. Anomalous ultrafast dynamics of hot plasmonic electrons in nanostructures with hot spots. *Nat. Nanotechnol.* **2015**, *10*, 770.

(13) Sykes, M. E.; Stewart, J. W.; Akselrod, G. M.; Kong, X.-T.; Wang, Z.; Gosztola, D. J.; Martinson, A. B. F.; Rosenmann, D.; Mikkelsen, M. H.; Govorov, A. O.; Wiederrecht, G. P. Enhanced generation and anisotropic Coulomb scattering of hot electrons in an ultra-broadband plasmonic nanopatch metasurface. *Nat. Commun.* **2017**, *8*, 986.

(14) Negrín-Montecelo, Y.; Comesaña Hermo, M.; Khorashad, L. K.; Sousa-Castillo, A.; Wang, Z.; Pérez-Lorenzo, M.; Liedl, T.; Govorov, A. O.; Correa-Duarte, M. A. Photophysical Effects behind the Efficiency of Hot Electron Injection in Plasmon-Assisted Catalysis: The Joint Role of Morphology and Composition. *ACS Energy Lett.* **2020**, *5*, 395.

(15) Hecht, B.; Sick, B.; Wild, U. P.; Deckert, V.; Zenobi, R.; Martin, O. J. F.; Pohl, D. W. Scanning near-field optical microscopy with aperture probes: Fundamentals and applications. *J. Chem. Phys.* **2000**, *112*, 7761.

(16) Anger, P.; Bharadwaj, P.; Novotny, L. Enhancement and Quenching of Single-Molecule Fluorescence. *Phys. Rev. Lett.* **2006**, *96*, 113002.

(17) Senellart, P.; Solomon, G.; White, A. High-performance semiconductor quantum-dot single-photon sources. *Nat. Nanotechnol.* **2017**, *12*, 1026.

(18) Lindquist, N. C.; Nagpal, P.; McPeak, K. M.; Norris, D. J.; Oh, S.-H. Engineering metallic nanostructures for plasmonics and nanophotonics. *Rep. Prog. Phys.* **2012**, *75*, 036501.

(19) Liu, M.; Lee, T.-W.; Gray, S. K.; Guyot-Sionnest, P.; Pelton, M. Excitation of Dark Plasmons in Metal Nanoparticles by a Localized Emitter. *Phys. Rev. Lett.* **2009**, *102*, 107401.

(20) Giannini, V.; Fernández-Domínguez, A. I.; Heck, S. C.; Maier, S. A. Plasmonic Nanoantennas: Fundamentals and Their Use in Controlling the Radiative Properties of Nanoemitters. *Chem. Rev.* **2011**, *111*, 3888.

(21) Lalanne, P.; Yan, W.; Vynck, K.; Sauvan, C.; Hugonin, J.-P. Light Interaction with Photonic and Plasmonic Resonances. *Laser Photonics Rev.* **2018**, *12*, 1700113.

(22) Zworski, M. Resonances in physics and geometry. *Notices Am. Math. Soc.* **1999**, *46*, 319.

(23) Lalanne, P.; et al. Quasinormal mode solvers for resonators with dispersive materials. *J. Opt. Soc. Am. A* **2019**, *36*, 686.

(24) Sehmi, H. S.; Langbein, W.; Muljarov, E. A. Optimizing the Drude-Lorentz model for material permittivity: Method, program, and examples for gold, silver, and copper. *Phys. Rev. B: Condens. Matter Mater. Phys.* **2017**, *95*, 115444.

(25) Garcia-Vergara, M.; Demésy, G.; Zolla, F. Extracting an accurate model for permittivity from experimental data: hunting complex poles from the real line. *Opt. Lett.* **2017**, *42*, 1145.

(26) Johnson, P. B.; Christy, R. W. Optical Constants of the Noble Metals. *Phys. Rev. B* **1972**, *6*, 4370.

(27) Pomplun, J.; Burger, S.; Zschiedrich, L.; Schmidt, F. Adaptive finite element method for simulation of optical nano structures. *Phys. Status Solidi B* **2007**, *244*, 3419.

(28) Schneider, P.-I.; Srocka, N.; Rodt, S.; Zschiedrich, L.; Reitzenstein, S.; Burger, S. Numerical optimization of the extraction efficiency of a quantum-dot based single-photon emitter into a single-mode fiber. *Opt. Express* **2018**, *26*, 8479.

(29) Sauvan, C.; Hugonin, J.-P.; Maksymov, I. S.; Lalanne, P. Theory of the Spontaneous Optical Emission of Nanosize Photonic and Plasmon Resonators. *Phys. Rev. Lett.* **2013**, *110*, 237401.

(30) Feibelman, P. J. Microscopic calculation of surface-plasmon dispersion and damping. *Phys. Rev. B* **1974**, *9*, 5077.

(31) Tsuei, K.-D.; Plummer, E. W.; Feibelman, P. J. Surface-plasmon dispersion in simple metals. *Phys. Rev. Lett.* **1989**, *63*, 2256.

(32) Hartland, G. V. Optical Studies of Dynamics in Noble Metal Nanostructures. *Chem. Rev.* **2011**, *111*, 3858.

(33) Genzel, L.; Martin, T. P.; Kreibig, U. Dielectric function and plasma resonances of small metal particles. *Z. Phys. B: Condens. Matter Quanta* **1975**, *21*, 339.

(34) Kreibig, U.; Vollmer, M. *Optical Properties of Metal Clusters*; Springer: Berlin, 1995.

(35) Kraus, W. A.; Schatz, G. C. Plasmon resonance broadening in small metal particles. *J. Chem. Phys.* **1983**, *79*, 6130.

(36) Lermé, J. Size Evolution of the Surface Plasmon Resonance Damping in Silver Nanoparticles: Confinement and Dielectric Effects. *J. Phys. Chem. C* **2011**, *115*, 14098.

(37) Uskov, A. V.; Protsenko, I. E.; Mortensen, N. A.; O'Reilly, E. P. Broadening of Plasmonic Resonance Due to Electron Collisions with Nanoparticle Boundary: a Quantum Mechanical Consideration. *Plasmonics* **2014**, *9*, 185.

(38) Santiago, E. Y.; Besteiro, L. V.; Kong, X.-T.; Correa-Duarte, M. A.; Wang, Z.; Govorov, A. O. Efficiency of Hot-Electron Generation in Plasmonic Nanocrystals with Complex Shapes: Surface-Induced Scattering, Hot Spots, and Interband Transitions. *ACS Photonics* **2020**, *7*, 2807.

(39) Govorov, A. O.; Zhang, H.; Gun'ko, Y. K. Theory of Photoinjection of Hot Plasmonic Carriers from Metal Nanostructures into Semiconductors and Surface Molecules. *J. Phys. Chem. C* **2013**, *117*, 16616.

(40) Ziman, J. M. *Principles of the Theory of Solids*, 2nd ed.; Cambridge University Press, 1972.

(41) Tanner, D. B. *Optical Effects in Solids*; Cambridge University Press, 2019.

(42) Tamm, I.; Schubin, S. Zur Theorie des Photoeffektes an Metallen. *Eur. Phys. J. A* **1931**, *68*, 97.

(43) Brodskii, A. M.; Gurevich, Y. Y. Theory of External Photoeffect from the Surface of a Metal. *Sov. Phys. - JETP* **1968**, *27*, 114.

(44) Protsenko, I. E.; Uskov, A. V. Photoemission from metal nanoparticles. *Phys.-Usp.* **2012**, *55*, 508.

(45) Zhukovsky, S. V.; Babicheva, V. E.; Uskov, A. V.; Protsenko, I. E.; Lavrinenko, A. V. Enhanced Electron Photoemission by Collective Lattice Resonances in Plasmonic Nanoparticle-Array Photodetectors and Solar Cells. *Plasmonics* **2014**, *9*, 283.

(46) Brown, A. M.; Sundararaman, R.; Narang, P.; Goddard, W. A.; Atwater, H. A. Nonradiative Plasmon Decay and Hot Carrier Dynamics: Effects of Phonons, Surfaces, and Geometry. *ACS Nano* **2016**, *10*, 957.

(47) Besteiro, L. V.; Kong, X.-T.; Wang, Z.; Hartland, G.; Govorov, A. O. Understanding Hot-Electron Generation and Plasmon Relaxation in Metal Nanocrystals: Quantum and Classical Mechanisms. *ACS Photonics* **2017**, *4*, 2759.

(48) Kittel, C. *Introduction to Solid State Physics*, 8th ed.; Wiley: New York, 2005.

(49) Ford, G.; Weber, W. Electromagnetic interactions of molecules with metal surfaces. *Phys. Rep.* **1984**, *113*, 195.

(50) Sousa-Castillo, A.; Comesaña Hermo, M.; Rodríguez-González, B.; Pérez-Lorenzo, M.; Wang, Z.; Kong, X.-T.; Govorov, A. O.; Correa-Duarte, M. A. Boosting Hot Electron-Driven Photocatalysis through Anisotropic Plasmonic Nanoparticles with Hot Spots in Au−TiO2 Nanoarchitectures. *J. Phys. Chem. C* **2016**, *120*, 11690.

(51) Baturina, O. A.; Epshteyn, A.; Simpkins, B. S.; Bhattarai, N.; Brintlinger, T. H.; Santiago, E. Y.; Govorov, A. O. Comparing Photoelectrochemical Methanol Oxidation Mechanisms for Gold versus Titanium Nitride Nanoparticles Dispersed in TiO2Matrix. *J. Electrochem. Soc.* **2019**, *166*, H485.

(52) Khorashad, L. K.; Besteiro, L. V.; Correa-Duarte, M. A.; Burger, S.; Wang, Z. M.; Govorov, A. O. Hot Electrons Generated in Chiral Plasmonic Nanocrystals as a Mechanism for Surface Photochemistry and Chiral Growth. *J. Am. Chem. Soc.* **2020**, *142*, 4193.

(53) Heinzelmann, H.; Pohl, D. W. Scanning near-field optical microscopy. *Appl. Phys. A: Solids Surf.* **1994**, *59*, 89.

(54) Chen, J.; Badioli, M.; Alonso-González, P.; Thongrattanasiri, S.; Huth, F.; Osmond, J.; Spasenović, M.; Centeno, A.; Pesquera, A.; Godignon, P.; Zurutuza Elorza, A.; Camara, N.; de Abajo, F. J. G.; Hillenbrand, R.; Koppens, F. H. L. Optical nano-imaging of gate-tunable graphene plasmons. *Nature* **2012**, *487*, 77.

(55) Giugni, A.; Torre, B.; Allione, M.; Das, G.; Wang, Z.; He, X.; Alshareef, H. N.; Di Fabrizio, E. Experimental Route to Scanning Probe Hot-Electron Nanoscopy (HENs) Applied to 2D Material. *Adv. Opt. Mater.* **2017**, *5*, 1700195.

(56) Wang, X.; Braun, K.; Zhang, D.; Peisert, H.; Adler, H.; Chassé, T.; Meixner, A. J. Enhancement of Radiative Plasmon Decay by Hot Electron Tunneling. *ACS Nano* **2015**, *9*, 8176.

8.3 Purcell enhancement with coupled eigenmodes

By continuously changing the system parameters of a nanoresonator, a coupling of the underlying resonances can lead to a significant increase in the Q-factor of one of the resonances. This increase is due to constructive and destructive resonance interference and the associated suppression of radiation losses. The resulting high Q-factor resonance is also called quasi BIC [105] and the associated effect of increased energy confinement is used in various nanophotonics applications [99, 106, 107].

With Ref. [71], we demonstrate how different numerical methods can be used together to comprehensively study coupled resonances and their effect on the Purcell enhancement of a dipole emitter placed in a nanodisk. To engineer a quasi-BIC, we vary the aspect ratio of the disk and compute the eigenmodes and eigenfrequencies for the different aspect ratios with the linearization approach presented in Section 8.1. Based on the computed eigenfrequencies, the Q-factor and the condition for the appearance of the quasi-BIC are evaluated. Then, we place a dipole emitter in the nanodisk and use the Riesz projection expansion approach given by Eq. (2.4) to investigate the contribution of the quasi-BIC as well as the contributions of the other resonances to the resonance expansion of the Purcell factor. We further compute the Riesz projection expansion of the energy flux density in the far field of the nanodisk, given by Eq. (4.1). This allows to understand how the interference between the individual resonances effects the radiation pattern of the light source.

In the following, Ref. [71] is reprinted, which is published by the American Physical Society under the terms of the Creative Commons Attribution 4.0 International license; [Rémi Colom, Felix Binkowski, Fridtjof Betz, Yuri Kivshar, and Sven Burger. Enhanced Purcell factor for nanoantennas supporting interfering resonances. *Phys. Rev. Res.* 4, 023189 (2022). DOI: 10.1103/PhysRevResearch.4.023189.]

Enhanced Purcell factor for nanoantennas supporting interfering resonances

Rémi Colom,[1] Felix Binkowski ⬤,[1] Fridtjof Betz ⬤,[1] Yuri Kivshar,[2] and Sven Burger ⬤[1,3,*]

[1]*Zuse Institute Berlin, Takustraße 7, 14195 Berlin, Germany*
[2]*Nonlinear Physics Center, Research School of Physics, Australian National University, Canberra ACT 2601, Australia*
[3]*JCMwave GmbH, Bolivarallee 22, 14050 Berlin, Germany*

We study the effect of coupled resonances and quasibound states in the continuum (quasi-BICs) on the Purcell factor in dielectric resonant nanoantennas. We analyze numerically interfering resonances in a nanodisk *with* and *without* a substrate when the modes are coupled to an emitter localized inside the nanodisk, and we quantify the modal contributions to the Purcell factor also reconstructing the radiation patterns of the resonant system. It is revealed that the Purcell effect can be boosted substantially for a strong coupling of resonances in the quasi-BIC regime.

I. INTRODUCTION

Resonances play a central role in the control of light-matter interactions in nanophotonics. Plasmonic resonances enable such a control via large near-field enhancements [1,2], which allows, e.g., for realizing plasmonic nanoantennas to tailor the radiation from quantum emitters [3,4]. Recently, the excitation of Mie-type resonant modes [5,6] in high-refractive-index dielectric resonators has proven to be very useful for a wide range of applications, from the enhancement of nonlinear effects to a resonant control of the phase in metasurfaces [7,8]. One important figure of merit for measuring the effect of resonances on light-matter interactions is their quality factor (*Q factor*), that quantifies the ability of a structure to trap light and to enhance the electromagnetic fields.

Nanoresonators act as nanoantennas for strongly localized light sources, like quantum dots or defects in crystalline lattices, which can allow for the realization of efficient single-photon sources by enhancing the emission of light [9,10]. Such a control of the emission via the modification of the electromagnetic environment is a concept that dates back to the pioneering work of Purcell [11] performed in the microwave range followed by the experiments of Drexhage [12] that demonstrated the possibility of controlling the lifetime of fluorescent molecules in the visible range. This phenomenon is ubiquitous, and it has also been used to control the resonant scattering by dielectric nanorod antennas [13].

The figure of merit that quantifies the emission enhancement is called the *Purcell factor* [11], and it is proportional to the *Q* factor. Optical nanoantennas were first realized with plasmonic materials [3,4], but recently dielectric resonators have been shown to allow for large enhancements

of the Purcell factor via the excitation of both electric and magnetic optically-induced Mie-type resonances [14,15]. The excitation of magnetic resonances presents the advantage of enhancing light emission also via the magnetic dipole transitions. This effect was first theoretically predicted [15–17] and confirmed later in experiments [18–20]. This is a very promising application for dielectric nanoantennas as the enhancement of light emission empowered by the magnetic dipole resonances is an emerging area of research [21,22]. The enhancement of the Purcell factor was used successfully to improve the emission of quantum dots in silicon nanoantennas [23] and also for metallic and hybrid nanoantennas [24]. Control of the emission can also be achieved dynamically [25]. Finally, nanoantennas can also be designed to enhance the performance of quantum emitters, providing promising platforms for the realization of single-photon sources [26].

Bound states in the continuum (BICs) appear as a special type of nonradiating modes associated with an infinite *Q* factor [27]. Such states can originate from different physical mechanisms [28,29]. Symmetry protected BICs occur in photonic crystal slabs, and they result from the impossibility of these modes to couple to propagating fields outside the photonic crystal because of symmetry restrictions [27,30]. Further, the so-called accidental BICs appear from interferences between several resonances [27,28]. They are observed when a system parameter is varied continuously. This concept was introduced in quantum mechanics where the coupling between resonances is controlled by engineering the potential [31].

In optics, one of the first attempts to study BICs was made in the physics of photonic crystals [32]. While BICs can be realized in gratings or photonic crystals which are infinite in two directions, it is much more challenging to observe such BICs in compact structures and even more in subwavelength systems [27]. The existence of BICs, also called *embedded eigenstates*, was predicted theoretically in a coated nanosphere where the permittivity of the outer shell vanishes [33]. In more realistic configurations, it is still possible to take advantage of the coupling of resonances in nanostructures to

---

*burger@zib.de

increase the Q factor of one resonance, even if it does not lead to accidental BICs with infinite Q factors. In photonics, such an approach was suggested to enhance the Q factors of the modes of optical microcavities [34] and coupled dielectric nanopillars [35]. It was shown recently that high-refractive index nanodisks supporting multiple resonances are a good platform to employ this approach [36–38]. Due to similarity of this approach with accidental BICs [31], the large Q factors achieved through the interference of several resonances are called *quasi-BICs*. Quasi-BICs have been observed experimentally in AlGaAs nanodisks [39], and they have been used in various applications [28,40] including nonlinear optics [41–43] and lasing from a single nanoparticle [44]. Compared to photonic crystal cavities, ring resonators, and other setups [4], such compact nanostructures supporting quasi-BICs exhibit lower Q factors and Purcell enhancements [45]. However, their relatively small device footprint allows these resonators to be used, e.g., as meta-atoms in metasurfaces [46].

Unlike BICs, which lead to a perfect confinement of light, quasi-BICs suffer from residual radiation losses. As a consequence, for a rigorous treatment of quasi-BICs it is important to use quasinormal modes (QNMs) and associated complex eigenfrequencies which generalizes modal approaches to dissipative and non-Hermitian systems [45,47,48]. The influence of quasi-BICs on light-matter interactions and, in particular, their coupling to a light source can be quantified by using QNM expansions. The QNM analysis of the coupling of an electromagnetic dipole source to an optical resonator, i.e., the modal expansion of the Purcell factor, has been carried out through several approaches [15,49–52].

In this paper, we study quasi-BICs numerically. We consider dielectric nanoresonators either *with* or *without* a substrate and demonstrate that they can support interfering resonances with a strong coupling between a pair of modes. We choose to design the structure with the refractive index of GaAs. The motivations behind this choice come from the fact that including a dipole emitter into such a structure can be realized using modern nanofabrication methods allowing to include a quantum dot in GaAs nanodisk [53]. We carry out numerical simulations with a localized source embedded into the resonator to demonstrate different physical regimes. Modal expansions of the Purcell factor and far-field patterns reveal a complex interplay between different modal contributions interfering destructively in the spectral vicinity of quasi-BICs, yielding a strong enhancement of the Purcell factor and single modal excitation when the parameters of the source and resonator are tuned to match the quasi-BIC conditions.

The major steps followed in this article are illustrated in Fig. 1. In Sec. II, we vary the aspect ratio D/H of a GaAs nanodisk to control the interference between the two modes of the nanodisk with or without a substrate. In particular, the strong coupling between these modes leads to the appearance of a high-Q mode: the quasi-BIC resonance. Section III considers the coupling of a dipole source with the nanodisk, leading to a complex electromagnetic response as seen in Fig. 1(b). Modal expansions are employed to analyze the role of the interference between the nanodisk modes for the coupling with the dipole. These expansions enable to identify how
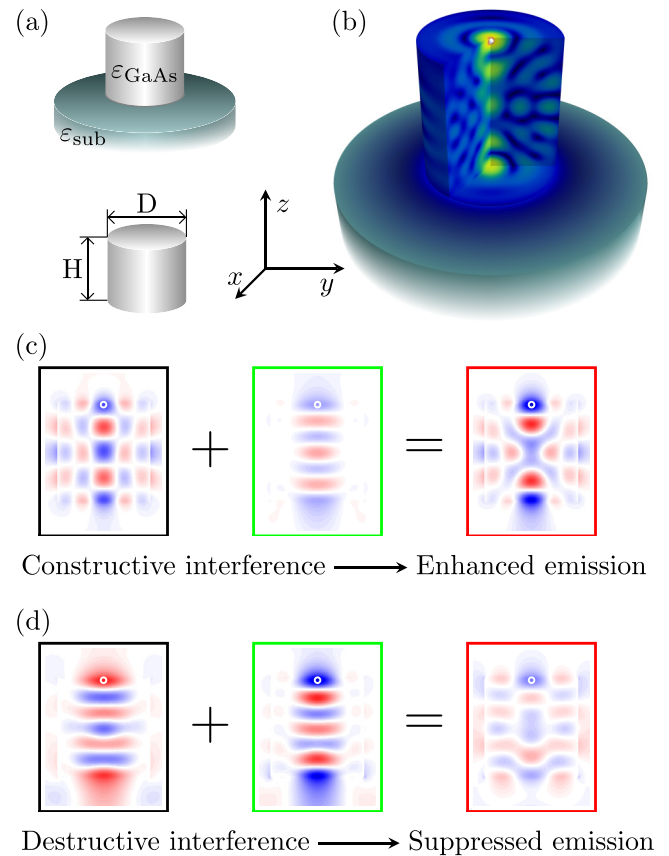

FIG. 1. Principle of the enhanced and suppressed emission with interfering resonances. (a) Schematics of GaAs nanodisks with and without a substrate. The aspect ratio D/H is tuned to control the interference between the two main modes of the nanodisk. (b) Visualization of the electromagnetic field distribution resulting from a dipole emitter, represented by a white sphere, which is located below the top face of the nanodisk. Its frequency is chosen to excite the two modes of interest. (c, d) 2D cross-sections through the dominant two modal fields (left) and the total field distribution (right) visualizing the real part of the y field component. Red and blue colors correspond to negative and positive fields, respectively. The emitter position is indicated with a white circle. (c) When the two modal fields are excited in phase they interfere constructively, leading to enhancement of dipole emission. (d) Out-of-phase excitation of the two modal fields at a different dipole emission frequency, results in suppressed emission.

the constructive interference between two modal contributions leads to the enhancement of the dipole emission, as illustrated in Fig. 1(c). However, destructive interference leads to the inhibition of the dipole emission, as illustrated in Fig. 1(d). The modal analysis of the radiation pattern is carried out in Sec. IV. Finally, Sec. V concludes the paper.

II. QUASI-BICS IN ISOLATED NANODISKS

To understand the appearance of quasi-BIC states, first we review the theoretical approach employed to study the mode coupling [34,54,55]. A good insight in the physics of strong coupling for interfering resonances can be gained from a phenomenological model of mode coupling that involves the two

modes with the uncoupled eigenfrequencies $\omega_{\mathrm{un},1}$ and $\omega_{\mathrm{un},2}$. When these two eigenfrequencies are far apart in the complex plane, there is no coupling between them. However, when the eigenfrequencies get close to each other, the coupling has to be taken into account and modifies the trajectories of these eigenfrequencies when a parameter is varied. The eigenfrequencies of the coupled modes can be found as the eigenvalues of an effective two-mode Hamiltonian, and they are equal to

$$\omega_{\pm} = \left(\frac{\omega_{\mathrm{un},1} + \omega_{\mathrm{un},2}}{2} \right) \pm \sqrt{\gamma},$$

where

$$\gamma = \left(\frac{\omega_{\mathrm{un},1} - \omega_{\mathrm{un},2}}{2} \right)^2 + v^2$$

with v being the coupling coefficient between the modes [54]. We are interested in the regime where these two resonances are close to each other, and therefore we assume that $\Re(\omega_{\mathrm{un},1}) = \Re(\omega_{\mathrm{un},2})$ and v is real as in Ref. [54].

As explained in Refs. [34,54], two regimes of the mode coupling may be realized depending on the relation between v and $\frac{1}{2}(\omega_{\mathrm{un},1} - \omega_{\mathrm{un},2})$. When $2v < |\Im(\omega_{\mathrm{un},1} - \omega_{\mathrm{un},2})|$, the mode eigenvalues become

$$\omega_{\pm} = \left(\frac{\omega_{\mathrm{un},1} + \omega_{\mathrm{un},2}}{2} \right) \pm i\sqrt{|\gamma|},$$

and one observes that the coupling mostly alters the imaginary part of the eigenvalues resulting in an avoided crossing of the imaginary parts of the coupled eigenvalues and a crossing of their real parts. This behavior is a direct signature of the mode weak coupling. However, if $2v > |\Im(\omega_{\mathrm{un},1} - \omega_{\mathrm{un},2})|$, then the mode eigenvalues are presented as

$$\omega_{\pm} = \left(\frac{\omega_{\mathrm{un},1} + \omega_{\mathrm{un},2}}{2} \right) \pm \sqrt{|\gamma|},$$

suggesting that the coupling of the eigenmodes mostly alters the real part of the eigenfrequencies yielding, this time, an avoided crossing of the real parts of the coupled eigenvalues and a crossing of the imaginary parts. A more detailed discussion on the coupling regimes between modes for a purely real or a purely imaginary coupling constant can be found in the Appendix. In the following, we discuss how the mode coupling may result in the appearance of a hybridized quasi-BIC mode.

We consider a Gallium Arsenide (GaAs) nanodisk resonator with a height $H = 1260$ nm and varying diameter D in two different configurations: The nanodisk is just surrounded by air (case 1), and, the nanodisk is placed on a glass substrate and surrounded by a super-space of air (case 2). The optical properties of the system are investigated in the near-infrared wavelength range; the corresponding constant relative permittivities in our model are $\varepsilon_{\mathrm{GaAs}} = 11.56$, $\varepsilon_{\mathrm{sub}} = 2.25$, and $\varepsilon_{\mathrm{air}} = 1.0$. The time-harmonic optical fields are modeled using Maxwell's equations,

$$\nabla \times \mu_0^{-1} \nabla \times \mathbf{E}(\mathbf{r}, \omega) - \epsilon(\mathbf{r})\omega^2 \mathbf{E}(\mathbf{r}, \omega) = i\omega \mathbf{J}(\mathbf{r}), \quad (1)$$

where μ_0 is the vacuum permeability, $\epsilon(\mathbf{r})$ is the permittivity, and $\mathbf{J}(\mathbf{r})$ the source current density. For numerically solving Eq. (1), we use an adaptive, higher-order finite element

method (FEM) [56]. For computing the eigenmodes $\mathbf{E}_n$ of the system and their associated eigenfrequencies ω_n, i.e., solutions to Eq. (1) where $\mathbf{J} = 0$, the cylindrical symmetry of the system is taken into account. Only modes with an azimuthal quantum number equal to 1 or -1 are investigated because these are the only ones excited by a dipole located on the axis of rotation, which is the configuration we are investigating in the second part of this study. Furthermore, only the component of the polarization normal to the symmetry axis can couple to the modes of interest and therefore we restrict to a polarization with $z = 0$. Without loss of generality we chose a y-polarized dipole.

To find a quasi-BIC condition, the interference between two modes of the structure has to be tuned [34,36,57]. This is done by varying the geometry parameter, D, and computing eigenmodes $\mathbf{E}_n$ and their associated eigenfrequencies ω_n, where n is the mode index. Note that alternatively, a perturbation approach based on QNMs may be employed for finding the quasi-BICs [58]. Figures 2(a), 2(b) 2(e), and 2(f) show how the normalized frequency, $\Re(\omega_n H/2c)$, and the Q factor,

$$Q = -\frac{1}{2} \frac{\Re(\omega_n)}{\Im(\omega_n)},$$

depend on the aspect ratio D/H. In Figs. 2(a) and 2(b), the case where the GaAs nanodisk is located in air is considered. It can be observed that the real part of the eigenfrequencies is showing a repulsion behavior at $D/H = 0.909$ and an almost coinciding peak reaching $Q \approx 800$ is observed for the Q factor of one of the modes while a minimum is seen for the other mode. As discussed above, this behavior is an indication of strong coupling between the two modes. The high-Q mode can thus be considered to be a quasi-BIC. Figures 2(e) and 2(f) show the results for the second case, where the nanodisk is put on a glass substrate. It can be observed that, for the investigated modes and parameter range, the real part of the eigenfrequencies shows a crossing at $D/H = 0.933$. We observe a peak of the Q factor reaching $Q \approx 400$ at $D/H = 0.92$. In fact, this peak is linked to the anti-crossing or level-repulsion occurring for the imaginary parts of the eigenfrequencies. This avoided crossing of the imaginary parts of the eigenfrequencies shows up in Fig. 2(f) at about $D/H = 0.944$. The qualitative analysis based on the effective Hamiltonian discussed above shows that this behavior is an indication of weak coupling between the two modes. The transition from strong to weak coupling when a substrate is added indicates that there must be an exceptional point, i.e., a condition for which the two coupled eigenvalues would become degenerated [59], when continuously varying the refractive index of the substrate from 1 to 1.5 [54,55,60,61]. To conclude the discussion on the avoided crossing of the eigenfrequencies, we show, in Figs. 2(c), 2(d), 2(g), and 2(h), the field patterns associated with both modes when the Q factor is maximized. For the case without substrate, this occurs for $D/H = 0.909$ while, when the substrate is added, the maximum occurs for an aspect ratio of $D/H = 0.92$. This helps to understand the level repulsion observed since, in both cases, the modes have apparently very different field patterns: The high-Q mode field is concentrated in hot spots located at the top and bottom of the disk while, for the low-Q mode,
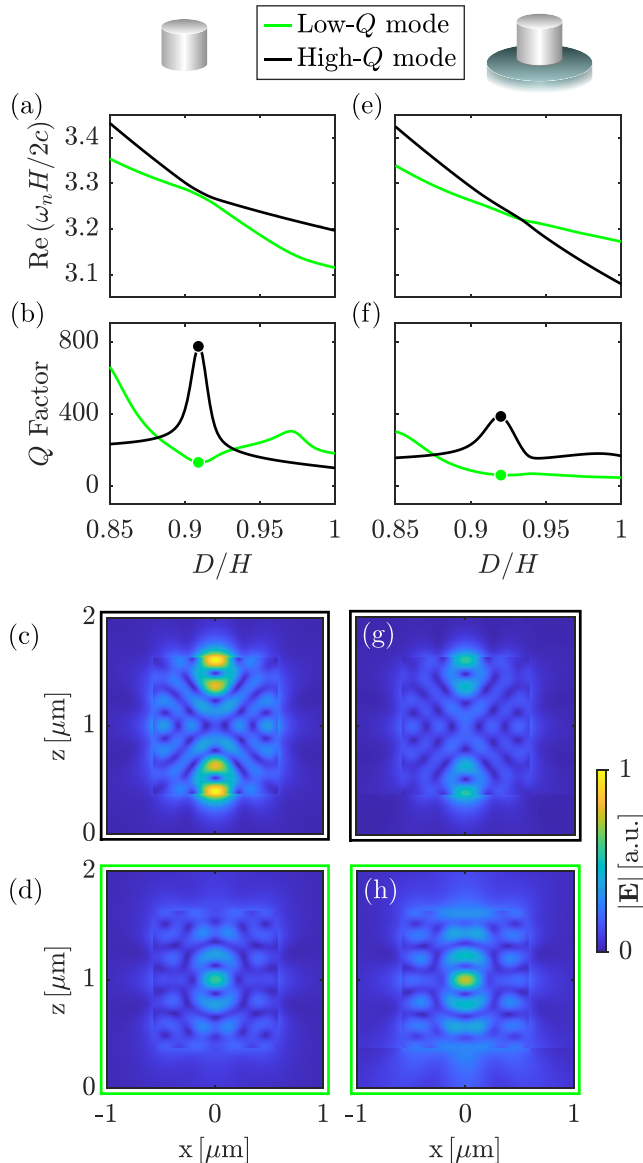
FIG. 2. Real parts of two eigenfrequencies of interest (a, e) and corresponding Q factors (b, f) as function of nanodisk aspect ratio D/H. Avoided crossing of the real parts and local maximum and minimum of the Q factors at $D/H = 0.909$ indicate strong coupling for the nanodisk *without* substrate (a, b). Crossing of the real parts of two eigenfrequencies at $D/H = 0.93$ and avoided crossing of the Q factor curves at $D/H = 0.944$ leading to a peak at $D/H = 0.92$ indicate weak coupling for the nanodisk *with* substrate (e, f). Field intensity maps $|\mathbf{E}|$ of the QNMs in an *x-z* cross-section through the 3D field distribution. Panel (c) [respectively, panel (d)] corresponds to the high-Q (respectively, low-Q) mode of the isolated nanodisk [at the aspect ratio indicated by the black (respectively, green) dot in panel (b)]. Panel (g) [respectively, panel (h)], corresponds to the high-Q (respectively, low-Q) mode of the nanodisk with substrate [black (respectively, green) dot in panel (f)].

it is concentrated at the center of the disk. This apparent difference in the localization of the modes certainly prevents their merging.

III. COUPLING OF A POINT SOURCE TO A NANORESONATOR

Now, we turn to the study of a dipole emitter coupled to the investigated nanoresonator considering the two cases, the nanoresonator with and without substrate. It is worth noting that the coupling of a dipole with a BIC in an array of nanoparticles have already been studied [62], but we will here focus on the coupling of a dipole with the quasi-BIC arising in an individual nanodisk. We consider Maxwell's equations, given by Eq. (1), with the current density $\mathbf{J} = \mathbf{j}\delta(\mathbf{r} - \mathbf{r}_d)$ that is a point source located at $\mathbf{r}_d$. The Purcell factor, which is used to quantify the enhancement of the emission, is defined as $\Gamma(\omega) = -\{\Re[\mathbf{E}(\omega, \mathbf{r}_d) \cdot \mathbf{j}^*(\omega, \mathbf{r}_d)]\}/[2\Gamma_b(\omega)]$, where $\Gamma_b(\omega)$ describes the emission of the dipole in a homogeneous medium of the permittivity ϵ_{GaAs}. The interest of studying the Purcell factor and its modal analysis is twofold. On the one hand, one can see how a mode with a Q factor as large as the one of the quasi-BIC can affect the dipole emission. On the other hand, looking at the modal analysis of the Purcell factor would allow to use it as a probe to study the interplay between several modes. This is particularly interesting for quasi-BICs since interferences between modes are at the origin of their formation.

To do so, we start by considering the Purcell factor for a dipole located at the maximum of the field amplitude of the high-Q mode. This position is on the symmetry axis of the nanodisk, about 30 nm below the top face.

The consequences of the interplay between resonances at the origin of the quasi-BIC can be better understood by carrying out a modal analysis of the Purcell factor. Our method for deriving modal expansions relies on the use of Riesz projections [52,63]. The modal expansion of the Purcell factor reads as

$$\Gamma_{tot}(\omega) = \sum_{n=1}^{2} \Gamma_n(\omega) + \Gamma_{background}(\omega), \qquad (2)$$

where Γ_n are the modal contributions to the Purcell factor that are computed using contour integrals around the eigenfrequencies. Here, we take into account only the two interfering modes, i.e., the modes which are also shown in Fig. 2. The modal Purcell factors Γ_1 and Γ_2 are contributions corresponding to these two modes. The term $\Gamma_{background}$ contains the contributions of all other poles as well as the nonresonant background [52,63]. Finally, Γ_{tot} corresponds to the total expansion including both the modal and background contributions. The different black markers indicate the wavelengths at which the radiation patterns are computed in Fig. 4. Details about the modal expansions are provided in the Appendix.

First, we look at the coupling of the dipole to the nanoresonator with the geometry corresponding to the maximum of the Q factor in Fig. 2. The results of the modal analysis of the Purcell factor are displayed in Fig. 3(a), for a nanodisk in air with an aspect ratio $D/H = 0.909$, and, in Fig. 3(c), for a nanodisk on a substrate with an aspect ratio $D/H = 0.92$. In both cases, the peak observed in the Purcell factor spectrum can be directly linked to the modal contribution corresponding to the high-Q mode. In the region around the peak, the contributions from the low-Q mode and the background are very small or even negligible. This demonstrates that, for a
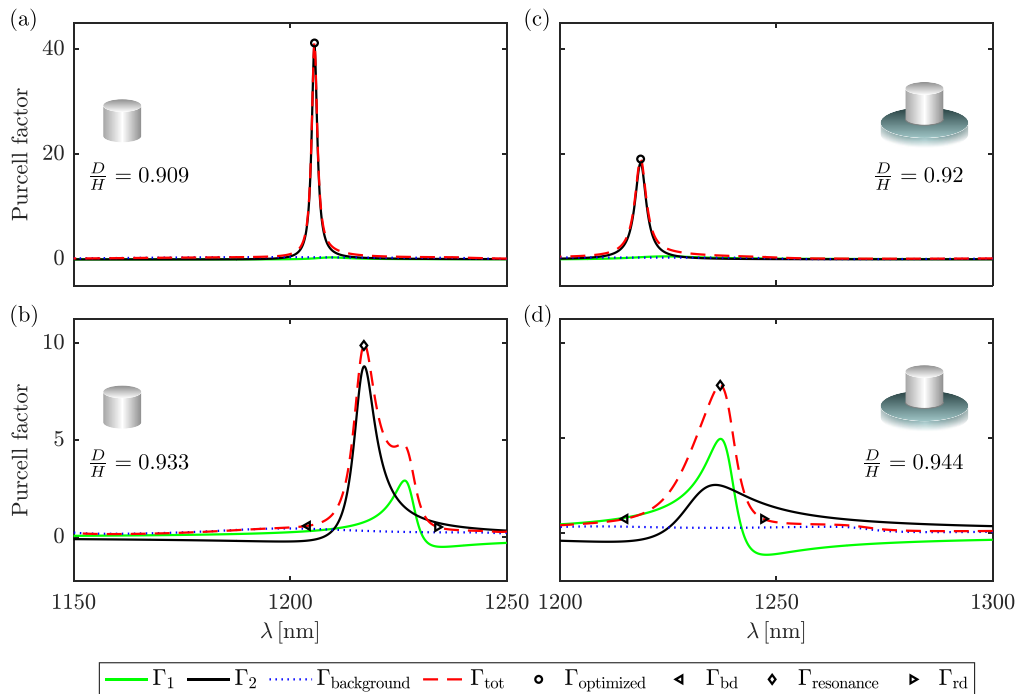
FIG. 3. Modal analysis of the wavelength (λ) dependent Purcell factor Γ for a y-polarized dipole located on the symmetry axis 20 nm and 27 nm below the top face of the nanodisk in the case without substrate (a, b) and with substrate (c, d), respectively. (a) Modal expansion for the aspect ratio $D/H = 0.909$ (maximum Q factor in Fig. 2(b). The high-Q mode corresponds to the modal Purcell factor Γ_2 (a black solid curve) and is solely responsible for the peak of the total Purcell factor Γ_{tot} (dashed red curve) at around 1205 nm. The contributions of the low-Q mode Γ_1 (green solid curve) and of the background $\Gamma_{background}$ (dotted blue line) are negligible. (b) Modal expansion for $D/H = 0.933$ (crossing of Q factors in Fig. 2(b). Both modal terms Γ_1 and Γ_2 are of the same order of magnitude and destructively interfere in regions where they are of different sign. The impact of $\Gamma_{background}$ is constant and negligible in resonant regions. (c) Modal expansion for $D/H = 0.92$ (peak of the high Q factor in Fig. 2(f). The high-Q mode corresponds to Γ_2 and is responsible for the peak of Γ_{tot} at around 1220 nm. (d) Modal expansion for $D/H = 0.944$ (avoided crossing of Q factors in Fig. 2(f). The modal terms interfere, as in (b). The markers $\Gamma_{optimized}$, Γ_{bd}, $\Gamma_{resonance}$, and Γ_{rd} indicate the wavelengths for which far-field patterns are displayed in Fig. 4.

resonator supporting a quasi-BIC, an emitter may easily excite nearly exclusively this resonance. We note that the quasi-BIC allows to reach a high Purcell factor of $\Gamma \approx 40$ in the case without substrate and $\Gamma \approx 20$ in the case with substrate.

It is also worth looking at configurations where one can expect that the contributions to the Purcell factor from the two main modes would be of the same order of magnitude. This would allow us to investigate the interplay between modal contributions. This is the reason for showing, in Fig. 3(b), the Purcell factor for an aspect ratio of $D/H = 0.933$ for the disk without substrate corresponding to the crossing of the Q factor of the two modes in Fig. 2(b). For the case with substrate, we consider the aspect ratio $D/H = 0.944$ as it corresponds to the avoided crossing of the imaginary parts of the eigenvalues as can be seen from the Q-factor trajectories in Fig. 2(f). This avoided crossing is caused by the interference of the interacting modes. Therefore, we expect that the interference will be seen in the contributions of the modal expansion. The Purcell factor again shows a distinct maximum, with a value of $\Gamma \approx 8$ with substrate and $\Gamma \approx 10$ without substrate. However, as expected, both modal contributions have the same order of magnitude. Also, the qualitative shape of both spectra of the modal Purcell factors are approximately mirror-symmetric to each other with respect to the resonance wavelength. This behavior yields the fact that, away from

the resonance, the signs of the modal contributions of the two modes are opposite, leading to destructive interference in these spectral regions. This is the case in Fig. 3(b) for wavelengths below $\sim$1210 nm and above $\sim$1230 nm. For the case including a substrate in Fig. 3(d), we observe a similar behavior for wavelengths below $\sim$1225 nm and above $\sim$1245 nm. The destructive interference between modes has been used previously to qualitatively describe the appearance of quasi-BICs [40]. In the present study, we show that the effect can be quantified by using modal expansion techniques.

Note that the interplay between the modes at the optimal aspect ratio becomes visible when the position of the dipole is moved away from the hot spot of the high-Q mode. Corresponding simulation results can be found in the Appendix.

IV. MODAL ANALYSIS OF RADIATION PATTERNS

It is well known that the coupling with nanostructures can alter the radiation pattern of a quantum emitter [3]. This ability to control the emission pattern of a dipole emitter with nanostructures has a great practical interest since it can improve the collection of the emitted field with an optical system. A modal analysis allows to understand how each mode but also the interferences between modes modifies the emission pattern. We will consider the far-field pattern of the energy flux density
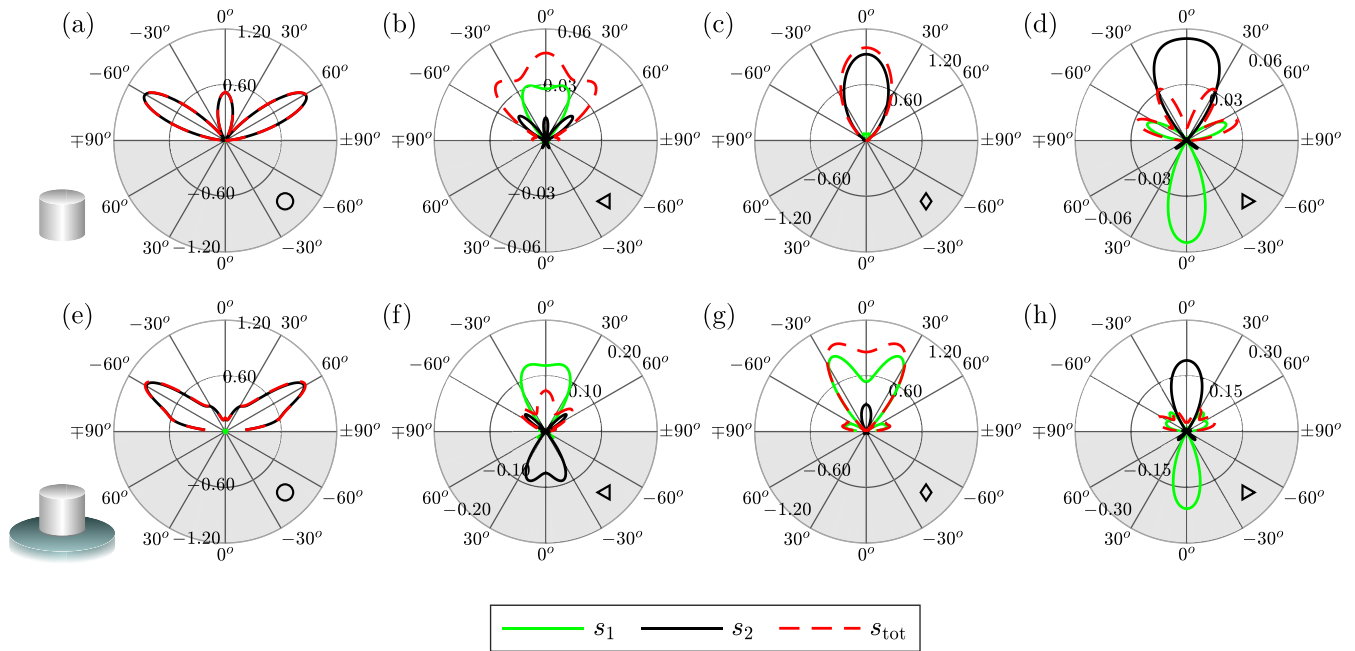
FIG. 4. Modal decomposition of the θ-dependent, normalized radiation patterns toward the top for a dipole on the symmetry axis 20 nm and 27 nm below the top face of the nanodisk in the case without substrate (a–d) and with substrate (e–h), respectively. The green (black) solid curve corresponds to the angle-resolved, far-field modal energy flux s_1 (s_2) corresponding to the low-Q (high-Q) mode. The red dashed curve corresponds to the total energy flux s_{tot}. The upper half of each diagram shows positive contributions while the lower half in gray shows negative contributions. The dipole emission wavelengths correspond to the different Γ markers in Fig. 3 which are reproduced in the right bottom of each emission diagram. Panels (a, e) show the on-resonant far-field radiation for nanodisks supporting the quasi-BIC ($D/H = 0.909$ and $\lambda = 1206$ nm, respectively, $D/H = 0.92$ and $\lambda = 1219$ nm) with clearly dominating contribution from the high-Q mode. Panels (b–d) [respectively, panels (f–h)] show the far-field radiation for nanodisks with aspect ratios of $D/H = 0.933$, respectively, $D/H = 0.944$ (i.e., at the avoided crossing, respectively, crossing of the eigenfrequencies, cf. Figs. 2(a) and 2(e) for on-resonant sources [$\lambda = 1217$ nm, 1237 nm in panels (c) and (g)] and off-resonant sources [$\lambda = 1204$ nm, 1234 nm, 1219 nm, and 1247 nm in panels (b), (d), (f), and (h), respectively]. While for on-resonant sources a single mode is predominantly contributing to the far-field pattern (c, g), in off-resonant settings, the two relevant modes can interfere constructively (b) or destructively (d, f, h), as can be seen from the equal or different signs of the two dominant modal contributions in each case.

defined as $s(\mathbf{r}, \omega) = \frac{1}{2}\Re[\mathbf{E}^*(\mathbf{r}, \omega) \times \frac{1}{i\omega\mu_0}\nabla \times \mathbf{E}(\mathbf{r}, \omega)] \cdot \mathbf{n}$, i.e., the projection of the Poynting vector on the normal vector $\mathbf{n}$ in the direction of field propagation. The modal expansion of $s(\mathbf{r}, \omega)$ is computed using Riesz projections [63,64] leading to the expression $s(\mathbf{r}, \omega) = \sum_{n=1}^{2} s_n(\mathbf{r}, \omega) + s_{\text{background}}(\mathbf{r}, \omega)$, where $\mathbf{r}$ is a point located in the far-field. We will in particular look at the dependency of the radiation pattern with θ in the x-z plane. In Fig. 4, the field patterns radiated by the dipole upwards toward the air are plotted for different wavelengths and for different aspect ratios. In Figs. 4(a)–4(d), results are shown for the nanodisk without substrate for aspect ratios equal to 0.909 and 0.933 while Figs. 4(g)–4(h) display results for the nanodisk on a substrate for aspect ratios equal to 0.92 and 0.944. Please note that the lower region of the plot shown in gray does not correspond to the field radiated downwards but to the negative modal contributions. Negative contributions are particularly important here, since, as for the Purcell factor, they are linked to the interferences between different modal contributions. Radiation pattern toward the substrate are actually shown in the Appendix. In Figs. 4(a) and 4(e), we show the radiation pattern and its modal expansion at the aspect ratio and wavelength of the quasi-BIC. Just like for the Purcell factor, one mode has a much larger Q factor than

the other, it is not surprising to find that the radiation pattern can then be almost entirely understood from the contribution of the high-Q mode while the contributions from the low-Q mode is negligible compared to the contribution of the high-Q mode. The results of the modal expansion of the radiation pattern for the nanodisk without substrate with the aspect ratio equal to 0.933 are plotted in Figs. 4(b)–4(d). These computations are made for the wavelengths on both sides of the main peak in Fig. 3(b), with 1204 nm, 1217 nm, and 1234 nm in Figs. 4(b)–4(d), respectively.

For $\lambda = 1204$ nm, we obtain a positive contribution for both the modes summing up to a radiation lobe between $\sim \pm 45°$. For $\lambda = 1217$ nm, the main contribution is from mode 2 leading to a quite directional emission between $\sim \pm 30°$. Eventually, for $\lambda = 1234$ nm, an interference between the two main modal contributions is observed with a positive contribution from mode 2 between $\pm 30°$ and a negative contribution of mode 1 in the same range. In Figs. 4(f)–4(h), we show the results of the modal expansions for the nanodisk on substrate with $D/H = 0.944$ for the wavelengths 1215 nm, 1237 nm, and 1247 nm, respectively. In Fig. 4(f), for $\lambda = 1215$ nm, the mode 1 has a positive contribution for angles between roughly 30 and -30 degrees while the mode 2 has a negative

contribution in the same range of angles. Consequently, the total radiation pattern is suppressed, resulting from the interference between several modes. A very analogous behavior is observed at $\lambda = 1247$ nm in Fig. 4(h), however, in this case, mode 1 has a negative contribution while mode 2 has a positive contribution. There is, again, a strong interference between the two modes and the far-field pattern cannot be understood without taking this interference into account. Finally, in Fig. 4(g), for $\lambda = 1237$ nm corresponding to the peak of the Purcell factor in Fig. 3(b), we observe that the contribution from both modes of interest add up leading to a larger amplitude of the radiation by the dipole and to a confined far-field pattern.

V. CONCLUSIONS

We have numerically analyzed dielectric nanodisk resonators which support multiple resonances in overlapping frequency ranges. Using a finite-element-method-based framework, regimes where the resonators support quasi-BIC resonances have been investigated. The impact of the resonances on the Purcell factor describing the emission enhancement of a localized source has been shown in the quasi-BIC regime as well as in adjacent parameter regimes where several competing resonances are excited. The modal contributions to the Purcell factor have been computed using the Riesz projection method, and it has been shown that a single QNM causes the strongly enhanced dipole emission in the quasi-BIC situation. Further, we have investigated the modal, angular resolved far-field spectrum in on-resonance as well as off-resonance conditions. This demonstrated that modal interference strongly impacts both, far-field emission strength as well as angular resolved radiation patterns. It has been shown that micron-scale dielectric resonators supporting quasi-BICs allow for high Purcell enhancement as well as for highly directed emission of light. We expect that, apart from the gained insight in the complex interference behavior in multimodal resonators, these findings will allow for the design of efficient and robust future photonic components, such as single-photon emitters for quantum technology applications.

APPENDIX A: RIESZ PROJECTION PRINCIPLE AND RESULTS

Our approach for carrying out modal expansions relies on Riesz projections [52,63,64]. In a first step, the quantity of interest at real frequencies ω_0 is expressed as a contour integral using Cauchy's integral formula. To this end, it has to be analytically continued to the complex frequency plane. In a second step, the resonance expansion is obtained by deforming the contour around ω_0 until it encloses neighboring poles of the physical system and by the application of Cauchy's residue theorem. Each summand of the expansion corresponds to a contour integral.

Using the example of the Purcell factor $\Gamma(\omega_0) = -\frac{1}{2}\Re[\mathbf{E}(\omega_0, \mathbf{r}_d) \cdot \mathbf{j}^*(\omega_0, \mathbf{r}_d)]/\Gamma_b(\omega_0)$, whose expansion is shown in Fig. 3 of the main document, the first step yields

$$\Gamma(\omega_0) = -\frac{1}{2\Gamma_b(\omega_0)} \oint_{C_0} \frac{\Re[\mathbf{E}(z, \mathbf{r}_d) \cdot \mathbf{j}^*(z, \mathbf{r}_d)]}{z - \omega_0} dz,$$

where C_0 is a contour around ω_0. The second step results in the desired expansion of the Purcell factor,

$$\Gamma(\omega_0) = \sum_n \Gamma_n(\omega_0) + \Gamma_{\text{background}}(\omega_0),$$

with

$$\Gamma_n(\omega_0) = -\frac{1}{2\Gamma_b(\omega_0)}$$
$$\times \oint_{C_n} \frac{\Re[\mathbf{E}(z, \mathbf{r}_d) \cdot \mathbf{j}^*(z, \mathbf{r}_d)]}{z - \omega_0} dz \quad \text{and}$$
$$\Gamma_{\text{background}}(\omega_0) = -\frac{1}{2\Gamma_b(\omega_0)}$$
$$\times \oint_{C_{\text{background}}} \frac{\Re[\mathbf{E}(z, \mathbf{r}_d) \cdot \mathbf{j}^*(z, \mathbf{r}_d)]}{z - \omega_0} dz.$$

The contour C_n is the contour around the nth pole and $C_{\text{background}}$ is the large outer contour. Please refer to Fig. 5 and note that, for quantities linear in the electric field, such as the Purcell factor in the given form, the complex conjugate poles located in the upper half of the complex plane can be ignored. The integrals are computed numerically using the trapezoidal rule for the used circular and ellipsoidal contours.

In Sec. IV, we expand the far-field pattern of the radiated flux which is quadratic in the electric field, $s[\mathbf{E}(\omega), \mathbf{E}^*(\omega)] = \frac{1}{2}\Re[\mathbf{E}^*(\omega) \times \frac{1}{i\omega\mu_0}\nabla \times \mathbf{E}(\omega)] \cdot \mathbf{n}$, and hence involves its complex conjugate. The method for expanding quadratic forms was developed in [63]. The application of Cauchy's residue theorem requires a holomorphic expression and therefore does not allow for complex conjugation. As the electric field is a real quantity in the time domain, we have $\mathbf{E}^*(\omega) = \mathbf{E}(-\omega)$ for real ω. With the analytic continuation to the complex plane $\mathbf{E}^\circ(\omega)$ of $\mathbf{E}(-\omega)$, the holomorphic expression $s[\mathbf{E}(\omega), \mathbf{E}^\circ(\omega)] = \frac{1}{2}\Re[\mathbf{E}^\circ(\omega) \times \frac{1}{i\omega\mu_0}\nabla \times \mathbf{E}(\omega)] \cdot \mathbf{n}$ is defined. The poles of $\mathbf{E}^\circ(\omega)$ are located in the upper part of the complex plane. They are the complex conjugates of the resonance poles associated with $\mathbf{E}(\omega)$ as shown in Fig. 5. The expansion of $s[\mathbf{E}(\omega), \mathbf{E}^\circ(\omega)]$ consequently features resonant terms from poles in the lower and the upper part of the complex plane. Following this approach [63], one can derive the
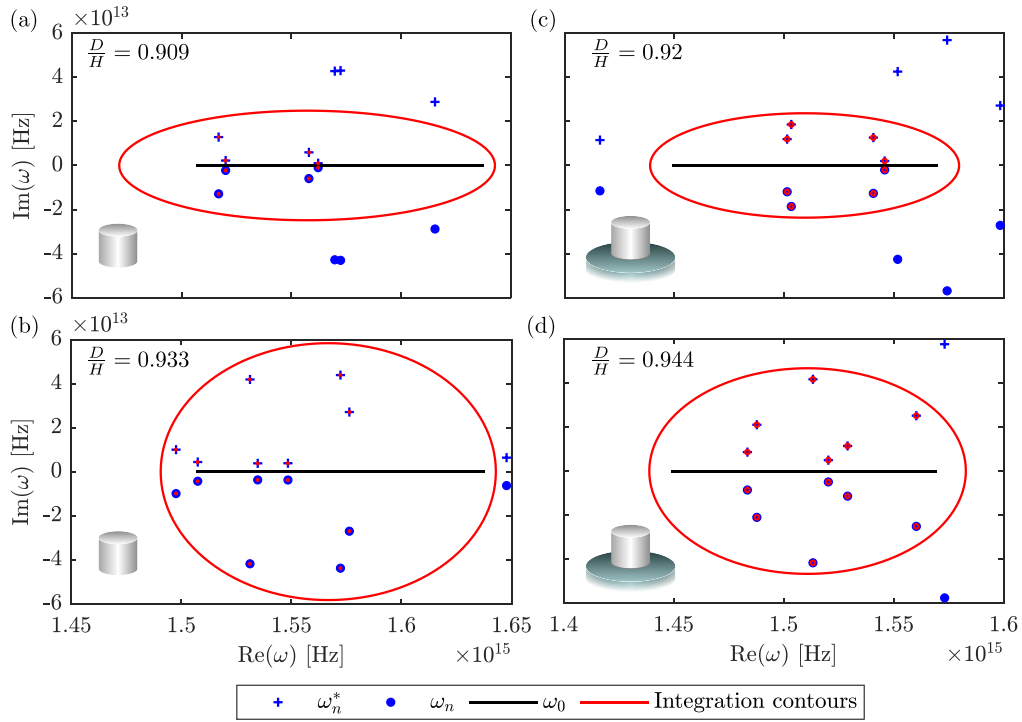
FIG. 5. Contours used for the modal expansions of Purcell factor and emission pattern of a nanodisk with different aspect ratios D/H, either isolated or placed on a substrate. While the emission pattern is based on a quadratic form and requires contours around the complex conjugate resonance frequencies ω_n^*, which are the poles of $\mathbf{E}^\circ(\omega)$, the circular contours in the upper half space can be ignored for the Purcell factor.

expansion of $s[\mathbf{E}(\omega), \mathbf{E}^\circ(\omega)]$,

$$
\begin{aligned}
s[\mathbf{E}(\omega_0), \mathbf{E}^\circ(\omega_0)] = & -\sum_n \frac{1}{2i\pi} \oint_{C_n} \frac{s[\mathbf{E}(z), \mathbf{E}^\circ(z)]}{z - \omega_0} dz \\
& -\sum_n \frac{1}{2i\pi} \oint_{C_n^*} \frac{s[\mathbf{E}(z), \mathbf{E}^\circ(z)]}{z - \omega_0} dz \\
& + \frac{1}{2i\pi} \oint_{C_{\text{background}}} \frac{s[\mathbf{E}(z), \mathbf{E}^\circ(z)]}{z - \omega_0} dz,
\end{aligned}
$$

where C_n is again the contour around the nth pole and $C_{\text{background}}$ is the large background contour. As mentioned above, we have to add the contours around poles in the upper part of the complex plane, which we denote by C_n^*. The expansion of the radiation pattern toward the air is discussed in Sec. IV. Here, for the sake of completeness, we show the expansion of the radiation toward the substrate at the same wavelengths and aspect ratios as in Fig. 4. Overall, the same behavior is observed for the flux radiated toward the substrate as it was for the flux radiated toward the air. In Fig. 6(a), one
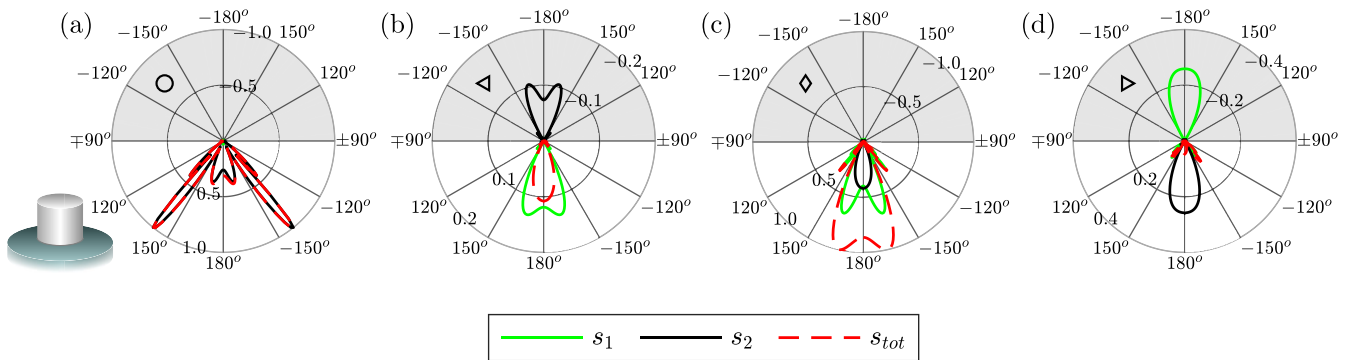
FIG. 6. Modal analysis of the radiation pattern toward the substrate for a dipole located on the symmetry axis 27 nm below the upper base of the nanodisk. The black markers refer to Fig. 3 where they mark the corresponding wavelengths. The optimized system ($D/H = 0.92$) shown in panel (a) illustrates the dominance of a single mode. For panels (b)–(d) the aspect ratio is $D/H = 0.944$. Here, the radiation pattern results from the interference between two dominant modes. In panel (b), the pattern is shown at a wavelength blue shifted from the maximal Purcell enhancement, in panel (c), at the maximum and, in panel (d), at a red shifted wavelength.

can see that the modal contribution from the high-Q mode dominates all the other contributions. Figures 6(b)–6(d) show once more that the radiation pattern of the flux results from the interference of the two main modes. In Figs. 6(b) and 6(d), they interfere destructively and, in Fig. 6(c), constructively.

APPENDIX B: COUPLING OF RESONANCES

In the main text, we employed a phenomenological method to study the mode coupling. We used the following expressions for the coupled eigenfrequencies:

$$\omega_\pm = \left(\frac{\omega_{\mathrm{un},1} + \omega_{\mathrm{un},2}}{2}\right) \pm \sqrt{\gamma}, \tag{B1}$$

where

$$\gamma = \left(\frac{\omega_{\mathrm{un},1} - \omega_{\mathrm{un},2}}{2}\right)^2 + v^2, \tag{B2}$$

with v being the coupling coefficient. While we then focused on explaining the crossings and avoided crossings of real and imaginary parts of the resonances as a consequence of different coupling regimes, these formulas can provide further insight into the couplings between resonances. Some additional results based on these formulas are provided in the following.

We will study the following uncoupled resonance frequencies:

$$\omega_{\mathrm{un},1} = 1 - i0.01,$$
$$\omega_{\mathrm{un},2} = 1 + \Delta - i(0.01 + \Delta\omega_i). \tag{B3}$$

For this study, we keep a fixed value of $\Delta\omega_i = 0.0025$ and study the trajectories of the coupled eigenvalues when Δ is varied. The impact of the value of v on the coupling of resonances will be studied for two cases: in the first case v is real-valued and positive and in the second case v^2 is purely imaginary. We will also study the impact of the coupling of the resonances on their respective Q factor.

1. Coupling of resonance for v^2 real and positive

Let us first study the coupling of resonances for a coupling coefficient v which is real and positive. A careful study of the behavior of the function γ in Eq. (B2) reveals three different behaviors depending on the relative values of γ and $\Delta\omega_i$. We can start by reexpressing γ for $\omega_{\mathrm{un},1}$ and $\omega_{\mathrm{un},2}$ defined in Eq. (B3):

$$\gamma = \left(\frac{\Delta - i\Delta\omega_i}{2}\right)^2 + v^2$$
$$= \frac{\Delta^2 + 4v^2 - \Delta\omega_i^2}{4} - i\frac{\Delta * \Delta\omega_i}{2}. \tag{B4}$$
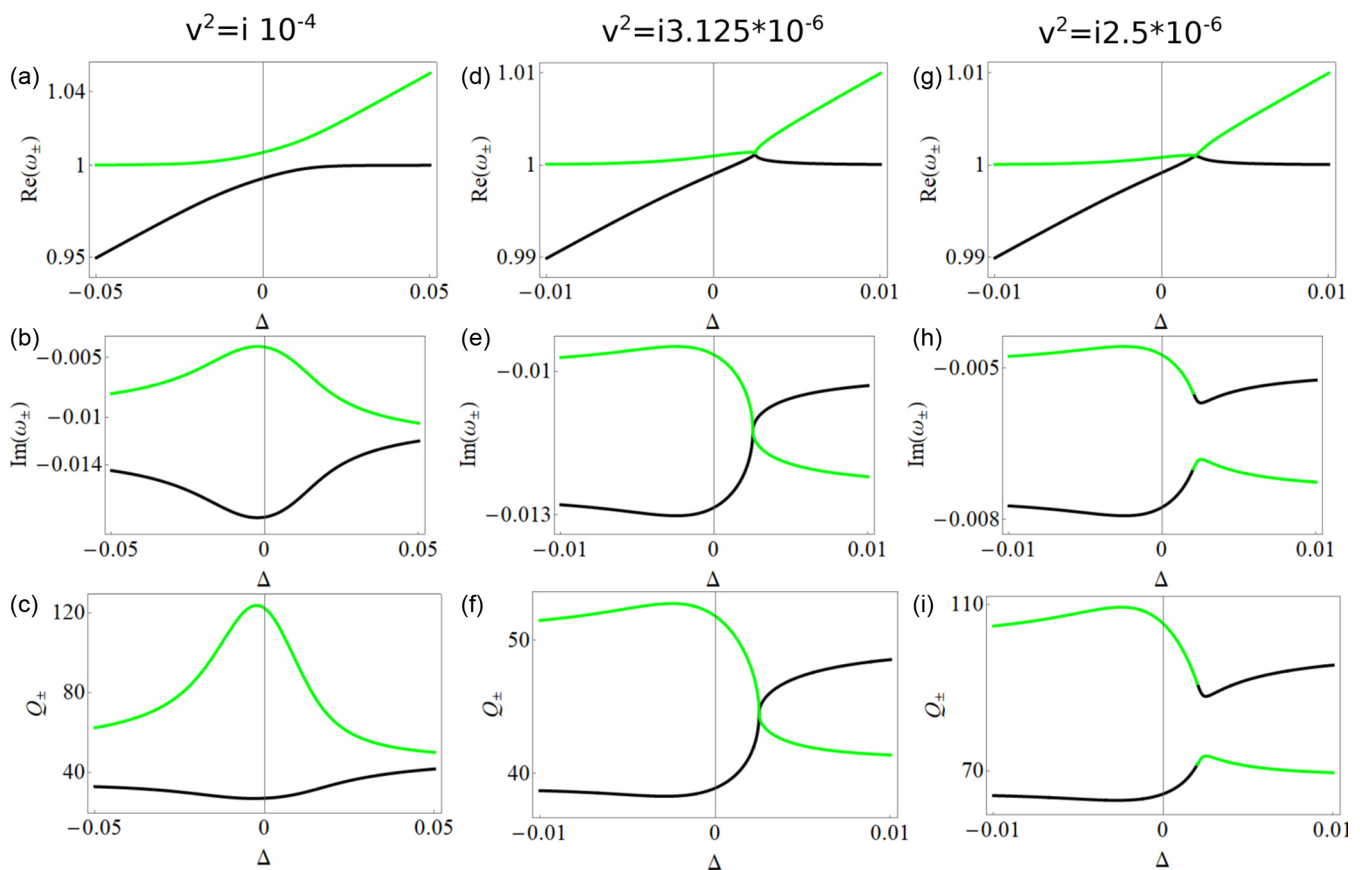
FIG. 7. Real parts $\mathrm{Re}(\omega_\pm)$, imaginary parts $\mathrm{Im}(\omega_\pm)$ and Q factors $Q_\pm$ of the two coupled frequencies $\omega_\pm$ as a function of the difference of the real parts of the uncoupled eigenfrequencies $\Delta = \mathrm{Re}(\omega_{un,2} - \omega_{un,1})$. The trajectories are given for three different couplings v^2, with v being real and positive. For better readability a vertical line is shown at $\Delta = 0$.
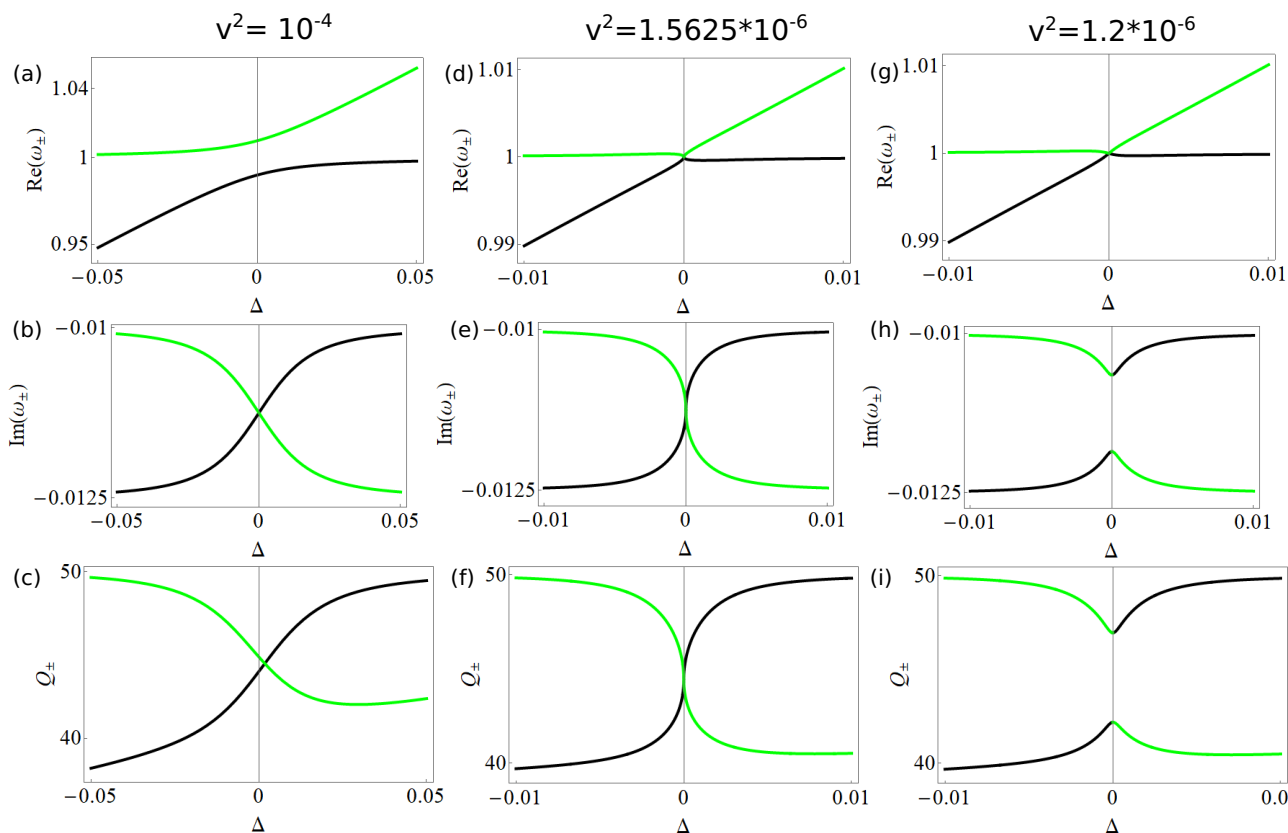
FIG. 8. Real parts $\mathrm{Re}(\omega_\pm)$, imaginary parts $\mathrm{Im}(\omega_\pm)$ and Q factors $Q_\pm$ of the two coupled frequencies $\omega_\pm$ as a function of the difference of the real parts of the uncoupled eigenfrequencies $\Delta = \mathrm{Re}(\omega_{un,2} - \omega_{un,1})$. The trajectories are given for three different couplings $v^2 = iu$, with u being real and positive. For better readability a vertical line is shown at $\Delta = 0$.

One notices that the real part of γ cancels out for $\Delta = \pm\sqrt{\Delta\omega_i^2 - 4v^2}$[1] while its imaginary part cancels out for $\Delta = 0$. Studying the roots of the real part of γ, three regimes of coupling can then be distinguished depending on the relative values of v^2 and $\Delta\omega_i^2$: $v^2 > \frac{\Delta\omega_i^2}{4}$, $v^2 = \frac{\Delta\omega_i^2}{4}$, and $v^2 < \frac{\Delta\omega_i^2}{4}$. In the example we study, $\frac{\Delta\omega_i^2}{4} = 1.5625 * 10^{-6}$. We then plot the trajectories of the real and imaginary parts of the coupled eigenvalues for v^2 larger, equal and smaller than $1.5625 * 10^{-6}$. The results are plotted in the following figures along with the variation of the Q factor as a function of Δ.

In Figs. 7(a)–7(c), we plot these trajectories for $v^2 = 10^{-4}$ and thus larger than $1.5625 * 10^{-6}$. The trajectories of the eigenvalues display a behavior typical for a strong coupling as discussed in the main text with an avoided crossing of the real parts and a crossing of the imaginary parts. On both sides of this crossing, the Q factor of one mode increases while the Q factor of the other one decreases.

The trajectories of the eigenvalues when $v^2 = 1.5625 * 10^{-6}$ are shown in Figs. 7(d)–7(f). It is clearly seen that the real part and the imaginary parts cross at $\Delta = 0$. The two eigenfrequencies are thus completely degenerated at $\Delta = 0$ which is linked to the existence of an exceptional point, a degeneracy existing in non-Hermitian systems. The behavior of the Q factor is similar to the one observed in Fig. 7(c).

Finally, the trajectories for $v^2 < 1.5625 * 10^{-6}$ are shown in Figs. 7(g)–7(i). In this case, there is a crossing of the real part and an avoided crossing of the imaginary part. ω_+ and ω_-

are actually swapped on one side and the other of $\Delta = 0$. This behavior might certainly be seen as a jump from one Riemann sheet to the other.

2. Coupling of resonance for v^2 purely imaginary

A similar analysis to the one done in the previous section can be performed for v^2 which is purely imaginary $v^2 = iu$ with u being real-valued. γ can then be rewritten in the following way:

$$\gamma = \left(\frac{\Delta - i\Delta\omega_i}{2}\right)^2 + v^2$$

$$= \frac{\Delta^2 - \Delta\omega_i^2}{4} - i\frac{\Delta * \Delta\omega_i - 2u}{2}. \tag{B5}$$

This time, the roots of the real part of γ occur for $\Delta = \pm\Delta\omega_i$ while the imaginary part of γ vanishes for $\Delta = \frac{2u}{\Delta\omega_i}$. The different regimes of coupling now depend on the relative values of $\Delta\omega_i$ and $\frac{2u}{\Delta\omega_i}$ or equivalently the relative values of u and $\frac{\Delta\omega_i^2}{2}$. We will then study the coupling of resonances when $u > \frac{\Delta\omega_i^2}{2}$, $u = \frac{\Delta\omega_i^2}{2}$ and finally $u < \frac{\Delta\omega_i^2}{2}$. In the case we study, $\frac{\Delta\omega_i^2}{2} = 3.125 * 10^{-6}$. The trajectories of the coupled eigenvalues for $u = 10^{-4}$ so larger than $\frac{\Delta\omega_i^2}{2}$ are shown in Figs. 8(a)–8(c). These trajectories display a strong coupling behavior with an avoided crossing of the real parts of the coupled eigenvalues. This avoided crossing coincide this time

with a peal of the imaginary part of one eigenvalue and a dip of the other one. As a consequence there is a peak of the Q factor associated with one eigenvalue and a dip of the Q factor of the other eigenvalue.

The trajectories of the eigenvalues for $u = 3.125 10^{-6}$ which is equal to $\frac{\Delta \omega_i^2}{2}$ are shown in Figs. 8(d)–8(f). This reveals the existence of an degeneracy of the eigenvalue, i.e., an exceptional point, where both the real and imaginary parts of the two eigenvalues are identical.

Finally, when $u = 2.5 10^{-6}$ which is smaller than $\frac{\Delta \omega_i^2}{2}$ the trajectories of the eigenvalues are displayed the behavior observed in Figs. 8(g)–8(i). These trajectories reveal a weak coupling behavior with a crossing of the real part of the coupled eigenvalues and an anticrossing of the imaginary part.

APPENDIX C: ADDITIONAL CALCULATIONS FOR THE EMISSION OF A DIPOLE EMITTER

In the main text we keep the position of the dipole emitter fixed and show how the coupling effects the modal contributions $\Gamma_n(\omega)$ of the Purcell enhancement at the hot spot of the high-Q mode. $\Gamma_n(\omega)$ depends on the electric field strength at the dipole position and if the quasi BIC condition is met, the contribution of the low-Q mode at this point is much smaller. For a slightly altered aspect ratio the field values become comparable and interference can be observed. Instead of varying the aspect ratio, one can also consider the enhancement at different dipole positions. For the sake of completeness in
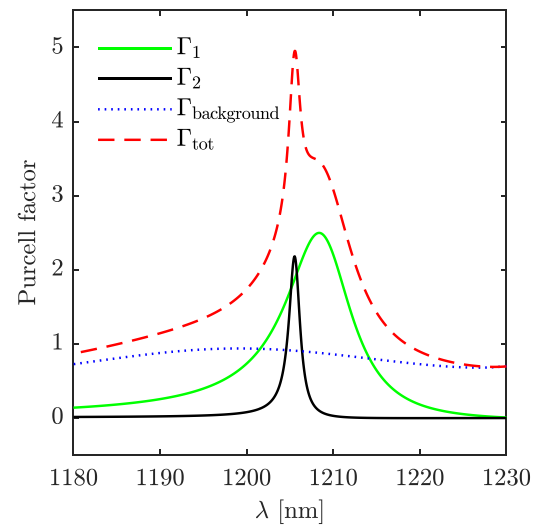
FIG. 9. Purcell factor for a dipole located close to the hot spot of the low-Q mode, on the symmetry axis 700 nm above the bottom of the nanodisk. The contributions of both modes are similar and positive at this position leading to a total Purcell factor which is the superposition of the two main modes.

Fig. 9 we provide a corresponding example where the contributions of both modes are similar. For this example the dipole is positioned at the symmetry axis close to the center of the nanodisk 700 nm above the bottom face.

---

[1] S. A. Maier and H. A. Atwater, Plasmonics: Localization and guiding of electromagnetic energy in metal/dielectric structures, J. Appl. Phys. **98**, 011101 (2005).

[2] S. A. Maier, *Plasmonics: Fundamentals and Applications* (Springer Science & Business Media, Berlin, 2007).

[3] L. Novotny and N. Van Hulst, Antennas for light, Nat. Photon. **5**, 83 (2011).

[4] L. Novotny and B. Hecht, *Principles of Nano-optics* (Cambridge University Press, Cambridge, UK, 2012).

[5] A. B. Evlyukhin, C. Reinhardt, A. Seidel, B. S. Luk'yanchuk, and B. N. Chichkov, Optical response features of Si-nanoparticle arrays, Phys. Rev. B **82**, 045404 (2010).

[6] A. García-Etxarri, R. Gómez-Medina, L. S. Froufe-Pérez, C. López, L. Chantada, F. Scheffold, J. Aizpurua, M. Nieto-Vesperinas, and J. J. Sáenz, Strong magnetic response of submicron silicon particles in the infrared, Opt. Express **19**, 4815 (2011).

[7] A. I. Kuznetsov, A. E. Miroshnichenko, M. L. Brongersma, Y. S. Kivshar, and B. Luk'yanchuk, Optically resonant dielectric nanostructures, Science **354**, aag2472 (2016).

[8] A. I. Barreda, J. M. Saiz, F. González, F. Moreno, and P. Albella, Recent advances in high refractive index dielectric nanoantennas: Basics and applications, AIP Adv. **9**, 040701 (2019).

[9] I. Aharonovich, S. Castelletto, D. A. Simpson, C.-H. Su, A. D. Greentree, and S. Prawer, Diamond-based single-photon emitters, Rep. Prog. Phys. **74**, 076501 (2011).

[10] P. Lodahl, S. Mahmoodian, and S. Stobbe, Interfacing single photons and single quantum dots with photonic nanostructures, Rev. Mod. Phys. **87**, 347 (2015).

[11] E. M. Purcell, Spontaneous emission probabilities at radio frequencies, Phys. Rev. **69**, 674 (1946).

[12] K. Drexhage, Influence of a dielectric interface on fluorescence decay time, J. Lumin. **1**, 693 (1970).

[13] A. L. Holsteen, S. Raza, P. Fan, P. G. Kik, and M. L. Brongersma, Purcell effect for active tuning of light scattering from semiconductor optical antennas, Science **358**, 1407 (2017).

[14] P. Albella, M. A. Poyli, M. K. Schmidt, S. A. Maier, F. Moreno, J. J. Sáenz, and J. Aizpurua, Low-loss electric and magnetic field-enhanced spectroscopy with subwavelength silicon dimers, J. Phys. Chem. C **117**, 13573 (2013).

[15] X. Zambrana-Puyalto and N. Bonod, Purcell factor of spherical Mie resonators, Phys. Rev. B **91**, 195422 (2015).

[16] B. Rolly, B. Bebey, S. Bidault, B. Stout, and N. Bonod, Promoting magnetic dipolar transition in trivalent lanthanide ions with lossless Mie resonances, Phys. Rev. B **85**, 245432 (2012).

[17] M. K. Schmidt, R. Esteban, J. Sáenz, I. Suárez-Lacalle, S. Mackowski, and J. Aizpurua, Dielectric antennas—A suitable platform for controlling magnetic dipolar emission, Opt. Express **20**, 13636 (2012).

[18] M. Sanz-Paz, C. Ernandes, J. U. Esparza, G. W. Burr, N. F. van Hulst, A. Maitre, L. Aigouy, T. Gacoin, N. Bonod, M. F. Garcia-Parajo *et al.*, Enhancing magnetic light emission with all-dielectric optical nanoantennas, Nano Lett. **18**, 3481 (2018).

[19] A. Vaskin, S. Mashhadi, M. Steinert, K. E. Chong, D. Keene, S. Nanz, A. Abass, E. Rusak, D.-Y. Choi, I. Fernandez-Corbaton *et al.*, Manipulation of magnetic dipole emission from Eu^{3+} with Mie-resonant dielectric metasurfaces, Nano Lett. **19**, 1015 (2019).

[20] H. Sugimoto and M. Fujii, Magnetic Purcell enhancement by magnetic quadrupole resonance of dielectric nanosphere antenna, ACS Photon. **8**, 1794 (2021).

[21] S. Karaveli and R. Zia, Spectral Tuning by Selective Enhancement of Electric and Magnetic Dipole Emission, Phys. Rev. Lett. **106**, 193004 (2011).

[22] D. G. Baranov, R. S. Savelev, S. V. Li, A. E. Krasnok, and A. Alù, Modifying magnetic dipole spontaneous emission with nanophotonic structures, Laser Photonics Rev. **11**, 1600268 (2017).

[23] V. Rutckaia, F. Heyroth, A. Novikov, M. Shaleev, M. Petrov, and J. Schilling, Quantum dot emission driven by Mie resonances in silicon nanostructures, Nano Lett. **17**, 6886 (2017).

[24] A. Barreda, S. Hell, M. Weissflog, A. Minovich, T. Pertsch, and I. Staude, Metal, dielectric, and hybrid nanoantennas for enhancing the emission of single quantum dots: A comparative study, J. Quant. Spectrosc. Radiat. Transfer **276**, 107900 (2021).

[25] B. Casabone, C. Deshmukh, S. Liu, D. Serrano, A. Ferrier, T. Hümmer, P. Goldner, D. Hunger, and H. de Riedmatten, Dynamic control of Purcell enhanced emission of erbium ions in nanoparticles, Nat. Commun. **12**, 3570 (2021).

[26] A. S. Zalogina, R. Savelev, E. V. Ushakova, G. Zograf, F. Komissarenko, V. Milichko, S. Makarov, D. Zuev, and I. Shadrivov, Purcell effect in active diamond nanoantennas, Nanoscale **10**, 8721 (2018).

[27] C. W. Hsu, B. Zhen, A. D. Stone, J. D. Joannopoulos, and M. Soljačić, Bound states in the continuum, Nat. Rev. Mater. **1**, 16048 (2016).

[28] K. Koshelev, A. Bogdanov, and Y. Kivshar, Meta-optics and bound states in the continuum, Sci. Bull. **64**, 836 (2019).

[29] P. Tonkaev and Y. Kivshar, High-Q dielectric Mie-resonant nanostructures, JETP Lett. **112**, 615 (2020).

[30] J. Lee, B. Zhen, S.-L. Chua, W. Qiu, J. D. Joannopoulos, M. Soljačić, and O. Shapira, Observation and Differentiation of Unique High-Q Optical Resonances Near Zero Wave Vector in Macroscopic Photonic Crystal Slabs, Phys. Rev. Lett. **109**, 067401 (2012).

[31] H. Friedrich and D. Wintgen, Interfering resonances and bound states in the continuum, Phys. Rev. A **32**, 3231 (1985).

[32] C. W. Hsu, B. Zhen, J. Lee, S.-L. Chua, S. G. Johnson, J. D. Joannopoulos, and M. Soljačić, Observation of trapped light within the radiation continuum, Nature (London) **499**, 188 (2013).

[33] F. Monticone and A. Alu, Embedded Photonic Eigenvalues in 3D Nanostructures, Phys. Rev. Lett. **112**, 213903 (2014).

[34] J. Wiersig, Formation of Long-Lived, Scarlike Modes Near Avoided Resonance Crossings in Optical Microcavities, Phys. Rev. Lett. **97**, 253901 (2006).

[35] Q. H. Song and H. Cao, Improving Optical Confinement in Nanostructures Via External Mode Coupling, Phys. Rev. Lett. **105**, 053902 (2010).

[36] M. V. Rybin, K. L. Koshelev, Z. F. Sadrieva, K. B. Samusev, A. A. Bogdanov, M. F. Limonov, and Y. S. Kivshar, High-Q

Supercavity Modes in Subwavelength Dielectric Resonators, Phys. Rev. Lett. **119**, 243901 (2017).

[37] A. A. Bogdanov, K. L. Koshelev, P. V. Kapitanova, M. V. Rybin, S. A. Gladyshev, Z. F. Sadrieva, K. B. Samusev, Y. S. Kivshar, and M. F. Limonov, Bound states in the continuum and Fano resonances in the strong mode coupling regime, Adv. Photonics **1**, 016001 (2019).

[38] K. Koshelev and Y. Kivshar, Dielectric resonant metaphotonics, ACS Photon. **8**, 102 (2021).

[39] E. Melik-Gaykazyan, K. Koshelev, J.-H. Choi, S. S. Kruk, A. Bogdanov, H.-G. Park, and Y. Kivshar, From Fano to quasi-BIC resonances in individual dielectric nanoantennas, Nano Lett. **21**, 1765 (2021).

[40] K. Koshelev, A. Bogdanov, and Y. Kivshar, Engineering with bound states in the continuum, Opt. Photon. News **31**, 38 (2020).

[41] L. Carletti, K. Koshelev, C. De Angelis, and Y. Kivshar, Giant Nonlinear Response at the Nanoscale Driven by Bound States in the Continuum, Phys. Rev. Lett. **121**, 033903 (2018).

[42] L. Carletti, S. S. Kruk, A. A. Bogdanov, C. De Angelis, and Y. Kivshar, High-harmonic generation at the nanoscale boosted by bound states in the continuum, Phys. Rev. Research **1**, 023016 (2019).

[43] K. Koshelev, S. Kruk, E. Melik-Gaykazyan, J.-H. Choi, A. Bogdanov, H.-G. Park, and Y. Kivshar, Subwavelength dielectric resonators for nonlinear nanophotonics, Science **367**, 288 (2020).

[44] V. Mylnikov, S. T. Ha, Z. Pan, V. Valuckas, R. Paniagua-Domínguez, H. V. Demir, and A. I. Kuznetsov, Lasing action in single subwavelength particles supporting supercavity modes, ACS Nano **14**, 7338 (2020).

[45] P. Lalanne, W. Yan, K. Vynck, C. Sauvan, and J.-P. Hugonin, Light interaction with photonic and plasmonic resonances, Laser Photon. Rev. **12**, 1700113 (2018).

[46] K. Koshelev, S. Lepeshov, M. Liu, A. Bogdanov, and Y. Kivshar, Asymmetric Metasurfaces with high-Q Resonances Governed by Bound States in the Continuum, Phys. Rev. Lett. **121**, 193903 (2018).

[47] P. T. Kristensen, K. Herrmann, F. Intravaia, and K. Busch, Modeling electromagnetic resonators using quasinormal modes, Adv. Opt. Photon. **12**, 612 (2020).

[48] T. Wu, M. Gurioli, and P. Lalanne, Nanoscale light confinement: the Q's and V's, ACS Photon. **8**, 1522 (2021).

[49] C. Sauvan, J.-P. Hugonin, I. S. Maksymov, and P. Lalanne, Theory of the Spontaneous Optical Emission of Nanosize Photonic and Plasmon Resonators, Phys. Rev. Lett. **110**, 237401 (2013).

[50] R.-C. Ge, P. T. Kristensen, J. F. Young, and S. Hughes, Quasinormal mode approach to modelling light-emission and propagation in nanoplasmonics, New J. Phys. **16**, 113048 (2014).

[51] E. A. Muljarov and W. Langbein, Exact mode volume and Purcell factor of open optical systems, Phys. Rev. B **94**, 235438 (2016).

[52] L. Zschiedrich, F. Binkowski, N. Nikolay, O. Benson, G. Kewes, and S. Burger, Riesz-projection-based theory of light-matter interaction in dispersive nanoresonators, Phys. Rev. A **98**, 043806 (2018).

[53] A. Kaganskiy, F. Gericke, T. Heuser, T. Heindel, X. Porte, and S. Reitzenstein, Micropillars with a controlled number of site-controlled quantum dots, Appl. Phys. Lett. **112**, 071101 (2018).

[54] C.-H. Yi, J. Kullig, M. Hentschel, and J. Wiersig, Non-Hermitian degeneracies of internal–external mode pairs in dielectric microdisks, Photon. Res. **7**, 464 (2019).

[55] W. D. Heiss, Repulsion of resonance states and exceptional points, Phys. Rev. E **61**, 929 (2000).

[56] J. Pomplun, S. Burger, L. Zschiedrich, and F. Schmidt, Adaptive finite element method for simulation of optical nano structures, Phys. Stat. Sol. **244**, 3419 (2007).

[57] L. Huang, L. Xu, M. Rahmani, D. Neshev, and A. E. Miroshnichenko, Pushing the limit of high-Q mode of a single dielectric nanocavity, Adv. Photon. **3**, 016004 (2021).

[58] W. Yan, P. Lalanne, and M. Qiu, Shape Deformation of Nanoresonator: A Quasinormal-Mode Perturbation Theory, Phys. Rev. Lett. **125**, 013901 (2020).

[59] W. D. Heiss, The physics of exceptional points, J. Phys. A: Math. Theor. **45**, 444016 (2012).

[60] S. R.-K. Rodriguez, Classical and quantum distinctions between weak and strong coupling, Eur. J. Phys. **37**, 025802 (2016).

[61] Z.-L. Deng, F.-J. Li, H. Li, X. Li, and A. Alù, Extreme diffraction control in metagratings leveraging bound states in the continuum and exceptional points, Laser Photon. Rev., 2100617 (2022).

[62] D. R. Abujetas and J. A. Sánchez-Gil, Near-field excitation of bound states in the continuum in all-dielectric metasurfaces through a coupled electric/magnetic dipole model, Nanomaterials **11**, 998 (2021).

[63] F. Binkowski, F. Betz, R. Colom, M. Hammerschmidt, L. Zschiedrich, and S. Burger, Quasinormal mode expansion of optical far-field quantities, Phys. Rev. B **102**, 035432 (2020).

[64] F. Betz, F. Binkowski, and S. Burger, RPEXPAND: Software for Riesz projection expansion of resonance phenomena, SoftwareX **15**, 100763 (2021).

[65] R. Colom, F. Binkowski, F. Betz, Y. Kivshar, and S. Burger, Source code and simulation results for nanoantennas supporting an enhanced Purcell factor due to interfering resonances, Zenodo, 2022, https://doi.org/10.5281/zenodo.6565850.

Bibliography

[1] S. A. Maier and H. A. Atwater. Plasmonics: Localization and guiding of electromagnetic energy in metal/dielectric structures. *J. Appl. Phys.* 98, 011101 (2005). DOI: 10.1063/1.1951057.

[2] L. Novotny and N. van Hulst. Antennas for light. *Nat. Photonics* 5, 83 (2011). DOI: 10.1038/nphoton.2010.237.

[3] L. Novotny and B. Hecht. *Principles of Nano-Optics, 2nd ed.* Cambridge University Press: Cambridge (2012).

[4] N. C. Lindquist, P. Nagpal, K. M. McPeak, et al. Engineering metallic nanostructures for plasmonics and nanophotonics. *Rep. Prog. Phys.* 75, 036501 (2012). DOI: 10.1088/0034-4885/75/3/036501.

[5] S. Nie and S. R. Emory. Probing Single Molecules and Single Nanoparticles by Surface-Enhanced Raman Scattering. *Science* 275, 1102 (1997). DOI: 10.1126/science.275.5303.1102.

[6] J. Langer, D. Jimenez de Aberasturi, J. Aizpurua, et al. Present and Future of Surface-Enhanced Raman Scattering. *ACS Nano* 14, 28 (2020). DOI: 10.1021/acsnano.9b04224.

[7] Y. Zhang, S. He, W. Guo, et al. Surface-Plasmon-Driven Hot Electron Photochemistry. *Chem. Rev.* 118, 2927 (2018). DOI: 10.1021/acs.chemrev.7b00430.

[8] C. Wu, K. Wang, M. Batmunkh, et al. Multifunctional nanostructured materials for next generation photovoltaics. *Nano Energy* 70, 104480 (2020). DOI: 10.1016/j.nanoen.2020.104480.

[9] P. Tockhorn, J. Sutter, A. Cruz, et al. Nano-optical designs for high-efficiency monolithic perovskite–silicon tandem solar cells. *Nat. Nanotechnol.* 17, 1214 (2022). DOI: 10.1038/s41565-022-01228-8.

[10] M. S. Tame, K. R. McEnery, S. K. Özdemir, et al. Quantum plasmonics. *Nature Phys.* 9, 329 (2013). DOI: 10.1038/nphys2615.

[11] P. Senellart, G. Solomon, and A. White. High-performance semiconductor quantum-dot single-photon sources. *Nat. Nanotechnol.* 12, 1026 (2017). DOI: 10.1038/nnano.2017.218.

[12] J. Wang, F. Sciarrino, A. Laing, et al. Integrated photonic quantum technologies. *Nat. Photonics* 14, 273 (2020). DOI: 10.1038/s41566-019-0532-1.

[13] K. J. Vahala. Optical microcavities. *Nature* 424, 839 (2003). DOI: 10.1038/nature01939.

[14] B. Luk'yanchuk, N. I. Zheludev, S. A. Maier, et al. The Fano resonance in plasmonic nanostructures and metamaterials. *Nat. Mater.* 9, 707 (2010). DOI: 10.1038/nmat2810.

[15] P. Lalanne, W. Yan, K. Vynck, et al. Light Interaction with Photonic and Plasmonic Resonances. *Laser Photonics Rev.* 12, 1700113 (2018). DOI: `10.1002/lpor.201700113`.

[16] K. Y. Billah and R. H. Scanlan. Resonance, Tacoma Narrows bridge failure, and undergraduate physics textbooks. *Am. J. Phys.* 59, 118 (1991). DOI: `10.1119/1.16590`.

[17] P. Lancaster. *Lambda-matrices and Vibrating Systems.* Dover Publications: Mineola, New York (2002).

[18] A. Aslanyan, L. Parnovski, and D. Vassiliev. Complex resonances in acoustic waveguides. *Q. J. Mech. Appl. Math.* 53, 429 (2000). DOI: `10.1093/qjmam/53.3.429`.

[19] S. Hein, T. Hohage, and W. Koch. On resonances in open systems. *J. Fluid Mech.* 506, 255 (2004). DOI: `10.1017/S0022112004008584`.

[20] Y. B. Zel'dovich. On the theory of unstable states. *Sov. Phys. JETP* 12, 542 (1961).

[21] R. M. More and E. Gerjuoy. Properties of Resonance Wave Functions. *Phys. Rev. A* 7, 1288 (1973). DOI: `10.1103/PhysRevA.7.1288`.

[22] P. Hislop and I. Sigal. *Introduction to spectral theory. With applications to Schrödinger operators.* Springer: New York (1996).

[23] M. Zworski. Resonances in physics and geometry. *Notices Amer. Math. Soc.* 46, 319 (1999).

[24] S. Dyatlov and M. Zworski. *Mathematical theory of scattering resonances.* American Mathematical Society: Providence, Rhode Island (2019).

[25] T. Wu, M. Gurioli, and P. Lalanne. Nanoscale Light Confinement: the Q's and V's. *ACS Photonics* 8, 1522 (2021). DOI: `10.1021/acsphotonics.1c00336`.

[26] B. Wang, P. Yu, W. Wang, et al. High-Q Plasmonic Resonances: Fundamentals and Applications. *Adv. Opt. Mater.* 9, 2001520 (2021). DOI: `10.1002/adom.202001520`.

[27] E. M. Purcell. Spontaneous emission probabilities at radio frequencies. *Phys. Rev.* 69, 681 (1946). DOI: `10.1103/PhysRev.69.674`.

[28] C. Sauvan, J.-P. Hugonin, I. S. Maksymov, et al. Theory of the Spontaneous Optical Emission of Nanosize Photonic and Plasmon Resonators. *Phys. Rev. Lett.* 110, 237401 (2013). DOI: `10.1103/PhysRevLett.110.237401`.

[29] D. A. Vajner, L. Rickert, T. Gao, et al. Quantum Communication Using Semiconductor Quantum Dots. *Adv. Quantum Technol.* 5, 2100116 (2022). DOI: `10.1002/qute.202100116`.

[30] P. Lalanne, W. Yan, A. Gras, et al. Quasinormal mode solvers for resonators with dispersive materials. *J. Opt. Soc. Am. A* 36, 686 (2019). DOI: `10.1364/JOSAA.36.000686`.

[31] G. Demésy, A. Nicolet, B. Gralak, et al. Non-linear eigenvalue problems with GetDP and SLEPc: Eigenmode computations of frequency-dispersive photonic open structures. *Comput. Phys. Commun.* 257, 107509 (2020). DOI: `10.1016/j.cpc.2020.107509`.

[32] T. Wu, D. Arrivault, W. Yan, et al. Modal analysis of electromagnetic resonators: User guide for the MAN program. *Comput. Phys. Commun.* 284, 108627 (2023). DOI: `10.1016/j.cpc.2022.108627`.

[33] V. Mehrmann and H. Voss. Nonlinear eigenvalue problems: a challenge for modern eigenvalue methods. *GAMM Mitt.* 27, 121 (2005). DOI: `10.1002/gamm.201490007`.

[34] S. Güttel and F. Tisseur. The Nonlinear Eigenvalue Problem. *Acta Numer.* 26, 1 (2017). DOI: `10.1017/S0962492917000034`.

[35] N. W. Ashcroft and N. D. Mermin. *Solid state physics.* Holt, Rinehardt and Winston: New York (1976).

[36] H. S. Sehmi, W. Langbein, and E. A. Muljarov. Optimizing the Drude-Lorentz model for material permittivity: Method, program, and examples for gold, silver, and copper. *Phys. Rev. B* 95, 115444 (2017). DOI: `10.1103/PhysRevB.95.115444`.

[37] M. Garcia-Vergara, G. Demésy, and F. Zolla. Extracting an accurate model for permittivity from experimental data: hunting complex poles from the real line. *Opt. Lett.* 42, 1145 (2017). DOI: `10.1364/OL.42.001145`.

[38] W. Yan, R. Faggiani, and P. Lalanne. Rigorous modal analysis of plasmonic nanoresonators. *Phys. Rev. B* 97, 205422 (2018). DOI: `10.1103/PhysRevB.97.205422`.

[39] Y. Saad. *Numerical Methods for Large Eigenvalue Problems, 2nd ed.* SIAM: Philadelphia (2011).

[40] H. M. Lai, P. T. Leung, K. Young, et al. Time-independent perturbation for leaking electromagnetic modes in open systems with application to resonances in microdroplets. *Phys. Rev. A* 41, 5187 (1990). DOI: `10.1103/PhysRevA.41.5187`.

[41] P. T. Leung, S. Y. Liu, and K. Young. Completeness and orthogonality of quasi-normal modes in leaky optical cavities. *Phys. Rev. A* 49, 3057 (1994). DOI: `10.1103/PhysRevA.49.3057`.

[42] E. A. Muljarov, W. Langbein, and R. Zimmermann. Brillouin-Wigner perturbation theory in open electromagnetic systems. *EPL* 92, 50010 (2010). DOI: `10.1209/0295-5075/92/50010`.

[43] Q. Bai, M. Perrin, C. Sauvan, et al. Efficient and intuitive method for the analysis of light scattering by a resonant nanostructure. *Opt. Express* 21, 27371 (2013). DOI: `10.1364/OE.21.027371`.

[44] F. Zolla, A. Nicolet, and G. Demésy. Photonics in highly dispersive media: the exact modal expansion. *Opt. Lett.* 43, 5813 (2018). DOI: `10.1364/OL.43.005813`.

[45] E. A. Muljarov and T. Weiss. Resonant-state expansion for open optical systems: generalization to magnetic, chiral, and bi-anisotropic materials. *Opt. Lett.* 43, 1978 (2018). DOI: `10.1364/OL.43.001978`.

[46] S. Franke, S. Hughes, M. Kamandar Dezfouli, et al. Quantization of Quasinormal Modes for Open Cavities and Plasmonic Cavity Quantum Electrodynamics. *Phys. Rev. Lett.* 122, 213901 (2019). DOI: `10.1103/PhysRevLett.122.213901`.

[47] P. T. Kristensen, K. Herrmann, F. Intravaia, et al. Modeling electromagnetic resonators using quasinormal modes. *Adv. Opt. Photon.* 12, 612 (2020). DOI: `10.1364/AOP.377940`.

[48] A. Gras, P. Lalanne, and M. Duruflé. Nonuniqueness of the quasinormal mode expansion of electromagnetic Lorentz dispersive materials. *J. Opt. Soc. Am. A* 37, 1219 (2020). DOI: `10.1364/JOSAA.394206`.

[49] T. Wu, D. Arrivault, M. Duruflé, et al. Efficient hybrid method for the modal analysis of optical microcavities and nanoresonators. *J. Opt. Soc. Am. A* 38, 1224 (2021). DOI: `10.1364/JOSAA.428224`.

[50] S. Both and T. Weiss. Resonant states and their role in nanophotonics. *Semicond. Sci. Technol.* 37, 013002 (2021). DOI: `10.1088/1361-6641/ac3290`.

[51] C. Tao, Y. Zhong, and H. Liu. Quasinormal Mode Expansion Theory for Mesoscale Plasmonic Nanoresonators: An Analytical Treatment of Nonclassical Electromagnetic Boundary Condition. *Phys. Rev. Lett.* 129, 197401 (2022). DOI: `10.1103/PhysRevLett.129.197401`.

[52] C. Sauvan, T. Wu, R. Zarouf, et al. Normalization, orthogonality, and completeness of quasinormal modes of open systems: the case of electromagnetism [Invited]. *Opt. Express* 30, 6846 (2022). DOI: `10.1364/OE.443656`.

[53] A. Nicolet, G. Demésy, F. Zolla, et al. Physically agnostic quasi normal mode expansion in time dispersive structures: From mechanical vibrations to nanophotonic resonances. *Eur. J. Mech. A Solids* (2022). DOI: `10.1016/j.euromechsol.2022.104809`.

[54] J. Asakura, T. Sakurai, H. Tadano, et al. A numerical method for nonlinear eigenvalue problems using contour integrals. *JSIAM Lett.* 1, 52 (2009). DOI: `10.14495/jsiaml.1.52`.

[55] E. Polizzi. Density-matrix-based algorithm for solving eigenvalue problems. *Phys. Rev. B* 79, 115112 (2009). DOI: `10.1103/PhysRevB.79.115112`.

[56] W.-J. Beyn. An integral method for solving nonlinear eigenvalue problems. *Linear Algebra Its Appl.* 436, 3839 (2012). DOI: `10.1016/j.laa.2011.03.030`.

[57] S. Yokota and T. Sakurai. A projection method for nonlinear eigenvalue problems using contour integrals. *JSIAM Lett.* 5, 41 (2013). DOI: `10.14495/jsiaml.5.41`.

[58] M. V. Barel and P. Kravanja. Nonlinear eigenvalue problems and contour integrals. *J. Comput. Appl. Math.* 292, 526 (2016). DOI: `https://doi.org/10.1016/j.cam.2015.07.012`.

[59] M. V. Barel. Designing rational filter functions for solving eigenvalue problems by contour integration. *Linear Algebra Its Appl.* 502, 346 (2016). DOI: `10.1016/j.laa.2015.05.029`.

[60] B. Gavin, A. Miedlar, and E. Polizzi. FEAST eigensolver for nonlinear eigenvalue problems. *J. Comput. Sci.* 27, 107 (2018). DOI: `10.1016/j.jocs.2018.05.006`.

[61] M. El-Guide, A. Miedlar, and Y. Saad. A rational approximation method for solving acoustic nonlinear eigenvalue problems. *Eng. Anal. Bound. Elem.* 111, 44 (2020). DOI: 10.1016/j.enganabound.2019.10.006.

[62] P. Jorkowski, K. Schmidt, C. Schenker, et al. Adapted Contour Integration for Nonlinear Eigenvalue Problems in Waveguide Coupled Resonators. *IEEE Trans. Antennas Propag.* 70, 499 (2022). DOI: 10.1109/TAP.2021.3111413.

[63] U. Hohenester, N. Reichelt, and G. Unger. Nanophotonic resonance modes with the nanobem toolbox. *Comput. Phys. Commun.* 276, 108337 (2022). DOI: 10.1016/j.cpc.2022.108337.

[64] L. Zschiedrich, F. Binkowski, N. Nikolay, et al. Riesz-projection-based theory of light-matter interaction in dispersive nanoresonators. *Phys. Rev. A* 98, 043806 (2018). DOI: 10.1103/PhysRevA.98.043806.

[65] F. Binkowski, L. Zschiedrich, M. Hammerschmidt, et al. Modal analysis for nanoplasmonics with nonlocal material properties. *Phys. Rev. B* 100, 155406 (2019). DOI: 10.1103/PhysRevB.100.155406.

[66] F. Binkowski, F. Betz, R. Colom, et al. Quasinormal mode expansion of optical far-field quantities. *Phys. Rev. B* 102, 035432 (2020). DOI: 10.1103/PhysRevB.102.035432.

[67] F. Binkowski, L. Zschiedrich, and S. Burger. A Riesz-projection-based method for nonlinear eigenvalue problems. *J. Comput. Phys.* 419, 109678 (2020). DOI: 10.1016/j.jcp.2020.109678.

[68] F. Binkowski, F. Betz, M. Hammerschmidt, et al. Computation of eigenfrequency sensitivities using Riesz projections for efficient optimization of nanophotonic resonators. *Commun. Phys.* 5, 202 (2022). DOI: 10.1038/s42005-022-00977-1.

[69] F. Binkowski, L. Zschiedrich, and S. Burger. An auxiliary field approach for computing optical resonances in dispersive media. *J. Eur. Opt. Soc.-Rapid Publ.* 15, 3 (2019). DOI: 10.1186/s41476-019-0098-z.

[70] F. Binkowski, T. Wu, P. Lalanne, et al. Hot Electron Generation through Near-Field Excitation of Plasmonic Nanoresonators. *ACS Photonics* 8, 1243 (2021). DOI: 10.1021/acsphotonics.1c00231.

[71] R. Colom, F. Binkowski, F. Betz, et al. Enhanced Purcell factor for nanoantennas supporting interfering resonances. *Phys. Rev. Res.* 4, 023189 (2022). DOI: 10.1103/PhysRevResearch.4.023189.

[72] F. Betz, F. Binkowski, M. Hammerschmidt, et al. Resonance expansion of quadratic quantities with regularized quasinormal modes. *Phys. Status Solidi A*, 2200892 (2023). DOI: 10.1002/pssa.202200892.

[73] F. Jelezko, C. Tietz, A. Gruber, et al. Spectroscopy of Single N-V Centers in Diamond. *Single Mol.* 2, 255260 (2001). DOI: 10.1002/1438-5171(200112)2:4<255::AID-SIMO255>3.0.CO;2-D.

[74] S. K. H. Andersen, S. Bogdanov, O. Makarova, et al. Hybrid Plasmonic Bullseye Antennas for Efficient Photon Collection. *ACS Photonics* 5, 692 (2018). DOI: 10.1021/acsphotonics.7b01194.

[75] P. Monk. *Finite Element Methods for Maxwell's Equations.* Clarendon Press: Oxford (2003).

[76] L. Demkowicz. *Computing with hp-ADAPTIVE FINITE ELEMENTS: Volume 1 One and Two Dimensional Elliptic and Maxwell Problems (1st ed.)* Chapman and Hall/CRC: New York (2006). DOI: `10.1201/9781420011685`.

[77] L. Demkowicz, J. Kurtz, D. Pardo, et al. *Computing with hp-ADAPTIVE FINITE ELEMENTS: Volume II Frontiers: Three Dimensional Elliptic and Maxwell Problems with Applications (1st ed.)* Chapman and Hall/CRC: New York (2007). DOI: `10.1201/9781420011692`.

[78] J. Pomplun, S. Burger, L. Zschiedrich, et al. Adaptive finite element method for simulation of optical nano structures. *Phys. Status Solidi B* 244, 3419 (2007). DOI: `10.1002/pssb.200743192`.

[79] *JCMwave, JCMsuite.* `https://jcmwave.com/jcmsuite/`. Accessed: April 2023.

[80] J.-P. Berenger. A Perfectly Matched Layer for the Absorption of Electromagnetic Waves. *J. Comput. Phys.* 114, 185 (1994). DOI: `10.1006/jcph.1994.1159`.

[81] L. Zschiedrich. *Transparent boundary conditions for Maxwell's equations: Numerical concepts beyond the PML method.* PhD thesis (2009). DOI: `10.17169/refubium-7589`.

[82] P. R. Amestoy, I. S. Duff, J.-Y. L'Excellent, et al. A Fully Asynchronous Multifrontal Solver Using Distributed Dynamic Scheduling. *SIAM J. Matrix Anal. Appl.* 23, 15 (2001). DOI: `10.1137/S0895479899358194`.

[83] M. Bollhöfer, O. Schenk, R. Janalik, et al. "State-of-the-Art Sparse Direct Solvers". *Parallel Algorithms in Computational Science and Engineering.* Ed. by A. Grama and A. H. Sameh. Birkhäuser: Cham (2020). DOI: `10.1007/978-3-030-43736-7_1`.

[84] L. Trefethen and J. Weideman. The Exponentially Convergent Trapezoidal Rule. *SIAM Rev.* 56, 385 (2014). DOI: `10.1137/130932132`.

[85] P. B. Johnson and R. W. Christy. Optical Constants of the Noble Metals. *Phys. Rev. B* 6, 4370 (1972). DOI: `10.1103/PhysRevB.6.4370`.

[86] S. Raza, S. I. Bozhevolnyi, M. Wubs, et al. Nonlocal optical response in metallic nanostructures. *J. Phys. Condens. Matter* 27, 183204 (2015). DOI: `10.1088/0953-8984/27/18/183204`.

[87] A. D. Boardman. *Electromagnetic Surface Modes. Hydrodynamic Theory of Plasmon-Polaritons on Plane Surfaces.* Wiley: New York (1982).

[88] R. Ruppin. Extinction properties of thin metallic nanowires. *Opt. Commun.* 190, 205 (2001). DOI: `10.1016/S0030-4018(01)01063-X`.

[89] K. R. Hiremath, L. Zschiedrich, and F. Schmidt. Numerical solution of nonlocal hydrodynamic Drude model for arbitrary shaped nano-plasmonic structures using Nédélec finite elements. *J. Comp. Phys.* 231, 5890 (2012). DOI: `10.1016/j.jcp.2012.05.013`.

[90] G. Toscano, S. Raza, A.-P. Jauho, et al. Modified field enhancement and extinction by plasmonic nanowire dimers due to nonlocal response. *Opt. Express* 20, 4176 (2012). DOI: 10.1364/OE.20.004176.

[91] O. Schnitzer, V. Giannini, S. A. Maier, et al. Surface plasmon resonances of arbitrarily shaped nanometallic structures in the small-screening-length limit. *Proc. Royal Soc. A* 472, 20160258 (2016). DOI: 10.1098/rspa.2016.0258.

[92] J. D. Jackson. *Classical Electrodynamics, 3rd ed.* Wiley: New York (1998).

[93] L. Rickert, T. Kupko, S. Rodt, et al. Optimized designs for telecom-wavelength quantum light sources based on hybrid circular Bragg gratings. *Opt. Express* 27, 36824 (2019). DOI: 10.1364/OE.27.036824.

[94] Z. Shao, W. Porod, C. S. Lent, et al. An eigenvalue method for open-boundary quantum transmission problems. *J. Appl. Phys* 78, 2177 (1995). DOI: 10.1063/1.360132.

[95] A. I. Kuznetsov, A. E. Miroshnichenko, M. L. Brongersma, et al. Optically resonant dielectric nanostructures. *Science* 354, aag2472 (2016). DOI: 10.1126/science.aag2472.

[96] P. West, S. Ishii, G. Naik, et al. Searching for better plasmonic materials. *Laser Photonics Rev.* 4, 795 (2010). DOI: 10.1002/lpor.200900055.

[97] N. Nikolova, J. Bandler, and M. Bakr. Adjoint techniques for sensitivity analysis in high-frequency structure CAD. *IEEE Trans. Microw. Theory Techn.* 52, 403 (2004). DOI: 10.1109/TMTT.2003.820905.

[98] S. Burger, L. Zschiedrich, J. Pomplun, et al. Fast simulation method for parameter reconstruction in optical metrology. *Proc. SPIE* 8681, 380 (2013). DOI: 10.1117/12.2011154.

[99] K. Koshelev, S. Kruk, E. Melik-Gaykazyan, et al. Subwavelength dielectric resonators for nonlinear nanophotonics. *Science* 367, 288 (2020). DOI: 10.1126/science.aaz3985.

[100] G. Kewes, F. Binkowski, S. Burger, et al. Heuristic Modeling of Strong Coupling in Plasmonic Resonators. *ACS Photonics* 5, 4089 (2018). DOI: 10.1021/acsphotonics.8b00766.

[101] F. Betz, F. Binkowski, and S. Burger. RPExpand: Software for Riesz projection expansion of resonance phenomena. *SoftwareX* 15, 100763 (2021). DOI: 10.1016/j.softx.2021.100763.

[102] S. Linic, P. Christopher, and D. B. Ingram. Plasmonic-metal nanostructures for efficient conversion of solar to chemical energy. *Nat. Mater.* 10, 911 (2011). DOI: 10.1038/nmat3151.

[103] M. L. Brongersma, N. J. Halas, and P. Nordlander. Plasmon-induced hot carrier science and technology. *Nat. Nanotechnol.* 10, 25 (2015). DOI: 10.1038/nnano.2014.311.

[104] G. V. Hartland, L. V. Besteiro, P. Johns, et al. What's so Hot about Electrons in Metal Nanoparticles? *ACS Energy Lett.* 2, 1641 (2017). DOI: 10.1021/acsenergylett.7b00333.

[105] C. W. Hsu, B. Zhen, A. D. Stone, et al. Bound states in the continuum. *Nat. Rev. Mater.* 1, 16048 (2016). DOI: `10.1038/natrevmats.2016.48`.

[106] K. Koshelev, A. Bogdanov, and Y. Kivshar. Meta-optics and bound states in the continuum. *Sci. Bull.* 64, 836 (2019). DOI: `10.1016/j.scib.2018.12.003`.

[107] V. Mylnikov, S. T. Ha, Z. Pan, et al. Lasing Action in Single Subwavelength Particles Supporting Supercavity Modes. *ACS Nano* 14, 7338 (2020). DOI: `10.1021/acsnano.0c02730`.